

**DIRECTED SELF-ASSEMBLY IN BLOCK POLYMER THIN
FILMS: AN INVESTIGATION WITH NEUTRON SCATTERING
AND *IN SITU* ANALYSIS TOOLS**

by

Cameron K. Shelton

A dissertation submitted to the Faculty of the University of Delaware in partial fulfillment of the requirements for the degree of Doctor of Philosophy in Chemical Engineering

Summer 2017

© 2017 Cameron K. Shelton
All Rights Reserved

**DIRECTED SELF-ASSEMBLY IN BLOCK POLYMER THIN
FILMS: AN INVESTIGATION WITH NEUTRON SCATTERING
AND *IN SITU* ANALYSIS TOOLS**

by

Cameron K. Shelton

Approved: _____
Abraham M. Lenhoff, Ph.D.
Chair of the Department of Chemical and Biomolecular Engineering

Approved: _____
Babatunde A. Ogunnaike, Ph.D.
Dean of the College of Engineering

Approved: _____
Ann L. Ardis, Ph.D.
Senior Vice Provost for Graduate and Professional Education

I certify that I have read this dissertation and that in my opinion it meets the academic and professional standard required by the University as a dissertation for the degree of Doctor of Philosophy.

Signed:

Thomas H. Epps, III, Ph.D.
Professor in charge of dissertation

I certify that I have read this dissertation and that in my opinion it meets the academic and professional standard required by the University as a dissertation for the degree of Doctor of Philosophy.

Signed:

Norman J. Wagner, Ph.D.
Member of dissertation committee

I certify that I have read this dissertation and that in my opinion it meets the academic and professional standard required by the University as a dissertation for the degree of Doctor of Philosophy.

Signed:

Michael E. Mackay, Ph.D.
Member of dissertation committee

I certify that I have read this dissertation and that in my opinion it meets the academic and professional standard required by the University as a dissertation for the degree of Doctor of Philosophy.

Signed:

Yun Liu, Ph.D.
Member of dissertation committee

I certify that I have read this dissertation and that in my opinion it meets the academic and professional standard required by the University as a dissertation for the degree of Doctor of Philosophy.

Signed:

Joseph A. Dura, Ph.D.
Member of dissertation committee

ACKNOWLEDGMENTS

I first would like to thank my advisor, Thomas Epps. He has provided invaluable support and guidance over the course of my research in the last five years. He also has always encouraged a culture of high standards without which I would not have grown as much as I have. Most importantly, I would like to thank him for allowing me to become an independent thinker and to guide my research. Even when some of my ideas seemed unachievable, he was always willing to discuss projects with me and test theories in pursuit of knowledge.

I also would like to acknowledge my committee members: Norman Wagner, Michael Mackay, Yun Liu, and Joseph Dura. Prof. Wagner has been a key supporter from day one, especially when it came to the use of neutron scattering and moving to the National Institute of Standards and Technology (NIST). I felt I could always talk with him about research or life and for that I am grateful. I am appreciative for Prof. Mackay agreeing to serve on my committee and offering helpful insights and suggestions on my work. I also am thankful for all the support Dr. Liu has given me as a member on my committee and during my visits for beamtime at NIST. I am grateful for the immeasurable support and advice given by Dr. Dura and for all the time he devoted to teach me neutron reflectometry, even when it required late nights and weekends.

Next, I would like to acknowledge my fellow group members for all their help and support throughout my time at the University of Delaware. I first would like to thank previous group members for mentoring me and teaching me everything I needed

to know to become successful. In particular, Ming Luo and Jillian Emerson for being my primary mentors and helping me with anything and everything that arose, Liz Kelley for teaching me the ins and outs of NIST and neutron scattering and for grabbing lunch with me or listening to me ramble after long nights on the neutron beam, Sarah Mastroianni for informing me of the most important “unwritten rules” of graduate school, being a distraction when stress levels were high, and always being there to talk out research problems, and Kai Mayeda, Matt Green, Angela Holmberg, and Wei-Fan Kuan for providing guidance throughout the course of my research. I also would like to thank all my fellow thin film group members for their help: Tom Gartner, Jack Saltwick, Doug Scott, Sophia Freaney, and James Mannino. To my two classmates in the Epps Research Group, Kaleigh Reno and Chad Greco, I want to say thank you for being there through classes, exams, and research. We survived it all, and I am glad we did it together. I would like to thank Melody Morris for all her research advice and assistance and, more importantly, for providing helpful distractions. Lastly, I would like to acknowledge all the other graduate students I have had the pleasure of working with: Shu Wang, Tiffany Suekama, Rashida Ruddock, Emma da Baets, Laurens Heusele, Priyanka Ketcarr, Gregory Peterson, and Thu Vi.

I also appreciate all my collaborators at NIST. In particular, I would like to acknowledge Ron Jones, my mentor at NIST throughout my research project. I am incredibly grateful he was willing to take the time to teach me how to set up and run experiments, navigate the NIST culture, and plan for a life after graduate school. I also would like to thank Dan Neumann, Paul Butler, Brian Maranville, Brian Kirby, Katie Weigandt, and Amanda McDermott for helping me at NIST.

I owe a debt of gratitude to all the staff that helped me with any and every problem I came across throughout my Ph.D. I especially would like to thank Kathie Young for keeping me sane with all the necessary forms and deadlines. I also would like to thank Chaoying Ni, Frank Kriss, and Jennifer Sloppy in the Keck Advanced Materials Characterization Lab for all their help with the microscopy that was needed in my project.

Finally, I would like to thank all my family and friends, without whom none of this would be possible. I would like to start by acknowledging my friends from the University of Virginia, Matt Kelly, Erika Svirnovskiy, and Cynthia Zahrah, for always checking in and keeping my spirits up in the crazy life that is graduate school. I also would like to thank all my friends at the University of Delaware, especially Ryan Patet, Chad Greco, Andrew Tibbits, Chris Long, and Kay Siu for helping me have fun and being supportive when times were tough. I also greatly appreciate all the love, help, and support my family has given me, especially my mom, dad, and older brother Chris. You all always believed in me and made sure I had everything I needed to be successful, and for that I am very grateful. Finally, I would like to thank my fiancé Katie for being by my side throughout this whole process. When times were good, you celebrated with me, and when times were tough, you picked me up. You always supported me whether I was near or far and I cannot wait to start the next adventure with you.

TABLE OF CONTENTS

LIST OF TABLES	xiv
LIST OF FIGURES	xv
ABSTRACT	xliii

Chapter

1	BLOCK POLYMER THIN FILM SELF-ASSEMBLY	1
1.1	Introduction	1
1.2	Thermodynamics of Bulk Block Polymer Self-Assembly	2
1.3	Confinement Effects in Thin Films	5
1.3.1	Film Thickness Effects	6
1.3.2	Substrate Surface Effects	8
1.3.3	Free Surface Effects	11
1.4	Annealing Techniques for Order/Orientation Control	12
1.4.1	Thermal Annealing	13
1.4.2	Solvent Vapor Annealing	14
1.4.2.1	Solvent Choice	15
1.4.2.2	Solvent Uptake and Annealing Time	17
1.4.2.3	Solvent Removal Rate	18
1.5	Directed Self-Assembly Techniques	19
1.5.1	Graphoepitaxy and Chemical Prepatterning	19
1.5.2	Zone Casting/Annealing	21
1.5.3	Shear-Alignment	24
1.5.3.1	Hard Shear	25
1.5.3.2	Soft Shear	26
1.5.4	Electrical/Magnetic Field Alignment	28
1.6	<i>In Situ</i> Measurements During Annealing	29

1.7	Dissertation Overview	29
REFERENCES		32
2	EXPERIMENTAL METHODS AND CHARACTERIZATION TECHNIQUES	45
2.1	Substrate Modification	45
2.1.1	Ultra-Violet Ozone	45
2.1.2	Chlorosilane Deposition	46
2.1.3	Random Copolymer Monolayers	47
2.2	Contact Angle Goniometry	48
2.3	Thin Film Casting.....	50
2.3.1	Spin Coating	50
2.3.2	Flow Coating	51
2.4	Block Polymer Thin Film Processing	52
2.4.1	Thermal Annealing.....	52
2.4.2	Solvent Vapor Annealing	53
2.5	Polydimethylsiloxane Preparation for Shear-Alignment	55
2.6	Spectral Reflectance	55
2.7	Optical Microscopy	58
2.8	Atomic Force Microscopy	58
2.9	X-Ray Scattering	61
2.9.1	Small-Angle X-Ray Scattering.....	62
2.9.2	X-Ray Reflectivity.....	64
2.10	Neutron Scattering.....	65
2.10.1	Small-Angle Neutron Scattering	65
2.10.2	Neutron Reflectometry	67
2.11	Mass Spectroscopy	69
REFERENCES		71
3	DECOUPLING OF SUBSTRATE SURFACE INTERACTIONS IN BLOCK POLYMER THIN FILM SELF-ASSEMBLY	76

3.1	Introduction	76
3.2	Materials and Methods	80
3.2.1	Substrate Surface Modification and Characterization	80
3.2.2	Polymer Film Preparation and Characterization	81
3.3	Results and Discussion	83
3.3.1	Substrate Wetting Behavior	84
3.3.2	Through-Film Propagation of Substrate Surface Effects	90
3.3.3	<i>In Situ</i> Study of Hole Formations	93
3.3.4	Substrate/Free Surface Competition	95
3.3.4.1	Identifying Critical Film Thicknesses with Optical Microscopy	95
3.3.4.2	Verifying Transition Regions with Atomic Force Microscopy	97
3.4	Prediction of Substrate Surface Energy Effects	101
3.4.1	Wetting Behavior and Through-Film Driving Force	101
3.4.2	Maximum Propagation of Substrate Surface Energy Effects	104
3.5	Conclusions	108
	REFERENCES	110
4	<i>IN SITU</i> NEUTRON SCATTERING DURING SOLVENT VAPOR ANNEALING OF CYLINDRICAL BLOCK POLYMER THIN FILMS	114
4.1	Introduction	114
4.2	Materials and Methods	117
4.2.1	Preparation and Characterization of Thin Films	117
4.2.2	Solvent Vapor Annealing	118
4.2.3	<i>In Situ</i> Small-Angle Neutron Scattering	119
4.2.4	<i>In Situ</i> Neutron Reflectometry	121
4.3	Results and Discussion	122
4.3.1	Neutral/Slightly Selective Solvents	122
4.3.1.1	Solvent Diffusion and Segregation	122
4.3.1.2	Nanostructure Reorganization Effects	127
4.3.1.3	Substrate to Free Surface Solvent Profiles	133

4.3.2	Highly Selective Solvents.....	137
4.4	Conclusions	140
REFERENCES.....		142
5	MANIPULATION OF SHEAR-ALIGNMENT EFFECTS IN BLOCK POLYMER THIN FILMS.....	147
5.1	Introduction	148
5.2	Materials and Methods	151
5.2.1	Thin Film Casting and Characterization.....	151
5.2.2	Polydimethylsiloxane Pad Preparation.....	152
5.2.3	Small-Angle Neutron Scattering during Solvent Vapor Annealing with Soft Shear.....	153
5.3	Results and Discussion.....	155
5.3.1	Kinetics of Solvent Vapor Annealing with Soft Shear.....	155
5.3.2	Tuning Polydimethylsiloxane Swelling/Shear <i>via</i> Elasticity	162
5.3.3	Controlling Alignment Drying Fronts.....	166
5.3.3.1	Drying Rate Effects	166
5.3.3.2	Gradient Thickness Polydimethylsiloxane Pads	168
5.4	Shear-Alignment during Casting.....	170
5.5	Conclusions	174
REFERENCES.....		176
6	QUANTIFICATION OF SALT DISTRIBUTIONS IN BLOCK POLYMER ELECTROLYTE THIN FILMS.....	180
6.1	Introduction	181
6.2	Materials and Methods	183
6.2.1	Preparation of Salt-Doped Polymer Electrolyte Solutions and Films	183
6.2.2	Neutron Reflectometry of Salt-Doped Polymer Films.....	184
6.3	Lithium Salt Distribution from Neutron Reflectometry.....	186
6.4	Conclusions	194
REFERENCES.....		196

7	CONCLUSIONS AND FUTURE WORK.....	198
7.1	Dissertation Summary	198
7.1.1	Substrate Modification for Through-Film Order and Orientation Control.....	199
7.1.2	Nanostructure Reorganization Pathways during Solvent Vapor Annealing and Solvent Vapor Annealing with Soft Shear	201
7.1.3	Determination of Lithium Salt Distribution in Block Polymer Electrolyte Films	204
7.1.4	Concluding Remarks	205
7.2	Future Directions.....	206
7.2.1	Patterned Polydimethylsiloxane Thickness/Elasticity.....	206
7.2.2	Shear-Alignment during Film Casting	209
7.2.3	Reversible Roughening of Substrate Surfaces	211
7.2.4	Directing Designer Block Polymer Self-Assembly.....	215
7.2.5	Advancing Neutron Scattering of Block Polymer Thin Films ..	218
	REFERENCES.....	222
	Appendix	
A	SUPPORTING INFORMATION FOR CHAPTER 3	230
	REFERENCES.....	235
B	SUPPORTING INFORMATION FOR CHAPTER 4	236
B.1	SANS Broad Peak Model Analysis to Calculate Solvent Concentration	249
B.2	Incommensurability Between Film Thickness, Layer Thickness, and Number of Layers.....	256
	REFERENCES.....	259
C	SUPPORTING INFORMATION FOR CHAPTER 5	260
	REFERENCES.....	267
D	SUPPORTING INFORMATION FOR CHAPTER 6	268
D.1	Salt-Doped POEM Contrast Match with PS Calculations	271

REFERENCES	272
E TEXT AND FIGURE REPRINT PERMISSIONS	273

LIST OF TABLES

Table 2.1:	Common block polymer morphologies and corresponding SAXS peak locations.....	63
Table 3.1:	Average water and diiodomethane contact angle measurements along with corresponding surface energies for bare silica and chlorosilane monolayer substrates	84
Table 4.1:	Broad peak model fit parameters for SIS thin films swollen with <i>d</i> -benzene.....	125

LIST OF FIGURES

- Figure 1.1: Potential technologies enabled and/or improved through BP thin film self-assembly into nanometer-scale periodic structures. Adapted with permission from Hu, H. *et al. Soft Matter* **2014**, 10, 3867-3889, Copyright 2014 The Royal Society of Chemistry.¹⁰ 2
- Figure 1.2: Theoretical phase diagram for AB diblock copolymer melts indicating the regions in which BPs disorder or form ordered spherical (S), cylindrical (C), gyroid network (G), or lamellar (L) structures as determined by self-consistent field theory and the Flory-Huggins polymer-polymer interaction parameter (χ), degree of polymerization (N), and block volume fractions (f). The phase diagram was adapted with permission from Matsen, M. W. *Macromolecules* **2012**, 45, 2161-2165, Copyright 2012 American Chemical Society.¹⁵ The 3-D morphology illustrations were adapted with permission from Lynd, N. A. *et al. Prog. Polym. Sci.* **2008**, 33, 875-893, Copyright 2008, Elsevier.¹⁶ 4
- Figure 1.3: Top-view optical micrograph of a gradient thickness poly(*n*-butyl acrylate-*b*-methyl methacrylate) BP film. Scale bar represents 10 μm . At incommensurate thicknesses, energetically unfavorable chain stretching and compression resulted in the formation of incomplete layers of thickness L_0 called islands and holes as shown in the side-view schematic; at commensurate thicknesses, chain stretching and compression is mitigated and featureless surfaces are formed. The thickness difference between commensurate areas is equal to L_0 7
- Figure 1.4: Cross-sectional transmission electron micrographs of PS-PMMA films on substrates modified with random PS-PMMA brushes with (a) 58 vol% and (b) 70 vol% PS in the random PS-PMMA monolayers. The films are approximately 400 nm thick, and the scale bar equals 100 nm. Because the surface energy of the 58 vol% PS monolayer was closer to a neutral condition, the substrate-polymer interaction did not propagate through the film as far as the 70 vol% PS monolayer, and the orientation of the nanostructures changed due to free surface interactions. Adapted with permission from Xu, T. *et al. Macromolecules* **2005**, 38, 2802-2805, Copyright 2005 American Chemical Society.⁴⁶ 10

- Figure 1.5: Scanning electron micrographs of oven annealed cylinder-forming PS-PMMA films over a range of different annealing times and temperatures. The width of one image is 500 nm. Adapted with permission from Majewski, P. W. and Yager, K. G. *Soft Matter* **2016**, 12, 281-294, Copyright 2016 The Royal Society of Chemistry.⁸¹ 14
- Figure 1.6: Atomic force micrographs (top row) and GISAXS profiles (bottom row) for PHEMA-PMMA films (a, b) as-cast, annealed in (c, d) 80/20 vol/vol, (e, f) 50/50 vol/vol, and (g, h) 20/80 vol/vol THF/MeOH for 45 min, and annealed in (i, j) 50/50 vol/vol THF/MeOH for 3 – 4 h. Adapted with permission from Chavis, M. A. *et al. Adv. Funct. Mater.* **2015**, 25, 3057-3065, Copyright 2016 John Wiley & Sons, Inc.¹¹⁴ 17
- Figure 1.7: Schematic representation of the chemical preprocessing technique in which a phenylethyltrichlorosilane (PETS) self-assembled monolayer (SAM), photoresist, and soft X-rays were used to generate PS and PMMA preferential patterns, on which PS-PMMA BP films were cast and thermally annealed. With this technique, a multitude of patterns can be produced including lines, bends, jogs, and T-junctions. The chemical prepatterning schematic was adapted with permission from Kim, S. O. *et al. Nature* **2003**, 424, 411-414, Copyright 2003 Nature Publishing Group.¹³⁶ The lines/bends and jogs/T-junction micrographs were adapted with permission from Chang, T.-H. *et al. Sci. Rep.* **2016**, 6, 31407, Copyright 2016 The Authors, and Liu, G. *et al. Adv. Funct. Mater.* **2010**, 20, 1251-1257, Copyright 2010 John Wiley & Sons, Inc, respectively.^{137, 138} 21
- Figure 1.8: Schematic of laser zone annealing technique used to order and align BP thin film nanostructures: Photothermal gradients generated from a high-intensity laser and a light-absorbing germanium monolayer improved ordering kinetics by at least three orders of magnitude and provided nanoscale control over directionality to produce patterns such as T-junctions. Adapted with permission from Majewski, P. W. and Yager, K. G. *ACS Nano*, **2015**, 9, 3896-3906, Copyright 2015 American Chemical Society.¹⁵⁸ 24

Figure 1.9: Schematic representation of SVA-SS. A PDMS pad, with initial dimensions L_0 and W_0 , is placed on a BP film and exposed to solvent vapor. The solvent vapor swells the PDMS to new dimensions L and W and provides mobility to the polymer chains in the film. During solvent removal, a drying front propagates from one corner of the PDMS to align nanostructures until solvent is completely removed from the system. Adapted with permission from Qiang <i>et al. Soft Matter</i> , 2014 , 10, 6068-6076, Copyright 2014 The Royal Society of Chemistry. ¹⁷⁵	27
Figure 2.1: Visual representation of the different surface energy components of Young's equation for a liquid drop on a solid surface. Adapted with permission from Makkonen, L. <i>J. Phys. Conden. Matter</i> 2016 , 28, 135001, Copyright 2016 IOP Publishing Ltd. ¹⁹	49
Figure 2.2: Schematic of flow coating setup with key parameters labeled. As the motor stage holding the substrate is drawn under the casting blade with speed U , polymer solution is left behind. Then, the solvent evaporates from the solution leaving behind a dry polymer film. Adapted with permission from Davis, R. L. <i>et al. Langmuir</i> , 2014 , 30, 5637, Copyright 2014 American Chemical Society. ²⁹	52
Figure 2.3: Schematic of RSVA. The flat tip needle directs the solvent into specific areas of the film to induce nanostructure reorganization. In combination with an x-y motor stage, 2-D patterns can be drawn into the BP film with solvent vapors. Adapted with permission from Seppala, J. E. <i>et al. ACS Nano</i> , 2012 , 6, 9855, Copyright 2012 American Chemical Society. ³³	54
Figure 2.4: Visual description of spectral reflectance setup (left side), which uses a fiber optic cable to generate light that reflects off the sample and to measure the intensity of light as it returns. As the light travels through different layers of the film/substrate (right side), it is either reflected or transmitted. The intensity and phase (ϕ) of the reflected light produces a reflection pattern, which can be modeled using refractive index (n) and extinction coefficient (k) parameters of the different layers to extract the film thickness (d). Images from Filmetrics.com. ³⁷	57
Figure 2.5: Graphic of the key components of an atomic force microscope. Image from the Virtual Microscope Imaging Technology Group, University of Illinois at Urbana-Champaign. ⁴²	59

- Figure 2.6: Scattering geometry for SAXS scattering experiments. Incident X-rays with wavelength λ normal to the sample (\mathbf{k}) are scattered by electron cloud interactions to new angles (\mathbf{k}_s). The difference between \mathbf{k}_s and \mathbf{k} is referred to as \mathbf{q} , which is related to the size scale of the features in the sample. 63
- Figure 2.7: Schematic of specular NR geometry with incident and reflected neutron angles. Neutrons striking the sample can either reflect off or transmit through each layer in the film. The reflections from each layer constructively and destructively interfere to generate the recorded intensity profiles as a function of the scattering variable Q_z . Top image adapted with permission from Demkowicz, M.J. and Majewski, J. *Metals* **2016**, 6, 20, Copyright 2016 by the authors.⁶⁸ Bottom image adapted with permission from Piscitelli, F. *et al. Proc. R. Soc. A*, **2016**, 472, 20150711, Copyright 2016 by the authors.⁶⁹ 68
- Figure 2.8: Diagram of the key pieces of a mass spectrometer. The sample is ionized and accelerated by an ion source into the mass analyzer that deflects the ions on the basis of their mass-to-charge (m/z) ratios. Then, ions strike the ion detector at different locations determined by the deflection, and the relative abundance of each ion is measured. Image from Thermo Fisher Scientific.⁷⁴ 70
- Figure 3.1: OM images of commensurate (t_C) and incommensurate film thickness regions for bare silica and chlorosilane monolayers as indicated by presence (or lack) of islands and holes. Bare silica, aceto silane, and benzyl silane substrates constrained PMMA-PnBA to asymmetric wetting as commensurate thicknesses were noted at a half-integer L_0 thickness. Films cast on methacryl and n -butyl silane substrates exhibited symmetric wetting as island and hole formations were present at half-integer L_0 thicknesses. The location of island and hole formations indicated bare silica, aceto silane, and benzyl silane substrates were preferential for PMMA, and methacryl silane and n -butyl silane substrates were preferential for PnBA. The scale bar represents 10 μm and applies to all micrographs. Reprinted with permission from Shelton C. K. and Epps, T. H., III *Macromolecules* **2015**, 48, 4572-4580, Copyright 2015 American Chemical Society.³⁵ ... 86

Figure 3.2: Comparison between predicted (dotted line intersecting x-axis) and experimentally determined (dotted line intersecting y-axis) wetting behavior of PMMA-*Pn*BA on different substrate surfaces using decoupled (black circles) and total (white squares) surface energy approaches. Shaded quadrants represent incongruities between predicted and experimental results. Negative interfacial energy differences predict that the *Pn*BA block has a lower interfacial energy with the substrate and will wet the substrate surface, while positive interfacial energy differences predict that the PMMA block has a lower interfacial energy and will wet the substrate surface. The *Pn*BA block was expected to wet the free surface in all cases due to its lower total surface energy. Reprinted with permission from Shelton C. K. and Epps, T. H., III *Macromolecules* **2015**, 48, 4572-4580, Copyright 2015 American Chemical Society.³⁵ 88

Figure 3.3: Scheme depicting wetting behavior in BP thin films using three cases. In Case 1, PMMA has a lower interfacial energy than *Pn*BA, and a net long-range attractive force is present, resulting in asymmetric wetting. In Case 2, long-range, repulsive interactions exist at the substrate-PMMA interface as the higher surface energy PMMA layer separates the lower surface energy substrate and *Pn*BA layers. Therefore, *Pn*BA segregates to the substrate, stabilizing the substrate-polymer interactions and resulting in symmetric wetting. In Case 3, *Pn*BA has a lower interfacial energy, there is a net attractive interaction in the system, and symmetric wetting is predicted. Aligning each case to the appropriate system, as shown in the plot, accurately matched predicted and experimental results. Reprinted with permission from Shelton C. K. and Epps, T. H., III *Macromolecules* **2015**, 48, 4572-4580, Copyright 2015 American Chemical Society.³⁵ 90

- Figure 3.4: Hole sizes on aceto silane, benzyl silane, methacryl silane, and *n*-butyl silane surfaces (black circles), UVO treated benzyl silane and *n*-butyl silane surfaces (gray circles), and bare silica (white circles) substrates. Two equations were used to compare with hole size: (a) Equation 3.3, in which the attractive forces were described using the total surface energy, and (b) Equation 3.2, in which the attractive forces were decoupled. The dotted red line represents a linear fit to the data. Though the two fits have similar R^2 values (0.92 for the total surface energy equation and 0.96 for the decoupled surface energy equation), the total surface energy equation did not capture the expected trend in hole size, with the major deviation noted at lower interfacial energy differences. The decoupled surface energy equation ($R^2 = 0.96$) captured the experimental trend more accurately over the entire data range. Reprinted with permission from Shelton C. K. and Epps, T. H., III *Macromolecules* **2015**, 48, 4572-4580, Copyright 2015 American Chemical Society.³⁵ 92
- Figure 3.5: (a) Schematic of *in situ* anneal setup with a sealed Linkam thermal stage under an optical microscope. The Linkam thermal stage heated the film to 175 °C using a 3 °C/min heat ramp for consistency with vacuum oven annealed samples. (b) Size measurements from holes produced on bare silica and benzyl silane substrates over 24 h indicated expected nucleation and growth kinetics, followed by island and hole stabilization at equilibrium sizes, that match those from oven annealed samples. The scale bar represents 20 μm and can be applied to all micrographs. Reprinted with permission from Shelton C. K. and Epps, T. H., III *Macromolecules* **2015**, 48, 4572-4580, Copyright 2015 American Chemical Society.³⁵ 94
- Figure 3.6: Stitched OM images of gradient thickness PMMA-*Pn*BA films on bare silica and chlorosilane-modified substrates. Films were imaged up to thicknesses at which islands and holes disappeared at integer domain spacing (nL_0) thicknesses for asymmetric wetting substrates (bare silica, aceto silane, benzyl silane) and at half-integer domain spacing ($[n+0.5]L_0$) thicknesses for symmetric wetting substrates (methacryl silane, *n*-butyl silane). The red boxes indicate the critical film thickness at which island and hole formations were expected but not present at the free surface. The scale bar applies to all micrographs. Reprinted with permission from Shelton, C. K. and Epps, T. H., III *Macromolecules* **2016**, 49, 574-580.⁵⁴ 97

Figure 3.7: Free surface AFM images of PMMA-*Pn*BA gradient thickness films on bare silica substrates. After the film thickness surpassed the critical propagation distance of substrate surface effects (287 nm), there was a distinct change in the surface nanostructure behavior caused by the substrate/free surface competition. At substrate dominant thicknesses (top row), perpendicular *Pn*BA cylinders (brown) perforate through PMMA domains (yellow). At substrate/free surface competition thicknesses (bottom row), the lower surface energy *Pn*BA is driven to the free surface, causing the cylinders to “fold” and appear as short parallel cylinders. All images were taken from the bulk film, outside of island and hole formations. The free surface structure did not change on island and hole formations except at the bulk film interface where large thickness differences produced artificial stretched domains. The scale bar represents 200 nm and applies to all AFM images. Reprinted with permission from Shelton, C. K. and Epps, T. H., III *Macromolecules* **2016**, 49, 574-580.⁵⁴ 99

Figure 3.8: FWHM values of the primary peak from the azimuthally averaged FFT intensity spectrum from AFM images capturing the free surface nanostructure orientation of gradient thickness PMMA-*Pn*BA films on bare silica, aceto silane, benzyl silane, methacryl silane, and *n*-butyl silane substrates. The shaded region indicates the FWHM value ($\approx 0.06-0.08$), at which a significant orientation change occurred. The colored arrows represent the estimated critical film thickness (from OM) at which films cast on each substrate crossed this FWHM threshold. The critical film thicknesses determined using AFM matched well with those measured from OM. The decrease in FWHM in aceto silane and bare silica samples is attributed to a possible transition to a free surface dominated nanostructure with a more uniform orientation at larger film thicknesses. The lines connecting data points are to guide the eye and do not represent a mathematical fit to the data. Reprinted with permission from Shelton, C. K. and Epps, T. H., III *Macromolecules* **2016**, 49, 574-580.⁵⁴ 101

Figure 3.9: Composite prediction of surface wetting and through-film behavior to pinpoint necessary substrate surface energy conditions to achieve prescribed substrate wetting behavior. The dotted lines separate the plot into three possible substrate wetting behaviors (PMMA preferential, PnBA preferential, and neutral) using the total surface energy and Hamaker constant analysis. The neutral region indicates a non-preferential substrate region as the total surface energy and Hamaker constant calculations result in a different block being preferential, although the strength of either of these parameters can dominate and force a preferential substrate (*e.g.*, methacryl silane). The gradient across the plot represents the change in the substrate self-assembly driving force calculated using the decoupled surface energy. Reprinted with permission from Shelton C. K. and Epps, T. H., III *Macromolecules* **2015**, 48, 4572-4580, Copyright 2015 American Chemical Society.³⁵ 103

Figure 3.10: Propagation distances of substrate surface effects for PMMA-PnBA BP films on modified substrates. OM was used to identify the critical film thicknesses (gray circles) at which island and hole formations disappeared marking the transition between the substrate surface dominant (below dashed red line) and substrate/free surface competition (above dashed red line) film thicknesses. AFM was employed to characterize free surface nanostructure orientation on films of increasing film thickness as either substrate dominant effects (uniform nanostructure orientation; white circles) or substrate/free surface competition effects (mixed nanostructure orientation; black circles). The dashed red line is to guide the eye and does not represent a mathematical fit to the data. Reprinted with permission from Shelton, C. K. and Epps, T. H., III *Macromolecules* **2016**, 49, 574-580.⁵⁴ 105

- Figure 3.11: Comparison of total (Equation 3.1; black circles), long-range (Equation 3.4; white squares), and decoupled (Equation 3.2; gray triangles) interfacial energies used to track the propagation of the substrate surface effect. The lines between data points are to guide the eye. Although the results from total and decoupled interfacial energy formalisms described no clear trend, those from the long-range interfacial energy equation depicted an increase in propagation distance with increasing substrate interfacial energy difference at lower differences. Additionally, the long-range equation indicated a possible plateau in the critical film thickness at larger interfacial energy differences, a result that mirrored AFM data in Figure 3.10; the long-range data points in Figure 3.11 are the transition (grey) points from Figure 3.10. Reprinted with permission from Shelton, C. K. and Epps, T. H., III *Macromolecules* **2016**, 49, 574-580.⁵⁴ 107
- Figure 3.12: Comparison of critical propagation depths of the substrate surface field for PMMA-PnBA and PS-PMMA BP systems. These depths are normalized by system-dependent L_0 's and plotted versus normalized long-range interfacial energy differences. The substrate interfacial energy difference was normalized relative to the total surface energy difference between the blocks. PS-PMMA data was taken from the literature.⁸ The lines between data points are to guide the eye. Reprinted with permission from Shelton, C. K. and Epps, T. H., III *Macromolecules* **2016**, 49, 574-580.⁵⁴ 108
- Figure 4.1: Plot of azimuthally averaged SANS intensity profiles from SIS films exposed to different partial pressures (p/p_{sat}) of *d*-benzene. The Bragg peak at $Q^* \approx 0.020 \text{ \AA}^{-1}$ corresponded to a nearest-neighbor $L_0 = 36 \text{ nm}$ that did not change with p/p_{sat} . Reprinted with permission from Shelton, C. K. *et al. Macromolecules* **2016**, 49, 7525-7534, Copyright 2016 American Chemical Society.⁴¹ 124
- Figure 4.2: Solvent content in PS and PI domains calculated from broad peak model fits to azimuthally averaged SANS intensity profiles indicated that the normalized *d*-benzene mol% (moles *d*-benzene in PS [or PI] divided by moles *d*-benzene plus PS [or PI]) was always higher in the PS domains compared to the PI domains (*i.e.*, the solvent was PS-preferential). Additionally, the ratio of solvent to polymer within a particular domain increased with p/p_{sat} . Error bars were calculated by propagating differences of $\pm 5 \text{ vol\%}$ total solvent in the film through the calculations. Reprinted with permission from Shelton, C. K. *et al. Macromolecules* **2016**, 49, 7525-7534, Copyright 2016 American Chemical Society.⁴¹ 126

Figure 4.3: NR profiles (data points) and model fits (black lines) for *d*-benzene swollen SIS films at different p/p_{sat} in the order that they were run from top to bottom. Upon exposure to solvent vapor, the film increased in thickness (t) due to solvent swelling and developed repeating parallel cylinder layers as evidenced by the narrowing of Kiessig fringes and the formation of a Bragg peak, respectively. In general, L_z decreased with the value of p/p_{sat} . However, L_z increased slightly from $p/p_{sat} = 0.93$ to $p/p_{sat} = 0.84$. The NR profiles have been vertically offset for clarity. Reprinted with permission from Shelton, C. K. *et al. Macromolecules* **2016**, 49, 7525-7534, Copyright 2016 American Chemical Society.⁴¹ 129

Figure 4.4: Schematic detailing the process by which SIS nanostructures restructured during SVA. SVA promoted layering of parallel cylinders by swelling the film to impart chain mobility *via* reduction of the T_g of the glassy PS domains below the annealing temperature (25 °C). To account for the film thickness (t) reduction during solvent removal from $p/p_{sat} = 0.93$ to $p/p_{sat} = 0.84$, n decreased, rather than L_z , to prevent unfavorable compression of the polymer chains. However, commensurability conditions from mismatches in t and n and an increased χ_{PS-PI} led to slightly stretched layers ($L_z = 27$ to $L_z = 29$). When there was not enough solvent in the film to lower the PS T_g below 25 °C ($p/p_{sat} \leq 0.59$), n could no longer adjust to account for thickness changes; instead, the average L_z decreased with the value of p/p_{sat} to account for the change in t . The error in t was recorded as ± 10 nm to account for roughness at the free surface that limited the accuracy of film thickness measurements. Although the SANS and NR profiles suggest the in-plane and out-of-plane structure is not perfectly-ordered, the schematic depicts uniform parallel cylinder morphology for clarity in describing the mechanisms for domain restructuring. Reprinted with permission from Shelton, C. K. *et al. Macromolecules* **2016**, 49, 7525-7534, Copyright 2016 American Chemical Society.⁴¹ 132

- Figure 4.5: NR data (open blue circles) and multilayer model fit (black line) for $p/p_{sat} = 0.93$. The inset plot details the free surface (depth = 0) to substrate ρ profile from the model fit. The oscillating ρ with depth resulted from the layer model incorporating pure PI (lower initial ρ and less solvent) and PS/PI mixture layers (higher initial ρ and more solvent). As shown in the illustration, PS/PI layers contained cylindrical domains, and pure PI layers represented the space between nearest neighbor cylindrical layers. Reprinted with permission from Shelton, C. K. *et al. Macromolecules* **2016**, 49, 7525-7534, Copyright 2016 American Chemical Society.⁴¹ 134
- Figure 4.6: Solvent profiles of *d*-benzene in SIS films from the free surface (depth = 0) to substrate (depth = 1). At $p/p_{sat} \leq 0.59$, large deviations from through-film solvent uniformity were noted. The average solvent concentration in the film at each p/p_{sat} was in reasonable agreement with the values determined by SANS at the same p/p_{sat} values (dashed lines). The lines between data points are to guide the eye. Reprinted with permission from Shelton, C. K. *et al. Macromolecules* **2016**, 49, 7525-7534, Copyright 2016 American Chemical Society.⁴¹ 136
- Figure 4.7: NR profiles of dry SIS films (top profile), fully swollen SIS films (second profile; swollen with 10 mL/min *d*-acetone-rich nitrogen), and SIS films dried to nitrogen/*d*-acetone to diluent nitrogen ratios of 8:2, 6:4, 4:6, and 0:10 (third profile to bottom). Broad Bragg peaks developed at $Q_z = 0.021 \text{ \AA}^{-1}$ and $Q_z = 0.040 \text{ \AA}^{-1}$ after exposure to *d*-acetone. The Bragg peaks shifted to higher Q_z values as the film was deswelled. 138
- Figure 4.8: NR profiles of dry *d*SI*d*S films (top profile), fully swollen *d*SI*d*S films (second profile; swollen with 10 mL/min *d*-hexane-rich nitrogen), and dried to nitrogen/*d*-hexane to diluent nitrogen ratios (mL/min:mL/min) of 8:2, 6:4, 4:6, and 0:10 (third profile to bottom). A broad Bragg peak in the dry film disappeared after swelling and deswelling with *d*-hexane. 140

- Figure 5.1: Temporal series of SANS profiles that track BP and PDMS swelling and deswelling during (a) SVA-SS or (b) SVA. An order of magnitude drop in the primary peak scattering intensity was recorded during SVA-SS processing; a similar intensity drop was not noted during SVA processing. However, the primary peak scattering intensity for the SVA-SS sample returned to initial levels as the film was deswelled. *Note: the SVA-SS profiles have higher absolute scattering intensities in comparison to SVA profiles due to increased background scattering from the PDMS pads.*⁴¹ 156
- Figure 5.2: SANS scattering data and representative AFM phase images with FFTs of *dSIIdS* films after SVA-SS (a, b, c) or SVA (d, e, f), respectively. SANS data and AFM images of films subjected to SVA-SS had anisotropic rings (anisotropy highlighted with dashed white circles) and displayed well-ordered nanostructures, respectively, in contrast to the isotropic rings and mixed nanostructure orientations noted in the analysis of films exposed to SVA alone. SVA-SS FFTs from AFM were dot patterns rather than crescent patterns as obtained from the SANS data on similar samples, as the smaller AFM scan area (μm^2) was not able to capture the full film behavior in a manner similar to the SANS studies (mm^2). The scale bars in both AFM images represent 250 nm.⁴¹ 159
- Figure 5.3: Azimuthally averaged SANS profiles for as-cast and fully swollen *dSIIdS* films at different solvent-rich stream to diluent stream flow rates (10:0, 8:2, and 6:4 - mL/min:mL/min). The scattering intensity of the primary peak (at $Q = 0.015 \text{ \AA}^{-1}$) decreased as solvent concentration increased (10:0 > 8:2 > 6:4). The as-cast profile had a less intense primary peak than the 8:2 and 6:4 samples due to the lack of solvent swelling. The primary peak intensity increased within the first 30 minutes of solvent swelling as shown in Figure 5.1. The degree of PDMS swelling increased with increasing solvent concentration as indicated by the rise in background scattering, in comparison to as-cast samples, primarily as a result of larger PDMS (diffuse) scattering volumes. Error bars represent one standard deviation from the measured intensity and were calculated during data reduction.⁴¹ 161

- Figure 5.4: SANS data and representative AFM images for *dSI**dS* films subjected to SVA-SS from PDMS pads with elastomer-to-curing agent ratios (wt:wt) of 5:1 [most elastic, least swelling], 10:1, 15:1, or 20:1 [least elastic, most swelling]. SANS scattering data are shown in the first column as a function of elastomer-to-curing agent ratio. Azimuthally averaged profiles are presented in the second column, in which the diffraction peaks are marked by yellow arrows. Annularly averaged profiles are displayed in the third column, in which blue arrows mark the peak locations and are used to highlight changes in alignment direction from single direction (5:1 and 10:1; 2 peaks), to poorly-aligned (15:1; no high-intensity peaks), to multiple direction (20:1; 4 peaks). AFM phase images and corresponding orientation parameter values (*S*; calculated from FFTs of the micrographs) are shown in the fourth column. The scale bar for the AFM images represents 250 nm and applies to all micrographs. Error bars in plots represent one standard deviation from the measured intensity and were calculated during data reduction.⁴¹ 163
- Figure 5.5: AFM phase images captured at each corner and the middle of the *dSI**dS* film, which visually indicated the direction of nanostructure alignment throughout the film after SVA-SS with a 20:1 elastomer-to-curing agent PDMS pad. No alignment was detected in the middle of the film. The scale bar represents 250 nm and applies to all AFM images.⁴¹ 165
- Figure 5.6: SANS scattering data (first row) of *dSI**dS* films after SVA-SS with different nitrogen flow rates used to deswell the film (3 mL/min [slowest deswell], 5 mL/min, and 7 mL/min [fastest deswell]). A second order peak in azimuthally averaged SANS patterns (second row) was present at all nitrogen flow rates (peaks marked by yellow arrows). However, an increase in the nitrogen flow (from 3 mL/min to 5 mL/min) led to a change from two alignment directions (four-peak annular pattern [third row]; peaks marked by blue arrows) to a single alignment direction (two-peak annular pattern). With a 7 mL/min nitrogen flow during deswell, only low-intensity annular peaks were measured. The 3 mL/min, 5 mL/min, and 7 mL/min flow rates and dimensions of the SVA chamber were used to calculate τ_{CSTR} values of 0.51 min, 0.30 min, and 0.22 min, respectively. Error bars represent one standard deviation from the measured intensity and were calculated during data reduction.⁴¹ 167

- Figure 5.7: Comparison of SANS scattering data for *dSI/dS* films exposed to the same SVA-SS conditions but with uniform thickness or 2° gradient thickness 20:1 elastomer-to-curing agent ratio PDMS pads. SANS data obtained post SVA-SS after the PDMS pad was removed. *S* values of 0.74 and 0.81 were calculated from annularly averaged intensity profiles (not shown) with uniform and gradient thickness PDMS pads, respectively.⁴¹ 169
- Figure 5.8: Illustration of shear casting setup (side view) with motorized stage (substrate placed on top of stage), glass casting blade, and flexible PDMS blade. The polymer solution is deposited on the substrate as the substrate is drawn beneath the glass blade. A solvent evaporation front develops as the polymer solution is deposited. To induce a shear force, the flexible blade drags across the drying film at a distance at which there is enough solvent to promote chain mobility. Image courtesy of John Saltwick..... 171
- Figure 5.9: AFM images of SIS thin films flow coated (as cast; top row) and shear cast (middle row) from polymer solutions with 5:95 *o*-xylene:THF (mass%:mass%) solvent mixtures. Shear cast films were thermally annealed after casting (bottom row) to improve nanostructure ordering and increase grain sizes. Image courtesy of John Saltwick..... 173
- Figure 6.1: Schematic of the procedure to generate lamellar-forming, salt-doped PS-POEM thin films. Reprinted with permission from Gilbert, J. B. *et al. ACS Nano* **2014**, 9, 512-520, Copyright 2014 American Chemical Society.¹² 184
- Figure 6.2: Illustration of NR setup for measuring lithium salt distributions in PS-POEM films. Neutrons were directed at PS-POEM films held in reflectivity geometries *via* an aluminum sample holder and elastic clamps. Scattering from the uncoated silicon wafers, sample holder, and clamp was prevented through the addition of a borated aluminum mask between the neutron source and the samples.²⁰ 186
- Figure 6.3: Plot of POEM domain ρ values ($\rho_{POEM/salt}$) at different salt concentrations (vol%) with LiTFSI, Li triflate, and Li perchlorate salts. At salt concentrations of 23 vol% (LiTFSI), 28 vol% (Li triflate), and 18 vol% (Li perchlorate), the POEM domain is contrast matched with the PS domain ($\rho_{PS} = 1.41 \times 10^{-6} \text{ \AA}^{-2}$; black dotted line).²⁰ 187

- Figure 6.4: PS-POEM films doped with lithium salt as viewed by neutrons at the PS-POEM contrast match point (top row; blue = ρ of POEM; red = ρ of PS) along with predictive ρ (middle row) and reflectometry (bottom row) profiles. Even distributions of salt within the POEM layers (a) resulted in reflectivity profiles with no Bragg peaks. Central localization of the salt within the POEM layers (b) resulted in multiple Bragg peaks (highlighted by yellow arrows). Depths were normalized such that 0.00 was the free surface and 1.00 was the substrate surface.²⁰ 188
- Figure 6.5: NR profiles (black data points) and model fits (red lines) of neat PS-POEM films (top profiles) and films doped with (a) LiTFSI, (b) Li triflate, and (c) Li perchlorate salts at [EO]:[Li] ratios of 45:1, 22:1, and 11:1. Bragg peaks (highlighted with yellow arrows) shifted to smaller Q_z values and decreased in intensity relative to the rest of the NR profile as salt concentration increased (from top to bottom profiles). Bragg peaks were not present in films doped with an 11:1 [EO]:[LiTFSI] ratio. Error bars represent one standard deviation from the measured intensity and were calculated during data reduction.²⁰ ... 190
- Figure 6.6: Fit (solid circles) vs. calculated (empty circles) $\rho_{POEM/salt}$ values for POEM domains doped with Li perchlorate (top row), Li triflate (middle row), and LiTFSI (bottom row). Calculated $\rho_{POEM/salt}$ values were determined with the ideal mixing assumption. Error bars were calculated as the standard deviation between every $\rho_{POEM/salt}$ value (*i.e.*, each layer) in the film.²⁰ 192
- Figure 6.7: NR profiles (black data points) and model fits (red lines) for neat PS-POEM films and films doped with LiTFSI at 45:1, 22:1, and 11:1 [EO]:[Li] ratios (left side; profiles from Figure 6.5), and ρ profiles as a function of film depth (right side; normalized from 0.0 [free surface] to 1.0 [substrate surface]). As the salt concentration in the film was increased, the $\rho_{POEM/salt}$ values increased towards ρ_{PS} until a contrast match point ($\rho_{POEM/salt} = \rho_{PS}$) was achieved at approximately [EO]:[Li] = 11:1. Bragg peaks (highlighted by yellow arrows) in the NR profiles were not present at an 11:1 ratio. Furthermore, ρ models indicated a change in salt concentration in POEM layers from the free to substrate surface. Error bars in NR profiles represent one standard deviation from the measured intensity and were calculated during data reduction.²⁰ 194

Figure 7.1: Images and schematics of Teflon molds with machined patterns for preparing PDMS pads with 2° gradients in thickness that can direct the drying front propagation during SVA-SS in (a) bends or (b) spirals.	208
Figure 7.2: (a) Schematic of parallel-plate rheometer used to induce shear-alignment of a BP thin film with a viscous PDMS oil. (b) The applied stress was larger farther away from the center of the rheometer, and longer shear times (c → d → e → f) improved in the ordering of the nanostructures. Reprinted with permission from Davis, R. L. <i>et al. Macromolecules</i> 2015 , 48, 5339-5347, Copyright 2015 American Chemical Society. ⁵⁶	211
Figure 7.3: (a) A visual depiction of parallel and perpendicular nanostructures on roughened substrates is shown. Preferential (<i>i.e.</i> , attractive) surfaces typically orient domains parallel to the substrate, but maintaining the wetting of one domain on the rough substrate induces energetic penalties that are mitigated when domains orient perpendicular to the substrate. (b) As the roughness of the substrate (D_f) is increased, the likelihood of perpendicular orientations increases due to increasing entropic penalties. Left image adapted with permission from Sivaniah, E. <i>et al. Macromolecules</i> 2005 , 38, 1837-1849, Copyright 2005 American Chemical Society. ⁷⁵ Right image reprinted with permission from Kulkarni, M. M. <i>et al. Macromolecules</i> 2012 , 45, 4303-4314, Copyright 2012 American Chemical Society. ⁷⁰	212
Figure 7.4: Photographs of LCE films at room temperature (25 °C) and after heating to 175 °C. A nine-peak roughness pattern appears in the film at higher temperatures and reversibly flattens when the temperature is decreased. Reprinted with permission from Ware, T. H. <i>et al. Science</i> 2015 , 347, 982-984, Copyright 2016 by the American Association for the Advancement of Science. ⁸²	214
Figure 7.5: Height (left) and phase (right) atomic force micrographs of PS-POFPMA films with perpendicular lamellae structures after SVA with a neutral solvent. The scale bar represents 200 nm and applies to both images.....	216

- Figure 7.6: Through-film phase diagram for a cylindrical-forming BP thin film generated from RSANS. RSANS was used to probe the in-plane and out-of-plane features simultaneously to determine at what film thicknesses the substrate and free surface interactions competed to reorient domains. Adapted with permission from Zhang, *et al. ACS Nano* **2008**, 2, 2331-2341, Copyright 2008 American Chemical Society.¹¹⁸ 221
- Figure A.1: Optical micrographs of ≈ 103 nm ($2.5 L_0$) thick poly(methyl methacrylate-*b*-*n*-butyl methacrylate) (PMMA-*Pn*BA) films on *n*-butyl silane substrates and ≈ 90 nm ($2.2L_0$) thick PMMA-*Pn*BA films on aceto silane substrates after thermal annealing at 175 °C for 24 or 48 h. On *n*-butyl silane substrates, 103 nm was an incommensurate film thickness, but coherent island and hole formations were not expected due to the minimal propagation depth of the *n*-butyl silane surface field. On aceto silane substrates, 90 nm was an incommensurate film thickness, and island and hole formations were expected and present. As there were no distinct changes in the imaged structures at 24 h vs. 48 h, 24 h appeared to be sufficient time for microdomain equilibration. Reprinted with permission from Shelton, C. K. and Epps, T. H., III *Macromolecules* **2016**, 49, 574-580.¹ 230
- Figure A.2: Optical micrographs of PMMA-*Pn*BA films on *n*-butyl silane modified substrates displayed distinct island and hole formations at (a) 62 nm thicknesses, less defined islands and holes at (b) 103 nm, and no distinct islands and holes at (c) 144 nm thicknesses. For the specimens shown in images b and c, it is likely that the enthalpic competition between the substrate and free surfaces hindered island and hole formation.^{2,3} Proximal to defects on thicker films (d, e), islands and holes were more prominent likely due to additional entropic interactions that enhanced the substrate surface field influence.⁴ The scale bar applies to all micrographs. Reprinted with permission from Shelton, C. K. and Epps, T. H., III *Macromolecules* **2016**, 49, 574-580.¹ 231

- Figure A.3: Atomic force microscopy (AFM) images of PMMA-*Pn*BA films at substrate dominant (no outline), transition (gray outline), and substrate/free surface competition (black outline) thicknesses on chlorosilane-modified substrates. A change in the free surface nanostructure from perpendicular cylinders to parallel, or folded, cylinders was noted once the transition thickness was reached on each substrate. The change in nanostructure orientation was correlated directly to the disappearance of islands and holes measured by optical microscopy as shown in Figure 3.6. The scale bar represents 200 nm and applies to all images. Reprinted with permission from Shelton, C. K. and Epps, T. H., III *Macromolecules* **2016**, 49, 574-580.¹ 232
- Figure A.4: Plots of full-width half-max (FWHM) values calculated from azimuthally averaged fast Fourier transformation intensity spectrum measured from free surface AFM images of gradient thickness PMMA-*Pn*BA films on bare silica and chlorosilane-modified substrates. The plots revealed an increase in the FWHM of the primary peak (location marked by an arrow) indicating the transition of film thickness from the substrate dominant region to the substrate/free surface competition region. The onset of the transition was consistent for all substrate surfaces (shaded region; FWHM \approx 0.06-0.08) and matched the transition region measured *via* optical microscopy. The extra peaks found on the benzyl and methacryl silane traces (location marked by stars) were artifacts from the AFM/FFT processing and not free surface structures. Reprinted with permission from Shelton, C. K. and Epps, T. H., III *Macromolecules* **2016**, 49, 574-580.¹ 233
- Figure A.5: Comparison of critical propagation depths of the substrate surface field between two AB diblock copolymer (PMMA-*Pn*BA and poly[styrene-*b*-methyl methacrylate] [PS-PMMA]) systems using long-range interfacial energy differences and film thicknesses normalized by system-dependent L_0 's. PS-PMMA data were taken from literature, and the same initial linear increase followed by the possible onset of a plateau as interfacial energy difference increased was noted.² The inset plot is rescaled to focus on the PS-PMMA data for clarity. The lines between data points are to guide the eye. Reprinted with permission from Shelton, C. K. and Epps, T. H., III *Macromolecules* **2016**, 49, 574-580.¹ 234

- Figure B.1: Atomic force microscopy (AFM) images of as-cast and solvent annealed poly(styrene-*b*-isoprene-*b*-styrene) (SIS) films (cylindrical nanostructures) used in the neutron reflectometry (NR) and small-angle neutron scattering (SANS) experiments. SIS films exposed to *d*-benzene during SANS showed a marginal improvement (2.5 h anneal) in ordering in comparison to as-cast films, but the ordering greatly improved in films exposed to *d*-benzene during NR (8 h anneal). The shorter SANS data collection times were desired to ensure that the *C* variable (intensity) in the broad peak models was changing solely as a function of the solvent concentration and not as a function of improved ordering. *Note: the SVA times used herein were not long enough to cause damage to the films (e.g., dewetting) as demonstrated by optical micrographs of films following SVA (see rightmost panels).* Reprinted with permission from Shelton, C. K. *et al. Macromolecules* **2016**, 49, 7525-7534, Copyright 2016 American Chemical Society.¹ 236
- Figure B.2: Mass spectrometry (MS) profiles for nitrogen bubbled through deuterated benzene (*d*-benzene) obtained at the chamber outlet. Solvent partial pressure was adjusted by changing the ratio of the volumetric flow rates of nitrogen as a pure stream and *d*-benzene-rich nitrogen. Fragmentation patterns for *d*-benzene, nitrogen, oxygen, and water were used to identify the components associated with each MS peak as well as the relative amount of each component in the gaseous stream.² The relative amount of *d*-benzene (*p*) was divided by the saturated vapor pressure (p_{sat}) of *d*-benzene at 25 °C to calculate the p/p_{sat} values used in the analyses.³ Reprinted with permission from Shelton, C. K. *et al. Macromolecules* **2016**, 49, 7525-7534, Copyright 2016 American Chemical Society.¹ 237
- Figure B.3: (a) Illustration and (b) photograph of SANS sample cell for *in situ* SVA experiments. The sample cell housed two SIS films (400 ± 4 nm each) facing inward, towards a sealed air gap. Spacers were utilized to create the air gap through which solvent vapor flowed. Quartz glass windows were used as neutron transparent windows to reduce scattering from the sample cell. Adapted with permission from Shelton, C. K. *et al. Macromolecules* **2016**, 49, 7525-7534, Copyright 2016 American Chemical Society.¹ 238

Figure B.4:	(a) Illustration and (b) photograph of NR <i>in situ</i> SVA sample cell. The aluminum sample cell housed a 200 ± 2 nm thick SIS films with inlets and outlets for solvent vapor exposure and was mounted at a reflectivity geometry with the neutron beam. Borated aluminum shields (not shown in illustration) were placed around the neutron beam inlet and outlet to prevent scattering from the film holder or screws from reaching the detector. The dismantled sample chamber is shown in (c) and the schematics for the different components are presented in Figures B.5 to B.12. Adapted with permission from Shelton, C. K. <i>et al. Macromolecules</i> 2016 , 49, 7525-7534, Copyright 2016 American Chemical Society. ¹	239
Figure B.5:	Schematic for NR <i>in situ</i> SVA sample cell lid with photograph for reference. The lid enclosed the film sample to trap solvent vapor inside the chamber during annealing	240
Figure B.6:	Schematic for NR <i>in situ</i> SVA sample cell base plate with photograph for reference. The base plate housed the solvent inlet and outlet and the piping for a continuous circulating water bath to control the temperature.	241
Figure B.7:	More detailed schematic of base plate features with photograph for reference. Each breakdown describes where different holes or ports are located for a given application (<i>e.g.</i> , solvent inlet, solvent outlet, water bath inlet, water bath outlet).	242
Figure B.8:	Schematic for NR <i>in situ</i> SVA sample cell clamps, which were used to hold the films upright in the neutron beam.	243
Figure B.9:	Schematic for NR <i>in situ</i> SVA sample cell stilts with photograph for reference. The stilts were used to raise the sample into the neutron beam. Holes were cut in the stilts to help cool them if higher temperatures are used during annealing.	244
Figure B.10:	Schematic for NR <i>in situ</i> SVA sample cell mask and photograph for reference. The mask was used to prevent scattering from hardware (<i>e.g.</i> , screws) that might otherwise affect NR profiles. A calculation for the max Q was conducted to ensure appropriate Q ranges could be reached with the masks.	245
Figure B.11:	Schematic for the full, assembled NR <i>in situ</i> SVA sample cell.	246
Figure B.12:	Schematic for NR <i>in situ</i> SVA sample cell with water bath and solvent vapor ports added.	247

Figure B.13: Broad peak model fits to small-angle neutron scattering 1-D profiles at different values of p/p_{sat} . In the broad peak model, the parameters C , Q^* , ζ , m , and B represent the intensity of the primary peak, the Q location of the primary peak, the correlation length of the features, a scaling factor, and background in the scattering, respectively. The model fit parameters were optimized using SASView software. Most of the parameters remained relatively constant with changing p/p_{sat} , including the Q location of the primary peak (Q^*) at $\approx 0.02 \text{ \AA}^{-1}$, which indicated the domain spacing (L_0) was effectively constant with p/p_{sat} . The C parameter varied with p/p_{sat} and described the change in amplitude of the primary peak. The decrease in C with p/p_{sat} indicated that the contrast between domains had decreased. The value of C was used to calculate the contrast ($[\Delta\rho]^2$) between the polymer domains ($[\Delta\rho]^2 = [\rho_{PS/d\text{-benzene}} - \rho_{PI/d\text{-benzene}}]^2$) at each p/p_{sat} as described in Section B.1. Reprinted with permission from Shelton, C. K. *et al. Macromolecules* **2016**, 49, 7525-7534, Copyright 2016 American Chemical Society.¹ 248

Figure B.14: Temporal NR profiles of SIS films from a dry, as-cast state to a p/p_{sat} value of 0.93. The different plots show the change in the profile from (a) an initial, dry state (time = 0 h) to 1 h after solvent exposure, (b) a 1 h to 2 h solvent exposure time, (c) a 2 h to 4 h after solvent exposure time, (d) a 4 h to 7 h after solvent exposure time, and (e) a 7 h to 8 h after solvent exposure time. During SVA exposure, the gap between Kiessig fringes narrowed, and a Bragg peak developed, which indicated the film swelled (at a rate of at least 2.3 nm/min), and a repeating out-of-plane structure formed (parallel cylinders), respectively. The SIS film was annealed until two or three profiles overlapped (e) to indicate that a steady-state condition had been reached. The bottom right plot (f) focuses on the Bragg peak, as the peak changed more significantly than the rest of the profile and therefore was the most noteworthy indicator of steady-state. Reprinted with permission from Shelton, C. K. *et al. Macromolecules* **2016**, 49, 7525-7534, Copyright 2016 American Chemical Society.¹ .. 251

Figure B.15: Temporal NR profiles of SIS films from a p/p_{sat} value of 0.93 to a p/p_{sat} value of 0.84. The different plots show the change in the profile from (a) a fully swollen film ($p/p_{sat} = 0.93$ at time = 0 h) to a 1 h $p/p_{sat} = 0.84$ annealing time, (b) a 1 h to 2 h $p/p_{sat} = 0.84$ annealing time, (c) a 2 h to 4 h $p/p_{sat} = 0.84$ annealing time, (d) a 4 h to 7 h $p/p_{sat} = 0.84$ annealing time, (e) a 7 h to 11 h $p/p_{sat} = 0.84$ annealing time, and (f) an 11 h to 12 h $p/p_{sat} = 0.84$ annealing time. Upon deswelling, the gap between Kiessig fringes widened, and the Bragg peak location shifted to lower Q_z , which indicated the film thickness decreased (at a rate of at least 0.9 nm/min), and the layer spacing (L_z) increased. The bottom plot (g) focuses on the Bragg peak, as the peak changed more significantly than the rest of the profile and therefore was the most noteworthy indicator of equilibration. Reprinted with permission from Shelton, C. K. *et al. Macromolecules* **2016**, 49, 7525-7534, Copyright 2016 American Chemical Society.¹ 252

Figure B.16: Temporal NR profiles of SIS films from a p/p_{sat} value of 0.84 to a p/p_{sat} value of 0.59. The different plots show the change in the profile from (a) an equilibrated $p/p_{sat} = 0.84$ state (at time = 0 h) to a 1 h $p/p_{sat} = 0.59$ annealing time, (b) a 1 h to 2 h $p/p_{sat} = 0.59$ annealing time, (c) a 2 h to 4 h $p/p_{sat} = 0.59$ annealing time, (d) a 4 h to 7 h $p/p_{sat} = 0.59$ annealing time, (e) a 7 h to 8 h $p/p_{sat} = 0.59$ annealing time, and (f) an 8 h to 9 h $p/p_{sat} = 0.59$ annealing time. Upon deswelling, the gap between Kiessig fringes widened, and the Bragg peak location shifted to higher Q_z , which indicated the film thickness decreased (at a rate of at least 0.9 nm/min), and the L_z decreased. The bottom plot (g) focuses on the Bragg peak, as the peak changed more significantly than the rest of the profile and therefore was the most noteworthy indicator of equilibration. Reprinted with permission from Shelton, C. K. *et al. Macromolecules* **2016**, 49, 7525-7534, Copyright 2016 American Chemical Society.¹ 253

Figure B.17: Temporal NR profiles of SIS films from a p/p_{sat} value of 0.59 to a p/p_{sat} value of 0.43. The different plots show the change in the profile from (a) an equilibrated $p/p_{sat} = 0.59$ state (at time = 0 h) to a 1 h $p/p_{sat} = 0.43$ annealing time, (b) a 1 h to 2 h $p/p_{sat} = 0.43$ annealing time, (c) a 2 h to 4 h $p/p_{sat} = 0.43$ annealing time, (d) a 4 h to 7 h $p/p_{sat} = 0.43$ annealing time, and (e) a 7 h to 11 h $p/p_{sat} = 0.43$ annealing time. Upon deswelling, the gap between Kiessig fringes widened, and the Bragg peak location shifted to higher Q_z , which indicated the film thickness decreased (at a rate of at least 0.9 nm/min), and the L_z decreased. The bottom right plot (f) focuses on the Bragg peak, as the peak changed more significantly than the rest of the profile and therefore was the most noteworthy indicator of equilibration. Reprinted with permission from Shelton, C. K. *et al. Macromolecules* **2016**, 49, 7525-7534, Copyright 2016 American Chemical Society.¹ .. 254

Figure B.18: Temporal NR profiles of SIS films from a p/p_{sat} value of 0.43 to a redried state. The different plots show the change in the profile from (a) an equilibrated $p/p_{sat} = 0.43$ state (at time = 0 h) to a 1 h exposure to a dry nitrogen flow and (b) a 1 h to 2 h exposure time to a dry nitrogen flow. Upon deswelling, the gap between Kiessig fringes widened, and the Bragg peak location shifted to higher Q_z , which indicated the film thickness decreased (at a rate of at least 0.9 nm/min), and the L_z decreased. The bottom plot (c) focuses on the Bragg peak, as the peak changed more significantly than the rest of the profile and therefore was the most noteworthy indicator of equilibration. Reprinted with permission from Shelton, C. K. *et al. Macromolecules* **2016**, 49, 7525-7534, Copyright 2016 American Chemical Society.¹ 255

Figure B.19: Multilayer model fits (black lines) to NR data (open colored circles) for the as-cast and redried films as well as at each value of p/p_{sat} . The model parameters accounted for n number of layers with individual thickness and ρ parameters. Using this model and refl1D fitting software,⁷ the calculated profiles demonstrated good agreement with the measured profiles ($\chi^2 < 5$) and produced a free surface (depth = 0) to substrate ρ profile shown in the inset plots. For p/p_{sat} values of 0.93 and 0.84, the ρ profiles showed an oscillatory trend that likely was caused by the difference in solvent uptake of pure PI and mixed PI/PS layers. At values of $p/p_{sat} \leq 0.59$, the oscillatory trend was not as consistent (regions of lower amplitude oscillations) due to the PS domain transitioning to a glassy state that limited solvent diffusion through the film. Additionally, the Bragg peak was broader for values of $p/p_{sat} \leq 0.59$, which suggested greater disorder in the layered structure. Once all the solvent was removed from the film (redried), the oscillatory trend returned due to the ordered layering of domains. The solvent concentration through the film thickness at each p/p_{sat} was extracted from the resulting ρ profiles using known polymer and solvent ρ values, and molar fractions of the PS and PI domains in the dry SIS BP. Reprinted with permission from Shelton, C. K. *et al. Macromolecules* **2016**, 49, 7525-7534, Copyright 2016 American Chemical Society.¹ 257

Figure B.20: Multilayer model fits (black lines) to $p/p_{sat} = 0.84$ reflectivity profiles (open green circles) consisting of ten (left) or twelve (right) repeating layers (n). The total film thickness (t) remained constant for each fit, but the layer thickness (L_z) changed to achieve commensurability between the t and n . The $n = 10$ model fit the reflectivity data with a $\chi^2 = 1.47$. The $n = 12$ model had a significantly higher χ^2 ($\chi^2 = 442$) due to mismatched Bragg peak and Kiessig fringe locations when comparing the reflectivity data to the model fit. This large discrepancy between the refined $n = 12$ model fit and the reflectivity data provides a further indication that there was a change in the number of layers (from 12 to 10) in the film upon deswelling. Reprinted with permission from Shelton, C. K. *et al. Macromolecules* **2016**, 49, 7525-7534, Copyright 2016 American Chemical Society.¹ .. 258

- Figure C.1: Small-angle neutron scattering (SANS) azimuthally-averaged intensity profiles for poly(deuterated styrene-*b*-isoprene-*b*-deuterated styrene) (*dSI*d*S*) films subjected to toluene solvent vapor annealing (SVA) (a) with or (b) without soft shear. SVA with soft shear (SVA-SS) was implemented through the placement of polydimethylsiloxane (PDMS) pads on the films to induce shear forces as the pad swelled and deswelled while in contact with the film. SVA-SS or SVA was conducted with a 3 h swelling time and 10 mL/min toluene-rich nitrogen flow rates during swelling, and 3 mL/min diluent nitrogen flow rates during film deswelling. For both SVA-SS and SVA, the location of the primary peak shifted from $Q = 0.018 \text{ \AA}^{-1}$ to $Q = 0.015 \text{ \AA}^{-1}$, which was indicative of an increase in domain spacing (L_0) from 35 nm to 42 nm. Also, there was a difference in intensity of the primary peak for SVA-SS vs. SVA; the primary peak intensity decreased for samples treated by SVA-SS and increased slightly for samples treated *via* SVA.¹ 260
- Figure C.2: AFM images of *dSI*d*S* films after SVA or SVA-SS with the same swelling (10 mL/min toluene-rich nitrogen flow rate for 3 h) and deswelling (3 mL/min diluent nitrogen flow rate) conditions. The SVA-SS image was obtained from a portion of the film that the PDMS pad did not shear. Both micrographs indicate a mixture of parallel and perpendicular cylinders and featureless areas. The scale bar represents 250 nm and applies to both images.¹ 261
- Figure C.3: AFM images of *dSI*d*S* films exposed to different toluene-rich to diluent stream flow rate ratios (10:0, 8:2, or 6:4) during SVA-SS swelling. Shear forces from the swelling of the PDMS pad resulted led to well-ordered and aligned nanostructures across the film in the 10:0 sample. At an 8:2 ratio (reduced PDMS swelling relative to 10:0), the shear fields appear to be sufficient to align domains but not large enough to generate either a high degree of ordering or defect removal. At a 6:4 ratio, shear-alignment was not readily apparent. The scale bar represents 250 nm and applies to all images.¹ 261

- Figure C.4: AFM images from a *dSi/dS* film subjected to toluene SVA-SS using a PDMS pad fabricated with a 20:1 elastomer to curing agent ratio and a 2° gradient in thickness. The location of the AFM images in the figure is relative to where the images were taken in the film as indicated by the schematic in the top left corner. The alignment direction of the nanostructures remained consistent throughout the film. Slight differences in the apparent alignment direction likely were the result of orientation changes of the AFM when moving between locations. The scale bar represents 500 nm and applies to all images.¹ 262
- Figure C.5: Photograph of shear casting device in which the flexible PDMS, shearing blade was attached to the same holder as the glass, casting blade (schematic of this setup is shown in Figure 5.8). A silicon substrate was placed on a motor stage, which was programmed to move at a set speed for film casting. A polymer solution was deposited between the glass blade and silicon substrate to produce a film upon movement of the stage. The flexible blade dragged across the top of the film immediately after casting to shear-align the nanostructure. This setup used a single device to hold the two blades but offered less control over the distance between the two blades and the downward force of the flexible blade.² 263
- Figure C.6: (a) Schematic of shear casting device in which the flexible PDMS, shearing blade and glass, casting blade were attached to separate, stationary holders along with photographs of the setup: (b) side view, (c) top view, and (d) front view. This setup provided more control over the distance between the two blades and the downward force of the flexible blade. Photos courtesy of John Saltwick. 264
- Figure C.7: Illustration of potential shear casting device for industrial scale roll-to-roll processing. A flexible substrate is dipped into a reservoir of polymer solution to generate a film that is thinned by a rigid blade (*i.e.*, thickness control is provided by the rigid blade). A flexible blade shears the drying film immediately after casting to align the nanostructure before the substrate is transferred to the next step in the process.² 265

- Figure C.8: Photograph of a poly(styrene-*b*-isoprene-*b*-styrene) film after shear casting that depicts significant film damage (left side of image). The damage was caused by the presence of too much solvent in the film when the flexible, PDMS blade was dragged across the free surface. The PDMS blade did not interact with the right side of the film (undamaged area). 265
- Figure C.9: Plot of drying curves for pure *o*-xylene (green data points) and 50:50 (black data points), 25:75 (red data points), and 5:95 (blue data points) mixtures (mass%:mass%) of *o*-xylene:tetrahydrofuran (THF). The THF evaporated almost immediately after casting, and an increase in the *o*-xylene content increased the drying time. The green and black lines did not reach a thickness of zero because measurements were stopped before the solvent had dried completely. Figure courtesy of John Saltwick. 266
- Figure D.1: Poly(styrene-*b*-oligo[oxyethylene] methacrylate) (PS-POEM) films doped with lithium salt as viewed by neutrons (blue = scattering length density [ρ] of POEM; red = ρ of PS) at the PS-POEM contrast match point (top row) along with predictive ρ (middle row) and neutron reflectometry (NR; bottom row) profiles. Films without salt-doping (a) result in NR profiles with Bragg peaks (highlighted with yellow arrows) related to the domain spacing. (b) Central localization of the salt within the POEM layers results in additional Bragg peaks related to the thickness between low ρ portions of the film (*i.e.*, PS-POEM interfaces). Depths were normalized such that 0.00 is the free surface and 1.00 is the substrate surface.¹ 268
- Figure D.2: NR profiles (black data points) and model fits (red lines) for neat PS-POEM films and films doped with lithium trifluoromethanesulfonate (Li triflate) at 45:1, 22:1, and 11:1 [EO]:[Li] ratios (left side), and ρ profiles as a function of film depth (right side; normalized from 0.0 [free surface] to 1.0 [substrate surface]). As the salt concentration increased, the $\rho_{POEM/salt}$ values increased (as indicated by ρ profiles and the decrease in relative intensity of Bragg peaks [highlighted by yellow arrows]), but a contrast match point was not reached at the [EO]:[Li] ratios studied, herein. Error bars in NR profiles represent one standard deviation from the measured intensity and were calculated during data reduction.¹ 269

Figure D.3: NR profiles (black data points) and model fits (red lines) for neat PS-POEM films and films doped with lithium perchlorate (Li perchlorate) at 45:1, 22:1, and 11:1 [EO]:[Li] ratios (left side), and ρ profiles as a function of film depth (right side; normalized from 0.0 [free surface] to 1.0 [substrate surface]). As the salt concentration increased, the $\rho_{POEM/salt}$ values increased (as indicated by ρ profiles and the decrease in relative intensity of Bragg peaks [highlighted by yellow arrows]), but a contrast match point was not reached at the [EO]:[Li] ratios studied, herein. Error bars in NR profiles represent one standard deviation from the measured intensity and were calculated during data reduction.¹ 270

ABSTRACT

Block polymers (BPs) have attracted significant attention for emerging nanotechnologies such as nanolithographic masks, nanotemplates, nanoporous membranes, organic photovoltaics, and lithium ion battery membranes due to their ability to self-assemble into periodic assemblies of nanoscale features. Many of these applications require thin film geometries, which have additional confinement interactions in comparison to bulk self-assembly that must be understood to control nanostructure orientation, ordering, and alignment precisely. Two approaches to study the nuanced effects of these additional interactions are *in situ* characterization and neutron scattering, used concurrently or independently. With these techniques, more predictive and optimized methods to direct self-assembly can be established to unlock the full potential of BP thin films in commercial and research applications. In this dissertation work, four aspects of BP thin film self-assembly were explored with these powerful characterization tools. First, chlorosilane-modified substrate surfaces were employed to investigate the effect of the substrate-polymer interaction on nanostructure orientation and ordering. Predictive formalisms were developed that defined substrate wetting behavior, nanostructure ordering, and through-film orientation control as a function of total and decoupled (dispersive and polar) substrate-polymer interfacial energy components. Second, solvent vapor annealing was studied with *in situ* small-angle neutron scattering (SANS), neutron reflectometry (NR), and selective deuteration to determine how factors such as solvent-polymer

interactions and solvent concentration affected BP thin film self-assembly. Next, *in situ* SANS during solvent vapor annealing with soft shear (SVA-SS) was used to track shear-induced nanostructure disordering and ordering. By understanding the kinetic pathways during SVA-SS, more robust and high-throughput methods to define the alignment direction(s) were developed. Lastly, lithium salt-doped poly(styrene-*b*-oligo[oxyethylene] methacrylate) films were investigated with NR to achieve the first high-resolution, non-destructive, and quantitative analysis regarding how lithium salts distribute within the conducting domain of BP electrolyte thin films. Overall, the work in this dissertation contributes predictive and translatable approaches to direct self-assembly and the design of powerful characterization strategies to extract key information from BP thin film systems to improve their rational design and application.

Chapter 1

BLOCK POLYMER THIN FILM SELF-ASSEMBLY

1.1 Introduction

A block polymer (BP) is comprised of two or more chemically-distinct polymer “blocks” that are covalently bound to form one continuous chain. Repulsive polymer-polymer interactions between the blocks leads to phase separation, but the covalent connectivity prevents macroscopic phase separation. The combined effects result in nanoscale self-assembly into periodic morphologies such as body-centered cubic spheres, hexagonally-packed cylinders, hexagonally-perforated lamellae, gyroid networks, and lamellae, which are useful for a wide variety of applications.¹⁻³ The diversity of polymer chemistries, compositions, functionalities, molecular weights, and architectures also provides nearly limitless potential for emerging nanotechnologies.^{4,5} In particular, BPs constrained into thin film geometries ($< 1 \mu\text{m}$ in thickness) have proven effectiveness in technologies including nanolithography, nanotemplating, separation membranes, ion-conducting membranes, and photovoltaic devices as shown in Figure 1.1.⁶⁻¹¹ The use of BP thin films for these applications requires precise control over nanostructure morphology, orientation, and ordering. Therefore, a more complete understanding of how to tune BP thin film self-assembly is necessary to unlock their full potential in shaping the field of nanotechnology.

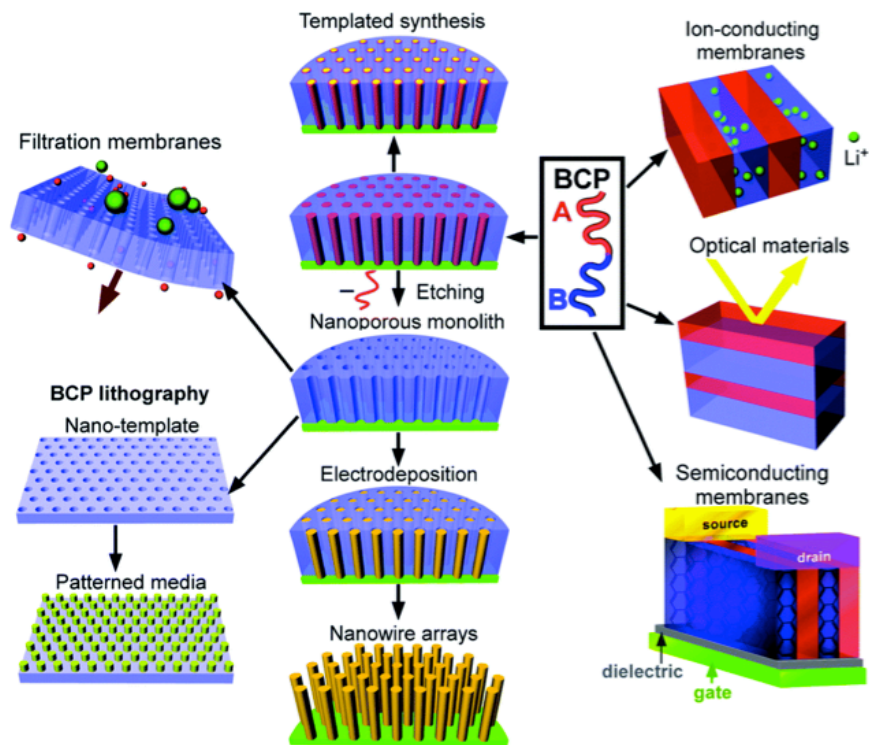


Figure 1.1: Potential technologies enabled and/or improved through BP thin film self-assembly into nanometer-scale periodic structures. Adapted with permission from Hu, H. *et al. Soft Matter* **2014**, *10*, 3867-3889, Copyright 2014 The Royal Society of Chemistry.¹⁰

1.2 Thermodynamics of Bulk Block Polymer Self-Assembly

BPs self-assemble according to three main parameters in bulk systems: the polymer-polymer Flory-Huggins interaction parameter (χ) between each of the blocks, the degree of polymerization (N), and the volume fractions of each block (f).^{1, 12} Additional factors such as chain architecture (*e.g.*, linear, star, cyclic, graft, *etc.*), chain flexibility (flexible *vs.* stiff), and interfacial profile (*e.g.*, tapered interface) also can affect the resulting morphology.^{4, 13, 14} For a diblock copolymer, a typical phase diagram and the most common morphologies are shown in Figure 1.2. In the phase diagram of Figure 1.2, the y -axis is the segregation strength (χN) and the x -axis is the

volume fraction of one of the two blocks.^{15, 16} The segregation strength is a dimensionless measurement of the attractive and repulsive interactions between the individual polymer blocks and is the product of χ and N . According to Flory-Huggins theory, χ represents the interactions between the polymer blocks and can be calculated from Equation 1.1 using the Boltzmann constant (k_B), temperature (T), and contact energy between i and j segments (ϵ_{ij}).²

$$\chi_H = \frac{1}{k_B T} \left[\epsilon_{ij} - \frac{1}{2} (\epsilon_{ii} + \epsilon_{jj}) \right] \quad (1.1)$$

The χ value calculated from Equation 1.1 denotes a purely enthalpic contribution (χ_H) and commonly is paired with an entropic contribution (χ_S) estimate of 0.34 as shown in Equation 1.2.¹⁷

$$\chi = \chi_H + \chi_S = \chi_H + 0.34 \quad (1.2)$$

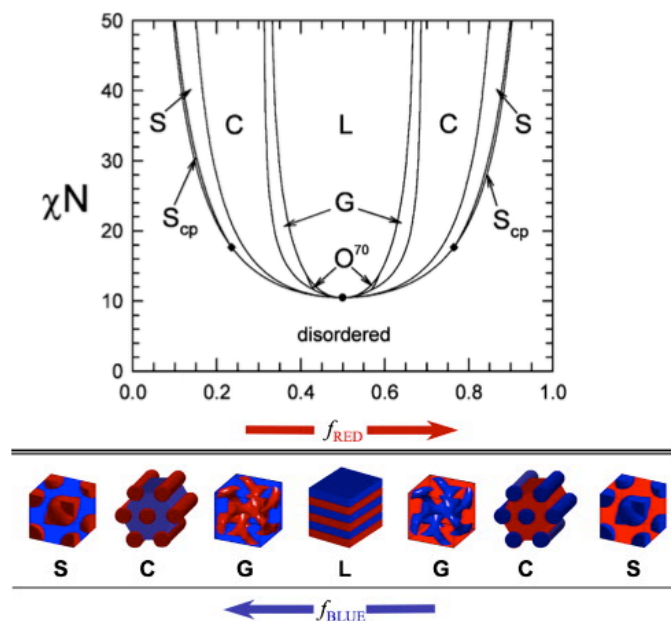


Figure 1.2: Theoretical phase diagram for AB diblock copolymer melts indicating the regions in which BPs disorder or form ordered spherical (S), cylindrical (C), gyroid network (G), $Fddd$ (O^{70}) or lamellar (L) structures as determined by self-consistent field theory and the Flory-Huggins polymer-polymer interaction parameter (χ), degree of polymerization (N), and block volume fractions (f). The phase diagram was adapted with permission from Matsen, M. W. *Macromolecules* **2012**, 45, 2161-2165, Copyright 2012 American Chemical Society.¹⁵ The 3-D morphology illustrations were adapted with permission from Lynd, N. A. *et al. Prog. Polym. Sci.* **2008**, 33, 875-893, Copyright 2008, Elsevier.¹⁶

When χN is below a certain critical value, entropy dominates the energetic penalty of mixing polymer blocks, and a disordered phase is formed. An increase in χN past the critical value results in phase separation. This conversion from a disordered phase to an ordered phase is called an order-disorder transition (ODT). For symmetric diblock copolymers ($f_A = f_B = 0.5$), the ODT occurs at $\chi N = 10.495$, as calculated using self-consistent field theory (SCFT).¹⁸ BPs also can undergo order-order transitions (OOTs) between different morphologies provided phase separation

occurs and either the χ or f value is altered. The χ and f value can be modified through techniques such as mixing the BP with additives such as homopolymer chains or salt,¹⁹⁻²² introducing solvent swelling,²³⁻²⁵ or changing the temperature as shown in Equation 1.3, in which α and β are enthalpic and entropic coefficients for a particular BP.^{17, 26, 27}

$$\chi = \frac{\alpha}{T} + \beta \quad (1.3)$$

The size scale, or domain spacing (L_0), of the nanostructures that form during phase separation typically is between 5-100 nm and is related to the χ and N values and the chain architecture. For a symmetric diblock copolymer in the strong segregation regime, L_0 can be calculated using Equation 1.4, in which α is the persistence length of the polymer blocks.²⁸

$$L_0 = \alpha \chi^{1/3} N^{2/3} \quad (1.4)$$

1.3 Confinement Effects in Thin Films

BPs with thicknesses less than approximately 1 μm , which typically is within one or two orders of magnitude of the nanostructure L_0 , experience confinement constraints due to thin film geometries that can alter the bulk self-assembly.⁸ Conceptually, BPs attempting to accommodate a specific film thickness can encounter energetically unfavorable chain stretching and compression that drive self-assembly into conformations that mitigate these entropic penalties such as the formation of islands and holes and the reorientation of nanostructures.²⁹⁻³¹ Surface-polymer interfaces also can provide enthalpic and entropic interactions that influence self-assembly.³² For a given BP thin film, there are two polymer interfaces that are either

substrate (*e.g.*, silicon, gold, mica, *etc.*) or free (*i.e.*, air) surfaces. Films with two substrate surfaces, one substrate and one free surface, and two free surfaces are referred to as hard confinement, soft confinement, and free-standing films, respectively.⁶ Among these categories, soft confinement films are the most widely used for the applications mentioned previously and will be the focus of the work in this dissertation.

A summary of the different forces that drive BP self-assembly in soft confinement thin films was provided by Edwards *et al.* as shown in Equation 1.5.³³

$$F = F_{elastic} + F_{polymer} + F_{substrate} + F_{air} \quad (1.5)$$

In Equation 1.5, F is the total free energy per chain of the film and is the sum of the elastic energy from chain stretching and compression ($F_{elastic}$), the interaction between the individual polymer blocks ($F_{polymer}$), and the substrate-polymer ($F_{substrate}$) and free surface-polymer (F_{air}) surface energies. To direct the self-assembly of BP thin films, each of these interactions has to be defined as they can strongly affect nanostructure morphology, orientation, and ordering.

1.3.1 Film Thickness Effects

The thickness of BP thin films dictates self-assembly through commensurability conditions that affect the degree of chain stretching and compression. Essentially, a specific BP has an energetically favorable L_0 that is dependent on polymer-polymer interactions. Chain stretching and compression can lead to changes in the nanostructure morphology or orientation if films are cast at thicknesses that are not commensurate with the characteristic L_0 . For example, Matsen *et al.* demonstrated that BP thin film nanostructures cast at incommensurate thicknesses can transition from parallel to perpendicular lamellae, a process that

mitigates chain stretching and compression.³¹ If polymer-polymer or surface-polymer interactions prevent nanostructure changes from reducing entropic penalties, incomplete film layers with thicknesses equal to L_0 can form at the free surface into macroscopic structures referred to as islands and holes that reduce entropic penalties associated with chain stretching and compression (Figure 1.3).³⁴⁻³⁶

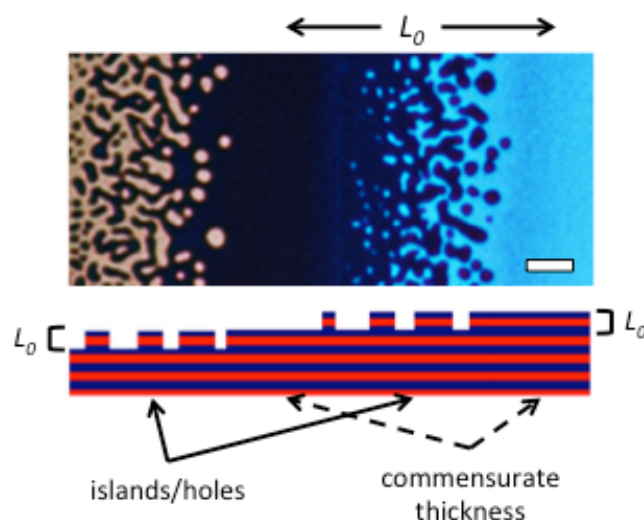


Figure 1.3: Top-view optical micrograph of a gradient thickness poly(*n*-butyl acrylate-*b*-methyl methacrylate) BP film. Scale bar represents 10 μm . At incommensurate thicknesses, energetically unfavorable chain stretching and compression resulted in the formation of incomplete layers of thickness L_0 called islands and holes as shown in the side-view schematic; at commensurate thicknesses, chain stretching and compression is mitigated and featureless surfaces are formed. The thickness difference between commensurate areas is equal to L_0 .

In addition to the characteristic L_0 of the BP, commensurability conditions are dependent on substrate and free surface-polymer interactions. For lamellae- or cylinder-forming diblock copolymers, surfaces that are preferential for one block

typically result in parallel nanostructures, and the preferential block forms a wetting layer with the surface.⁶⁻⁸ If the same block is preferential for both surfaces, the wetting behavior is referred to as symmetric wetting and commensurate thicknesses (t_c) occur at integer multiples of the domain spacing ($t_c = nL_0$; $n = 1, 2, 3, \dots$). If a different block is preferential at each surface, the wetting behavior is referred to as asymmetric wetting and commensurate thicknesses occur at half-integer multiples of the domain spacing ($t_c = [n+0.5]L_0$; $n = 1, 2, 3, \dots$). If neither block is preferential, or there is a weak preference, a neutral surface-polymer interaction exists and the nanostructures typically orient perpendicular to the substrate to reduce chain stretching and compression.³⁷ Furthermore, if one surface is neutral and the other is preferential, island and hole formations develop with thicknesses equal to $0.5L_0$.³⁸⁻⁴⁰

1.3.2 Substrate Surface Effects

Substrate surface interactions strongly influence BP thin film orientation,⁴¹⁻⁴³ morphology,³⁴ ordering,^{44, 45} bulk nanostructure uniformity,⁴⁶⁻⁴⁸ and stability by manipulating both interfacial (wetting behavior) and through-film phenomena.^{8, 49} Morphology changes also can occur as one block is depleted from the bulk film to interact with the substrate depending on the volume fractions of the individual blocks.⁵⁰ For example, hexagonally-perforated lamellae structures (HPL; lamellar stacks with the minority block lamellar domains penetrated by hexagonally packed cylinders of the majority block) can develop if the majority component block forms a wetting layer in cylindrical BP thin film systems.³⁴ This effect explains why network structures are difficult to arrange in thin film systems.^{51, 52} Depletion of one or both layers can destabilize network morphologies and collapse the domains to cylindrical structures. If neither block is preferential for the substrate, a neutral substrate-polymer

interaction exists and the nanostructures orient perpendicular to the substrate.⁶ Furthermore, in some systems the energetically favorable or unfavorable substrate-polymer interactions result in the destabilization of the film and dewetting.⁴⁹

The preference of the substrate towards a particular block can be determined from interfacial energies associated with each substrate-polymer interaction ($\Delta\gamma_A$), which can be calculated using the surface energy of the polymer block (γ_A) and the substrate (γ_S) as shown in Equation 1.6.⁵³

$$\Delta\gamma_A = |\gamma_S - \gamma_A| \quad (1.6)$$

The block with the lowest interfacial interaction is considered preferential for the substrate, but if the two interfacial energy values are approximately equal, the substrate is considered to be neutral.^{54, 55} The difference between the interfacial energy values provides an estimate of the strength of the substrate-polymer interaction on self-assembly.⁵³ The larger the interfacial energy difference, the more influence the substrate has over self-assembly including larger energetic penalties for forming defects.^{44, 45} Smaller defect densities in the film improve the overall ordering and help drive the formation of larger grains; large grains are necessary for the aforementioned applications.

In addition to orientation, ordering, and morphological effects, substrate-polymer interactions can direct through-film nanostructure uniformity.^{46, 56} The effects of substrate-polymer interactions propagate as a field through the film thickness.⁵⁷ This interaction can drive the orientation of nanostructures, so the stronger the interaction the farther one continuous orientation persists through the film.^{41, 58} At some critical film thickness, the substrate-polymer interaction competes with the free surface-polymer interaction, which can result in a change in orientation

or a mixed orientation.^{56, 59} Further increases in film thickness result in a dominant free surface-polymer interaction that dictates the orientation. Xu *et al.* demonstrated this phenomenon using cross-sectional transmission electron microscopy images to capture the onset of each transition in the film thickness as a function of substrate surface energy for poly(styrene-*b*-methyl methacrylate) (PS-PMMA) films on substrates modified with PS-PMMA random copolymer brushes, as shown in Figure 1.4.⁴⁶ The critical film thickness is dependent on the substrate-polymer interfacial energy, the competing free surface-polymer interfacial energy, and the polymer-polymer interactions.⁶⁰

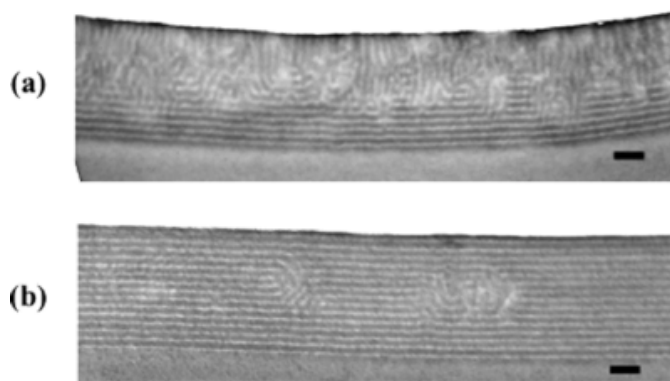


Figure 1.4: Cross-sectional transmission electron micrographs of PS-PMMA films on substrates modified with random PS-PMMA brushes with (a) 58 vol% and (b) 70 vol% PS in the random PS-PMMA monolayers. The films are approximately 400 nm thick, and the scale bar equals 100 nm. Because the surface energy of the 58 vol% PS monolayer was closer to a neutral condition, the substrate-polymer interaction did not propagate through the film as far as the 70 vol% PS monolayer, and the orientation of the nanostructures changed due to free surface interactions. Adapted with permission from Xu, T. *et al. Macromolecules* **2005**, 38, 2802-2805, Copyright 2005 American Chemical Society.⁴⁶

To direct the desired self-assembly in BP thin films *via* substrate-polymer interactions, the substrate surface can be modified to tune the surface energy and subsequent interaction with the individual polymer blocks. Traditional methods to change the substrate surface energy involve depositing a monolayer of either a random copolymer or small molecule mimics, such as chlorosilanes with different side-chain functionalities that match the polymer blocks, on the substrate.^{34, 37, 53, 56, 60-68} The monolayer coverage can be altered further using ultra-violet ozone or X-ray radiation to expose the underlying substrate and vary the surface energy.^{56, 69-72}

Rather than modifying the substrate surface energy, the creation of entropic substrate-polymer penalties *via* roughening of the substrate surface can lead to the formation of perpendicular nanostructure orientations.⁷³⁻⁷⁶ Kulkarni *et al.* determined that increases in substrate roughness resulted in more entropic penalties for wetting with a single block and easier pathways to the development of neutral wetting conditions.⁷⁷ Rough substrates also can improve ordering in BP films provided the roughening is controlled in a periodic manner.⁷⁸ This effect was demonstrated by Park *et al.* with a saw-tooth patterned substrate that led to the generation of well-ordered perpendicular cylinders in poly(styrene-*b*-ethylene oxide) films upon annealing.⁷⁹ This technique of changing entropic substrate-polymer interactions also can be used to direct the self-assembly of BP films into specific patterns, a process referred to as graphoepitaxy and discussed further in Section 1.5.1.

1.3.3 Free Surface Effects

As with the substrate surface, the free surface can have a preferential interaction with one of the blocks in the BP. The block with the lower surface energy typically is preferential with the free surface, which can lead to the formation of a free

surface wetting layer.⁸ Because surface energy (γ) is temperature dependent ($d\gamma/dT$), preferential free surface interactions can be directed through modulation of the annealing temperature. For example, PS and PMMA have different initial surface energies ($\gamma_{PS} = 40.7 \text{ mJ/m}^2$, $\gamma_{PMMA} = 41.1 \text{ mJ/m}^2$) and different temperature dependencies ($d\gamma_{PS}/dT = -0.072 \text{ mJ/m}^2$, $d\gamma_{PMMA}/dT = -0.076 \text{ mJ/m}^2$).^{17, 41, 54} At a temperature of approximately 170 °C to 230 °C, the two blocks have relatively the same surface energy and a neutral free surface interaction is formed. Because the surface energies of most polymers do not naturally experience the same neutrality at reasonable temperatures as PS and PMMA, other techniques to tune the free surface interaction were developed such as solvent vapor annealing (SVA; Section 1.4.2) and top-coat modification.^{39, 40}

1.4 Annealing Techniques for Order/Orientation Control

During casting of BP thin films, polymer chains become kinetically trapped in as-cast states as the solvent evaporates; the as-cast morphology consists of small, isotropic grains randomly distributed and oriented in the film. The kinetic trapping occurs if at least one polymer block in the BP has a glass transition temperature (T_g) above room temperature. As the film dries, the BP shifts from a “rubbery” state to a “glassy” state that limits chain mobility and prevents reorganization. The films need to be annealed to convert the polymer chains back to the rubbery, mobile state to induce reorganization into larger grain sizes, higher degrees of ordering, and different orientations for commercial and research applications.⁸⁰ Two common annealing techniques that provide mobility to polymer chains are thermal and SVA.

1.4.1 Thermal Annealing

Thermal annealing is the process of heating a polymer film above the T_g of the polymer blocks, but below their degradation temperature, to shift the polymers from the glassy to rubbery state and promote nanostructure reorganization.⁸¹⁻⁸⁴ Two key factors that are adjusted during thermal annealing are the annealing temperature and time.^{54, 85, 86} Each of these factors can influence the reorganization of polymer domains as has been demonstrated in the literature.^{81, 87-89} In a systematic analysis of annealing temperature and time conducted by Majewski and Yager, a range of different orientations and degrees of ordering in PS-PMMA films were achieved as shown in Figure 1.5.⁸¹ OOT's also can occur as was demonstrated by Park *et al.* with poly(styrene-*b*-isoprene) films that transitioned from a hexagonally-perforated lamellae nanostructure to a gyroid network that was kinetically trapped when the film was quenched.⁹⁰ A more detailed description of the thermodynamic and kinetic equations related to thermal annealing effects can be found in the literature.⁸⁰

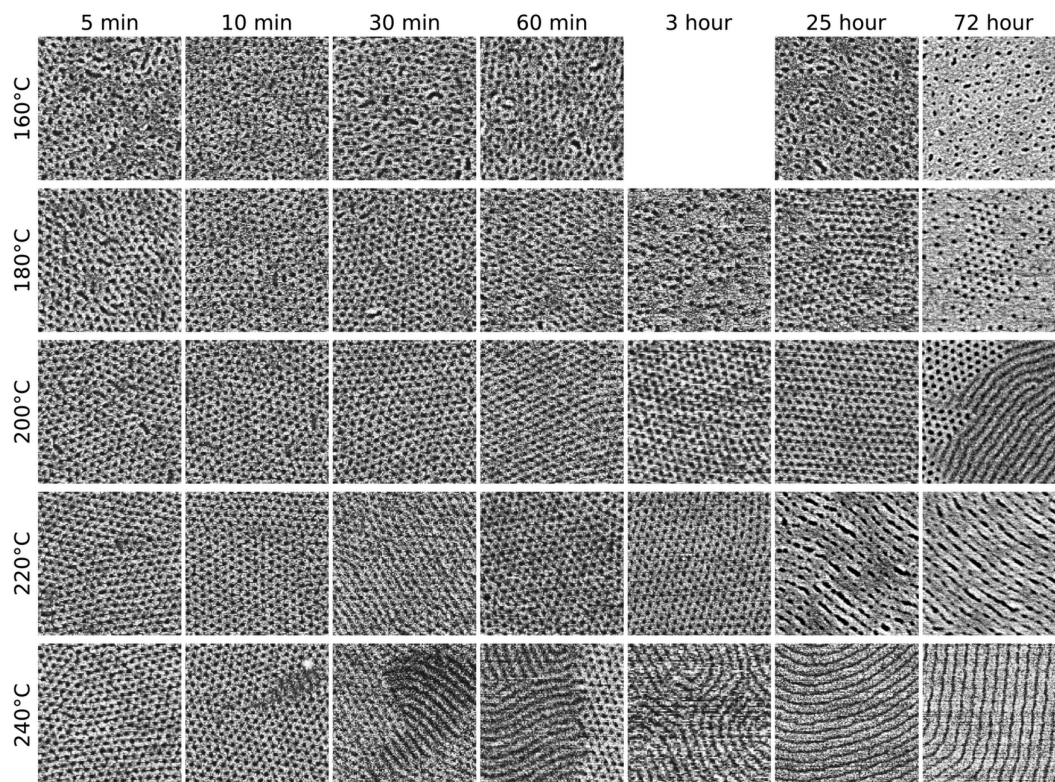


Figure 1.5: Scanning electron micrographs of oven annealed cylinder-forming PS-PMMA films over a range of different annealing times and temperatures. The width of one image is 500 nm. Adapted with permission from Majewski, P. W. and Yager, K. G. *Soft Matter* **2016**, 12, 281-294, Copyright 2016 The Royal Society of Chemistry.⁸¹

1.4.2 Solvent Vapor Annealing

SVA is an alternative approach to provide polymer chains the mobility to reorganize into lower energy states. SVA is the process of exposing a BP film to solvent vapors that swell the film, plasticize the polymer chains, and effectively lower the T_g .⁹¹ Provided the concentration of solvent exposed to the films is sufficient to lower the T_g below room temperature, the polymer chains have enough energy to reorganize and form more ordered structures.⁹² The solvent in the film and at the interfaces also can alter substrate and free surface interactions,⁹³⁻⁹⁵ polymer-polymer

interactions and relative block volume fractions,⁹⁶⁻¹⁰³ and commensurability conditions through manipulation of parameters such as solvent choice, solvent uptake, annealing time, and solvent removal rate.^{92, 97, 104-106} These influences can reduce film roughness, prevent film dewetting, and alter nanostructure orientation, domain sizes, and morphology.⁸

The traditional SVA method, bell jar SVA, seals a BP film and solvent reservoir in an airtight chamber for a set period of time that allows the film to swell and polymer domains to reorganize as the solvent saturates the chamber. Then, the solvent is removed instantaneously by opening the seal and permitting the solvent vapor to escape, a process that kinetically traps the polymer chains in their annealed state.^{55, 99, 101, 107, 108} Although literature has demonstrated the effectiveness of this technique, it does not provide tunability over solvent swelling and deswelling, which can have a large impact on final film structure. Therefore, flow SVA was developed to establish more defined control over solvent concentration levels (*i.e.*, solvent vapor pressure).^{98, 109, 110} Flow SVA modulates the solvent partial pressure by bubbling a carrier gas (*e.g.*, nitrogen) through solvent reservoirs and directing the solvent-rich stream into and out of the chamber housing the film. The ratio of solvent to carrier gas in the inlet stream affects the solvent concentration and film swelling and deswelling. Using flow SVA setups, several key parameters that direct the self-assembly have been recognized: solvent choice, solvent uptake and swollen film thickness, annealing time, and solvent removal rate.

1.4.2.1 Solvent Choice

The choice of solvent used during SVA can affect the nanostructure self-assembly, especially the morphology and orientation. The solvent vapor can alter

polymer-polymer and substrate and free surface interactions, which can change the energetically favorable wetting behavior at each surface, the relative block volume fractions, and the interfacial curvature.^{93, 94, 96, 103, 106, 111-115} For example, Gowd *et al.* demonstrated that swelling cylinder-forming poly(styrene-*b*-4-vinylpyridine) films with chloroform or 1,4-dioxane resulted in parallel or perpendicular cylinders, respectively.¹¹⁶ They attributed the differences to the solvent preference modulating the swelling pathways through the phase diagram including through an ODT when the films were annealed with chloroform. If confinement effects are mitigated *via* solvent exposure and swelling, metastable network formations can be kinetically trapped in thin film geometries. This phenomena was noted by She *et al.* when poly(styrene-*b*-lactide) films were annealed with chloroform, a nonpreferential solvent, on neutral substrates.⁵¹ The complete neutralization of confinement effects facilitated the bulk gyroid morphology to be stable in the ≈ 100 nm thick films.

The transition between different orientations or morphologies cannot be achieved with a single solvent in most instances, so multiple solvents are combined in set ratios.^{103, 114, 117} For example, Chavis *et al.* used mixtures of tetrahydrofuran (THF) and methanol (MeOH) to swell poly(2-hydroxyethyl methacrylate-*b*-methyl methacrylate) (PHEMA-PMMA) films and reversibly change the morphology between spherical, cylindrical, lamellar, and gyroid nanostructures (Figure 1.6).¹¹⁴ The different solvent-polymer interaction parameters for each solvent-polymer pair allowed the researchers to tune the swelling of the individual blocks to transition between morphologies, as tracked by grazing-incidence small-angle X-ray scattering (GISAXS), that were kinetically trapped when the solvent was removed from the film.

Interestingly, the same solvent conditions were used to produce gyroid networks and spheres, but longer annealing times led to the formation of different final structures.

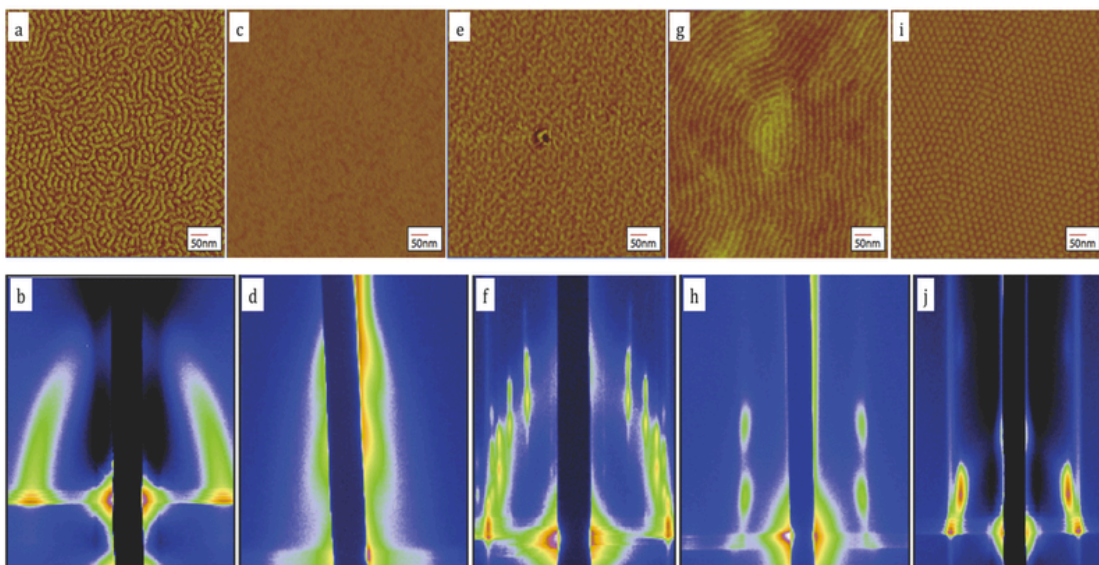


Figure 1.6: Atomic force micrographs (top row) and GISAXS profiles (bottom row) for PHEMA-PMMA films (a, b) as-cast, annealed in (c, d) 80/20 vol/vol, (e, f) 50/50 vol/vol, and (g, h) 20/80 vol/vol THF/MeOH for 45 min, and annealed in (i, j) 50/50 vol/vol THF/MeOH for 3 – 4 h. Adapted with permission from Chavis, M. A. *et al. Adv. Funct. Mater.* **2015**, 25, 3057-3065, Copyright 2016 John Wiley & Sons, Inc.¹¹⁴

1.4.2.2 Solvent Uptake and Annealing Time

In general, the annealing time and swollen film thickness are key parameters that must be controlled to produce the desired nanostructures.^{96, 100, 111, 118-121} The primary concern for solvent uptake involves thermodynamics and whether or not there is enough solvent present in the film to lower the T_g of the BP below the sample temperature. Then, the annealing time affects kinetics and whether or not the polymer chains have sufficient time to restructure into the lowest energy state.⁹¹ Additionally,

highly swollen films can overcome confinement affects to self-assemble into more ordered structures. For example, Zettl *et al.* used SVA of gradient thickness poly(styrene-*b*-butadiene) films to demonstrate how larger degrees of swelling led to better ordered nanostructures; the degree of swelling decreased as initial film thickness increased.⁹⁸

Although annealing time is easily controlled, solvent uptake requires more elaborate SVA setups such as flow SVA with *in situ* thickness measurements for precise regulation of solvent diffusion in the film.¹²² An understanding of how solvent partial pressure changes the amount of solvent diffusing into the film is needed to tune this parameter. Flory-Huggins theory provides an estimate of solvent uptake in BP thin films using Equation 1.7.¹²³

$$\ln\left(\frac{p}{p_{sat}}\right) = \chi_{H,p-s}\varphi_p^2 + \ln(1 - \varphi_p) + \left(1 - \frac{1}{N}\right)\varphi_p \quad (1.7)$$

In Equation 1.7, p is the partial pressure of solvent, p_{sat} is the saturated vapor pressure, $\chi_{H,p-s}$ is the enthalpic component of the polymer-solvent interaction parameter, and φ_p is the volume fraction of polymer in the swollen film. Estimation of the $\chi_{H,p-s}$ value, which can vary drastically in literature for the same polymer-solvent pair, can adversely affect the application of this equation.¹⁷ For this reason, Equation 1.7 typically is used in solvent vapor swelling experiments to determine $\chi_{H,p-s}$ from measured solvent partial pressure and swollen film thickness values.^{122, 124}

1.4.2.3 Solvent Removal Rate

A final important control parameter of SVA is the removal rate of solvent from the film, which can affect how the polymer chains transition from mobile to kinetically trapped states. Researchers have noted nanostructure order and orientation

differences by changing solvent removal rates.^{92, 106, 110, 111, 120, 125, 126} For example, using flow SVA of poly(styrene-*b*-isoprene-*b*-styrene) (SIS) films with controlled deswell rates between 0.05 nm/min and 0.5 nm/min, Albert *et al.* demonstrated how slower solvent removal rates can reorient nanostructures by creating a solvent removal front that propagates to the substrate surface.¹¹⁰ Furthermore, Elbs *et al.* explored how different solvent removal rates resulted in OOTs in poly(styrene-*b*-2-vinylpyridine-*b*-*tert*-butyl methacrylate) triblock polymers, including transitions to complex patterns such as double-gyroids, core-shell cylinders, and helix-wrapped cylinders.¹²⁵ A detailed analysis of SVA structural changes is presented in Chapter 4 that determines the transitions occur due to polymer-polymer and polymer-solvent thermodynamics and kinetic trapping.

1.5 Directed Self-Assembly Techniques

For many potential applications of BP thin films, the nanostructures must be aligned in a single direction or in a specific pattern.^{80, 127} Therefore, several directed self-assembly techniques have been developed to achieve defined directional or patterned control over nanostructure self-assembly.

1.5.1 Graphoepitaxy and Chemical Prepatterning

Graphoepitaxy is one of the more common approaches to direct nanostructure self-assembly due to its relatively unmatched control and flexibility.⁷ By etching trenches or periodic patterns in the substrate surface to change substrate-polymer interactions and define orientation and ordering energetics, graphoepitaxy has proven quite effective in producing high-degrees of ordering and uniform orientations in BP thin films.¹²⁸⁻¹³² It is well understood that the improved control over ordering and

orientation is the result of commensurability conditions between the walls and increased substrate-polymer interactions, as has been measured by SCFT simulations paired with experimentation.^{133, 134} For example, SCFT simulations conducted by Mickiewicz *et al.* demonstrated how different parameters affect the overall ordering of spherical nanostructures and predicted the formation of aperiodic structures.¹³⁵ However, graphoepitaxy requires etching of the substrate surface, which produces non-smooth films for templating and sacrifices valuable substrate area, and the lithographic writing required to etch patterns into the substrate can be expensive for large substrate areas.

As an alternative to graphoepitaxy, chemical pre patterning controls chemical deposition on the substrate to direct nanostructure pathways as demonstrated in Figure 1.7.¹³⁶⁻¹³⁸ Rather than etching away substrate, chemical pre patterning uses lithography and chemical treatment to define periodic areas of the substrate that are preferential and commensurate for each polymer block in the BP.¹³⁹⁻¹⁴¹ Then, the BP chains align in the pattern due to enthalpic preferences and the balancing of entropic forces that can dictate chain ordering and orientation.^{43, 142, 143} More complicated designs such as jogs, bends, and T-junctions have been fashioned with this approach.^{131, 137, 138, 144} The drawback of chemical pre patterning is that the template and BP nanostructure length scales often are similar, which results in a minimal gain from self-assembly.^{136, 145}

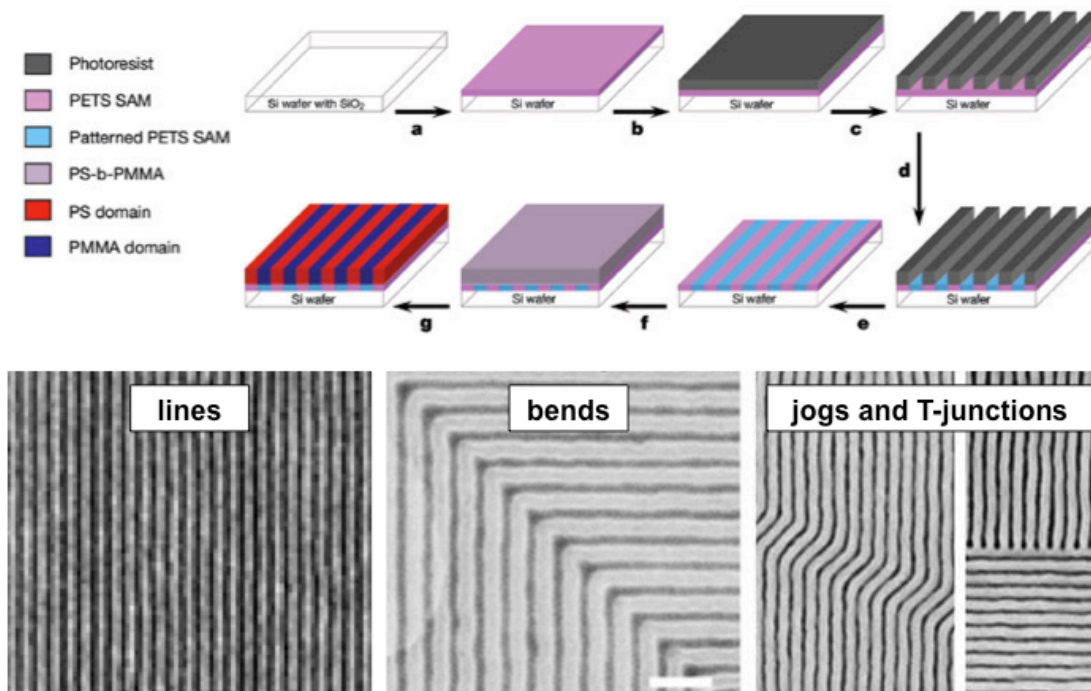


Figure 1.7: Schematic representation of the chemical preprocessing technique in which a phenylethyltrichlorosilane (PETS) self-assembled monolayer (SAM), photoresist, and soft X-rays were used to generate PS and PMMA preferential patterns, on which PS-PMMA BP films were cast and thermally annealed. With this technique, a multitude of patterns can be produced including lines, bends, jogs, and T-junctions. The chemical pre patterning schematic was adapted with permission from Kim, S. O. *et al. Nature* **2003**, 424, 411-414, Copyright 2003 Nature Publishing Group.¹³⁶ The lines/bends and jogs/T-junction micrographs were adapted with permission from Chang, T.-H. *et al. Sci. Rep.* **2016**, 6, 31407, Copyright 2016 The Authors, and Liu, G. *et al. Adv. Funct. Mater.* **2010**, 20, 1251-1257, Copyright 2010 John Wiley & Sons, Inc, respectively.^{137, 138}

1.5.2 Zone Casting/Annealing

Zone processing techniques exploit concentration or thermal gradients to generate sharp ordering fronts that guide self-assembly.¹²⁷ One such example is zone casting. Originally used to facilitate the growth of oriented small molecule crystals,¹⁴⁶ zone casting incorporates a narrow line-slit nozzle and moveable substrate to generate

highly-ordered BP nanostructures parallel or perpendicular to the substrate in one continuous motion.^{112, 147} Capillary forces between the slit and substrate produce a polymer solution meniscus that moves with the substrate during casting. Factors such as solution deposition rate, temperature, and substrate velocity tune the solidification front as the film dries, which leads to the creation of directionally-aligned nanostructures with minimal defects.

The generation of highly-ordered BP nanostructures also can be accomplished with sharp thermal gradients that anneal the film above the T_{ODT} , then quickly cool the film below the T_{ODT} . This process, termed hot zone annealing (HZA) by Hashimoto *et al.*, was employed to align nanostructures perpendicular to the thermal gradient across large areas of films.¹⁴⁸⁻¹⁵⁰ As an alternative to HZA, cold zone annealing (CZA) incorporates the same thermal gradients, but the maximum temperature does not exceed the T_{ODT} .¹⁵¹⁻¹⁵⁵ CZA can align polymer domains that are thermally-sensitive or large molecular weight BPs with T_{ODT} 's that are inaccessible with HZA.¹⁵¹ Furthermore, to improve the ordering kinetics, Singh *et al.* placed an elastomeric polydimethylsiloxane (PDMS) pad to the BP film to generate shear during directional expansion and contraction from the dynamic thermal field provided by CZA.¹⁵⁶ With this technique, termed cold zone annealing with soft shear (CZA-SS), the oscillatory shear imposed by the PDMS pad on the BP film provides near-perfect (>99%) ordering at relatively fast annealing speeds (≈ 0.2 mm/s) and in a manner amenable to roll-to-roll processing.¹⁵⁷

As an advancement of CZA, Majewski and Yager developed laser zone annealing (LZA), a process that exploits photothermal shear stresses to create thermal gradients of 4000 °C/mm used to direct BP nanostructures in a manner of seconds to

milliseconds.¹⁵⁸ In LZA, a high intensity laser is rastered across a film, cast on a light-absorbing layer (*e.g.*, germanium), with defined directional control (Figure 1.8).¹⁵⁸ The intense thermal gradient created by the laser generates a shear field that increases the ordering kinetics of the nanostructures by at least three orders of magnitude.^{158, 159} To achieve near-perfect alignment of nanostructures with the faster ordering kinetics, LZA with soft shear was developed by adding a PDMS pad for directional shear.¹⁶⁰ Majewski and Yager demonstrated that even shorter laser bursts over the course of milliseconds during LZA could provide breakup of grains and latent alignment pathways.¹⁶¹ A post-process thermal anneal reconnected the broken domains in the alignment direction for improved nanostructure ordering. Novel approaches such as these not only meet the time scales for alignment and degrees of ordering sought by industries but also are relatively universal to the growing number of BP systems.

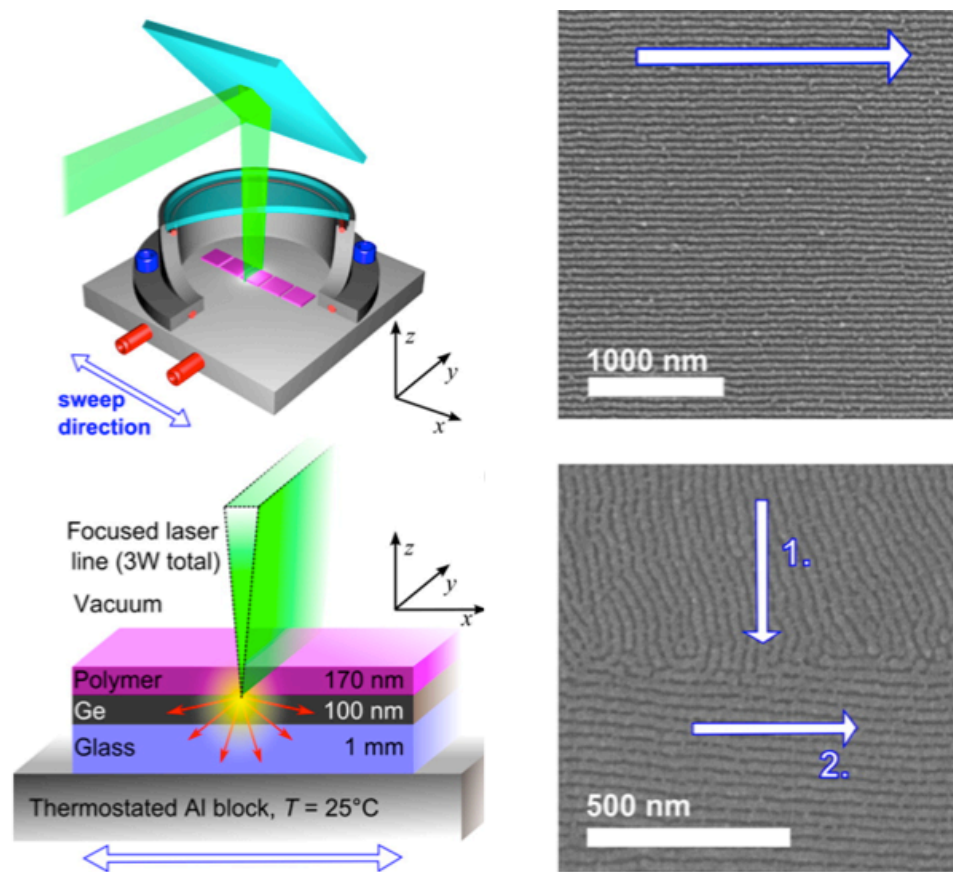


Figure 1.8: Schematic of laser zone annealing technique used to order and align BP thin film nanostructures: Photothermal gradients generated from a high-intensity laser and a light-absorbing germanium monolayer improved ordering kinetics by at least three orders of magnitude and provided nanoscale control over directionality to produce patterns such as T-junctions. Adapted with permission from Majewski, P. W. and Yager, K. G. *ACS Nano*, **2015**, 9, 3896-3906, Copyright 2015 American Chemical Society.¹⁵⁸

1.5.3 Shear-Alignment

As was discussed in Section 1.5.2, shear fields can direct the self-assembly of BP thin films. Shear-alignment techniques overcome energetic penalties of grain breakup and reorganization to align nanostructures in the direction of the shear force.^{10, 80, 127} Seminal work on the shear-alignment of BP thin films by Register and

coworkers, displaced cross-linked PDMS pads across the free surface of heated poly(styrene-*b*-ethylene-*alt*-propylene) films to generate well-ordered parallel cylinder nanostructures.¹⁶² With the advantages of low-cost and relative universality across different BP systems, the use of shear-alignment in BP thin films has grown significantly in recent years. The evolution of shear-alignment methods has led to several improvements and the development of numerous different shear-alignment strategies with two broad categories being hard and soft shear approaches.

1.5.3.1 Hard Shear

Hard shear processes exploit manual displacement of the PDMS pad in direct contact with the BP film to align nanostructures into large, continuous grains. To provide mobility to the polymer chains as the shear fields are applied, films are thermally annealed at a temperature above the T_g of the BP.¹⁶²⁻¹⁶⁴ This method has been employed for a wide-variety of polymer chemistries, morphologies, and orientation, and easily can be adjusted for different alignment areas by changing the size of the PDMS pad.^{163, 165-170} For example, Davis *et al.* demonstrated how extremely viscous PDMS gels (2,000,000 cps) can align BP nanostructures in a cone and plate rheometer, which demonstrates the relative ease in aligning nanostructures with shear fields.¹⁷¹ Hard-shear-aligned films also can be stacked to make nanosquare arrays or chemical prepatterns for seed-mediated alignment of BP films.^{172, 173} However, the alignment of nanostructures from hard shear approaches diminishes beyond the first layer in contact with the PDMS, and the time scales for high degrees of alignment typically are on the order of several hours.^{162, 171}

To overcome potential problems with high temperature degradation and long-time scales, Jeong *et al.* used solvent swelling rather than thermal treatment to provide

mobility to polymer chains.¹⁷⁴ By swelling a PDMS pad and manually dragging it across a BP film, they were able to achieve high degrees of ordering and alignment in PS-PDMS films over several minutes instead of hours. The close proximity of the solvent-swollen pad allowed solvent to diffuse into the film and provided mobility to the polymer chains during the application of shear. Furthermore, by adding multiple coating and alignment steps, crossed nanowire patterns were generated across large areas of the films.¹⁷⁴

1.5.3.2 Soft Shear

As an alternative to hard shear approaches, soft shear-alignment uses shear fields induced by differences in material properties. For example, CZA-SS and LZA-SS (discussed in Section 1.5.2) exploit thermal expansion differences to create shear fields. Another approach is to swell both the film and the PDMS pad simultaneously with SVA; this process is referred to as solvent vapor annealing with soft shear (SVA-SS).¹⁷⁵⁻¹⁷⁷ Isotropic swelling and deswelling of the PDMS pad on the film, which only swells vertically, generates a shear field in the direction of the swelling and drying fronts as shown in Figure 1.9.¹⁷⁵ Specifically, the swelling front shear field breaks up the nanostructures into smaller grains, and the drying front provides a shear direction during nanostructure re-assembly.^{161, 178} As demonstrated by Qiang *et al.*, SVA-SS can generate near-perfect alignment and ordering in minutes and in controllable directions and designs.^{175, 176}

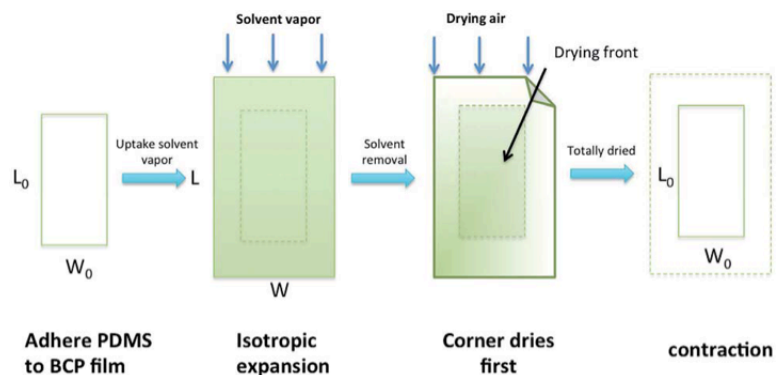


Figure 1.9: Schematic representation of SVA-SS. A PDMS pad, with initial dimensions L_0 and W_0 , is placed on a BP film and exposed to solvent vapor. The solvent vapor swells the PDMS to new dimensions L and W and provides mobility to the polymer chains in the film. During solvent removal, a drying front propagates from one corner of the PDMS to align nanostructures until solvent is completely removed from the system. Adapted with permission from Qiang *et al. Soft Matter*, **2014**, 10, 6068-6076, Copyright 2014 The Royal Society of Chemistry.¹⁷⁵

An expansion to SVA-SS, Luo *et al.* used raster solvent vapor annealing with soft shear (RSVA-SS) approach on an x-y motor stage to “write” patterns in SIS films at draw speeds on the order of $10 \mu\text{m/s}$.¹⁷⁹ RSVA is an SVA setup that dispenses controlled concentrations of solvent vapor directly into the BP *via* a flat-tipped needle held several hundred microns above the film.¹⁸⁰ The film rests on a motorized x-y stage to incorporate precise control over where the solvent is and is not injected into the polymer. Therefore, the swelling and drying fronts were defined and the researchers were able to direct the nanostructures in the patterns of their choosing. Furthermore, they demonstrated how the geometry of the rastering solvent injector can change from a needle to a slit to cover different surface areas in the same annealing time.¹⁷⁹ This approach is amenable to roll-to-roll processing of BP thin films for the high-throughput generation of aligned nanostructures.

1.5.4 Electrical/Magnetic Field Alignment

The use of electric or magnetic fields to direct the alignment of BP film nanostructures is well-established techniques in literature.^{10, 127} With electric field alignment, differences in dielectric permittivity between blocks result in the formation of well-ordered structures to reduce the orientation dependent electrostatic energy that develop when electric fields are applied to the BP.¹⁸¹⁻¹⁸⁷ Electric fields also can manipulate interactions to reorient nanostructures and cause morphology shifts.^{183, 188} For example, Xu *et al.* witnessed a transition from spherical to cylindrical domains in PS-PMMA BP films exposed to electric fields.¹⁸³ The electric field caused spheres to stretch and led to the coalescence of domains into ellipses and ultimately cylindrical structures. The restructuring process in the electric field requires the film to be heated above its ODT temperature (T_{ODT}) before restructuring can occur.¹⁰ Therefore, polymers with high T_{ODT} 's can degrade before alignment occurs, making the process unfavorable, and strong surface-polymer interactions can limit electric field alignment near interfaces, which can lead to non-uniform orientations through the film thickness.^{185, 189, 190}

In comparison to electric field alignment, magnetic field alignment occurs to minimize the orientation dependent magnetostatic energy from anisotropy in the magnetic susceptibility parameters between different blocks.^{10, 127} Therefore, magnetic field alignment is only feasible for BPs that have a block with a large magnetic susceptibility; this requirement normally applies to liquid crystalline (*e.g.*, poly[ethylene oxide-*b*-6-(4'-cyanobiphenyl-4-yloxy) hexyl methacrylate])¹⁹¹ or semi-crystalline (*e.g.*, poly[ethylene oxide-*b*-butadiene]) BPs.¹⁹² Even with this limitation, high degrees of ordering and orientation control with magnetic field alignment have been discussed in the literature.¹⁹³⁻¹⁹⁸

1.6 *In Situ* Measurements During Annealing

To study the interplay between BP thin film self-assembly kinetics and thermodynamics, researchers have conducted *in situ* experiments that track temporal domain restructuring during specific annealing processes.¹⁹⁹ These experiments have afforded key fundamental insights into various annealing approaches and have provided predictive control and tunability for the directed self-assembly of BP films. *In situ* measurements of BP films during annealing have been conducted with real space (*e.g.*, atomic force microscopy, optical microscopy) and reciprocal space (*e.g.*, X-ray scattering, neutron scattering) experimental techniques. Although real space techniques detail the actual nanostructures, reciprocal space techniques can provide large-scale information about small-scale features for improved statistical analysis. *In situ* experiments also can identify key parameters that go unnoticed in *ex situ* experimentation. Defining the underlying mechanisms governing each annealing technique has led to the development of improved and more universal directed self-assembly approaches.¹⁹⁹ Therefore, *in situ* experimentation is exploited heavily in this dissertation work, most notably in Chapters 3, 4, and 5.

1.7 Dissertation Overview

Significant work to improve BP thin film directed self-assembly and to create predictive formalisms, a fundamental understanding of the interplay between kinetics and thermodynamics, and advancements of current characterization and annealing approaches are described in this dissertation. Work in this dissertation focused on the development of innovative techniques to investigate the restructuring of nanoscale features over macroscopic areas and emphasized neutron scattering methods and *in situ* analysis tools to gain key insights about the kinetics of different directed self-

assembly procedures. Specifically, chlorosilane monolayers, gradient thickness films, and high-throughput optical microscopy were used to measure the nuanced effects of individual dispersive and polar components of the surface energy on BP nanostructure self-assembly in thin films.^{53, 56} Predictive maps were generated to define what orientation and degree of nanostructure ordering from the substrate to free surface would be expected provided the dispersive and polar surface energy components of the substrate and polymer blocks and the film thickness are known. In collaboration with the National Institute of Standards and Technology (NIST) Center for Neutron Research (NCNR), a series of *in situ* small-angle neutron scattering and neutron reflectometry (NR) experiments were conducted during SVA and SVA-SS to track nanostructure rearrangement kinetics and thermodynamics.^{92, 178} It was determined that the pathway to kinetic trapping of the polymer chains during solvent removal dictated the nanostructure formation in the film, and annealing protocols were developed to take advantage of these effects.⁹² From SVA-SS results, a key grain breakup step was discovered during solvent swelling that permitted nanostructure alignment during deswelling, and engineered methods were established to control drying fronts and alignment pathways.¹⁷⁸ Knowledge gleaned from *in situ* SVA-SS experiments led to the development of a novel flow coating device to cast and shear-align BP nanostructures simultaneously over the course of a few seconds. Lastly, NR was used as a non-destructive, high-resolution characterization tool to improve measurements of lithium salt distributions in BP electrolyte films. NR results for an array of different salts and salt concentrations provided strong evidence that lithium salts distribute evenly within the poly(oligo[oxyethylene]methacrylate) (POEM)

domains of PS-POEM BP thin films, which affects ion conductivity pathways in polymer electrolyte membranes.

In Chapter 2, a detailed description of the different surface and thin film characterization tools used in this dissertation is presented. In Chapter 3, the development of surface energy formalisms that describe how individual polar and dispersive surface energy components affect wetting behavior, through-film driving forces for self-assembly, and the propagation distance of the substrate surface energy effects is discussed. In Chapter 4, the use of *in situ* SANS and NR during SVA is explored to track solvent uptake and nanostructure reorganization as a function of solvent concentration. In Chapter 5, a kinetic and thermodynamic analysis of SVA-SS developed from *in situ* SANS experiments is detailed along with methods for improved directional control and ordering during SVA-SS and the development of a novel flow coating device that simultaneously casts and shear-aligns nanostructures. In Chapter 6, the use of NR to study how salt partitions within salt-doped BP electrolyte thin films and how the distribution affects conductivity kinetics for battery membrane applications is investigated. Chapter 7 concludes the dissertation with a summary of the main results and potential future studies of BP thin films to improve spatial control over SVA-SS with patterned PDMS, radially-align nanostructures with shear forces during spin coating, reversibly roughen substrate surfaces and simplify the generation of perpendicular nanostructures, explore novel BP architectures such as star BPs, and design next-generation neutron scattering tools to explore BP thin film self-assembly further.

REFERENCES

1. Bates, F. S.; Fredrickson, G. H. *Phys. Today* **1999**, 52, 32-38.
2. Bates, F. S. *Science* **1991**, 251, 898-905.
3. Fredrickson, G. H.; Bates, F. S. *Annu. Rev. Mater. Sci.* **1996**, 26, 501-550.
4. Bates, F. S.; Hillmyer, M. A.; Lodge, T. P.; Bates, C. M.; Delaney, K. T.; Fredrickson, G. H. *Science* **2012**, 336, 434-440.
5. Bates, C. M.; Bates, F. S. *Macromolecules* **2017**, 50, 3-22.
6. Faselka, M. J.; Mayes, A. M. *Annu. Rev. Mater. Sci.* **2001**, 31, 323-355.
7. Segalman, R. A. *Mater. Sci. Eng., R* **2005**, 48, 191-226.
8. Albert, J. N. L.; Epps, T. H., III. *Mater. Today* **2010**, 13, 24-33.
9. Hamley, I. W. *Prog. Polym. Sci.* **2009**, 34, 1161-1210.
10. Hu, H.; Gopinadhan, M.; Osuji, C. O. *Soft Matter* **2014**, 10, 3867-3889.
11. Bates, C. M.; Maher, M. J.; Janes, D. W.; Ellison, C. J.; Willson, C. G. *Macromolecules* **2013**, 47, 2-12.
12. Epps, T. H., III; O'Reilly, R. K. *Chem. Sci.* **2016**, 7, 1674-1689.
13. Hadjichristidis, N.; Floudas, G.; Pispas, S.; Hadjichristidis, N. *Macromolecules* **2001**, 34, 650-657.
14. Mai, Y.; Eisenberg, A. *Chem. Soc. Rev.* **2012**, 41, 5969-5985.
15. Matsen, M. W. *Macromolecules* **2012**, 45, 2161-2165.
16. Lynd, N. A.; Meuler, A. J.; Hillmyer, M. A. *Prog. Polym. Sci.* **2008**, 33, 875-893.
17. Brandrup, J.; Immergut, E. H.; Grulke, E. A., *Polymer handbook*. 4th ed.; Wiley: New York ; Chichester, 2004.

18. Glaser, J.; Medapuram, P.; Beardsley, T. M.; Matsen, M. W.; Morse, D. C. *Phys. Rev. Lett.* **2014**, 113, 068302.
19. Matsen, M. W. *Phys. Rev. Lett.* **1995**, 74, 4225-4228.
20. Matsen, M. W. *Macromolecules* **1995**, 28, 5765-5773.
21. Nakamura, I.; Balsara, N. P.; Wang, Z.-G. *Phys. Rev. Lett.* **2011**, 107, 198301.
22. Thelen, J. L.; Teran, A. A.; Wang, X.; Garetz, B. A.; Nakamura, I.; Wang, Z.-G.; Balsara, N. P. *Macromolecules* **2014**, 47, 2666-2673.
23. Hanley, K. J.; Lodge, T. P.; Huang, C.-I. *Macromolecules* **2000**, 33, 5918-5931.
24. Lodge, T. P.; Pudil, B.; Hanley, K. J. *Macromolecules* **2002**, 35, 4707-4717.
25. Alexandridis, P.; Spontak, R. J. *Curr. Opin. Colloid Interface Sci.* **1999**, 4, 130-139.
26. Bates, F. S.; Fredrickson, G. H. *Annu. Rev. Phys. Chem.* **1990**, 41, 525-557.
27. Sakamoto, N.; Hashimoto, T.; Han, C. D.; Kim, D.; Vaidya, N. Y. *Macromolecules* **1997**, 30, 1621-1632.
28. Walton, D. G.; Kellogg, G. J.; Mayes, A. M.; Lambooy, P.; Russell, T. P. *Macromolecules* **1994**, 27, 6225-6228.
29. Koneripalli, N.; Singh, N.; Levicky, R.; Bates, F. S.; Gallagher, P. D.; Satija, S. K. *Macromolecules* **1995**, 28, 2897-2904.
30. Knoll, A.; Horvat, A.; Lyakhova, K. S.; Krausch, G.; Sevink, G. J. A.; Zvelindovsky, A. V.; Magerle, R. *Phys. Rev. Lett.* **2002**, 89, 035501.
31. Matsen, M. W. *J. Chem. Phys.* **1997**, 106, 7781-7791.
32. Forrey, C.; Yager, K. G.; Broadaway, S. P. *ACS Nano* **2011**, 5, 2895-2907.
33. Edwards, E. W.; Montague, M. F.; Solak, H. H.; Hawker, C. J.; Nealey, P. F. *Adv. Mater.* **2004**, 16, 1315-1319.

34. Luo, M.; Seppala, J. E.; Albert, J. N. L.; Lewis, R. L.; Mahadevapuram, N.; Stein, G. E.; Epps, T. H., III. *Macromolecules* **2013**, 46, 1803-1811.
35. Smith, A. P.; Douglas, J. F.; Meredith, J. C.; Amis, E. J.; Karim, A. *J. Polym. Sci., Part B: Polym. Phys.* **2001**, 39, 2141-2158.
36. Smith, A. P.; Douglas, J. F.; Meredith, J. C.; Amis, E. J.; Karim, A. *Phys. Rev. Lett.* **2001**, 87, 015503.
37. Mansky, P.; Liu, Y.; Huang, E.; Russell, T. P.; Hawker, C. *Science* **1997**, 275, 1458-1460.
38. Maher, M. J.; Self, J. L.; Stasiak, P.; Blachut, G.; Ellison, C. J.; Matsen, M. W.; Bates, C. M.; Willson, C. G. *ACS Nano* **2016**, 10, 10152-10160.
39. Bates, C. M.; Seshimo, T.; Maher, M. J.; Durand, W. J.; Cushen, J. D.; Dean, L. M.; Blachut, G.; Ellison, C. J.; Willson, C. G. *Science* **2012**, 338, 775-779.
40. Kim, S.; Bates, C. M.; Thio, A.; Cushen, J. D.; Ellison, C. J.; Willson, C. G.; Bates, F. S. *ACS Nano* **2013**, 7, 9905-9919.
41. Han, E.; Stuen, K. O.; Leolukman, M.; Liu, C.-C.; Nealey, P. F.; Gopalan, P. *Macromolecules* **2009**, 42, 4896-4901.
42. Khanna, V.; Cochran, E. W.; Hexemer, A.; Stein, G. E.; Fredrickson, G. H.; Kramer, E. J.; Li, X.; Wang, J.; Hahn, S. F. *Macromolecules* **2006**, 39, 9346-9356.
43. Khaira, G. S.; Qin, J.; Garner, G. P.; Xiong, S.; Wan, L.; Ruiz, R.; Jaeger, H. M.; Nealey, P. F.; de Pablo, J. J. *ACS Macro Lett.* **2014**, 3, 747-752.
44. Nagpal, U.; Müller, M.; Nealey, P. F.; de Pablo, J. J. *ACS Macro Lett.* **2012**, 1, 418-422.
45. Edwards, E. W.; Stoykovich, M. P.; Müller, M.; Solak, H. H.; de Pablo, J. J.; Nealey, P. F. *J. Polym. Sci., Part B: Polym. Phys.* **2005**, 43, 3444-3459.
46. Xu, T.; Hawker, C. J.; Russell, T. P. *Macromolecules* **2005**, 38, 2802-2805.
47. Ji, S.; Liu, C.-C.; Liao, W.; Fenske, A. L.; Craig, G. S. W.; Nealey, P. F. *Macromolecules* **2011**, 44, 4291-4300.
48. Welander, A. M.; Craig, G. S. W.; Tada, Y.; Yoshida, H.; Nealey, P. F. *Macromolecules* **2013**, 46, 3915-3921.

49. Epps, T. H., III; DeLongchamp, D. M.; Fasolka, M. J.; Fischer, D. A.; Jablonski, E. L. *Langmuir* **2007**, 23, 3355-3362.
50. Krausch, G.; Magerle, R. *Adv. Mater.* **2002**, 14, 1579-1583.
51. She, M.-S.; Lo, T.-Y.; Ho, R.-M. *Macromolecules* **2014**, 47, 175-182.
52. Jin, S.; Yoon, J.; Heo, K.; Park, H.-W.; Kim, J.; Kim, K.-W.; Shin, T. J.; Chang, T.; Ree, M. *J. Appl. Crystallogr.* **2007**, 40, 950-958.
53. Shelton, C. K.; Epps, T. H., III. *Macromolecules* **2015**, 48, 4572-4580.
54. Mansky, P.; Russell, T. P.; Hawker, C. J.; Mays, J.; Cook, D. C.; Satija, S. K. *Phys. Rev. Lett.* **1997**, 79, 237-240.
55. Knoll, A.; Magerle, R.; Krausch, G. *J. Chem. Phys.* **2004**, 120, 1105-1116.
56. Shelton, C. K.; Epps, T. H., III. *Macromolecules* **2016**, 49, 574-580.
57. Russell, T. P.; Coulon, G.; Deline, V. R.; Miller, D. C. *Macromolecules* **1989**, 22, 4600-4606.
58. Shin, C.; Ahn, H.; Kim, E.; Ryu, D. Y.; Huh, J.; Kim, K.-W.; Russell, T. P. *Macromolecules* **2008**, 41, 9140-9145.
59. Zhang, X.; Berry, B. C.; Yager, K. G.; Kim, S.; Jones, R. L.; Satija, S.; Pickel, D. L.; Douglas, J. F.; Karim, A. *ACS Nano* **2008**, 2, 2331-2341.
60. Han, E.; Stuen, K. O.; La, Y.-H.; Nealey, P. F.; Gopalan, P. *Macromolecules* **2008**, 41, 9090-9097.
61. Ham, S.; Shin, C.; Kim, E.; Ryu, D. Y.; Jeong, U.; Russell, T. P.; Hawker, C. J. *Macromolecules* **2008**, 41, 6431-6437.
62. Huang, E.; Pruzinsky, S.; Russell, T. P.; Mays, J.; Hawker, C. J. *Macromolecules* **1999**, 32, 5299-5303.
63. Huang, E.; Russell, T. P.; Harrison, C.; Chaikin, P. M.; Register, R. A.; Hawker, C. J.; Mays, J. *Macromolecules* **1998**, 31, 7641-7650.
64. In, I.; La, Y.-H.; Park, S.-M.; Nealey, P. F.; Gopalan, P. *Langmuir* **2006**, 22, 7855-7860.

65. Ji, S.; Liu, C.-C.; Son, J. G.; Gotrik, K.; Craig, G. S. W.; Gopalan, P.; Himpfel, F. J.; Char, K.; Nealey, P. F. *Macromolecules* **2008**, *41*, 9098-9103.
66. Mansky, P.; Russell, T. P.; Hawker, C. J.; Pitsikalis, M.; Mays, J. *Macromolecules* **1997**, *30*, 6810-6813.
67. Albert, J. N. L.; Baney, M. J.; Stafford, C. M.; Kelly, J. Y.; Epps, T. H., III. *ACS Nano* **2009**, *3*, 3977-3986.
68. Albert, J. N. L.; Kim, J. D.; Stafford, C. M.; Epps, T. H., III. *Rev. Sci. Instrum.* **2011**, *82*, 065103.
69. Peters, R. D.; Yang, X. M.; Kim, T. K.; Sohn, B. H.; Nealey, P. F. *Langmuir* **2000**, *16*, 4625-4631.
70. Peters, R. D.; Yang, X. M.; Nealey, P. F. *Macromolecules* **2002**, *35*, 1822-1834.
71. Ashley, K.; Sehgal, A.; Amis, E. J.; Raghavan, D.; Karim, A. *Mater. Res. Soc. Symp. Proc.* **2001**, *700*, S4.7.1-S4.7.6.
72. Smith, A. P.; Sehgal, A.; Douglas, J. F.; Karim, A.; Amis, E. J. *Macromol. Rapid Commun.* **2003**, *24*, 131-135.
73. Ye, X.; Edwards, B. J.; Khomami, B. *Macromol. Rapid Commun.* **2014**, *35*, 702-707.
74. Man, X.; Tang, J.; Zhou, P.; Yan, D.; Andelman, D. *Macromolecules* **2015**, *48*, 7689-7697.
75. Yager, K. G.; Forrey, C.; Singh, G.; Satija, S. K.; Page, K. A.; Patton, D. L.; Douglas, J. F.; Jones, R. L.; Karim, A. *Soft Matter* **2015**, *11*, 5154-5167.
76. Sivaniah, E.; Hayashi, Y.; Matsubara, S.; Kiyono, S.; Hashimoto, T.; Fukunaga, K.; Kramer, E. J.; Mates, T. *Macromolecules* **2005**, *38*, 1837-1849.
77. Kulkarni, M. M.; Yager, K. G.; Sharma, A.; Karim, A. *Macromolecules* **2012**, *45*, 4303-4314.
78. Man, X.; Zhou, P.; Tang, J.; Yan, D.; Andelman, D. *Macromolecules* **2016**, *49*, 8241-8248.

79. Park, S.; Lee, D. H.; Xu, J.; Kim, B.; Hong, S. W.; Jeong, U.; Xu, T.; Russell, T. P. *Science* **2009**, 323, 1030-1033.
80. Majewski, P. W.; Yager, K. G. *J. Phys.: Condens. Matter* **2016**, 28, 403002.
81. Majewski, P. W.; Yager, K. G. *Soft Matter* **2016**, 12, 281-294.
82. Stuen, K. O.; Liu, C.; Welander, A. M.; Liu, G.; de Pablo, J. J.; Nealey, P. F.; Satapathy, D. K.; Nygård, K.; Bunk, O.; Solak, H. H.; van der Veen, J. F. *J. Vac. Sci. Technol., B* **2008**, 26, 2504-2508.
83. Liu, G.; Delcambre, S. P.; Stuen, K. O.; Craig, G. S. W.; De Pablo, J. J. *J. Vac. Sci. Technol., B* **2010**, 28, C6B13-C6B19.
84. Zhang, X.; Yager, K. G.; Fredin, N. J.; Ro, H. W.; Jones, R. L.; Karim, A.; Douglas, J. F. *ACS Nano* **2010**, 4, 3653-3660.
85. Zhang, X. H.; Berry, B. C.; Yager, K. G.; Kim, S.; Jones, R. L.; Satija, S.; Pickel, D. L.; Douglas, J. F.; Karim, A. *ACS Nano* **2008**, 2, 2331-2341.
86. Black, C. T.; Guarini, K. W. *J. Polym. Sci., Part A: Polym. Chem.* **2004**, 42, 1970-1975.
87. Shin, C.; Ryu, D. Y.; Huh, J.; Kim, J. H.; Kim, K.-W. *Macromolecules* **2009**, 42, 2157-2160.
88. Körstgens, V.; Wiedersich, J.; Meier, R.; Perlich, J.; Roth, S. V.; Gehrke, R.; Müller-Buschbaum, P. *Anal. Bioanal. Chem.* **2010**, 396, 139-149.
89. Gu, X.; Gunkel, I.; Hexemer, A.; Russell, T. P. *Macromolecules* **2016**, 49, 3373-3381.
90. Park, I.; Lee, B.; Ryu, J.; Im, K.; Yoon, J.; Ree, M.; Chang, T. *Macromolecules* **2005**, 38, 10532-10536.
91. Sinturel, C.; Vayer, M.; Morris, M.; Hillmyer, M. A. *Macromolecules* **2013**, 46, 5399-5415.
92. Shelton, C. K.; Jones, R. L.; Dura, J. A.; Epps, T. H., III *Macromolecules* **2016**, 49, 7525-7534.
93. Cavicchi, K. A.; Berthiaume, K. J.; Russell, T. P. *Polymer* **2005**, 46, 11635-11639.

94. Xuan, Y.; Peng, J.; Cui, L.; Wang, H.; Li, B.; Han, Y. *Macromolecules* **2004**, *37*, 7301-7307.
95. Lin, Z. Q.; Kim, D. H.; Wu, X. D.; Boosahda, L.; Stone, D.; LaRose, L.; Russell, T. P. *Adv. Mater.* **2002**, *14*, 1373-1376.
96. Jung, Y. S.; Ross, C. A. *Adv. Mater.* **2009**, *21*, 2540-2545.
97. Di, Z.; Posselt, D.; Smilgies, D.-M.; Papadakis, C. M. *Macromolecules* **2010**, *43*, 418-427.
98. Zettl, U.; Knoll, A.; Tsarkova, L. *Langmuir* **2010**, *26*, 6610-6617.
99. Chen, Y.; Huang, H.; Hu, Z.; He, T. *Langmuir* **2004**, *20*, 3805-3808.
100. Li, Y.; Huang, H.; He, T.; Gong, Y. *J. Phys. Chem. B* **2010**, *114*, 1264-1270.
101. Bang, J.; Kim, B. J.; Stein, G. E.; Russell, T. P.; Li, X.; Wang, J.; Kramer, E. J.; Hawker, C. J. *Macromolecules* **2007**, *40*, 7019-7025.
102. Hsieh, I. F.; Sun, H.-J.; Fu, Q.; Lotz, B.; Cavicchi, K. A.; Cheng, S. Z. D. *Soft Matter* **2012**, *8*, 7937-7944.
103. Paik, M. Y.; Bosworth, J. K.; Smilges, D.-M.; Schwartz, E. L.; Andre, X.; Ober, C. K. *Macromolecules* **2010**, *43*, 4253-4260.
104. Knoll, A.; Tsarkova, L.; Krausch, G. *Nano Lett.* **2007**, *7*, 843-846.
105. Hannon, A. F.; Bai, W.; Alexander-Katz, A.; Ross, C. A. *Soft Matter* **2015**, *11*, 3794-3805.
106. Bai, W.; Yager, K. G.; Ross, C. A. *Macromolecules* **2015**, *48*, 8574-8584.
107. Rodwogin, M. D.; Spanjers, C. S.; Leighton, C.; Hillmyer, M. A. *ACS Nano* **2010**, *4*, 725-732.
108. Kim, S. H.; Misner, M. J.; Xu, T.; Kimura, M.; Russell, T. P. *Adv. Mater.* **2004**, *16*, 226-231.
109. Cavicchi, K. A.; Russell, T. P. *Macromolecules* **2007**, *40*, 1181-1186.
110. Albert, J. N. L.; Young, W.-S.; Lewis, R. L.; Bogart, T. D.; Smith, J. R.; Epps, T. H., III. *ACS Nano* **2012**, *6*, 459-466.

111. Fukunaga, K.; Elbs, H.; Magerle, R.; Krausch, G. *Macromolecules* **2000**, *33*, 947-953.
112. Tang, C.; Tracz, A.; Kruk, M.; Zhang, R.; Smilgies, D.-M.; Matyjaszewski, K.; Kowalewski, T. *J. Am. Chem. Soc.* **2005**, *127*, 6918-6919.
113. Albert, J. N. L.; Bogart, T. D.; Lewis, R. L.; Beers, K. L.; Fasolka, M. J.; Hutchison, J. B.; Vogt, B. D.; Epps, T. H., III. *Nano Lett.* **2011**, *11*, 1351-1357.
114. Chavis, M. A.; Smilgies, D.-M.; Wiesner, U. B.; Ober, C. K. *Adv. Funct. Mater.* **2015**, *25*, 3057-3065.
115. Bosworth, J. K.; Paik, M. Y.; Ruiz, R.; Schwartz, E. L.; Huang, J. Q.; Ko, A. W.; Smilgies, D.-M.; Black, C. T.; Ober, C. K. *ACS Nano* **2008**, *2*, 1396-1402.
116. Gowd, E. B.; Marcus, B.; Manfred, S. *IOP Conf. Ser.: Mater. Sci. Eng.* **2010**, *14*, 012015.
117. Gotrik, K. W.; Hannon, A. F.; Son, J. G.; Keller, B.; Alexander-Katz, A.; Ross, C. A. *ACS Nano* **2012**, *6*, 8052-8059.
118. Di, Z.; Posselt, D.; Smilgies, D.-M.; Li, R.; Rauscher, M.; Potemkin, I. I.; Papadakis, C. M. *Macromolecules* **2012**, *45*, 5185-5195.
119. Zhang, J.; Posselt, D.; Sepe, A.; Shen, X.; Perlich, J.; Smilgies, D.-M.; Papadakis, C. M. *Macromol. Rapid Commun.* **2013**, *34*, 1289-1295.
120. Zhang, J.; Posselt, D.; Smilgies, D.-M.; Perlich, J.; Kyriakos, K.; Jaksch, S.; Papadakis, C. M. *Macromolecules* **2014**, *47*, 5711-5718.
121. Zhao, J.; Jiang, S.; Ji, X.; An, L.; Jiang, B. *Polymer* **2005**, *46*, 6513-6521.
122. Emerson, J. A.; Toolan, D. T. W.; Howse, J. R.; Furst, E. M.; Epps, T. H., III *Macromolecules* **2013**, *46*, 6533-6540.
123. Flory, P. J., *Principles of Polymer Chemistry*. Cornell University Press: Ithaca, United States, 1953.
124. Elbs, H.; Krausch, G. *Polymer* **2004**, *45*, 7935-7942.
125. Elbs, H.; Drummer, C.; Abetz, V.; Krausch, G. *Macromolecules* **2002**, *35*, 5570-5577.

126. Gu, X.; Gunkel, I.; Hexemer, A.; Gu, W.; Russell, T. P. *Adv. Mater.* **2014**, *26*, 273-281.
127. Luo, M.; Epps, T. H., III. *Macromolecules* **2013**, *46*, 7567-7579.
128. Cheng, J. Y.; Mayes, A. M.; Ross, C. A. *Nat. Mater.* **2004**, *3*, 823-828.
129. Li, M.; Ober, C. K. *Mater. Today* **2006**, *9*, 30-39.
130. Shuaigang, X.; XiaoMin, Y.; Erik, W. E.; Young-Hye, L.; Paul, F. N. *Nanotechnology* **2005**, *16*, S324.
131. Bang, J.; Jeong, U.; Ryu, D. Y.; Russell, T. P.; Hawker, C. J. *Adv. Mater.* **2009**, *21*, 4769-4792.
132. Cheng, J. Y.; Ross, C. A.; Smith, H. I.; Thomas, E. L. *Adv. Mater.* **2006**, *18*, 2505-2521.
133. Ginzburg, V. V.; Weinhold, J. D.; Trefonas, P. *J. Polym. Sci., Part B: Polym. Phys.* **2015**, *53*, 90-95.
134. Hannon, A. F.; Ding, Y.; Bai, W.; Ross, C. A.; Alexander-Katz, A. *Nano Lett.* **2014**, *14*, 318-325.
135. Mickiewicz, R. A.; Yang, J. K. W.; Hannon, A. F.; Jung, Y.-S.; Alexander-Katz, A.; Berggren, K. K.; Ross, C. A. *Macromolecules* **2010**, *43*, 8290-8295.
136. Kim, S. O.; Solak, H. H.; Stoykovich, M. P.; Ferrier, N. J.; de Pablo, J. J.; Nealey, P. F. *Nature* **2003**, *424*, 411-414.
137. Chang, T.-H.; Xiong, S.; Jacobberger, R. M.; Mikael, S.; Suh, H. S.; Liu, C.-C.; Geng, D.; Wang, X.; Arnold, M. S.; Ma, Z.; Nealey, P. F. *Sci. Rep.* **2016**, *6*, 31407.
138. Liu, G.; Thomas, C. S.; Craig, G. S. W.; Nealey, P. F. *Adv. Funct. Mater.* **2010**, *20*, 1251-1257.
139. Stoykovich, M. P.; Kang, H.; Daoulas, K. C.; Liu, G.; Liu, C.-C.; de Pablo, J. J.; Müller, M.; Nealey, P. F. *ACS Nano* **2007**, *1*, 168-175.
140. Wilmes, G. M.; Durkee, D. A.; Balsara, N. P.; Liddle, J. A. *Macromolecules* **2006**, *39*, 2435-2437.
141. Stoykovich, M. P.; Nealey, P. F. *Mater. Today* **2006**, *9*, 20-29.

142. Detcheverry, F. A.; Liu, G.; Nealey, P. F.; de Pablo, J. J. *Macromolecules* **2010**, 43, 3446-3454.
143. Edwards, E. W.; Müller, M.; Stoykovich, M. P.; Solak, H. H.; de Pablo, J. J.; Nealey, P. F. *Macromolecules* **2007**, 40, 90-96.
144. Stoykovich, M. P.; Müller, M.; Kim, S. O.; Solak, H. H.; Edwards, E. W.; de Pablo, J. J.; Nealey, P. F. *Science* **2005**, 308, 1442-1446.
145. Welander, A. M.; Kang, H.; Stuen, K. O.; Solak, H. H.; Müller, M.; de Pablo, J. J.; Nealey, P. F. *Macromolecules* **2008**, 41, 2759-2761.
146. Kimura, M.; Misner, M. J.; Xu, T.; Kim, S. H.; Russell, T. P. *Langmuir* **2003**, 19, 9910-9913.
147. Tang, C.; Wu, W.; Smilgies, D.-M.; Matyjaszewski, K.; Kowalewski, T. *J. Am. Chem. Soc.* **2011**, 133, 11802-11809.
148. Hashimoto, T.; Bodycomb, J.; Funaki, Y.; Kimishima, K. *Macromolecules* **1999**, 32, 952-954.
149. Bodycomb, J.; Funaki, Y.; Kimishima, K.; Hashimoto, T. *Macromolecules* **1999**, 32, 2075-2077.
150. Angelescu, D. E.; Waller, J. H.; Adamson, D. H.; Register, R. A.; Chaikin, P. M. *Adv. Mater.* **2007**, 19, 2687-2690.
151. Berry, B. C.; Bosse, A. W.; Douglas, J. F.; Jones, R. L.; Karim, A. *Nano Lett.* **2007**, 7, 2789-2794.
152. Singh, G.; Yager, K. G.; Smilgies, D.-M.; Kulkarni, M. M.; Bucknall, D. G.; Karim, A. *Macromolecules* **2012**, 45, 7107-7117.
153. Yager, K. G.; Fredin, N. J.; Zhang, X.; Berry, B. C.; Karim, A.; Jones, R. L. *Soft Matter* **2010**, 6, 92-99.
154. Ye, C.; Sun, Y.; Karim, A.; Vogt, B. D. *Macromolecules* **2015**, 48, 7567-7573.
155. Samant, S.; Strzalka, J.; Yager, K. G.; Kisslinger, K.; Grolman, D.; Basutkar, M.; Salunke, N.; Singh, G.; Berry, B.; Karim, A. *Macromolecules* **2016**, 49, 8633-8642.
156. Singh, G.; Yager, K. G.; Berry, B.; Kim, H.-C.; Karim, A. *ACS Nano* **2012**, 6, 10335-10342.

157. Singh, G.; Batra, S.; Zhang, R.; Yuan, H.; Yager, K. G.; Cakmak, M.; Berry, B.; Karim, A. *ACS Nano* **2013**, 7, 5291-5299.
158. Majewski, P. W.; Yager, K. G. *ACS Nano* **2015**, 9, 3896-3906.
159. Jacobs, A. G.; Liedel, C.; Peng, H.; Wang, L.; Smilgies, D.-M.; Ober, C. K.; Thompson, M. O. *Macromolecules* **2016**, 49, 6462-6470.
160. Majewski, P. W.; Yager, K. G. *Macromolecules* **2015**, 48, 4591-4598.
161. Majewski, P. W.; Yager, K. G. *Nano Lett.* **2015**, 15, 5221-5228.
162. Angelescu, D. E.; Waller, J. H.; Adamson, D. H.; Deshpande, P.; Chou, S. Y.; Register, R. A.; Chaikin, P. M. *Adv. Mater.* **2004**, 16, 1736-1740.
163. Angelescu, D. E.; Waller, J. H.; Register, R. A.; Chaikin, P. M. *Adv. Mater.* **2005**, 17, 1878-1881.
164. Nikoubashman, A.; Davis, R. L.; Michal, B. T.; Chaikin, P. M.; Register, R. A.; Panagiotopoulos, A. Z. *ACS Nano* **2014**, 8, 8015-8026.
165. Davis, R. L.; Chaikin, P. M.; Register, R. A. *Macromolecules* **2014**, 47, 5277-5285.
166. Nikoubashman, A.; Register, R. A.; Panagiotopoulos, A. Z. *Soft Matter* **2013**, 9, 9960-9971.
167. Chremos, A.; Chaikin, P. M.; Register, R. A.; Panagiotopoulos, A. Z. *Soft Matter* **2012**, 8, 7803-7811.
168. Pujari, S.; Keaton, M. A.; Chaikin, P. M.; Register, R. A. *Soft Matter* **2012**, 8, 5358-5363.
169. Marencic, A. P.; Wu, M. W.; Register, R. A.; Chaikin, P. M. *Macromolecules* **2007**, 40, 7299-7305.
170. Marencic, A. P.; Adamson, D. H.; Chaikin, P. M.; Register, R. A. *Phys. Rev. E Stat. Nonlin. Soft Matter Phys.* **2010**, 81, 011503.
171. Davis, R. L.; Michal, B. T.; Chaikin, P. M.; Register, R. A. *Macromolecules* **2015**, 48, 5339-5347.
172. Kim, S. Y.; Nunns, A.; Gwyther, J.; Davis, R. L.; Manners, I.; Chaikin, P. M.; Register, R. A. *Nano Lett.* **2014**, 14, 5698-5705.

173. Abate, A. A.; Vu, G. T.; Pezzutti, A. D.; García, N. A.; Davis, R. L.; Schmid, F.; Register, R. A.; Vega, D. A. *Macromolecules* **2016**, *49*, 7588-7596.
174. Jeong, J. W.; Hur, Y. H.; Kim, H.-j.; Kim, J. M.; Park, W. I.; Kim, M. J.; Kim, B. J.; Jung, Y. S. *ACS Nano* **2013**, *7*, 6747-6757.
175. Qiang, Z.; Zhang, Y.; Groff, J. A.; Cavicchi, K. A.; Vogt, B. D. *Soft Matter* **2014**, *10*, 6068-6076.
176. Qiang, Z.; Zhang, L.; Stein, G. E.; Cavicchi, K. A.; Vogt, B. D. *Macromolecules* **2014**, *47*, 1109-1116.
177. Qiang, Z.; Zhang, Y.; Wang, Y.; Bhaway, S. M.; Cavicchi, K. A.; Vogt, B. D. *Carbon* **2015**, *82*, 51-59.
178. Shelton, C. K.; Jones, R. L.; Epps, T. H., III. *in preparation*.
179. Luo, M.; Scott, D. M.; Epps, T. H., III. *ACS Macro Lett.* **2015**, *4*, 516-520.
180. Seppala, J. E.; Lewis, R. L.; Epps, T. H., III. *ACS Nano* **2012**, *6*, 9855-9862.
181. Amundson, K.; Helfand, E.; Quan, X.; Smith, S. D. *Macromolecules* **1993**, *26*, 2698-2703.
182. Amundson, K.; Helfand, E.; Quan, X.; Hudson, S. D.; Smith, S. D. *Macromolecules* **1994**, *27*, 6559-6570.
183. Xu, T.; Zvelindovsky, A. V.; Sevink, G. J. A.; Gang, O.; Ocko, B.; Zhu, Y.; Gido, S. P.; Russell, T. P. *Macromolecules* **2004**, *37*, 6980-6984.
184. Gurovich, E. *Phys. Rev. Lett.* **1995**, *74*, 482-485.
185. Xu, T.; Zhu, Y.; Gido, S. P.; Russell, T. P. *Macromolecules* **2004**, *37*, 2625-2629.
186. Mansky, P.; DeRouchey, J.; Russell, T. P.; Mays, J.; Pitsikalis, M.; Morkved, T.; Jaeger, H. *Macromolecules* **1998**, *31*, 4399-4401.
187. Schmidt, K.; Böker, A.; Zettl, H.; Schubert, F.; Hänsel, H.; Fischer, F.; Weiss, T. M.; Abetz, V.; Zvelindovsky, A. V.; Sevink, G. J. A.; Krausch, G. *Langmuir* **2005**, *21*, 11974-11980.
188. Tsori, Y.; Andelman, D. *Macromolecules* **2002**, *35*, 5161-5170.

189. Thurn-Albrecht, T.; DeRouchey, J.; Russell, T. P.; Jaeger, H. M. *Macromolecules* **2000**, *33*, 3250-3253.
190. Xu, T.; Hawker, C. J.; Russell, T. P. *Macromolecules* **2003**, *36*, 6178-6182.
191. Gopinadhan, M.; Majewski, P. W.; Osuji, C. O. *Macromolecules* **2010**, *43*, 3286-3293.
192. Grigorova, T.; Pispas, S.; Hadjichristidis, N.; Thurn-Albrecht, T. *Macromolecules* **2005**, *38*, 7430-7433.
193. Majewski, P. W.; Gopinadhan, M.; Osuji, C. O. *J. Polym. Sci., Part B: Polym. Phys.* **2012**, *50*, 2-8.
194. Gopinadhan, M.; Majewski, P. W.; Beach, E. S.; Osuji, C. O. *ACS Macro Lett.* **2012**, *1*, 184-189.
195. Majewski, P. W.; Gopinadhan, M.; Jang, W.-S.; Lutkenhaus, J. L.; Osuji, C. O. *J. Am. Chem. Soc.* **2010**, *132*, 17516-17522.
196. Sakurai, S. *Polymer* **2008**, *49*, 2781-2796.
197. Feng, X.; Tousley, M. E.; Cowan, M. G.; Wiesenauer, B. R.; Nejati, S.; Choo, Y.; Noble, R. D.; Elimelech, M.; Gin, D. L.; Osuji, C. O. *ACS Nano* **2014**, *8*, 11977-11986.
198. Rokhlenko, Y.; Gopinadhan, M.; Osuji, C. O.; Zhang, K.; O'Hern, C. S.; Larson, S. R.; Gopalan, P.; Majewski, P. W.; Yager, K. G. *Phys. Rev. Lett.* **2015**, *115*, 258302.
199. Shelton, C. K.; Epps, T. H., III *Polymer* **2016**, *105*, 545-561.

Chapter 2

EXPERIMENTAL METHODS AND CHARACTERIZATION TECHNIQUES

The experimental methods used to fabricate, process, and characterize block polymer (BP) thin films are detailed in this chapter. Specifically, the fundamental concepts behind each technique and how each was incorporated in the overall analysis of this dissertation are highlighted. Exact experimental conditions are provided in later chapters along with the collected results.

2.1 Substrate Modification

Substrate surfaces can be modified to alter substrate-polymer interactions and direct nanostructure orientation and ordering. The three most common techniques to change substrate surfaces are ultra-violet ozone (UVO) radiation, chlorosilane deposition, and random copolymer monolayers. In the following sections, the utility of each of these methods on silicon substrates will be discussed.

2.1.1 Ultra-Violet Ozone

UVO radiation is used to etch organic contaminants from the wafers and leave behind an oxide surface layer.¹ In this dissertation work, UVO was conducted in a UVO cleaner (model 342, Jelight Co., Inc.) for ≈ 1 h prior to film casting or substrate modification with chlorosilanes or random copolymers to ensure the substrate was clean and functionalized. A high-intensity UV light within the cleaner created ozone molecules that readily reacted with contaminant molecules on the substrate to form simpler volatile molecules such as CO_2 , H_2O , and N_2 ; more oxygenated chemical

moieties (*e.g.*, hydroxyl, carbonyl, carboxyl) are generated on the surface as a byproduct of this reaction.² After UVO cleaning, silicon wafers were rinsed with toluene and dried with nitrogen three times to remove any contaminants left on the surface. Controlled UVO also can etch chlorosilane and random copolymer monolayers to expose the underlying silicon oxide layer and tune the overall substrate surface energy.^{2,3}

2.1.2 Chlorosilane Deposition

For more precise tuning of polar and dispersive surface energy components, chlorosilanes with different side-chain groups can be deposited on the substrate surface.⁴⁻⁹ Chlorosilanes are a series of chemicals that have at least one silicon-chlorine bond that can react covalently with the oxide surface of silicon wafers after UVO cleaning. Chlorosilane functionality, or functionalities if one or more chlorosilanes are mixed, can include alkyl-, aromatic-, methacrylate-, acetyl-, and fluorinated groups that change the surface energy of chlorosilane-modified substrate surfaces. Furthermore, chlorosilane deposition can be paired with UVO or X-ray exposure after deposition to degrade the monolayer partially and modify the substrate surface energy, particularly the polar component.^{2, 8, 10, 11} Because chlorosilanes with multiple silicon-chlorine bonds form siloxane with the silicon substrates, only monochlorosilanes, chlorosilanes with one silicon-chlorine bond, were used in this dissertation.

In this dissertation, chlorosilane monolayers were deposited on UVO cleaned silicon substrates *via* liquid or vapor deposition. The liquid deposition technique exploits direct contact between the chlorosilane and the silicon substrate to accomplish substrate modification. In this approach, pure or mixed chlorosilanes (>1 mL) were

dropped on the substrates with a Pasteur pipette until a thin liquid layer covered the entirety of the wafer area. The chlorosilanes reacted with the substrate for 2 h in a sealed glass petri dish wrapped in aluminum foil to trap the volatile chlorosilanes. Modified substrates were rinsed with toluene and dried with nitrogen several times to remove any unreacted chlorosilane. Although liquid deposition is faster, Albert *et al.* demonstrated how vapor deposition could create controlled gradient monolayers of two or more chlorosilanes across a substrate surface to analyze the nuanced effects of substrate surface energy on BP self-assembly.⁴ Vapor deposition was conducted using a vacuum chamber to evaporate the chlorosilane, provided the vapor pressure was less than ≈ 5 torr at 100 °C, which then reacted as it passed over a cleaned silicon wafer.⁵ To ensure the chlorosilane had sufficient time to react, dynamic vacuum was pulled for 4 – 6 h.

2.1.3 Random Copolymer Monolayers

Random copolymer monolayers provide a compositional match to the BP film components for the generation of completely neutral substrate-polymer interactions. To functionalize a substrate with a random copolymer, the monolayer must be side- or end-chain grafted to the silicon to form a brush layer.¹²⁻¹⁷ Grafting the polymer to the substrate prevents it from dissolving when the polymer solution is cast. For this dissertation, glycidial methacrylate end groups were incorporated into the random copolymers and attached to the substrate through exposure to UV-radiation and thermal annealing to react the end-group with the silicon surface.

2.2 Contact Angle Goniometry

Contact angle goniometry is used to characterize the surface energy of the substrate before and after modification with chlorosilanes and random copolymers. The technique measures the contact angle of a liquid droplet on a solid surface, as the droplet shape and area are related to the solid-liquid interaction. If the drop is static on the substrate, the measured contact angle (θ) and surface energy are correlated according to Young's equation shown in Equation 2.1.¹⁸

$$\gamma_{LV} \cos(\theta) = \gamma_{SV} - \gamma_{SL} \quad (2.1)$$

In Equation 2.1, γ_{LV} is the surface tension of the liquid in equilibrium with its saturated vapor, γ_{SV} is the surface tension of the solid in equilibrium with the saturated vapor of the liquid (*i.e.*, surface energy of the solid [γ_S]), and γ_{SL} is the surface tension between the solid and liquid (Figure 2.1).¹⁹ Several adaptations of Young's equation have been developed to determine surface energy components of solid surfaces.²⁰⁻²³ One notable surface energy equation used in this dissertation is the Owens-Wendt equation (Equation 2.2), which decouples the total surface energy into individual dispersive (D) and polar (P) components.²⁰

$$(1 + \cos(\theta))\gamma_{LV} = 2\left(\sqrt{\gamma_S^D \gamma_{LV}^D} + \sqrt{\gamma_S^P \gamma_{LV}^P}\right) \quad (2.2)$$

The Owens-Wendt equation requires two contact angle fluids to calculate the different interactions. Preferably, the two fluids have substantially different dispersive and polar components (*i.e.*, one polar and one nonpolar fluid) to produce large differences in the measured contact angles and more accurate calculations. However, consistency in calculations and contact angle fluids is the most important factor to prevent surface energy variations on the order of ± 5 mJ/m². Because the comparable polymer, contact angle fluid, and substrate surface energy values in literature were calculated with the

Owens-Wendt equation, Equation 2.2 was used to evaluate the surface energies of modified substrates in this dissertation.

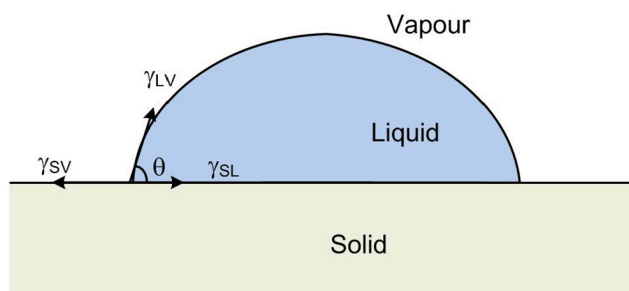


Figure 2.1: Visual representation of the different surface energy components of Young's equation for a liquid drop on a solid surface. Adapted with permission from Makkonen, L. *J. Phys. Conden. Matter* **2016**, 28, 135001, Copyright 2016 IOP Publishing Ltd.¹⁹

Dynamic contact angles can be measured in the form of advancing (θ_a) and receding (θ_r) angles. Dynamic contact angles can provide better estimates of the total surface energy and roughness than static contact angles, but both are effective when studying relative surface energy values and correlations.²⁴ Furthermore, dynamic contact angle measurements are difficult to gauge for contact angle fluids with large degrees of droplet spreading (*i.e.*, diiodomethane on nonpolar substrates and water on polar substrates); however, these fluids are necessary to calculate individual dispersive and polar surface energy components on substrate surfaces. Static contact angles from Millipore water (polar) and diiodomethane (non-polar) were used for analyses in this dissertation; however, future work should seek to incorporate dynamic contact angle measurements.

In this dissertation work, static contact angle measurements were recorded for each fluid by dispensing 0.3 μL of the fluid on the substrate surface with a Distriman pipette. The droplets were given sufficient time to equilibrate (≈ 0.1 s for water and ≈ 0.3 s for diiodomethane) before image analysis was conducted to measure the contact angle. First Ten Ångstroms software was used to record videos with frame-by-frame image breakdowns to ensure the droplet shape had stopped changing and to provide accurate measurements.

2.3 Thin Film Casting

To generate thin film geometries on a substrate surface, one of several different techniques can be used: spin coating, flow coating, dip coating, electrospray deposition, *etc.* Each casting method has its own set of advantages and disadvantages depending on factors such as desired film thickness, casting speed, solution volume, drying rate, *etc.*²⁵ To this end, two thin film casting methods were used in this dissertation, spin coating and flow coating.

2.3.1 Spin Coating

A typical spin coating process has three key steps. First, the polymer solution is deposited on the substrate to wet the entire surface area (≈ 0.2 mL). Then, the substrate is spun at high speeds (300-8000 rpm) to spread and spin off excess solution. The substrate is held in place in the spin coater during this step by pulling slight vacuum. Lastly, the remaining solution on the substrate evaporates over time, leaving behind a thin, uniform thickness BP film. The final film thickness (t) is dependent on factors such as the polymer solution concentration and viscosity but generally is

proportional to the inverse square root of the spin speed (ω) as shown in Equation 2.3.^{26, 27}

$$t \propto \frac{1}{\sqrt{\omega}} \quad (2.3)$$

Spin coating can be used to make uniform thickness films quickly and with relative ease and reproducibility. However, spin coating is a batch technique that has moderately low throughput in comparison to methods that are continuous or amenable to roll-to-roll processing. Furthermore, because a substantial portion of the polymer solution is lost during the spin-off stage of casting, spin coating requires large solution volumes, which can be difficult if polymer amounts are limited.

2.3.2 Flow Coating

In contrast to spin coating, flow coating (or blade coating) is a continuous process that generates a polymer film using a rigid casting blade and a programmable moving substrate (Figure 2.2).^{28, 29} The polymer solution is injected between the casting blade and the substrate at set volumes (10 – 250 μL), and the height and tilt between the glass blade and substrate is adjusted to control film thickness and uniformity. Then, the substrate is drawn underneath the glass blade at set velocities (1 – 20 mm/s); higher velocities result in thicker films. Flow coated films can be produced in a high-throughput manner without sacrificing thickness, precision, and reproducibility.²⁹ Additionally, flow coating can be used to generate both even thickness and gradient thickness films. By incorporating acceleration in the motor stage programming, the velocity increases as the substrate is drawn under the casting blade. The changing velocity gradually increases the amount of solution left by the blade and the thickness across the film. Gradient thickness films have proven useful

in providing libraries of data to measure the nuanced effects of film thickness parameters on self-assembly.^{6, 8, 9, 30}

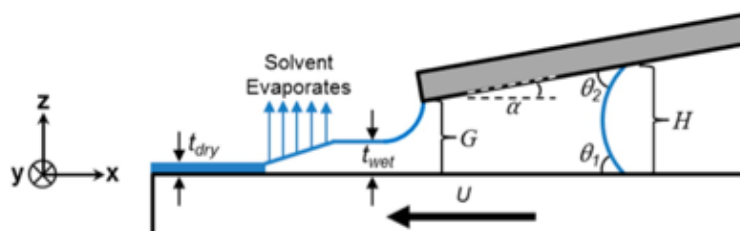


Figure 2.2: Schematic of flow coating setup with key parameters labeled. As the motor stage holding the substrate is drawn under the casting blade with speed U , polymer solution is left behind. Then, the solvent evaporates from the solution leaving behind a dry polymer film. Adapted with permission from Davis, R. L. *et al. Langmuir*, **2014**, 30, 5637, Copyright 2014 American Chemical Society.²⁹

2.4 Block Polymer Thin Film Processing

BP thin film nanostructures typically are poorly ordered and randomly oriented throughout the film after film casting. To manipulate the nanostructure morphology into lower energy states or directed self-assembly patterns, polymer chains need sufficient mobility to diffuse. The two most common strategies to provide polymer chain mobility are thermal annealing and solvent vapor annealing (SVA).

2.4.1 Thermal Annealing

Thermal annealing is the technique of heating a BP film above the glass transition temperatures (T_g) of the individual blocks without exceeding the degradation temperatures. Above their T_g , the polymer chains transition from a glassy state to a rubbery state, which enhances mobility to reorganize into lower energetic conformations.³¹ A more thorough description of thermal annealing can be found in

Section 1.4.1. For this dissertation, the majority of thermal annealing was conducted in a vacuum oven (Lindberg Blue M, ThermoScientific) at controlled temperatures between 100 °C and 200 °C and annealing times between 2 h and 48 h. For all samples that were oven annealed, vacuum was pulled until the pressure was below 20 mTorr. Then, the oven was turned on with a temperature ramp of approximately 3 °C/min to the set temperature. Hot plates also were used to thermally anneal BP films in air for faster sample throughput. The temperature of the hot plate surface was measured with a non-contact infrared thermometer. After annealing, all films were quenched on a metal plate to bring the polymer chains to room temperature and kinetically trap the nanostructures.

2.4.2 Solvent Vapor Annealing

SVA is the process of exposing a BP film to a solvent atmosphere that swells the film, plasticizes the polymer chains, and effectively lowers the T_g 's of the blocks below room temperature.³² SVA provides the same mobility to the BP as thermal annealing, but it does not risk potential film degradation from high temperatures. A more complete description of SVA can be found in Section 1.4.2.

Three different SVA setups were used for this dissertation: bell jar SVA, flow SVA, and raster solvent vapor annealing (RSVA). Each of these techniques is discussed in detail in Section 1.4.2. In bell jar SVA, BP films were placed inside an air-tight chamber with a solvent reservoir (\approx 5 mL in a 10 mL beaker). After a set anneal time, the chamber seal was broken to remove the solvent from the film instantaneously. Flow SVA was conducted to add regulation over solvent concentrations and swelling and deswelling rates. In flow SVA, a continuous solvent vapor stream was produced by flowing nitrogen through solvent bubblers at set flow

rates controlled *via* mass flow controllers. Multiple solvent bubblers were incorporated in series or parallel to increase the maximum solvent concentration and change the solvent concentration/composition, respectively. An additional diluent carrier gas stream also was included to regulate the partial pressure of solvent exposed to the films. RSVA was used to dictate the solvent concentration and diffusion locations by adding a flat-tipped needle to the flow SVA technique that directed where the film did and did not swell (Figure 2.3).³³ The motion, speed, and height of the needle above the film were controlled with a motorized stage and micrometers to regulate solvent flux, film coverage, and nanostructure rearrangement.

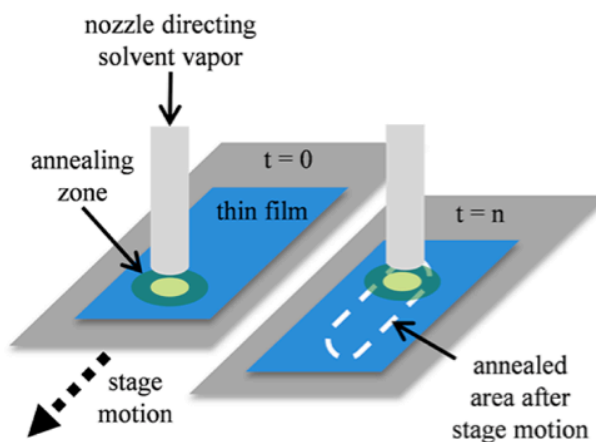


Figure 2.3: Schematic of RSVA. The flat tip needle directs the solvent into specific areas of the film to induce nanostructure reorganization. In combination with an x-y motor stage, 2-D patterns can be drawn into the BP film with solvent vapors. Adapted with permission from Seppala, J. E. *et al. ACS Nano*, **2012**, 6, 9855, Copyright 2012 American Chemical Society.³³

2.5 Polydimethylsiloxane Preparation for Shear-Alignment

Polydimethylsiloxane (PDMS) pads were placed on BP films and exposed to either flow SVA or RSVA to initiate shear alignment of domains *via* solvent vapor annealing with soft shear (SVA-SS).³⁴⁻³⁶ PDMS pads were produced by mixing appropriate ratios (5:1, 10:1, 15:1, or 20:1) of elastomer and initiator (Dow Corning Sylgard 184), pulling dynamic vacuum to remove bubbles, and pouring the elastomer into molds (*e.g.*, Teflon blocks, petri dishes, *etc.*). The amount of PDMS dispensed into each mold was calculated to generate 0.3 – 0.5 mm even thickness pads or gradient thickness PDMS pads with an initial thickness of 0.3 – 0.5 mm. Then, the PDMS was degassed for 30 min prior to heating in a vacuum oven at 65 °C for 3 h to crosslink the PDMS. Molds were removed from the oven after annealing and allowed to cool overnight before use. PDMS pads were placed on films slowly to reduce trapping air bubbles between the PDMS and BP that prevent shear forces.

2.6 Spectral Reflectance

Spectral reflectance (SR) was conducted to determine film thicknesses after casting and during SVA by measuring the intensity of light reflected from a BP film across a range of wavelengths (400 – 1000 nm). The incident and reflected light are normal to the film in contrast to ellipsometry, which quantifies light reflectance at an angle.³⁷ With SR, film thicknesses greater than approximately 10 nm can be assessed accurately in $\approx 0.1 - 5$ s. Ellipsometry can evaluate film thicknesses less than 10 nm, but $\approx 1 - 300$ s is needed per measurement. Furthermore, the integration of ellipsometry in a flow SVA system is more difficult without specially designed chambers that allow light to pass through at specific angles. Due to the lower

measurement time scales, easier operation, ability to measure through sealed glass chambers, and lower cost, SR was used in favor of ellipsometry for this dissertation.

During SR, reflection occurs when the incident light travels across the air/polymer and polymer/substrate interfaces. The amount of reflection is dependent on the refractive index (n) and extinction coefficient (k) of the two mediums at the particular interface. The reflected waves can experience either constructive (Equation 2.4) or destructive interference (Equation 2.5) depending on the phase relationship of the reflections, which can be calculated with n , k , the film thickness (t), and wavelength of light (λ) of each layer.

$$2nt = i\lambda \quad (2.4)$$

$$2nt = (i + 1/2)\lambda \quad (2.5)$$

Then, the reflected light intensity (R) at a particular λ can be determined with Equation 2.6, in which A and B are constants that include k , n , and roughness parameters.³⁷

$$R \approx A + B \cos\left(\frac{4\pi}{\lambda} nt\right) \quad (2.6)$$

Recording the total reflectance at each wavelength during an SR measurement produces a reflectance spectrum that can be modeled to extract the values of the parameters for each layer, including the film thickness, using Equation 2.6. A schematic of the SR process is shown in Figure 2.4.³⁷

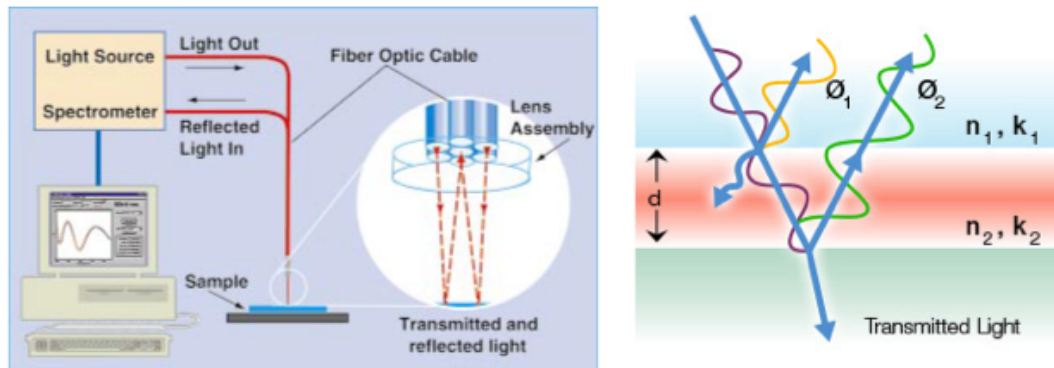


Figure 2.4: Visual description of spectral reflectance setup (left side), which uses a fiber optic cable to generate light that reflects off the sample and to measure the intensity of light as it returns. As the light travels through different layers of the film/substrate (right side), it is either reflected or transmitted. The intensity and phase (ϕ) of the reflected light produces a reflection pattern, which can be modeled using refractive index (n) and extinction coefficient (k) parameters of the different layers to extract the film thickness (d). Images from Filmetrics.com.³⁷

For this dissertation, BP film thicknesses were measured using a Filmetrics F20-UV reflectance spectrometer recording reflected light intensities over a range of wavelengths (400 – 1000 nm). Reflectance profiles were modeled with FILMeasure software that adjusted n and t values to produce calculated curves that matched the data with goodness of fits above 0.98.³⁸ However, if the value of n for the BP could be estimated from the volume fraction and n of the individual polymer blocks, only t was varied to generate more accurate fits; film thickness accuracy was within ± 2 nm. The parameters k and r were set to zero for all fits, which were considered reasonable estimates since none of the polymers used in this dissertation were optically active, and atomic force microscopy confirmed a typical surface roughness of less than 5 nm.

2.7 Optical Microscopy

Optical microscopy (OM) is a characterization tool that uses visible light reflected off or transmitted through BP thin films and one or more lenses to generate a magnified (0.2 μm resolution) view of the samples. Although this resolution is not sufficient to image the nanostructures, it is appropriate to capture island and hole formations that develop at incommensurate thicknesses.^{6, 8, 9, 39, 40} The slightly thicker/thinner areas of the film provide contrast that make island and hole formations easily visible and measurable with OM, which makes OM ideal for quickly screening commensurate and incommensurate thicknesses locations in BP films.³⁰

BP films were supported on silicon substrates in this dissertation, so OM images were collected in reflectance mode with a Nikon Eclipse LV100, 5 MP CCD camera. To study the substrate-polymer surface interactions, *in situ* OM experiments during thermal annealing were conducted to track island and hole growth. An airtight Linkam thermal stage with a thin glass-viewing window was used to heat the BP films in an Argon atmosphere under the microscope. The stage temperature was increased at a rate of 3 $^{\circ}\text{C}/\text{min}$ to match the vacuum oven, and the OM was programmed to capture images every 5 – 30 min until the surface feature sizes equilibrated. Recorded images were converted to binary and analyzed using ImageJ software to extract island and hole sizes and growth rates with Analyze Particles software.

2.8 Atomic Force Microscopy

Atomic force microscopy (AFM), also known as scanning force or scanning probe microscopy, is a characterization tool commonly used to study surface properties of samples (*e.g.*, surface features, friction, adhesive forces, conductivity, *etc.*) and was the primary method for imaging BP thin film nanostructures in this

dissertation.⁴¹ An atomic force microscope is comprised of four main components: the piezoelectric scanner, the cantilever with a sharp tip at the end, a photodiode detector, and a feedback system. With AFM, the intermolecular force between a sharp tip and the sample surface is determined by measuring deflections of the top cantilever that are amplified by a laser beam. The cantilever can be deflected by changes in height, softness, elasticity, and stickiness as it travels across a sample surface in the x-y plane. The deflections are recorded by the detector and can be viewed as real-space images. A diagram of an atomic force microscope is shown in Figure 2.5.⁴²

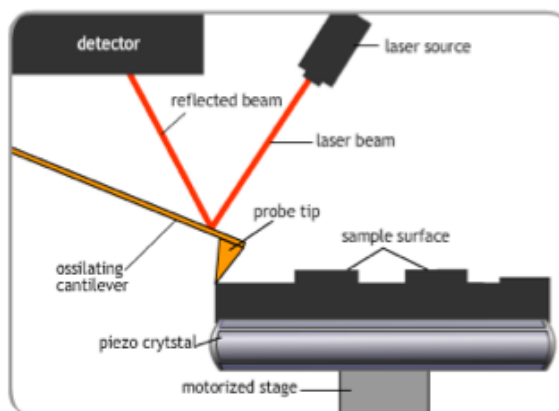


Figure 2.5: Graphic of the key components of an atomic force microscope. Image from the Virtual Microscope Imaging Technology Group, University of Illinois at Urbana-Champaign.⁴²

The scanners can operate by either moving the tip over a stationary sample (*e.g.*, Veeco Dimension), or by moving the sample under a stationary tip (*e.g.*, Veeco Multimode). If the tip is held stationary, less image noise from vibration effects and disruptions is recorded, but the sample stage is smaller and localized imaging (*e.g.*, imaging at an interface between shear-aligned and non-shear-aligned sections of film)

is more difficult. Conversely, a moving tip can accommodate larger samples and pinpoint imaging locations, which makes analyzing different film regions and gradient thickness films easier. Because BP films typically have large phase contrast between the two blocks and reasonable size-scales, high-quality images can be recorded with either scanner.

There are three scanning modes in which an AFM can operate: contact mode, non-contact mode, and tapping mode. In contact mode, the tip is brought to the film interface and dragged across the surface; contact is maintained with the feedback system even when the height changes. Contact mode AFM generates the highest resolution but is sensitive to frictional and adhesive forces that can distort images and damage the sample surface, especially in soft samples like BP films. In non-contact mode, the tip responds to repulsive surface interactions without ever making contact. Operating in non-contact mode prevents film damage but provides low-resolution images. Tapping mode combines the advantages between contact and non-contact modes by oscillating the tip to touch the sample surface intermittently.^{43, 44} Therefore, tapping mode operation provides high-resolution images without the tip being trapped in adhesive layers, without the tip or film being damaged and without the image being distorted.

In tapping mode, the amplitude of the oscillations can change in response to surface features, so the feedback system adjusts to maintain the amplitude set point. The cantilever oscillations and feedback controls can be tracked to produce a “height” image that shows topographic features and surface roughness. The cantilever also reacts to surfaces with different elastic moduli from phase lag in the oscillations that are detected by the photodiode detector. The responses are used to create the “phase”

image in which contrast is maximized if one block is glassy and the other is rubbery at room temperature. The ability to investigate nanostructure formations and surface features simultaneously with high-resolution and without long or expensive procedures (*e.g.*, staining domains) makes AFM an advantageous technique to study BP thin film self-assembly.⁴⁵

In this dissertation, BP film surface morphologies were examined with a Veeco Dimension microscope operating in tapping mode. Two different silicon probes (Tap 150G, BudgetSensors and ACL-20, AppNano) were used to image the films. The appropriate probe was chosen for each system on the basis of phase contrast. ACL-20 tips have a different force constant (20 – 95 N/m) than Tap 150G tips (4 N/m), which can produce more phase contrast in BP systems. For example, polystyrene and poly(methyl methacrylate) have similar T_g s and limited phase contrast, so ACL-20 tips provided higher-quality images. However, polystyrene (glassy) and polyisoprene (rubbery) have significant phase contrast, so less expensive Tap150G tips generated similar resolutions.

2.9 X-Ray Scattering

X-ray scattering is a reciprocal space characterization tool that is used to investigate in-plane (small-angle X-ray scattering [SAXS]) and out-of-plane (X-ray reflectivity [XRR]) morphology in BPs.^{46, 47} X-rays bombarding the sample interact with the electron clouds of the individual atoms and scatter according to the atomic composition; atoms with larger atomic number scatter more strongly than atoms with smaller atomic number.⁴⁸⁻⁵⁰ X-ray scattering experiments offer high flux, low divergence, and limited wavelength spread for high-resolution BP characterization even for laboratory-scale instruments.⁵¹

2.9.1 Small-Angle X-Ray Scattering

SAXS is operated in transmission geometries to analyze nanostructure morphologies and is one of the primary characterization tools for bulk BP investigations.⁴⁵ X-rays passing through a BP sample scatter at polymer-polymer interfaces according to electron density differences between BP domains. The scattering patterns from SAXS are recorded on a 2-D detector and are representative of the particular morphology. Typically, the domains in the bulk BP are oriented randomly relative to each other, and the scattering patterns consist of a series of isotropic rings spaced in relation to the nanostructure domain size and morphology.⁵² Isotropic SAXS patterns can be azimuthally integrated to produce 1-D traces with peaks located at q values associated with the ring locations. According to SAXS theory, q is the difference between the incident beam wavevector (\mathbf{k}) and the scattered beam wavevector (\mathbf{k}_s) and can be calculated with Equation 2.7, in which λ is the wavelength of the X-rays and θ is the scattering angle.

$$q = |\mathbf{q}| = \frac{4\pi}{\lambda} \sin \theta \quad (2.7)$$

A visual depiction of the scattering geometry of SAXS is shown in Figure 2.6. By combining Equation 2.7 with Bragg's Law (Equation 2.8), the interplanar (domain) spacing (d) of the BP can be determined as shown in Equation 2.9.

$$n\lambda = 2d \sin \theta \quad (2.8)$$

$$q = \frac{2\pi n}{d} \quad (2.9)$$

The scattering peak at an order of diffraction (n) of one is referred to as the primary peak (q^*) and corresponds to scattering from the (100) plane. With the primary peak, the domain spacing in the BP can be calculated directly from Equation 2.10.

$$d = \frac{2\pi}{q^*} \quad (2.10)$$

The primary peak location can be compared with other peak locations to generate peak ratios that correspond to particular morphologies as highlighted in Table 2.1.

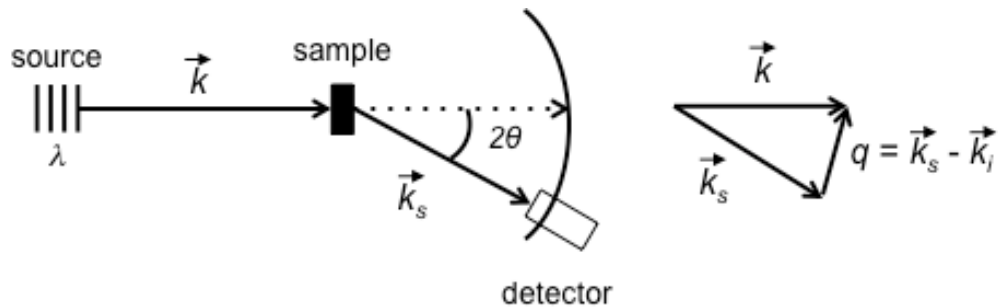


Figure 2.6: Scattering geometry for SAXS scattering experiments. Incident X-rays with wavelength λ normal to the sample (\mathbf{k}) are scattered by electron cloud interactions to new angles (\mathbf{k}_s). The difference between \mathbf{k}_s and \mathbf{k} is referred to as \mathbf{q} , which is related to the size scale of the features in the sample.

Table 2.1: Common block polymer morphologies and corresponding SAXS peak locations

Morphology	Peak ratio (q/q^*)
Lamellae	1, 2, 3, 4, 5, 6, ...
Body-centered cubic spheres	1, $\sqrt{2}$, $\sqrt{3}$, $\sqrt{4}$, $\sqrt{5}$, $\sqrt{6}$, ...
Hexagonally-packed cylinders	1, $\sqrt{3}$, $\sqrt{4}$, $\sqrt{7}$, $\sqrt{9}$, $\sqrt{12}$, ...
Gyroid network	$\sqrt{6}$, $\sqrt{8}$, $\sqrt{14}$, $\sqrt{16}$, $\sqrt{20}$, ...

In this dissertation, SAXS was used to characterize the bulk domain spacing and morphology of the BPs before film casting. Then, the nanostructures were compared to thin film counterparts. SAXS profiles were collected with a Rigaku SAXS instrument with a 2.2 kW sealed-tube X-ray source (Cu-K α , $\lambda = 1.54 \text{ \AA}$) and a

2 m sample-to-detector distance. BP samples were sealed within two Kapton layers in a stainless steel sample cell. The temperature of the BPs was modulated with a Linkam HFS91 CAP stage, and profiles were collected while the samples were under vacuum.

2.9.2 X-Ray Reflectivity

In contrast to SAXS, XRR is conducted to investigate out-of-plane structural and compositional details. XRR examines the thin film density, thickness, and interfacial roughness by measuring the intensity of X-rays reflecting off the sample at different angles. At incident angles of the X-rays below the critical angle of the BP film, total reflection is exhibited. As the incident angle increases, the X-ray beams penetrate the film, which causes the reflectivity to gradually decrease as a function of the roughness at the film surface. Constructive and destructive interference from X-rays reflecting off the film surface and the substrate surface create oscillating reflectivity profiles; the oscillating fringes are called Kiessig fringes.^{53,54} If a repeating out-of-plane structure (*e.g.*, parallel lamellae) is present in the film, internal film interfaces also scatter X-rays and Bragg peaks can form. From the locations and intensities of Kiessig fringes and Bragg peaks, sample parameters such as film thickness, domain spacing, interfacial roughness, surface roughness, and film composition can be modeled.^{55,56}

For this dissertation, XRR was used as a screening tool to check film quality before neutron scattering experiments. XRR was conducted on a Rigaku Ultima IV instrument using a parallel beam of Cu-K α radiation ($\lambda = 1.54 \text{ \AA}$). Specular XRR profiles were collected over a range of incident angles (θ) and detection angles (2θ) of reflected X-rays ($0^\circ < 2\theta < 4^\circ$). For all samples, the beam was sized to capture the

critical edge to produce the best model fits. Fits were provided for each XRR profiles using GlobalFit software.⁵⁷

2.10 Neutron Scattering

Neutron scattering is a reciprocal space characterization tool to measure structural and compositional aspects of BPs. Neutrons have no charge or electric dipole moment and interact with the nuclei of atoms rather than the electron cloud as in X-ray scattering.⁵⁸ Therefore, neutrons have a greater penetration depth of the sample and less beam-induced damage relative to X-rays.⁵¹ Although neutron sources cannot generate the same flux as X-ray sources, neutrons can more easily distinguish small atoms due to the ability to add contrast variation in organic molecules. Contrast variation is provided through isotopic replacement, the most common of which is replacing hydrogen with deuterium.⁵⁹ This technique creates significant contrast in the BP not present in typical X-ray scattering experiments without staining with heavy atoms. In this dissertation, contrast variation was combined with two forms of neutron scattering, small-angle neutron scattering (SANS) and neutron reflectometry (NR), to measure salt and solvent concentrations in BP films and to gain sufficient contrast for *in situ* experimentation during annealing in reasonable time-scales.

2.10.1 Small-Angle Neutron Scattering

SANS is conducted in transmission geometries, similar to SAXS, to investigate in-plane structural and compositional profiles of samples.⁶⁰⁻⁶⁴ However, neutron sources (*i.e.*, spallation sources or nuclear reactors) do not produce the same low wavelength spread of neutrons as is achievable with X-rays sources. Therefore, a series of filters, collimators, and velocity selectors focuses the wavelength spread in

the neutron beam directed at a sample.⁵⁹ Sample and source apertures are used to control the beam width. Larger wavelength spreads and apertures provide higher neutron fluxes but less resolution. After neutrons scatter off the sample, the scattering angles are recorded by a He³ 2-D detector. The detector can be positioned at different distances from the sample to measure different scattering angles and, therefore, different q ranges (*i.e.*, different size scales). The scattering intensity at each angle is dependent on the size scale of the nanostructures and the scattering length densities (ρ) of the components in the sample, which can be calculated with Equation 2.11.⁶⁵

$$\rho = \frac{\sum_{i=1}^n b_c}{v_m} \quad (2.11)$$

In Equation 2.11, b_c is the coherent nuclear scattering length of the i^{th} of n atoms in a molecule and v_m is the molecular volume of the sample.

SANS scattering data were reduced to account for neutron detection from background sources, scattering from the empty sample cell, and non-uniformities in detector sensitivity. Also, reduction equations correct for changes in neutron flux through measured transmission intensities (T) of the sample and empty cell. The exact equation to correct the scattering intensity ($I_{corrected}$) is shown in Equation 2.12 and can be executed with reduction software available from the National Institute of Standards and Technology (NIST) Center for Neutron Research (NCNR) website.⁶⁶

$$I_{corrected} = (I_{sample} - I_{background}) - \frac{T_{sample}}{T_{emptycell}} (I_{emptycell} - I_{background}) \quad (2.12)$$

Corrected SANS patterns can be plotted as azimuthally averaged intensity profiles that describe the scattering intensity as a function of q . Furthermore, SANS patterns can be plotted as annularly averaged intensity profiles that detail the scattering intensity as

a function of detector angle for a specific q value. Annular patterns are useful for determining if SANS patterns are isotropic or anisotropic, as was done in Chapter 5 for shear-aligned nanostructures.

In this dissertation work, all SANS data were collected on the 10 m SANS (NGB) instrument at the NCNR. Neutrons with incident wavelengths of 5 Å and 10 Å, a sample-to-detector distance of 5.2 m, and a 25 mm beamstop were used to probe appropriate q ranges related to the domain spacing of the BP samples ($0.005 \text{ \AA}^{-1} \leq q \leq 0.112 \text{ \AA}^{-1}$). A 12.7 mm diameter sample aperture was chosen to balance neutron flux and scattering resolution at these instrument conditions. SANS profiles were reduced and analyzed with IgorPro software (WaveMetrics) and NCNR SANS reduction macros.⁶⁶

2.10.2 Neutron Reflectometry

NR is operated in the same reflection geometry as XRR, but larger scattering differences between organic elements in BP films, especially when selective deuteration is incorporated, generate improved compositional analyses. During NR, incident neutrons strike the sample at an angle θ and are reflected at various angles.⁶⁷ In specular NR, only neutrons reflected at the same incident angle are recorded to study the out-of-plane characteristics of films. In off-specular NR, all scattering angles are measured to investigate both the out-of-plane and in-plane structure in films simultaneously. Only specular NR, depicted in Figure 2.7, was conducted for the work described in this dissertation due to the inability of off-specular NR to examine the appropriate nanoscale size range in reasonable times.^{61, 68-71}

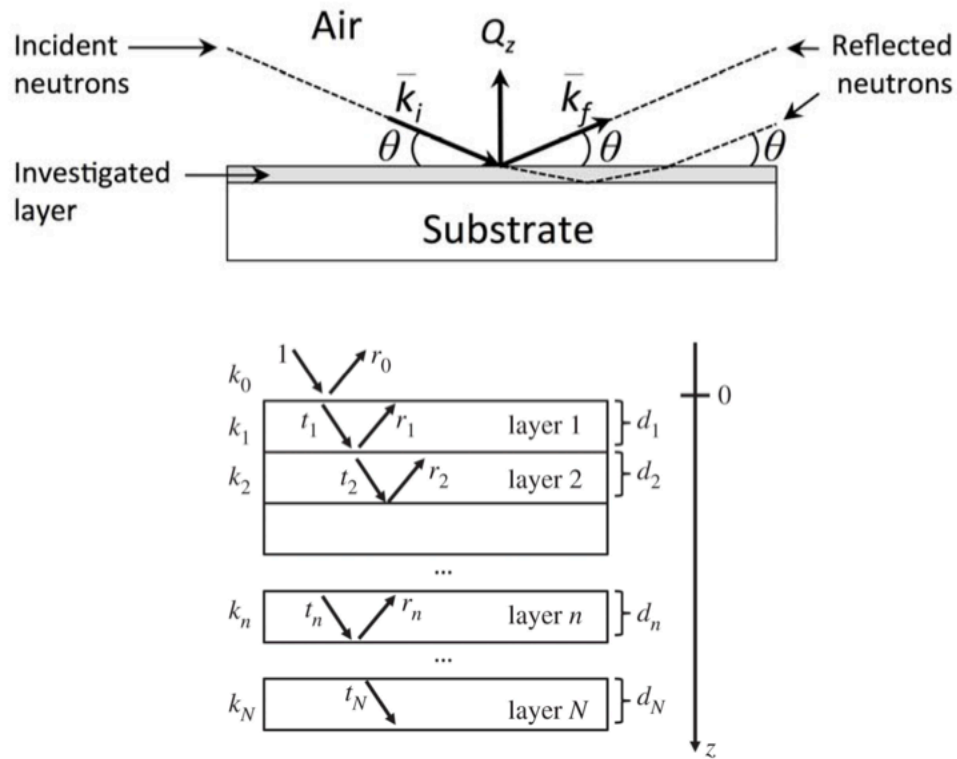


Figure 2.7: Schematic of specular NR geometry with incident and reflected neutron angles. Neutrons striking the sample can either reflect off or transmit through each layer in the film. The reflections from each layer constructively and destructively interfere to generate the recorded intensity profiles as a function of the scattering variable Q_z . Top image adapted with permission from Demkowicz, M.J. and Majewski, J. *Metals* **2016**, 6, 20, Copyright 2016 by the authors.⁶⁸ Bottom image adapted with permission from Piscitelli, F. *et al. Proc. R. Soc. A*, **2016**, 472, 20150711, Copyright 2016 by the authors.⁶⁹

Neutrons either transmit through or reflect off different layers in the nanostructured films at incident angles above the critical angle for total reflection. The transmission to reflection ratio is dependent on the scattering length density of the specific components in each layer of the film. The constructive and destructive interference of the reflected neutrons from the film-substrate and polymer-polymer

interfaces creates a series of Kiessig fringes and Bragg peaks, respectively, which are recorded in an intensity plot as a function of the scattering variable Q_z .⁵⁵ The distance between consecutive Kiessig fringes and Bragg peaks can be used to calculate the film thickness and domain spacing in the film. Also, the intensity profiles can be fit using reflectometry fitting software, such as reflpak and refl1D, to extract information about the film thickness, film composition, layer structure, and interfacial and surface roughness.⁷²

For this dissertation, NR experiments were conducted on the multi-angle grazing-incidence k-vector (MAGIK) instrument at the NCNR. Neutrons with an incident wavelength of 5 Å were directed at 64 mm long, 25 mm wide wafers coated with BP films. Borated aluminum shields were incorporated in sample assemblies to prevent reflections from sample holders and edges of the BP films. NR profiles covering Q_z ranges of a $0 \text{ \AA}^{-1} \leq Q_z \leq 0.1315 \text{ \AA}^{-1}$ and a step size of 0.0004 \AA^{-1} were reduced using reflred software and analyzed with reflfit and refl1D programs for modeling multilayer systems.⁷²

2.11 Mass Spectroscopy

Mass spectroscopy is used to measure the mass-to-charge ratio (m/z) of ions passing through a detector to determine the chemical breakup of in mixtures.⁷³ Mass spectrometers are comprised of three main features: an ion source, a mass analyzer, and an ion detector (Figure 2.8).⁷⁴ The ion source vaporizes and ionizes the input stream, which can be liquid, gas, or powder. The ions from the sample mixture are accelerated through the mass analyzer, where they encounter electric and/or magnetic fields that deflect the ions on paths that are determined by the m/z of the particular ion. Then, when the ions strike the ion detector, the amount of each ion is recorded.

Cracking patterns can be used to identify all components and their relative amounts provided the experimenter has some knowledge of what components are expected in the input stream. For this dissertation, gaseous mixtures were tested with a mass spectrometer (Hiden Analytical) to determine the partial pressure of solvent flowing from solvent bubblers to the sample chamber at different solvent-rich to diluent nitrogen ratios.

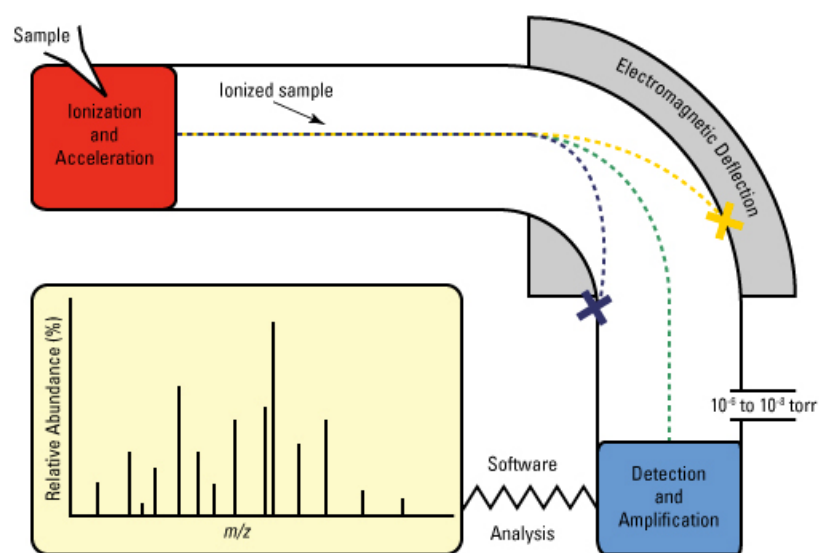


Figure 2.8: Diagram of the key pieces of a mass spectrometer. The sample is ionized and accelerated by an ion source into the mass analyzer that deflects the ions on the basis of their mass-to-charge (m/z) ratios. Then, ions strike the ion detector at different locations determined by the deflection, and the relative abundance of each ion is measured. Image from Thermo Fisher Scientific.⁷⁴

REFERENCES

1. Vig, J. R. *J. Vac. Sci. Technol.* **1985**, 3, 1027-1034.
2. Ashley, K.; Sehgal, A.; Amis, E. J.; Raghavan, D.; Karim, A. *Mater. Res. Soc. Symp. Proc.* **2001**, 700, S4.7.1-S4.7.6.
3. Roberson, S. V.; Fahey, A. J.; Sehgal, A.; Karim, A. *Appl. Surf. Sci.* **2002**, 200, 150-164.
4. Albert, J. N. L.; Baney, M. J.; Stafford, C. M.; Kelly, J. Y.; Epps, T. H., III *ACS Nano* **2009**, 3, 3977-3986.
5. Albert, J. N. L.; Kim, J. D.; Stafford, C. M.; Epps, T. H., III *Rev. Sci. Instrum.* **2011**, 82, 065103.
6. Luo, M.; Seppala, J. E.; Albert, J. N. L.; Lewis, R. L.; Mahadevapuram, N.; Stein, G. E.; Epps, T. H., III *Macromolecules* **2013**, 46, 1803-1811.
7. Peters, R. D.; Yang, X. M.; Kim, T. K.; Nealey, P. F. *Langmuir* **2000**, 16, 9620-9626.
8. Shelton, C. K.; Epps, T. H., III *Macromolecules* **2015**, 48, 4572-4580.
9. Shelton, C. K.; Epps, T. H., III *Macromolecules* **2016**, 49, 574-580.
10. Peters, R. D.; Yang, X. M.; Kim, T. K.; Sohn, B. H.; Nealey, P. F. *Langmuir* **2000**, 16, 4625-4631.
11. Peters, R. D.; Yang, X. M.; Nealey, P. F. *Macromolecules* **2002**, 35, 1822-1834.
12. Ji, S.; Liu, C.-C.; Son, J. G.; Gotrik, K.; Craig, G. S. W.; Gopalan, P.; Himpel, F. J.; Char, K.; Nealey, P. F. *Macromolecules* **2008**, 41, 9098-9103.
13. Mansky, P.; Liu, Y.; Huang, E.; Russell, T. P.; Hawker, C. *Science* **1997**, 275, 1458-1460.

14. Maher, M. J.; Bates, C. M.; Blachut, G.; Sirard, S.; Self, J. L.; Carlson, M. C.; Dean, L. M.; Cushen, J. D.; Durand, W. J.; Hayes, C. O.; Ellison, C. J.; Willson, C. G. *Chem. Mater.* **2014**, 26, 1471-1479.
15. In, I.; La, Y.-H.; Park, S.-M.; Nealey, P. F.; Gopalan, P. *Langmuir* **2006**, 22, 7855-7860.
16. Han, E.; Stuen, K. O.; La, Y.-H.; Nealey, P. F.; Gopalan, P. *Macromolecules* **2008**, 41, 9090-9097.
17. Edwards, E. W.; Stoykovich, M. P.; Müller, M.; Solak, H. H.; de Pablo, J. J.; Nealey, P. F. *J. Polym. Sci., Part B: Polym. Phys.* **2005**, 43, 3444-3459.
18. Young, T. *Phil. Trans. R. Soc. Lond.* **1805**, 95, 65-87.
19. Makkonen, L. *J. Phys.: Condens. Matter* **2016**, 28, 135001.
20. Owens, D. K.; Wendt, R. C. *J. Appl. Polym. Sci.* **1969**, 13, 1741-1747.
21. Girifalco, L. A.; Good, R. J. *J. Phys. Chem.* **1957**, 61, 904-909.
22. Fowkes, F. M. *End. Eng. Chem.* **1964**, 56, 40-52.
23. Wu, S. *J. Polym. Sci., Polym. Symp.* **1971**, 34, 19-30.
24. Wu, S. *Polymer Interface and Adhesion*. CRC Press 1982.
25. Zhang, X.; Douglas, J. F.; Jones, R. L. *Soft Matter* **2012**, 8, 4980-4987.
26. Sahu, N.; Parija, B.; Panigrahi, S. *Indian J. Phys.* **2009**, 83, 493-502.
27. Bornside, D. E.; Macosko, C. W.; Scriven, L. E. *J. Appl. Phys.* **1989**, 66, 5185-5193.
28. Stafford, C. M.; Roskov, K. E.; Epps, T. H., III; Fasolka, M. J. *Rev. Sci. Instrum.* **2006**, 77, 023908.
29. Davis, R. L.; Jayaraman, S.; Chaikin, P. M.; Register, R. A. *Langmuir* **2014**, 30, 5637-5644.
30. Smith, A. P.; Douglas, J. F.; Meredith, J. C.; Amis, E. J.; Karim, A. J. *Polym. Sci., Part B: Polym. Phys.* **2001**, 39, 2141-2158.
31. Albert, J. N. L.; Epps, T. H., III *Mater. Today* **2010**, 13, 24-33.

32. Sinturel, C.; Vayer, M.; Morris, M.; Hillmyer, M. A. *Macromolecules* **2013**, *46*, 5399-5415.
33. Seppala, J. E.; Lewis, R. L.; Epps, T. H., III *ACS Nano* **2012**, *6*, 9855-9862.
34. Qiang, Z.; Zhang, L.; Stein, G. E.; Cavicchi, K. A.; Vogt, B. D. *Macromolecules* **2014**, *47*, 1109-1116.
35. Qiang, Z.; Zhang, Y.; Groff, J. A.; Cavicchi, K. A.; Vogt, B. D. *Soft Matter* **2014**, *10*, 6068-6076.
36. Luo, M.; Scott, D. M.; Epps, T. H., III *ACS Macro Lett.* **2015**, *4*, 516-520.
37. *Taking the Mystery Out of Thin Film Measurement*. Filmetrics, Inc.: San Diego, 2006.
38. *FILMeasure, 4.12.0*. Filmetrics: San Diego, 2008.
39. Coulon, G.; Collin, B.; Ausserre, D.; Chatenay, D.; Russell, T. P. *J. Phys. France* **1990**, *51*, 2801-2811.
40. Heier, J.; Kramer, E. J.; Groenewold, J.; Fredrickson, G. H. *Macromolecules* **2000**, *33*, 6060-6067.
41. Magonov, S. N.; Reneker, D. H. *Annu. Rev. Mater. Sci.* **1997**, *27*, 175-222.
42. *Virtual Microscope*. Image Technology Group: Beckman Institute for Advanced Science and Technology, University of Illinois at Urbana-Champaign <http://virtual.itg.uiuc.edu/>
43. Knoll, A.; Magerle, R.; Krausch, G. *Macromolecules* **2001**, *34*, 4159-4165.
44. Busch, P.; Posselt, D.; Smilgies, D.-M.; Rheinländer, B.; Kremer, F. *Macromolecules* **2003**, *36*, 8717-8727.
45. Hamley, I. W. *Prog. Polym. Sci.* **2009**, *34*, 1161-1210.
46. Chu, B.; Hsiao, B. S. *Chem. Rev.* **2001**, *101*, 1727-1762.
47. Tolan, M., *X-ray Scattering from Soft-Matter Thin Films*. Springer-Verlag Berlin Heidelberg: 1999.
48. Stribeck, N., *X-Ray Scattering of Soft Matter*. Springer Berlin Heidelberg: 2007.

49. Stein, G. E., *Scattering Techniques for Thin Polymer Films. In Functional Polymer Films*, Wiley-VCH Verlag GmbH & Co. KGaA: 2011.
50. Shelton, C. K.; Epps, T. H., III *Polymer* **2016**.
51. Sivia, D. S., *Elementary Scattering Theory: For X-ray and Neutron Users*. OUP Oxford: 2011.
52. Rudman, R. *J. Chem. Educ.* **1990**, 67, A29.
53. Holy, V.; Kuběna, J.; Ohlídal, I.; Lischka, K.; Plotz, W. *Phys. Rev. B* **1993**, 47, 15896-15903.
54. Kiessig, H. *Annalen der Physik* **1931**, 402, 769-788.
55. Russell, T. P. *Mater. Sci. Rep.* **1990**, 5, 171-271.
56. Luo, M.; Brown, J. R.; Remy, R. A.; Scott, D. M.; Mackay, M. E.; Hall, L. M.; Epps, T. H., III *Macromolecules* **2016**, 49, 5213-5222.
57. *Integrated Thin Film Analysis Software GlobalFit (Reflectivity Analysis) User's Manual*. Rigaku Coporation.
58. Pynn, R. *Los Alamos Sci.* **1990**, 19, 1-31.
59. Hammouda, B., *Probing Nanoscale Structures: The SANS Toolbox*. NIST: 2008.
60. Russell, T. P.; Lambooy, P.; Barker, J. G.; Gallagher, P.; Satija, S. K.; Kellogg, G. J.; Mayes, A. M. *Macromolecules* **1995**, 28, 787-789.
61. Shelton, C. K.; Jones, R. L.; Dura, J. A.; Epps, T. H., III *Macromolecules* **2016**, 49, 7525-7534.
62. Huang, E.; Russell, T. P.; Harrison, C.; Chaikin, P. M.; Register, R. A.; Hawker, C. J.; Mays, J. *Macromolecules* **1998**, 31, 7641-7650.
63. Xu, T.; Hawker, C. J.; Russell, T. P. *Macromolecules* **2005**, 38, 2802-2805.
64. Kellogg, G. J.; Walton, D. G.; Mayes, A. M.; Lambooy, P.; Russell, T. P.; Gallagher, P. D.; Satija, S. K. *Phys. Rev. Lett.* **1996**, 76, 2503-2506.
65. Sears, V. F. *Neutron News* **1992**, 3, 26-37.
66. Kline, S. *J. Appl. Crystallogr.* **2006**, 39, 895-900.

67. Jackson, A. J., *Introduction to Small-Angle Neutron Scattering and Neutron Reflectometry*. NIST Center for Neutron Research: Gaithersburg, MD, 2008.
68. Demkowicz, M.; Majewski, J. *Metals* **2016**, 6, 20.
69. Piscitelli, F.; Khaplanov, A.; Devishvili, A.; Schmidt, S.; Höglund, C.; Birch, J.; Dennison, A. J. C.; Gutfreund, P.; Hall-Wilton, R.; Van Esch, P. *Proc. R. Soc. A* **2016**, 472.
70. Shelton, C. K.; Jones, R. L.; Epps, T. H., III *in preparation*.
71. Müller-Buschbaum, P.; Cubitt, R.; Petry, W. *Langmuir* **2003**, 19, 7778-7782.
72. Kienzle, P. A.; O'Donovan, K. V.; Ankner, J. F.; Berk, N. F.; Majkrzak, C. F. <http://www.ncnr.nist.gov/reflpak> **2000-2006**.
73. Boggess, B. J. *Chem. Educ.* **2001**, 78, 168.
74. *Overview of Mass Spectrometry for Protein Analysis*. ThermoFisher Scientific. <https://www.thermofisher.com/us/en/home/life-science/protein-biology/protein-biology-learning-center/protein-biology-resource-library/pierce-protein-methods/overview-mass-spectrometry.html.html>

Chapter 3

DECOUPLING OF SUBSTRATE SURFACE INTERACTIONS IN BLOCK POLYMER THIN FILM SELF-ASSEMBLY

In this chapter, the development of a series of predictive formalisms that define the interfacial and through-film substrate-polymer interactions in block polymer (BP) thin films is described. A systematic study was conducted with a suite of different chlorosilane monolayers to determine the effects of different total, dispersive, and polar surface energy components on the self-assembly of poly(methyl methacrylate-*b*-*n*-butyl acrylate) (PMMA-*Pn*BA) thin films. High-throughput analysis was achieved by using optical microscopy (OM) and gradient thickness films to investigate island and hole structures. Atomic force microscopy (AFM) supported the study by adding real-space images of nanostructure changes. A predictive approach for improving nanostructure ordering and orientation in BP thin films with appropriate chemical-tailoring of substrate-polymer surface interactions is provided from the work in this chapter. Text and figures are reproduced or adapted with permission from Shelton, C. K. and Epps, T. H., III *Macromolecules* **2015**, *48*, 4572-4580 and Shelton, C. K. and Epps, T. H., III *Macromolecules* **2016**, *49*, 574-580.

3.1 Introduction

The substrate-polymer interaction is one of the most significant factors affecting polymer wetting behavior,^{1,2} nanostructure orientation,³⁻⁷ nanostructure uniformity through the film,⁸⁻¹⁰ and defect density according to literature.^{11,12} However, directing each of these effects typically is the result of trial and error with

limited initial knowledge. As the number of potential BP systems continues to increase,¹³ experimental investigation of the full parameter-space in a given system is no longer feasible and must be replaced by predictive tools that incorporate the nuanced effects of surface interactions and film thickness on nanoscale morphology, ordering, and orientation.¹⁴

The substrate-polymer interactions typically are quantified by the interfacial energy ($\Delta\gamma$), or difference between the substrate (γ_S) and individual polymer block (γ_A) surface energies as discussed in Chapter 1, Section 1.3.2. Smaller magnitudes of $\Delta\gamma$ indicate more favorable enthalpic interactions between a particular polymer block and the substrate.¹⁵⁻¹⁷ Although the total surface energy often is used for substrate-polymer interaction analyses, Han *et al.* demonstrated its potential limitations when annealing poly(styrene-*b*-methyl methacrylate) (PS-PMMA) thin films on PS-PMMA random copolymer brushes modified with either a terminal hydroxyl, side-chain hydroxyl, or side-chain epoxy group.¹⁷ The total surface energies were similar on all three random copolymer brushes (for a given polystyrene composition in the brush), but the neutral wetting behavior occurred at different polystyrene compositions due to the differing polarity of functional groups. To account for these additional interactions, decoupled interfacial energy equations have been applied in the literature,^{1, 2, 5} but there has been a dearth of studies that cover a suitable range of distinct total, dispersive, and polar surface energies to define the individual component contributions and develop equations that predict wetting behavior, nanostructure ordering, and nanostructure orientation through the film.

As a visible complement to direct surface energy measurements, surface relief structures, more commonly referred to as ‘islands’ and ‘holes’, can provide detailed

information about substrate surface effects, both at the substrate-polymer interface and through the film thickness.^{1, 2, 18-21} Islands and holes are thicker and thinner regions on the film that form at the free surface to reduce thermodynamically unfavorable stretching and compression of polymer chains attempting to conform to an incommensurate film thickness.²² In a diblock copolymer, if the same polymer block wets the substrate and free surface (symmetric wetting), incommensurate film thicknesses occur at half-integer multiples ($n+0.5$, $n = 1, 2, 3, \dots$) of the polymer domain spacing (L_0).^{15, 23} If a different polymer block wets the substrate and free surface (asymmetric wetting), incommensurate film thicknesses occur at integer multiples (n) of L_0 .^{15, 23} Consequently, because the lower surface energy block is known to wet the free surface,²⁴ the topography at integer and half-integer L_0 thicknesses only depends on which polymer block wets the substrate surface.¹ Smith *et al.* demonstrated how gradient thickness films efficiently track island and hole formations on a single film rather than using individual films of discrete thickness.²¹ According to Smith *et al.*, island and hole formations appeared periodically at specific film thicknesses on gradient thickness films to relieve thermodynamic stress caused by stretched or compressed polymer chains oriented perpendicular to the substrate (more preferential polymer block driven to the substrate surface). On neutral (non-preferential) substrates, polymer chains are oriented parallel to the substrate thereby subduing chain stretching compression and the formation of islands and holes.¹⁹ With regards to through-film effects, Peters *et al.* used *n*-octadecyltrichlorosilane monolayers exposed to X-ray radiation at various dose rates to qualitatively determine that the size of island and hole formations on PS-PMMA films was related directly to the substrate interfacial interaction, as larger incompatibilities between substrate-

polymer surface energies resulted in larger island and hole formations.²⁰ To study the maximum propagation of substrate-polymer interaction effects, Xu *et al.* suggested that islands and holes do not form once the film thickness crosses into the substrate/free surface competition region,⁸ as the competition leads to a mixed nanostructure orientation that reduces chain stretching and compression, which makes island and hole formations unfavorable. Thus, using OM combined with gradient thickness films provided a high-throughput and robust method to track the location of incommensurate thicknesses and identify wetting behavior, through-film driving forces for self-assembly, and the critical propagation distance of substrate surface effects.

To achieve the most detailed analysis of substrate surface effects, the self-assembly of PMMA-*Pn*BA (hexagonally-perforated lamellae [HPL] morphology, $L_0 = 41$ nm) BP thin films on chlorosilane-modified substrates was explored. A range of total (30.2 mJ/m^2 to 77.4 mJ/m^2), dispersive (28.3 mJ/m^2 to 42.7 mJ/m^2), and polar (1.9 mJ/m^2 to 36.9 mJ/m^2) substrate surface energies was studied to elucidate the key substrate-polymer interactions responsible for defining the nanostructure ordering and orientation through the film thickness. Resulting substrate-polymer interaction effects were quantified visually by imaging island and hole formations on uniform and gradient thickness films. Furthermore, changes in island and hole growth rates as a function of surface energy were studied by thermally annealing films during *in situ* OM. Experimental results were paired with comparable predictive equations utilizing total and/or decoupled surface energy components to determine the impact of individual substrate-polymer interactions on substrate wetting behavior, through-film

self-assembly, and the maximum propagation depth of substrate-polymer interaction effects.

3.2 Materials and Methods

3.2.1 Substrate Surface Modification and Characterization

Benzyltrimethyl chlorosilane (benzyl silane), 2-acetoxyethyltrimethyl chlorosilane (aceto silane), 3-methacryloxypropyltrimethyl chlorosilane (methacryl silane), and *n*-butyltrimethyl chlorosilane (*n*-butyl silane) (Gelest Inc.) were used as received. Liquid and vapor deposition were conducted as described in Chapter 2, Section 2.1.2. Substrates with benzyl and *n*-butyl silane monolayers were subjected to ultra-violet ozone (UVO) treatments to investigate additional substrate surface energies. Exposure to UVO radiation for various times altered the measured water and diiodomethane contact angles in a predictable fashion.^{19, 25} Surface energy measurements were conducted as described in Chapter 2, Section 2.2.

The Owens-Wendt method, an extension of the Good-Girifalco geometric mean approximation, was utilized to calculate surface energy dispersive (γ_S^D) and polar (γ_S^P) terms from contact angle measurements.²⁶ The liquid surface energy values were $\gamma_{L,Water} = 72.8 \text{ mJ/m}^2$, $\gamma_{L,Water}^D = 21.8 \text{ mJ/m}^2$, $\gamma_{L,Water}^P = 51 \text{ mJ/m}^2$, $\gamma_{L,Diiio} = 50.8 \text{ mJ/m}^2$, $\gamma_{L,Diiio}^D = 50.8 \text{ mJ/m}^2$, $\gamma_{L,Diiio}^P = 0 \text{ mJ/m}^2$.²⁷ Reported contact angle measurements were averaged overall multiple spots (≈ 10) for each sample. One standard deviation of the data from repeated measurements was taken as the experimental uncertainty for a given sample. The experimental uncertainty was propagated through interfacial energy equations in the final analyses.

3.2.2 Polymer Film Preparation and Characterization

A PMMA-PnBA ($M_n = 69$ kg/mol; $D = 1.1$; $f_{PMMA} = 0.33$, $f_{PnBA} = 0.67$; $L_0 = 41$ nm) was purchased from Polymer Source Inc. and used as received. The polymer M_n , block volume fractions, L_0 , and bulk morphology were characterized by size exclusion chromatography (Viscotek, GPCmax VE-2001), nuclear magnetic resonance spectroscopy (Bruker, AVX400), AFM (Veeco Dimension 3100) and small-angle X-ray scattering, respectively. An HPL morphology was suggested for PMMA-PnBA thin films as AFM revealed perpendicular cylinders at the free surface where islands and holes were present, a phenomena caused by HPL structures.^{5, 28}

Polymer films were cast from 2.1 wt% PMMA-PnBA in tetrahydrofuran (Fisher Scientific, Optima) solutions using a flow coating apparatus to make gradient thickness films.²⁹ Film thickness was measured using a spectral reflectometer (Filmetrics, F20-UV). For surface feature size analysis, holes were analyzed at incommensurate thickness films (88-90 nm for symmetric wetting films and 60-64 nm and 106-108 nm for asymmetric wetting films). At these thicknesses, micron-scale bicontinuous surface structures gave way to individual hole formations. For surface feature location analysis, multiple shallow gradient films were made on each modified substrate (and bare silica) to reduce the gradient steepness on a single film and avoid thickness effects on structure formation, which appear in gradients above approximately ≈ 10 nm/mm according to literature.^{30, 31} In this study, the largest gradient used on any single film was approximately 1.6 nm/mm. All films were subjected to dynamic vacuum (20 mTorr) at room temperature to remove residual solvent before annealing under vacuum at 175 °C for 24 h to promote island and hole formation. After 24 h, films were removed from the vacuum oven and quenched on a metal plate to bring the films to room temperature and kinetically trap the

microstructures. To ensure that the 24 h annealing time was not a limiting factor in polymer chain reorganization, PMMA–P*n*BA films on *n*-butyl silane substrates were annealed for up to 48 h and saw no change in island and hole formations from OM. This result suggested that the surface structure had sufficient time to equilibrate at 24 h (see Appendix A, Figure A.1).

BP thin films were imaged with OM to evaluate micrometer length scale formations (islands and holes). Island and hole formations in optical micrographs were sized using ImageJ software. The procedure to analyze images was standardized into four steps: enhance contrast, remove noise, convert image to black and white, and measure feature sizes. Resolution dictated a minimum measurable feature size of 0.3 μm^2 . Additionally, circularity (related to the ratio of area to perimeter and equivalent to one for a perfect circle) was set to 0.75 or greater to remove formations that bridged during image analysis. The average area, standard deviation, and number of formations were recorded for use in data analysis. Error in OM critical film thickness measurements was recorded as $\pm 0.25L_0$ for bare silica, aceto silane, benzyl silane and $\pm 0.50L_0$ for methacryl silane and *n*-butyl silane substrates to account for resolution bias and ensure the true onset of island and hole disappearance was captured. *In situ* OM was conducted as described in Chapter 2, Section 2.7.

Nanometer length scale features (free surface morphology) were analyzed with AFM. FFTs performed on AFM images were generated and analyzed using ImageJ software. Furthermore, AFM was utilized to confirm the PMMA-P*n*BA morphology was consistent on all substrate surfaces thereby ensuring differences in substrate propagation were not caused by morphological effects.³²

3.3 Results and Discussion

For this surface energy study, PMMA-*Pn*BA was chosen as a model material because the individual polymer blocks had similar dispersive but different polar and total surface energies (PMMA: $\gamma_{total} = 41.1 \text{ mJ/m}^2$, $\gamma_D = 29.6 \text{ mJ/m}^2$, $\gamma_P = 11.5 \text{ mJ/m}^2$; *Pn*BA: $\gamma_{total} = 33.7 \text{ mJ/m}^2$, $\gamma_D = 30.4 \text{ mJ/m}^2$, $\gamma_P = 3.3 \text{ mJ/m}^2$ at 20 °C).²⁷ Furthermore, the change in dispersive component surface energy as a function of temperature ($d\gamma/dT$) was nearly identical between the two blocks (PMMA = $-0.076 \text{ mJ/m}^2 \cdot \text{K}$; *Pn*BA = $-0.070 \text{ mJ/m}^2 \cdot \text{K}$) thereby maintaining the difference in surface energies between PMMA and *Pn*BA at the annealing temperature (175 °C).²⁷ By minimizing dispersive component differences between the two blocks and altering polar interactions through substrate modification, total and decoupled surface energy effects could be explored in a systematic manner. The average total, dispersive, and polar surface energy components of the bare silica and chlorosilane-modified substrates used in this study are listed in Table 3.1 and match well with reported measurements found in literature (surface energy measurements were recorded for each substrate used in this analysis to account for variability in surface energy on a day-to-day basis).^{1, 2, 33, 34} Gradient thickness PMMA-*Pn*BA films were coated onto modified substrates *via* flow coating to determine commensurate and incommensurate thicknesses.²⁹

Table 3.1: Average water and diiodomethane contact angle measurements along with corresponding surface energies for bare silica and chlorosilane monolayer substrates

Substrate	Contact angle ^a (°)		Surface energy (mJ/m ²)		
	Water	Diiodomethane	Total	Dispersive	Polar
Bare silica	6.4 ± 0.3	33.5 ± 1.0	77.4 ± 0.5	42.7 ± 0.4	34.7 ± 0.3
Aceto silane	69.5 ± 2.0	49.0 ± 0.2	44.0 ± 0.8	34.8 ± 0.1	9.1 ± 0.8
Benzyl silane	81.6 ± 0.6	43.1 ± 0.4	41.3 ± 0.3	38.0 ± 0.2	3.3 ± 0.2
Methacryl silane	80.7 ± 0.7	49.9 ± 0.4	38.7 ± 0.3	34.3 ± 0.2	4.4 ± 0.3
<i>n</i> -Butyl silane	91.6 ± 1.2	60.2 ± 0.8	30.6 ± 0.6	28.4 ± 0.5	2.2 ± 0.3

^a The uncertainty in the contact angle represents one standard deviation of the data from repeated measurements and was propagated through calculations to determine surface energy uncertainty.

3.3.1 Substrate Wetting Behavior

To investigate the effect of substrate-polymer interaction on wetting behavior, film thicknesses were kept below 110 nm ($2.7 L_0$) to allow the substrate surface effect to propagate to the free surface.⁹ Wetting behavior was determined by locating island and hole formations at known film thicknesses using OM. For all substrates, *Pn*BA was expected to wet the free (air) surface, as it had a lower total surface energy (33.7 mJ/m²) than PMMA (41.1 mJ/m²).²⁴ Thus, symmetric or asymmetric wetting occurred when *Pn*BA or PMMA wet the substrate surface, respectively.

As shown in Figure 3.1, films coated on bare silica, aceto silane, and benzyl silane substrates were featureless at a half-integer L_0 thickness and indicated evidence of islands and holes at an integer L_0 thickness. Films coated on methacryl silane

substrates developed islands and holes at a half-integer L_0 thickness and were featureless at an integer L_0 thickness. Distinct island and hole formations were not present on 100 nm or thicker films on *n*-butyl silane substrates most likely due to the substrate/free surface competition,⁸ but thinner films (62 nm) on *n*-butyl silane substrates exhibited clear island and hole formations at incommensurate thicknesses. Therefore, experimental results indicated bare silica, aceto silane, and benzyl silane substrates were preferential for PMMA, but methacryl silane and *n*-butyl silane substrates were preferential for P*n*BA.

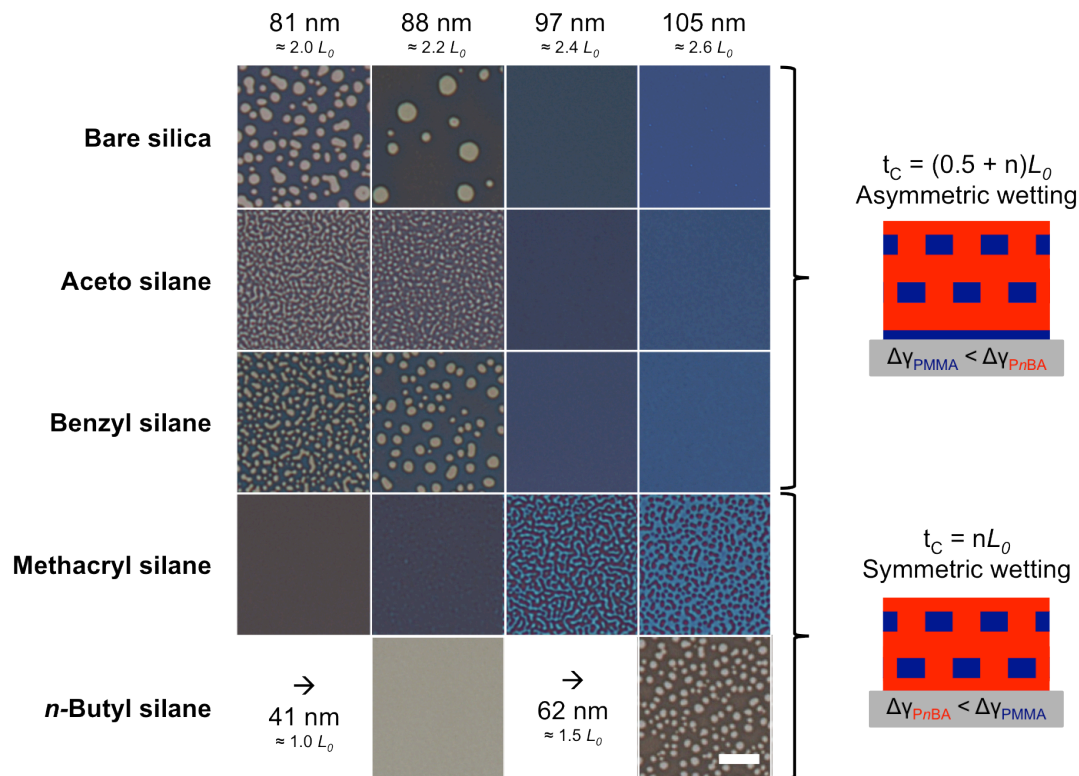


Figure 3.1: OM images of commensurate (t_C) and incommensurate film thickness regions for bare silica and chlorosilane monolayers as indicated by presence (or lack) of islands and holes. Bare silica, aceto silane, and benzyl silane substrates constrained PMMA- Pn BA to asymmetric wetting as commensurate thicknesses were noted at a half-integer L_0 thickness. Films cast on methacryl and n -butyl silane substrates exhibited symmetric wetting as island and hole formations were present at half-integer L_0 thicknesses. The location of island and hole formations indicated bare silica, aceto silane, and benzyl silane substrates were preferential for PMMA, and methacryl silane and n -butyl silane substrates were preferential for Pn BA. The scale bar represents 10 μ m and applies to all micrographs. Reprinted with permission from Shelton C. K. and Epps, T. H., III *Macromolecules* **2015**, 48, 4572-4580, Copyright 2015 American Chemical Society.³⁵

Initially, the experimental wetting behavior was compared to predictions from the standard total (Equation 3.1) and decoupled (Equation 3.2) surface energy

equations that calculate the interfacial interaction between the substrate (S) and one polymer block (A) in the BP.

$$\Delta\gamma_A^{Total} = |\gamma_S - \gamma_A| \quad (3.1)$$

$$\Delta\gamma^{Decoupled} = \gamma_A + \gamma_S - 2(\gamma_A^D \gamma_S^D)^{1/2} - 2(\gamma_A^P \gamma_S^P)^{1/2} \quad (3.2)$$

This comparison is shown in Figure 3.2. The decoupled surface energy equation matched the experimental results for all substrates except benzyl silane, for which the prediction was symmetric wetting, as opposed to the experimental result of asymmetric wetting. The total surface energy equation matched the experimental results for all substrates except methacryl silane, for which the prediction was asymmetric wetting, as opposed to the experimental result of symmetric wetting. Shaded quadrants on the plot indicate the discrepancies between predicted (top axis) and experimental (right axis) behavior.

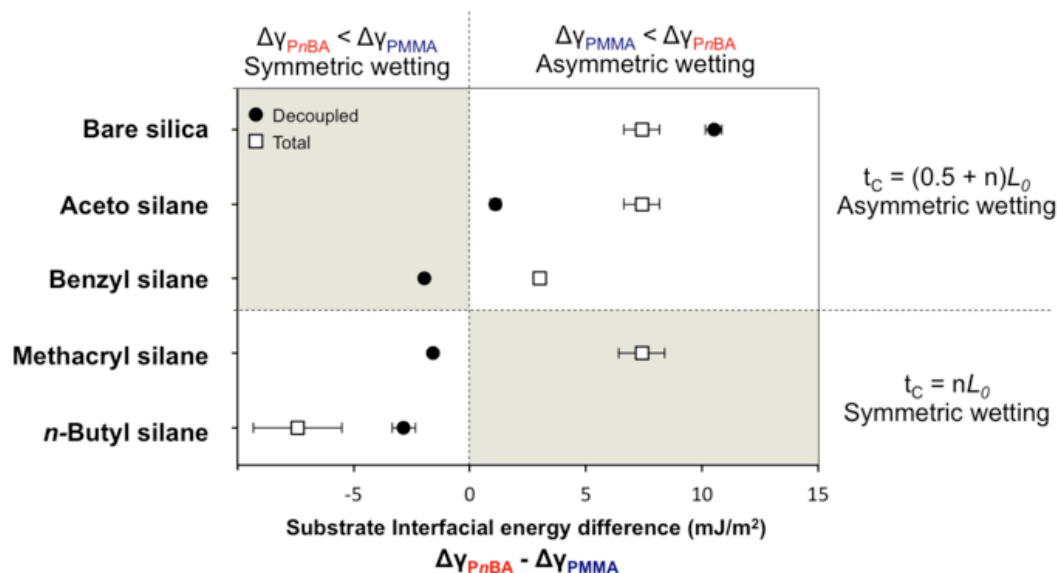


Figure 3.2: Comparison between predicted (dotted line intersecting x-axis) and experimentally determined (dotted line intersecting y-axis) wetting behavior of PMMA-*PnBA* on different substrate surfaces using decoupled (black circles) and total (white squares) surface energy approaches. Shaded quadrants represent incongruities between predicted and experimental results. Negative interfacial energy differences predict that the *PnBA* block has a lower interfacial energy with the substrate and will wet the substrate surface, while positive interfacial energy differences predict that the PMMA block has a lower interfacial energy and will wet the substrate surface. The *PnBA* block was expected to wet the free surface in all cases due to its lower total surface energy. Reprinted with permission from Shelton C. K. and Epps, T. H., III *Macromolecules* **2015**, 48, 4572-4580, Copyright 2015 American Chemical Society.³⁵

To eliminate inconsistencies between the experimental and predicted results, the Hamaker constant was introduced to define the long-range attractive or repulsive interactions. The Hamaker constant describes the attractive or repulsive nature of van der Waals interactions between two or more surfaces and is directly proportional to the total surface energy.³⁶ Positive Hamaker constants indicate a long-range, attractive

force between the substrate and polymer, and negative Hamaker constants indicate a long-range, repulsive force between the substrate and polymer.³⁷⁻³⁹ For the three-layer system at the substrate-polymer interface (substrate, PMMA block, PnBA block) the Hamaker constant becomes negative if the middle layer's surface energy is the maximum (*i.e.*, $\Delta\gamma_{PMMA} < \Delta\gamma_{PnBA}$ and $\gamma_{PMMA} > \gamma_S$).^{36, 40-43} The remaining polymer domains are constrained to the layering behavior driven by the preferential substrate-polymer wetting. Including the Hamaker constant in total surface energy analyses led to three cases that completely explained experimental substrate wetting behavior.

The description of each case and comparison with experimental results are shown in Figure 3.3. Case 1 describes when the substrate interfacial energy of PMMA is less than that of PnBA, and the Hamaker constant is positive. Therefore, the PMMA block segregates to the substrate surface, resulting in asymmetric wetting. In Case 2, the PMMA has a lower substrate interfacial energy than PnBA, but the Hamaker constant is negative for the system. Therefore, PnBA segregates to the substrate interface to reduce overall repulsive interactions in the system. This effect results in symmetric wetting. In Case 3, PnBA has a lower substrate interfacial energy, and the Hamaker constant is positive, leading to symmetric wetting. From surface energy values calculated for each modified substrate, Case 1 applied to bare silica, aceto silane, and benzyl silane substrates, Case 2 applied to methacryl silane substrates, and Case 3 applied to *n*-butyl silane substrates. By including Hamaker constant stabilities, each case accurately predicted the experimental wetting behavior on all surfaces. This result suggests that the inclusion of both short and long-range repulsive interactions is necessary to describe the complete surface energy/wetting behavior.

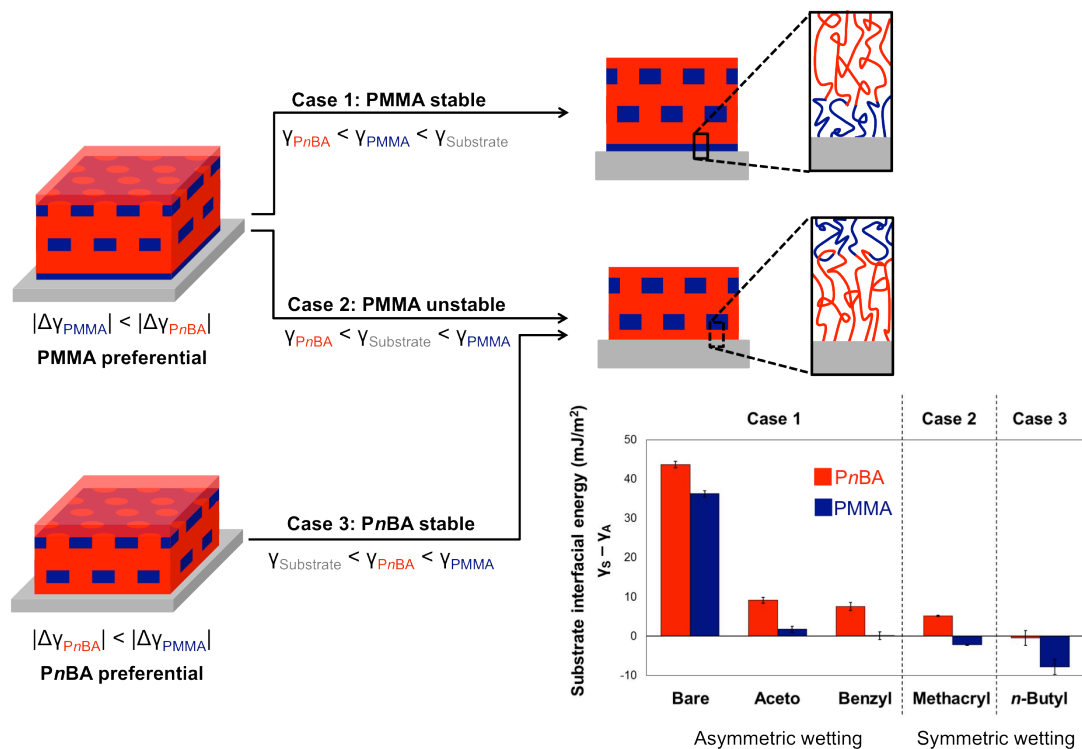


Figure 3.3: Scheme depicting wetting behavior in BP thin films using three cases. In Case 1, PMMA has a lower interfacial energy than PnBA, and a net long-range attractive force is present, resulting in asymmetric wetting. In Case 2, long-range, repulsive interactions exist at the substrate-PMMA interface as the higher surface energy PMMA layer separates the lower surface energy substrate and PnBA layers. Therefore, PnBA segregates to the substrate, stabilizing the substrate-polymer interactions and resulting in symmetric wetting. In Case 3, PnBA has a lower interfacial energy, there is a net attractive interaction in the system, and symmetric wetting is predicted. Aligning each case to the appropriate system, as shown in the plot, accurately matched predicted and experimental results. Reprinted with permission from Shelton C. K. and Epps, T. H., III *Macromolecules* **2015**, 48, 4572-4580, Copyright 2015 American Chemical Society.³⁵

3.3.2 Through-Film Propagation of Substrate Surface Effects

At film thicknesses greater than the contacting substrate-polymer layer, the short-range and long-range forces define substrate-polymer interactions with larger

incompatibilities creating stronger driving forces for nanostructure ordering and defect annihilation.^{20, 44} To examine the impact of decoupled dispersive and polar components on the through-film driving forces, films were cast at incommensurate and hole-forming thicknesses (≈ 88 - 90 nm for asymmetric wetting and ≈ 64 nm or ≈ 108 nm for symmetric wetting). Film thicknesses that formed holes were selected because holes have larger equilibrium sizes than islands thereby making them easier to measure accurately.¹⁹

The effect of individual dispersive and polar components was resolved from experimental results using two models: the Owens and Wendt model (Equation 3.2) and Equation 3.3 below.⁴⁵

$$\Delta\gamma_A = \gamma_A + \gamma_S - 2(\gamma_A\gamma_S)^{1/2} \quad (3.3)$$

Both models include the total surface energy to account for repulsive interactions at the interface, and both models incorporate long-range, attractive interactions using a geometric mean approach. However, only the Owens and Wendt model (Equation 3.2) separates the attractive interaction into dispersive and polar components. Measured hole sizes were matched with the corresponding interfacial energy differences calculated from each model (Figure 3.4). A linear trend line was fit to the data because literature suggests island and hole size should be directly proportional to surface energy.⁴⁶ The total surface energy model (Figure 3.4a) failed to describe the data on all substrates, especially for those substrates for which the polymer/substrate interfacial energy differences was relatively small. However, the decoupled surface energy model (Figure 3.4b) described the data accurately on all substrate surfaces. Differences in the model fits to the data highlight the importance

of incorporating decoupled surface energy components when predicting substrate-polymer interactions.

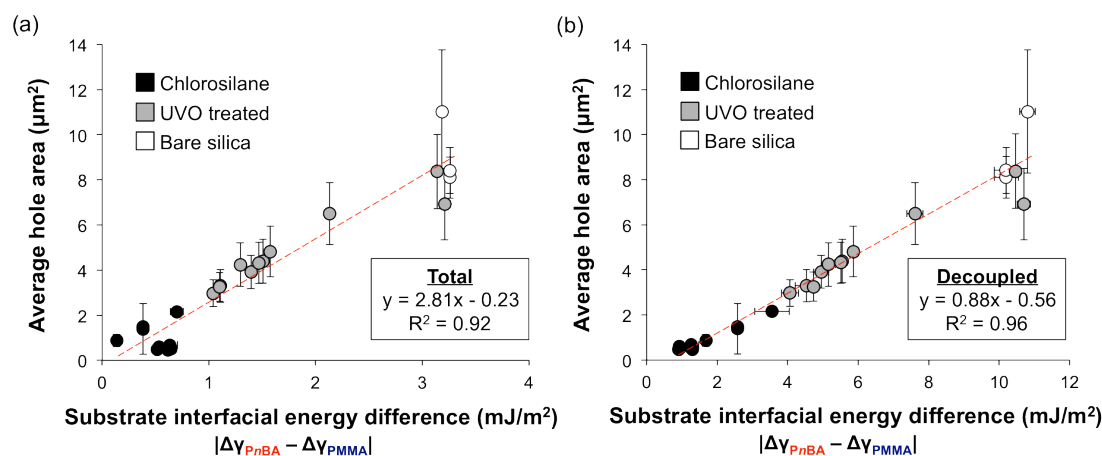


Figure 3.4: Hole sizes on aceto silane, benzyl silane, methacryl silane, and *n*-butyl silane surfaces (black circles), UVO treated benzyl silane and *n*-butyl silane surfaces (gray circles), and bare silica (white circles) substrates. Two equations were used to compare with hole size: (a) Equation 3.3, in which the attractive forces were described using the total surface energy, and (b) Equation 3.2, in which the attractive forces were decoupled. The dotted red line represents a linear fit to the data. Though the two fits have similar R^2 values (0.92 for the total surface energy equation and 0.96 for the decoupled surface energy equation), the total surface energy equation did not capture the expected trend in hole size, with the major deviation noted at lower interfacial energy differences. The decoupled surface energy equation ($R^2 = 0.96$) captured the experimental trend more accurately over the entire data range. Reprinted with permission from Shelton C. K. and Epps, T. H., III *Macromolecules* **2015**, 48, 4572-4580, Copyright 2015 American Chemical Society.³⁵

The major deviation between total and decoupled surface energy equation fits was noted on aceto silane, benzyl silane, methacryl silane, and *n*-butyl silane substrates for which total vs. decoupled surface energy equations separately predicted

dissimilar substrate-polymer block preferences. For example, benzyl silane substrates had a total surface energy close to PMMA but a polar surface energy close to PnBA. Each equation predicted different hole sizes for films on benzyl silane substrates, but only the decoupled equation's predictions aligned with experimental results. Thus, this decoupling of the surface energy into dispersive and polar components was necessary to describe through-film self-assembly mechanisms as the long-range, attractive forces were not considered properly when lumped into a total surface energy alone.

3.3.3 *In Situ* Study of Hole Formations

BP thin film self-assembly was examined by *in situ* OM during thermal annealing to ensure previously mentioned substrate effects were thermodynamic surface energy phenomena and not kinetic limitations. Literature on BP thin film kinetics indicates that islands and holes nucleate and grow to an equilibrium size, after which individual islands and holes can coalesce.^{22, 46-48} Therefore, using a 24 h oven anneal for experiments had the following constraints: 1) that the time frame was sufficient for the surface structures to reach a relatively stable size, 2) that the time frame was not long enough to lead to excessive coalescence that would obscure island and hole size measurements, and 3) that the wetting behavior did not change over the time frame due to film expansion, high-temperature, or kinetic effects.

In situ OM during thermal annealing of films coated on bare silica and benzyl silane substrates was accomplished using a sealed Linkam heating stage (Figure 3.5a). Bare silica and benzyl silane substrates were used because films on these substrates produced large hole features for accurate tracking. Images and sizing from *in situ*

measurements followed the expected nucleation and growth behavior and are shown in Figure 3.5b.

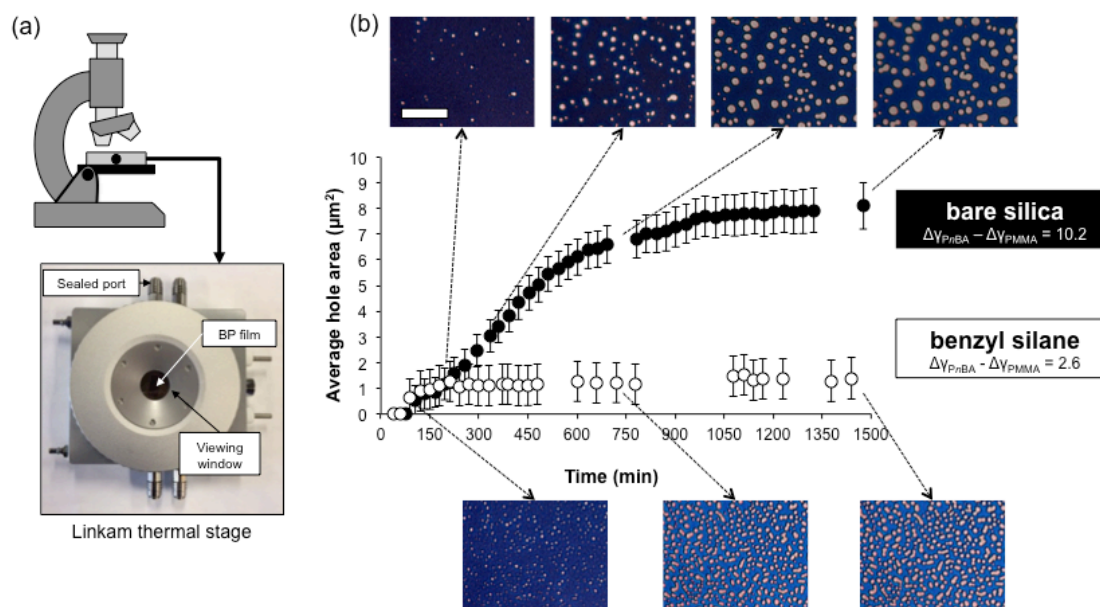


Figure 3.5: (a) Schematic of *in situ* anneal setup with a sealed Linkam thermal stage under an optical microscope. The Linkam thermal stage heated the film to 175 °C using a 3 °C/min heat ramp for consistency with vacuum oven annealed samples. (b) Size measurements from holes produced on bare silica and benzyl silane substrates over 24 h indicated expected nucleation and growth kinetics, followed by island and hole stabilization at equilibrium sizes, that match those from oven annealed samples. The scale bar represents 20 μm and can be applied to all micrographs. Reprinted with permission from Shelton C. K. and Epps, T. H., III *Macromolecules* **2015**, 48, 4572-4580, Copyright 2015 American Chemical Society.³⁵

Key results from the *in situ* studies supported findings from static experiments by ensuring the use of a 24 h anneal highlighted the thermodynamic effects in feature formation. First, within the 24 h time frame, holes grew to an equilibrium size that

matched well with oven-annealed samples (Figure 3.4). Films cast on bare silica and annealed in the vacuum oven and the Linkam stage for 24 h formed holes with average sizes of $8.4 \pm 0.9 \mu\text{m}^2$ and $8.1 \pm 0.9 \mu\text{m}^2$, respectively. Similarly, films cast on benzyl silane and annealed in the vacuum oven and the Linkam stage for 24 h formed holes with average sizes of $1.5 \pm 0.1 \mu\text{m}^2$ and $1.4 \pm 0.8 \mu\text{m}^2$, respectively. Second, coalescence was not excessive after an equilibrium size was reached. Third, no temporal changes in wetting behavior (*i.e.*, from asymmetric to symmetric) were captured during the testing of any individual substrates.

3.3.4 Substrate/Free Surface Competition

Substrate interaction effects propagate as a field through the film thickness to a critical film depth, at which substrate and free surface interaction effects compete and alter nanostructure orientation.^{3, 9, 24, 49} Studies probing the propagation depth of substrate surface field effects are found in the literature but indicate differing propagation depth relationships.^{3, 8, 50, 51} Several works suggest a limitless propagation depth of substrate surface field effects;^{8, 50} however, other studies describe a maximum propagation depth.^{3, 51} Because many applications require uniform nanostructure orientation through the entire film thickness, universal understanding of how key factors affect the propagation of substrate surface field effects is vital to tune substrate-polymer interactions and enhance film uniformity in an ever-expanding list of BP systems.¹³

3.3.4.1 Identifying Critical Film Thicknesses with Optical Microscopy

The maximum propagation distance of substrate-polymer interaction effects have been characterized using AFM,^{3, 9, 52} cross-sectional transmission electron

microscopy,^{3, 8} rotational small-angle neutron scattering,⁵¹ neutron reflectivity,^{8, 53} and grazing-incidence small-angle X-ray scattering^{4, 32, 50} in the literature. However, as an alternative to these time-intensive methods, tracking island and hole formations (topographic regions on the film's free surface caused by unfavorable stretching or compression of polymer chains at incommensurate thicknesses) on gradient thickness BP films with OM can be paired with interfacial energy measurements to pinpoint critical propagation distances.^{21, 22}

OM images of island and hole formations on gradient thickness PMMA-*Pn*BA films with bare silica and chlorosilane-modified (aceto, benzyl, methacryl, and *n*-butyl silane) substrates are shown in Figure 3.6. For each substrate, the last image (red box) marks the incommensurate thickness at which island and hole formations were expected but not present. The results revealed that PMMA-*Pn*BA films cast on bare silica substrates had the largest propagation of substrate effects, followed by aceto silane, benzyl silane, methacryl silane, and *n*-butyl silane modified substrates, an order that differs from the total surface energy predictions found in the literature.⁸ Images detailing island and hole disappearance for a gradient thickness PMMA-*Pn*BA film on an *n*-butyl silane substrate are shown in Appendix A, Figure A.2.

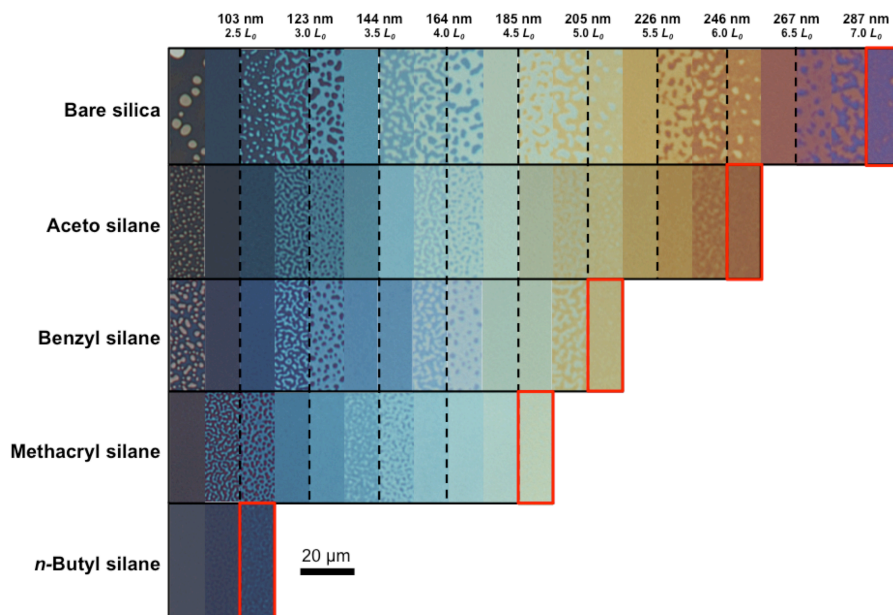


Figure 3.6: Stacked OM images of gradient thickness PMMA- Pn BA films on bare silica and chlorosilane-modified substrates. Films were imaged up to thicknesses at which islands and holes disappeared at integer domain spacing (nL_0) thicknesses for asymmetric wetting substrates (bare silica, aceto silane, benzyl silane) and at half-integer domain spacing ($[n+0.5]L_0$) thicknesses for symmetric wetting substrates (methacryl silane, n -butyl silane). The red boxes indicate the critical film thickness at which island and hole formations were expected but not present at the free surface. The scale bar applies to all micrographs. Reprinted with permission from Shelton, C. K. and Epps, T. H., III *Macromolecules* **2016**, 49, 574-580.⁵⁴

3.3.4.2 Verifying Transition Regions with Atomic Force Microscopy

To support high-throughput OM, AFM was used to verify a change in free surface nanostructure orientation at the onset of substrate/free surface competition regime. As shown in Figure 3.7, as the PMMA- Pn BA film thickness increased on bare silica substrates, the orientation of cylinders at the free surface began to deteriorate. AFM images of gradient thickness PMMA- Pn BA films on the chlorosilane-modified substrates are shown in Appendix A, Figure A.3. For a BP thin

film with an HPL morphology, this “folding” of cylinders at the free surface was consistent with nanostructure orientation changes found in literature.^{3, 53} Once the free surface interaction became comparable to the substrate surface interaction, the P*n*BA block content increased at the free surface. Consequently, in this region, adjacent P*n*BA cylinders “folded” and oriented parallel to the free surface to increase the P*n*BA coverage area.⁵⁵ This orientation change reduced chain stretching and compression caused by the substrate surface thereby mitigating the driving force for island and hole formation.

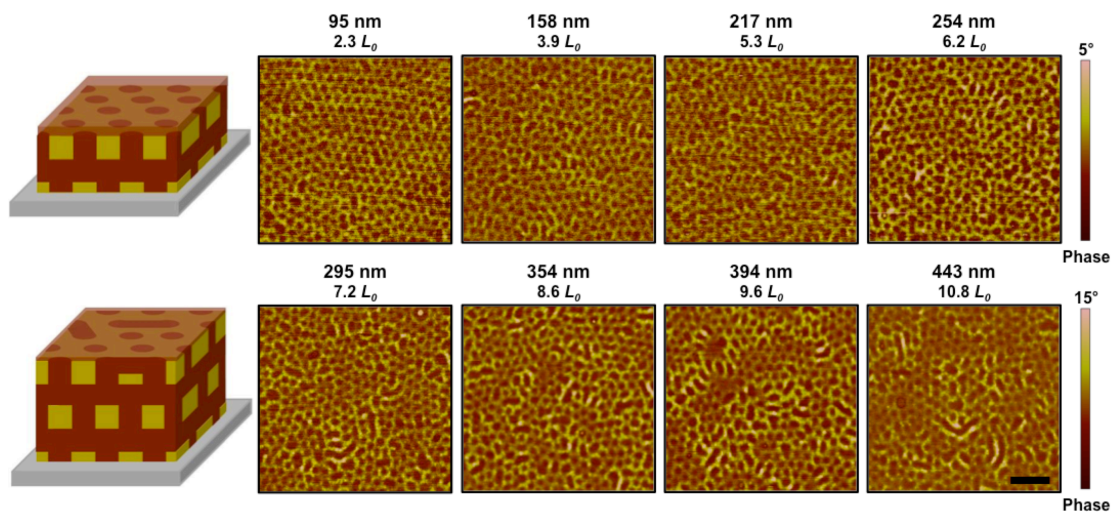


Figure 3.7: Free surface AFM images of PMMA-*Pn*BA gradient thickness films on bare silica substrates. After the film thickness surpassed the critical propagation distance of substrate surface effects (287 nm), there was a distinct change in the surface nanostructure behavior caused by the substrate/free surface competition. At substrate dominant thicknesses (top row), perpendicular *Pn*BA cylinders (brown) perforate through PMMA domains (yellow). At substrate/free surface competition thicknesses (bottom row), the lower surface energy *Pn*BA is driven to the free surface, causing the cylinders to “fold” and appear as short parallel cylinders. All images were taken from the bulk film, outside of island and hole formations. The free surface structure did not change on island and hole formations except at the bulk film interface where large thickness differences produced artificial stretched domains. The scale bar represents 200 nm and applies to all AFM images. Reprinted with permission from Shelton, C. K. and Epps, T. H., III *Macromolecules* **2016**, 49, 574-580.⁵⁴

Radial intensity profiles of fast Fourier transformations (FFTs) on PMMA-*Pn*BA film AFM phase images quantified the “folding” of *Pn*BA domains at different film thicknesses as found in the Appendix A, Figure A.4. Figure 3.8 shows the change in full-width half-max (FWHM) of the primary peak from the azimuthally averaged FFT intensity spectrum measured from free surface AFM images of gradient

thickness films on each substrate surface. At film thicknesses below the critical thickness, substrate-polymer interactions oriented nanostructures uniformly resulting in a narrow intensity peak and a low FWHM. Once substrate/free surface competition thicknesses were reached, “folding” of PnBA domains possibly caused the intensity peak to broaden resulting in a larger FWHM. The critical thicknesses at which significant orientation change was noted by AFM (shaded region; FWHM \approx 0.06-0.08 determined by the onset of a consistent increase in FWHM from bare silica samples) matched well with those determined from OM (colored arrows), suggesting the disappearance in island and hole formations (Figure 3.6) was influenced by nanostructure changes at the free surface (Figure 3.7).

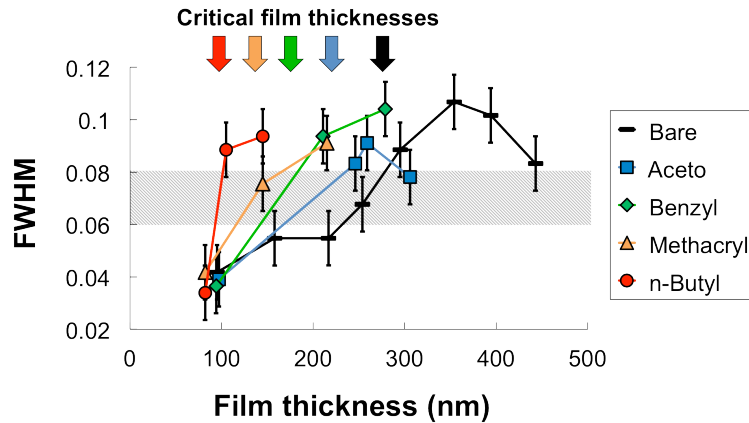


Figure 3.8: FWHM values of the primary peak from the azimuthally averaged FFT intensity spectrum from AFM images capturing the free surface nanostructure orientation of gradient thickness PMMA-*Pn*BA films on bare silica, aceto silane, benzyl silane, methacryl silane, and *n*-butyl silane substrates. The shaded region indicates the FWHM value (≈ 0.06 - 0.08), at which a significant orientation change occurred. The colored arrows represent the estimated critical film thickness (from OM) at which films cast on each substrate crossed this FWHM threshold. The critical film thicknesses determined using AFM matched well with those measured from OM. The decrease in FWHM in aceto silane and bare silica samples is attributed to a possible transition to a free surface dominated nanostructure with a more uniform orientation at larger film thicknesses. The lines connecting data points are to guide the eye and do not represent a mathematical fit to the data. Reprinted with permission from Shelton, C. K. and Epps, T. H., III *Macromolecules* **2016**, 49, 574-580.⁵⁴

3.4 Prediction of Substrate Surface Energy Effects

3.4.1 Wetting Behavior and Through-Film Driving Force

Combining the wetting behavior and through-film predictive equations provides the full picture of substrate surface self-assembly effects, as shown in Figure 3.9. The total surface energy (Equation 3.1) and Hamaker constant define the three possible wetting behavior regimes: PMMA preferential, *Pn*BA preferential, and

neutral (non-preferential) substrates. The neutral, or non-preferential region, represents substrate surface energies at which the total surface energy and Hamaker constant effects result in a different block being preferential. In some instances, neither set of interactions dominate and a true neutral surface is achieved; both polymer blocks segregate to the substrate and islands and holes do not form. In other instances (*e.g.*, PMMA-P n BA on methacryl silane), one set of interactions dominates and drives a particular wetting behavior. As is shown in this chapter, the latter case is more common when the total surface energies of the two polymer blocks are significantly different. The gradient across the plot represents changes in the substrate self-assembly driving force predicted using Equation 3.2 to describe through-film effects.

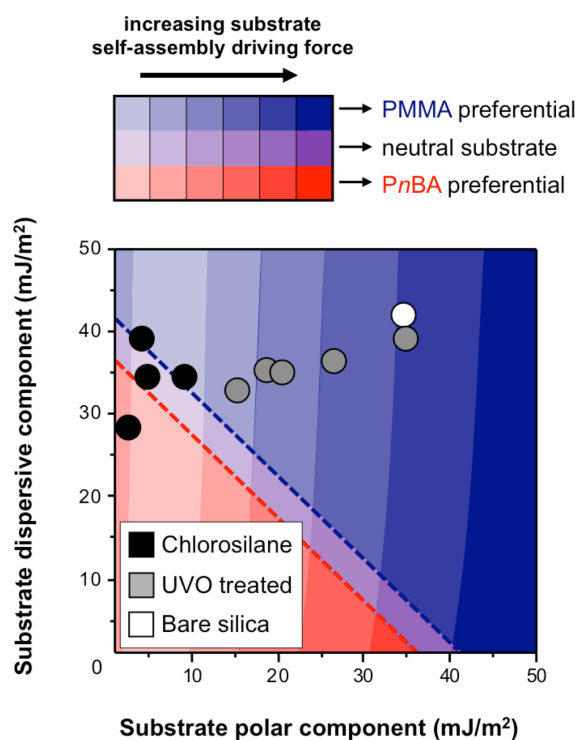


Figure 3.9: Composite prediction of surface wetting and through-film behavior to pinpoint necessary substrate surface energy conditions to achieve prescribed substrate wetting behavior. The dotted lines separate the plot into three possible substrate wetting behaviors (PMMA preferential, PnBA preferential, and neutral) using the total surface energy and Hamaker constant analysis. The neutral region indicates a non-preferential substrate region as the total surface energy and Hamaker constant calculations result in a different block being preferential, although the strength of either of these parameters can dominate and force a preferential substrate (*e.g.*, methacryl silane). The gradient across the plot represents the change in the substrate self-assembly driving force calculated using the decoupled surface energy. Reprinted with permission from Shelton C. K. and Epps, T. H., III *Macromolecules* **2015**, 48, 4572-4580, Copyright 2015 American Chemical Society.³⁵

3.4.2 Maximum Propagation of Substrate Surface Energy Effects

The propagation of substrate-polymer interfacial interaction effects investigation from gradient thickness films, OM, and AFM generated a self-assembly map compiled in Figure 3.10. This analysis determined long-range (LR) decoupled surface energy components were responsible for the critical propagation depth of substrate surface effects as described by Equation 3.4, a modification of the Owens and Wendt interfacial energy equation (Equation 3.2).²⁶

$$\Delta\gamma^{LR} = 2(\gamma_A^D \gamma_S^D)^{1/2} + 2(\gamma_A^P \gamma_S^P)^{1/2} \quad (3.4)$$

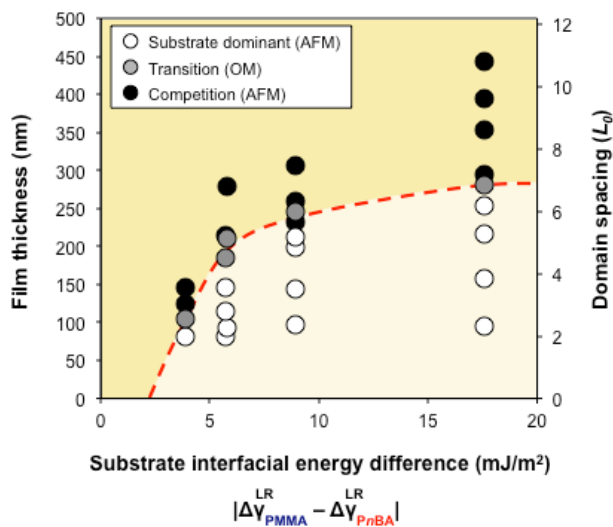


Figure 3.10: Propagation distances of substrate surface effects for PMMA-PnBA BP films on modified substrates. OM was used to identify the critical film thicknesses (gray circles) at which island and hole formations disappeared marking the transition between the substrate surface dominant (below dashed red line) and substrate/free surface competition (above dashed red line) film thicknesses. AFM was employed to characterize free surface nanostructure orientation on films of increasing film thickness as either substrate dominant effects (uniform nanostructure orientation; white circles) or substrate/free surface competition effects (mixed nanostructure orientation; black circles). The dashed red line is to guide the eye and does not represent a mathematical fit to the data. Reprinted with permission from Shelton, C. K. and Epps, T. H., III *Macromolecules* **2016**, 49, 574-580.⁵⁴

From the overall analysis presented in Figure 3.10, two key trends were noted. First, the propagation depth of substrate surface effects increased sharply, and almost linearly, at lower substrate interfacial energy difference values as expected.⁸ Second, the propagation depth began to plateau at larger interfacial energy differences following the initial sharp increase. This plateau mimicked the trend noted from substrate propagation studies focused on changes in annealing temperature and links results from temperature effects with those of surface energy effects, identifying a

maximum propagation limit only at larger interfacial energy differences that were not probed in earlier surface energy work.^{8, 51}

To examine the accuracy of the predictive interfacial energy equation, the critical propagation of substrate effects was mapped using Equations 3.1, 3.2, and 3.4 to compare the influence of total (short-range interactions; Equation 3.1), long-range (long-range interactions; Equation 3.4), and decoupled (short and long-range interactions; Equation 3.2) interfacial energy equations, as shown in Figure 3.11. In Figure 3.11, fitting the total (Equation 3.1) and decoupled (Equation 3.2) interfacial energy relationships to the OM data indicated no distinctive trend in the critical film thickness as a function of interfacial energy difference; however, the long-range (Equation 3.4) fit the data to the trend gleaned from OM and AFM results shown in Figure 3.10 (initial linear increase in critical film thickness followed by a possible plateau at higher interfacial energy differences). Therefore, the results suggest that the long-range dispersive and polar forces are the dominant substrate-polymer interactions that dictate the critical propagation depth of substrate surface effects. This result is supported by literature suggesting that the maximum propagation of substrate effects is closely related to long-range forces.⁴⁴

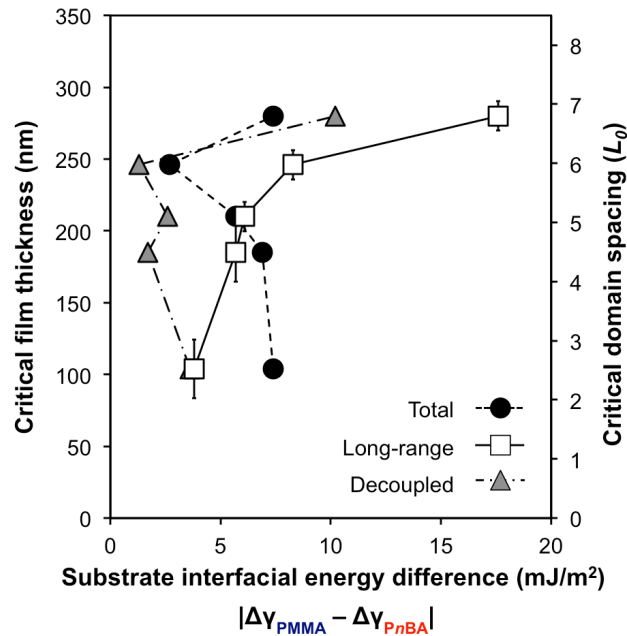


Figure 3.11: Comparison of total (Equation 3.1; black circles), long-range (Equation 3.4; white squares), and decoupled (Equation 3.2; gray triangles) interfacial energies used to track the propagation of the substrate surface effect. The lines between data points are to guide the eye. Although the results from total and decoupled interfacial energy formalisms described no clear trend, those from the long-range interfacial energy equation depicted an increase in propagation distance with increasing substrate interfacial energy difference at lower differences. Additionally, the long-range equation indicated a possible plateau in the critical film thickness at larger interfacial energy differences, a result that mirrored AFM data in Figure 3.10; the long-range data points in Figure 3.11 are the transition (grey) points from Figure 3.10. Reprinted with permission from Shelton, C. K. and Epps, T. H., III *Macromolecules* **2016**, 49, 574-580.⁵⁴

In Figure 3.12, literature measurements of the critical propagation depth of substrate surface effects in lamellar-forming PS-PMMA thin films were probed with the proposed formalism using a first-order approximation of decoupled surface energy values of provided data for substrates modified with PS-PMMA random copolymer brushes.^{22,36,49} The substrate interfacial energy difference has been normalized by the

difference in total surface energy between the two blocks ($|\gamma_A - \gamma_B|$) to aid comparison between the data sets. Figure 3.12 indicates a similar initial linear increase in substrate surface effects propagation distance as a function of interfacial energy, which is followed by a region that becomes less interfacial energy-dependent at larger energy differences. The non-normalized data are shown in Appendix A, Figure A.5.

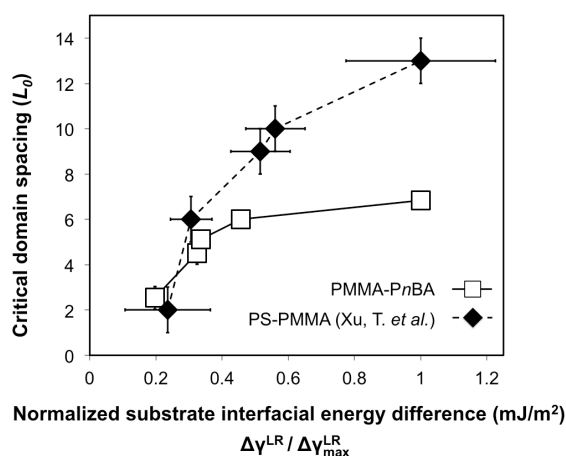


Figure 3.12: Comparison of critical propagation depths of the substrate surface field for PMMA-PnBA and PS-PMMA BP systems. These depths are normalized by system-dependent L_0 's and plotted versus normalized long-range interfacial energy differences. The substrate interfacial energy difference was normalized relative to the total surface energy difference between the blocks. PS-PMMA data was taken from the literature.⁸ The lines between data points are to guide the eye. Reprinted with permission from Shelton, C. K. and Epps, T. H., III *Macromolecules* **2016**, 49, 574-580.⁵⁴

3.5 Conclusions

This chapter developed a predictive understanding of the key substrate-polymer interactions that influence nanostructure ordering and orientation in BP thin film systems. A high-throughput approach exploiting the formation of island and hole

structures was used to investigate a large range of total, dispersive, and polar surface energy components. The results indicate that the repulsive nature of the total surface energy dominated wetting behavior thermodynamics at the substrate-polymer interface, while attractive contributions from individual dispersive and polar components significantly impacted through-film interactions and the maximum propagation distance of the interaction effects. The work detailed in this chapter provides an improved interpretation of the dominant substrate-polymer interactions affecting BP thin film self-assembly and facilitates an alternative method to screen chemically-modified substrates for desired orientation and ordering control using predictive equations with the appropriately decoupled surface energy components.

REFERENCES

1. Peters, R. D.; Yang, X. M.; Kim, T. K.; Sohn, B. H.; Nealey, P. F. *Langmuir* **2000**, *16*, 4625-4631.
2. Albert, J. N. L.; Baney, M. J.; Stafford, C. M.; Kelly, J. Y.; Epps, T. H., III. *ACS Nano* **2009**, *3*, 3977-3986.
3. Han, E.; Stuen, K. O.; Leolukman, M.; Liu, C.-C.; Nealey, P. F.; Gopalan, P. *Macromolecules* **2009**, *42*, 4896-4901.
4. Khanna, V.; Cochran, E. W.; Hexemer, A.; Stein, G. E.; Fredrickson, G. H.; Kramer, E. J.; Li, X.; Wang, J.; Hahn, S. F. *Macromolecules* **2006**, *39*, 9346-9356.
5. Luo, M.; Seppala, J. E.; Albert, J. N. L.; Lewis, R. L.; Mahadevapuram, N.; Stein, G. E.; Epps, T. H., III. *Macromolecules* **2013**, *46*, 1803-1811.
6. Khaira, G. S.; Qin, J.; Garner, G. P.; Xiong, S.; Wan, L.; Ruiz, R.; Jaeger, H. M.; Nealey, P. F.; de Pablo, J. J. *ACS Macro Lett.* **2014**, *3*, 747-752.
7. Kim, B. H.; Choi, Y.; Kim, J. Y.; Shin, H.; Kim, S.; Son, S.-W.; Kim, S. O.; Kim, P. *Adv. Mater.* **2014**, *26*, 4665-4670.
8. Xu, T.; Hawker, C. J.; Russell, T. P. *Macromolecules* **2005**, *38*, 2802-2805.
9. Ji, S.; Liu, C.-C.; Liao, W.; Fenske, A. L.; Craig, G. S. W.; Nealey, P. F. *Macromolecules* **2011**, *44*, 4291-4300.
10. Welander, A. M.; Craig, G. S. W.; Tada, Y.; Yoshida, H.; Nealey, P. F. *Macromolecules* **2013**, *46*, 3915-3921.
11. Nagpal, U.; Müller, M.; Nealey, P. F.; de Pablo, J. J. *ACS Macro Lett.* **2012**, *1*, 418-422.
12. Edwards, E. W.; Stoykovich, M. P.; Müller, M.; Solak, H. H.; de Pablo, J. J.; Nealey, P. F. *J. Polym. Sci., Part B: Polym. Phys.* **2005**, *43*, 3444-3459.

13. Bates, F. S.; Hillmyer, M. A.; Lodge, T. P.; Bates, C. M.; Delaney, K. T.; Fredrickson, G. H. *Science* **2012**, 336, 434-440.
14. Luo, M.; Epps, T. H., III. *Macromolecules* **2013**, 46, 7567-7579.
15. Segalman, R. A. *Mater. Sci. Eng., R* **2005**, 48, 191-226.
16. Mansky, P.; Russell, T. P.; Hawker, C. J.; Mays, J.; Cook, D. C.; Satija, S. K. *Phys. Rev. Lett.* **1997**, 79, 237-240.
17. Knoll, A.; Magerle, R.; Krausch, G. *J. Phys. Chem.* **2004**, 120, 1105-1116.
18. Kim, S.; Bates, C. M.; Thio, A.; Cushen, J. D.; Ellison, C. J.; Willson, C. G.; Bates, F. S. *ACS Nano* **2013**, 7, 9905-9919.
19. Smith, A. P.; Sehgal, A.; Douglas, J. F.; Karim, A.; Amis, E. J. *Macromol. Rapid Commun.* **2003**, 24, 131-135.
20. Peters, R. D.; Yang, X. M.; Nealey, P. F. *Macromolecules* **2002**, 35, 1822-1834.
21. Smith, A. P.; Douglas, J. F.; Meredith, J. C.; Amis, E. J.; Karim, A. *Phys. Rev. Lett.* **2001**, 87, 015503.
22. Coulon, G.; Collin, B.; Ausserre, D.; Chatenay, D.; Russell, T. P. *J. Phys. France* **1990**, 51, 2801-2811.
23. Fasolka, M. J.; Mayes, A. M. *Annu. Rev. Mater. Sci.* **2001**, 31, 323-355.
24. Albert, J. N. L.; Epps, T. H., III. *Mater. Today* **2010**, 13, 24-33.
25. Epps, T. H.; DeLongchamp, D. M.; Fasolka, M. J.; Fischer, D. A.; Jablonski, E. L. *Langmuir* **2007**, 23, 3355-3362.
26. Owens, D. K.; Wendt, R. C. *J. Appl. Polym. Sci.* **1969**, 13, 1741-1747.
27. Brandrup, J.; Immergut, E. H.; Grulke, E. A., *Polymer handbook*. 4th ed.; Wiley: New York ; Chichester, 2004.
28. Park, I.; Park, S.; Park, H.-W.; Chang, T.; Yang, H.; Ryu, C. Y. *Macromolecules* **2006**, 39, 315-318.
29. Stafford, C. M.; Roskov, K. E.; Epps, T. H., III; Fasolka, M. J. *Rev. Sci. Instrum.* **2006**, 77, 023908.

30. Kim, B. H.; Lee, H. M.; Lee, J.-H.; Son, S.-W.; Jeong, S.-J.; Lee, S.; Lee, D. I.; Kwak, S. U.; Jeong, H.; Shin, H.; Yoon, J.-B.; Lavrentovich, O. D.; Kim, S. O. *Adv. Funct. Mater.* **2009**, 19, 2584-2591.
31. Smith, A. P.; Douglas, J. F.; Meredith, J. C.; Amis, E. J.; Karim, A. J. *Polym. Sci., Part B: Polym. Phys.* **2001**, 39, 2141-2158.
32. Ham, S.; Shin, C.; Kim, E.; Ryu, D. Y.; Jeong, U.; Russell, T. P.; Hawker, C. J. *Macromolecules* **2008**, 41, 6431-6437.
33. Albert, J. N. L.; Kim, J. D.; Stafford, C. M.; Epps, T. H., III. *Rev. Sci. Instrum.* **2011**, 82, 065103.
34. Park, D.-H. *Nanotechnology* **2007**, 18, 355304.
35. Shelton, C. K.; Epps, T. H., III. *Macromolecules* **2015**, 48, 4572-4580.
36. Hiemenz, P. C.; Rajagopalan, R., *Principles of colloid and surface chemistry*. 3rd ed.; Marcel Dekker: New York, 1997.
37. Cai, X.-J.; Genzer, J.; Spontak, R. J. *Langmuir* **2014**, 30, 11689-11695.
38. Oron, A.; Davis, S. H.; Bankoff, S. G. *Reviews of Modern Physics* **1997**, 69, 931-980.
39. Brochardwyart, F.; Dimeglio, J. M.; Quere, D.; Degennes, P. G. *Langmuir* **1991**, 7, 335-338.
40. Bucknall, D. G. *Prog. Mater. Sci.* **2004**, 49, 713-786.
41. Chaudhury, M. K. *Mater. Sci. Eng., R* **1996**, 16, 97-159.
42. Sferrazza, M.; Heppenstall-Butler, M.; Cubitt, R.; Bucknall, D.; Webster, J.; Jones, R. A. L. *Phys. Rev. Lett.* **1998**, 81, 5173-5176.
43. Reiter, G. *Langmuir* **1993**, 9, 1344-1351.
44. Fowkes, F. M. *Ind. Eng. Chem.* **1964**, 56, 40-52.
45. Girifalco, L. A.; Good, R. J. *J. Phys. Chem.* **1957**, 61, 904-909.
46. Grim, P. C. M.; Nyrkova, I. A.; Semenov, A. N.; ten Brinke, G.; Hadziioannou, G. *Macromolecules* **1995**, 28, 7501-7513.

47. Heier, J.; Kramer, E. J.; Groenewold, J.; Fredrickson, G. H. *Macromolecules* **2000**, 33, 6060-6067.
48. Green, P. F.; Limary, R. *Adv. Colloid Interface Sci.* **2001**, 94, 53-81.
49. Russell, T. P.; Coulon, G.; Deline, V. R.; Miller, D. C. *Macromolecules* **1989**, 22, 4600-4606.
50. Shin, C.; Ahn, H.; Kim, E.; Ryu, D. Y.; Huh, J.; Kim, K.-W.; Russell, T. P. *Macromolecules* **2008**, 41, 9140-9145.
51. Zhang, X. H.; Berry, B. C.; Yager, K. G.; Kim, S.; Jones, R. L.; Satija, S.; Pickel, D. L.; Douglas, J. F.; Karim, A. *Acs Nano* **2008**, 2, 2331-2341.
52. Rockford, L.; Mochrie, S. G. J.; Russell, T. P. *Macromolecules* **2001**, 34, 1487-1492.
53. Huang, E.; Russell, T. P.; Harrison, C.; Chaikin, P. M.; Register, R. A.; Hawker, C. J.; Mays, J. *Macromolecules* **1998**, 31, 7641-7650.
54. Shelton, C. K.; Epps, T. H., III. *Macromolecules* **2016**, 49, 574-580.
55. Bai, W.; Hannon, A. F.; Gotrik, K. W.; Choi, H. K.; Aissou, K.; Lontos, G.; Ntetsikas, K.; Alexander-Katz, A.; Avgeropoulos, A.; Ross, C. A. *Macromolecules* **2014**, 47, 6000-6008.

Chapter 4

***IN SITU* NEUTRON SCATTERING DURING SOLVENT VAPOR ANNEALING OF CYLINDRICAL BLOCK POLYMER THIN FILMS**

The use of *in situ* small-angle neutron scattering (SANS) and neutron reflectometry (NR) to elucidate the importance of polymer-solvent interactions on morphology development during solvent vapor annealing (SVA) of block polymer (BP) thin films is detailed in this chapter. Judicious choice of nanostructure orientation (parallel to the substrate) permitted measurement of the preferential segregation of deuterated solvent (*d*-benzene, *d*-acetone, *d*-hexane) into cylinder-forming poly(styrene-*b*-isoprene-*b*-styrene) (SIS) films. A defining feature of the work in this chapter is the simultaneous tracking of nanostructure evolution and solvent segregation, enabled through the combination of SANS (in-plane features), NR (out-of-plane features), and solvent deuteration, which directly related polymer-solvent interactions to morphology reorganization. By linking polymer-solvent interactions to morphology evolution, an improved understanding of the interplay between the kinetic and thermodynamic effects that can direct the self-assembly and through-film periodicity of nanostructured thin films is developed in this chapter. Text and figures are reproduced or adapted with permission from Shelton, C. K., Jones, R. L., Dura, J. A., and Epps, T. H., III *Macromolecules* **2016**, 49, 7525-7534.

4.1 Introduction

Traditionally, SVA has been used as an alternative to thermal annealing for BP systems that are susceptible to thermal transitions and degradation or require infeasible

thermal annealing time scales.¹ However, SVA has several additional benefits that are discussed in Chapter 1, Section 1.4.2. A key underlying factor responsible for these effects is the solvent preference toward each polymer block. Therefore, a comprehensive study that elucidates how selective solvent segregation into individual polymer domains affects thin film self-assembly parameters is essential. This need for additional information is highlighted in a recent perspective that discusses the utility of more refined *in situ* annealing experiments for “detailed investigation of the BP films in both swollen and dried state” to develop a holistic understanding of polymer-solvent interactions and the resulting nanostructure “changes that occur in the equilibrium solvent swollen state and the changes during solvent removal and deswelling.”¹

A prevalent technique for *in situ* thin film/SVA studies is grazing-incidence small-angle X-ray scattering (GISAXS) to generate both lateral and through-film structural information in a single experiment.¹ Using GISAXS during SVA, researchers have studied how BP thin films restructure over time,²⁻⁹ change morphology as a function of solvent composition,^{4, 10-12} and increase/decrease in-plane (L_0) and out-of-plane (L_z) domain spacing.^{9, 11, 13, 14} Notably, these studies all focused on the ultimate effects of SVA rather than the underlying causes, *i.e.* solvent segregation and interactions with the polymer blocks. With GISAXS, scattering contrast is achieved from electron density differences between the two blocks.¹⁵ As a result, the scattering patterns detail how the polymer domains restructure during SVA rather than how the polymer-solvent interactions govern the restructuring. Additionally, recent studies have detailed evidence that X-ray beams can damage polymer films or influence structural evolution inadvertently, which can greatly affect

the resulting analysis.¹⁶⁻¹⁸ Thus, approaches that can directly and noninvasively probe changes in polymer-solvent interactions are necessary for a comprehensive understanding of SVA.

As an alternative or complement to X-ray scattering, neutron scattering offers many benefits ideally suited for studying solvent segregation and polymer-solvent interactions in BP thin films.¹⁹ In neutron scattering, contrast is achieved through differences in scattering length density (ρ), a parameter that can be modified by selectively deuterating chemical components.^{20, 21} Thus, contrast between polymer and solvent can be adjusted to track solvent diffusion and segregation into individual polymer blocks throughout the film. Although neutron scattering traditionally requires significantly longer data collection timescales than X-ray scattering,^{19, 22, 23} recent literature has demonstrated the utility of neutron scattering for the *in situ* analysis of interactions not easily measured with X-rays.²⁴⁻²⁹ For example, Kim *et al.* examined the effect of D₂O concentration on the morphology of poly(sulfonated styrene-*b*-methylbutylene) (PSS-PMB) BPs using *in situ* SANS.²⁴ They tracked the D₂O distribution in the individual domains and measured a high water content in the typically hydrophobic PSS block that possibly explained the improved proton transfer noted in PSS-PMB polymer electrolyte membranes.²⁴ Other studies have used *in situ* NR to measure substrate-to-free surface D₂O distributions in BP thin films, both throughout the film and within individual polymer domains, to relate those distributions to structural effects^{25, 27, 30} and to detect the emergence of lamellar phase segregation at interfaces between hydrophilic substrates and Nafion upon changing relative humidity.^{28, 29} However, in these systems hydrophobic/hydrophilic interactions were the dominant force directing domain restructuring; similar studies of

BPs focusing on domain restructuring as a function of Flory-Huggins polymer-solvent interactions ($\chi_{poly-sol}$) have not been reported in literature.

In this chapter, *in situ* neutron scattering was used to quantify the segregation of *d*-benzene into the polystyrene (PS) and polyisoprene (PI) domains of cylinder-forming SIS BP thin films as a function of atmospheric solvent concentration (solvent partial pressure). SANS (in-plane features) and NR (out-of-plane features) paired with solvent deuteration, as well as natural ρ differences between PS and PI domains, provided both polymer-polymer and polymer-solvent contrast. The enhanced polymer-solvent contrast permitted measurement of the solvent profiles through the film thickness, and these profiles could be related to measured changes in film thickness, lateral L_0 , vertical L_z , and number of stacked domains. Furthermore, *d*-acetone and *d*-hexane were tested to determine how highly selective solvents affect the same set of parameters. To improve contrast between PS and PI when swollen with *d*-hexane, which reduces contrast between the domains, a poly(deuterated styrene-*b*-isoprene-*b*-deuterated styrene) (*d*SI*d*S) BP was leveraged. The resulting analysis demonstrated how polymer-solvent interactions affect nanostructure reorganization and contributed a mechanistic understanding of the underlying factors that drive self-assembly during SVA.

4.2 Materials and Methods

4.2.1 Preparation and Characterization of Thin Films

The SIS triblock copolymer ($M_n = 118$ kg/mol; $\mathfrak{D} = 1.09$; block volume fractions: $f_S = 0.134$, $f_I = 0.732$, $f_S = 0.134$; cylindrical nanostructure) was obtained from DEXCO (V4211) and used as received. The *d*SI*d*S triblock copolymer ($M_n =$

160 kg/mol; $\bar{D} = 1.07$; block volume fractions: $f_S = 0.10$, $f_I = 0.78$, $f_S = 0.12$; cylindrical nanostructure) was synthesized (courtesy of Maëva Tureau) *via* sequential anionic polymerization of perdeuterated styrene (Acros, stabilized, 98+ atom% D) and isoprene (Acros, 98% stabilized) as described in the literature.³¹ Both polymers were characterized by size exclusion chromatography (Viscotek, GPCmax WE-2001), nuclear magnetic resonance spectroscopy (Bruker, AVX400), small-angle X-ray scattering, and atomic force microscopy (AFM).

SIS or *d*SI*d*S films were cast onto cleaned silicon wafers from 2.1 wt% and 3.1 wt% polymer in tetrahydrofuran (Optima) solutions by flow coating to produce 200 ± 2 nm and 400 ± 4 nm thickness films, respectively.³² As-cast film thickness was measured using a spectral reflectometer (Filmetrics, F20-UV) every 5 mm along the length of the film (total of 13 measurements across a 70 mm film). The free surface morphologies of as-cast and solvent annealed films were examined by tapping mode AFM (Veeco Dimension 3100) with silicon probes (Tap 150G, BudgetSensors).

4.2.2 Solvent Vapor Annealing

Thin films were annealed with *d*-benzene (99.6 atom% D, Sigma Aldrich), *d*-acetone (99.9 atom%, Sigma Aldrich), or *d*-hexane (99 atom%, Sigma Aldrich) vapor by bubbling nitrogen gas through a solvent reservoir (≈ 15 -20 mL) and directing the solvent-rich vapor stream into and out of the sample chamber. A pure nitrogen stream was mixed with the solvent-rich stream to manipulate the solvent concentration in the sample chamber. The solvent vapor and nitrogen were combined several feet before reaching the inlet port of the chamber to ensure the inlet flow was well-mixed prior to entering the chamber. The nitrogen flow rate in each stream was controlled with mass flow controllers (MKS Instruments Type 146C Cluster Gauge) with 0-10

mL/min set points. Using the two streams, nitrogen volumetric flow rate ratios (solvent-rich:diluent [mL/min:mL/min]) of 0:0 (as-cast), 10:0, 8:2, 6:4, 4:6, and 0:10 (redried) were used to anneal the films. For *d*-benzene, these flow rate ratios corresponded to p/p_{sat} values of 0, 0.93, 0.84, 0.59, 0.43, and 0; *d*-hexane and *d*-acetone partial pressures were not measured. Optical microscopy images (Nikon Eclipse LV100 equipped with a 5 MP CCD camera) of the SIS films after *in situ* experiments were captured to ensure the long solvent exposure times did not promote film dewetting that would affect SANS and NR profiles and alter the results (see Appendix B, Figure B.1).

The partial pressure of *d*-benzene at each ratio was measured using mass spectrometry (Hiden Analytical). To ensure that the *ex situ* mass spectrometry results matched those from the *in situ* scattering experiments, the same solvent bubbler, sample chamber (with film), and vapor flow lines were connected. Then, the partial pressure of solvent was measured at the sample chamber outlet to account for any possible changes in solvent composition due to film swelling. For each partial pressure, mass spectrometry signals for nitrogen ($m/z = 28$ amu), *d*-benzene ($m/z = 84$ amu), oxygen ($m/z = 32$ amu), and water ($m/z = 18$ amu) were measured over time until steady-state was reached (≈ 30 min.). Then, a more detailed scan from $m/z = 0.4$ to 90 was recorded and used to calculate p/p_{sat} *d*-benzene concentrations on the basis of literature fragmentation patterns.³³ The profiles recorded *via* mass spectrometry are shown in Appendix B, Figure B.2.

4.2.3 *In Situ* Small-Angle Neutron Scattering

To conduct *in situ* SANS/SVA experiments, a specially designed flow chamber was used to house two 400 ± 4 nm thick polymer films, which increased scattering

volumes and provided paths for solvent inlet and outlet as shown in Appendix B, Figure B.3. The neutron beam was directed through silica windows, and the chamber was held at 25 °C using continuous circulating water baths. Within the chamber, spacers were used to ensure films were exposed to a sufficient volume of *d*-benzene vapor. Two controlled flows of nitrogen were used to regulate the *d*-benzene concentration exposed to the film. One nitrogen stream passed through the *d*-benzene bubbler to carry solvent to the sample chamber, and the other stream passed directly into the sample chamber to dilute the concentration of *d*-benzene. Using this approach, equivalent *d*-benzene partial pressure to saturated vapor pressure ratios (p/p_{sat}) of 0, 0.93, 0.84, 0.59, and 0.43 were used to anneal the films. (Ratios determined from mass spectrometry measurements, see Appendix B, Figure B.2.)

SANS experiments were conducted using the NGB 10 m SANS instrument at the National Institute of Standards and Technology (NIST) Center for Neutron Research (NCNR). Neutrons with an incident wavelength (λ) of 5.0 Å and a wavelength divergence ($\Delta\lambda/\lambda$) of 0.15 were utilized for all runs in a 12.7 mm diameter incident beam. For each p/p_{sat} , neutron detector counts were measured at a 5.2 m sample to detector distance, with a 25 mm beamstop, and 120 min collection time. This configuration covered a Q range of $0.005 \text{ \AA}^{-1} \leq Q \leq 0.112 \text{ \AA}^{-1}$. To ensure the sample chamber *d*-benzene concentration and film thickness were at equilibrium, a shorter collection time (30 min) was used initially to determine if the azimuthally averaged scattering intensity profile remained unchanged over ≈ 1 h. Resulting SANS scattering data were reduced using Igor Pro (WaveMetrics) software with NCNR SANS reduction macros and plotted as azimuthally averaged intensity profiles.³⁴ The

azimuthally averaged intensity profiles were fit to a broad peak model and analyzed using SASView software.

4.2.4 *In Situ* Neutron Reflectometry

In situ NR experiments were conducted to measure the z-distribution (substrate-to-free surface) of solvent (*d*-benzene, *d*-acetone, or *d*-hexane) in SIS films at different values of p/p_{sat} . The NR setup included a sample chamber housing a single polymer film (200 ± 2 nm thick), held in a reflectivity geometry with the neutron beam, and a solvent vapor inlet and outlet port as shown in Appendix B, Figure B.4 (full schematics shown in Appendix B, Figures B.5 to B.12). The chamber was made of aluminum to remain transparent to neutrons in reflectivity geometries. Additionally, borated aluminum shields were added around the neutron beam inlet and outlet to prevent scattering from sample cell hardware (*e.g.*, screws). Nitrogen gas and solvent vapor were flowed through the chamber using the same solvent bubbler set-up as the SANS experiment at the same nitrogen volumetric flow rate ratios (solvent-rich:diluent [mL/min:mL/min]) of 0:0 (as-cast), 10:0, 8:2, 6:4, and 4:6; these ratios corresponded to *d*-benzene p/p_{sat} values of 0, 0.93, 0.84, 0.59, and 0.43, respectively (*d*-acetone and *d*-hexane p/p_{sat} values were not measured). After SVA, the samples were redried with pure nitrogen gas for an additional run to compare with the as-cast film for ‘before’ and ‘after’ snapshots of the change in polymer domain restructuring.

NR experiments were conducted using the multi-angle grazing-incidence k-vector (MAGIK) instrument at the NCNR. Neutrons with an incident wavelength of 5 Å were directed at a 64 mm long, 25 mm wide wafer with an 200 ± 2 nm thick SIS film within the *in situ* SVA chamber and held at 25 °C using continuous circulating water baths. At each p/p_{sat} , shorter Q_z range scans ($0 \text{ \AA}^{-1} \leq Q_z \leq 0.0439 \text{ \AA}^{-1}$) with a

step size of 0.0004 \AA^{-1} were recorded continuously until 2-3 consecutive profiles were identical within the measurements uncertainty. After equilibration, larger Q_z range scans ($0 \text{ \AA}^{-1} \leq Q_z \leq 0.1315 \text{ \AA}^{-1}$) with a step size of 0.0004 \AA^{-1} were recorded. Resulting reflectometry profiles were reduced using reflred software, and the reduced profiles were analyzed with reflfit and refl1D software programs incorporating multilayer models.³⁵

4.3 Results and Discussion

4.3.1 Neutral/Slightly Selective Solvents

SIS films on silica substrates were annealed with *d*-benzene vapor during neutron scattering to explore solvent diffusion, solvent segregation, and polymer-solvent interactions. The choice of polymer and solvent was ideal for this study for multiple reasons: at 25 °C, (1) the individual blocks in the SIS BP have different solubility parameters ($\delta_{PS} = 18.6 \text{ MPa}^{1/2}$ and $\delta_{PI} = 16.4 \text{ MPa}^{1/2}$),³⁶ with $\delta_{d\text{-benzene}} \approx 18.8 \text{ MPa}^{1/2}$,³⁶ imparting measurable differences in polymer-solvent interactions, (2) PS and PI have natural ρ differences ($\rho_{PS} = 1.41 \times 10^{-6} \text{ \AA}^{-2}$ and $\rho_{PI} = 0.273 \times 10^{-6} \text{ \AA}^{-2}$)³⁷ providing polymer-polymer contrast, (3) *d*-benzene has a significantly higher ρ than PS or PI ($\rho_{d\text{-benzene}} = 5.43 \times 10^{-6} \text{ \AA}^{-2}$)³⁷ offering polymer-solvent contrast, and (4) parallel cylinder morphologies have both in-plane and out-of-plane features that can be tracked using SANS and NR analysis, respectively.

4.3.1.1 Solvent Diffusion and Segregation

SANS scattering data from *in situ* SVA of SIS with *d*-benzene at each p/p_{sat} were azimuthally averaged to generate the intensity patterns shown in Figure 4.1. Two distinct characteristics were noted in the azimuthally averaged patterns. First, a

large intensity peak was measured at $Q^* \approx 0.020 \text{ \AA}^{-1}$ for all solvent conditions, corresponding to a 31 nm distance between (10) planes, d ($d = 2\pi/Q^*$). On the basis of the nanostructure geometry (parallel-oriented hexagonally-packed cylinders), this distance indicated a nearest-neighbor spacing $L_0 = 36 \text{ nm}$. The invariance of the peak position with p/p_{sat} suggested the lateral L_0 did not change significantly with solvent concentration, a result consistently reported in literature for slightly preferential or neutral solvents.^{4, 13, 14} Second, the scattering intensity of the Q^* peak increased with p/p_{sat} . From the ρ values for PS, PI, and *d*-benzene, the increase in intensity indicated the solvent partitioned preferentially into the PS domains of the film; the *d*-benzene mixed with the PS increased the contrast ($[\Delta\rho]^2$) relative to *d*-benzene mixed with PI ($[\Delta\rho]^2 = [\rho_{PS/d\text{-benzene}} - \rho_{PI/d\text{-benzene}}]^2$). Literature data are consistent with the solvent preference determined herein, as the *d*-benzene solubility parameter ($\delta_{d\text{-benzene}} \approx 18.8 \text{ MPa}^{1/2}$)³⁶ and literature $\chi_{poly-sol}$ values ($[\chi_{PS\text{-benzene}} = 0.37]$ ³⁸ and $[\chi_{PI\text{-benzene}} = 0.44]$ ³⁹) indicate that *d*-benzene is considered slightly preferential for PS over PI.⁴⁰

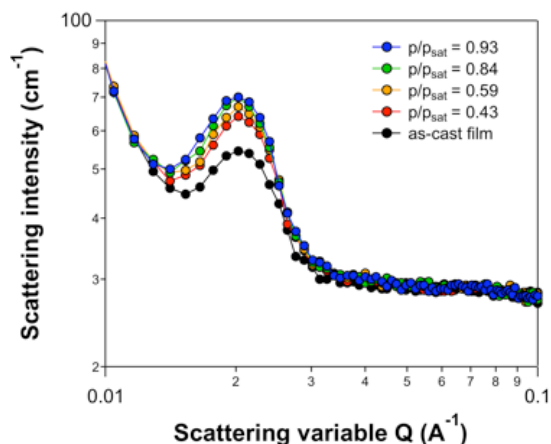


Figure 4.1: Plot of azimuthally averaged SANS intensity profiles from SIS films exposed to different partial pressures (p/p_{sat}) of *d*-benzene. The Bragg peak at $Q^* \approx 0.020 \text{ \AA}^{-1}$ corresponded to a nearest-neighbor $L_0 = 36 \text{ nm}$ that did not change with p/p_{sat} . Reprinted with permission from Shelton, C. K. *et al. Macromolecules* **2016**, 49, 7525-7534, Copyright 2016 American Chemical Society.⁴¹

SANS scattering data were fit to broad peak models in SasView to determine the degree of solvent partitioning into PS domains as a function of p/p_{sat} . The broad peak model (Equation 4.1) is ideal for modeling amorphous soft materials with scattering inhomogeneities such as cylindrical domains and profiles with only one Bragg peak over the measured Q range.⁴²⁻⁴⁴

$$I(Q) = \frac{C}{1 + (|Q - Q^*| \zeta)^m} + B \quad (4.1)$$

Within the broad peak model, B , ζ , and m remain relatively constant with solvent concentration; B accounts for the background signal, ζ represents the approximate correlation length of the domains (relatively unchanged according to pre- and post-SVA AFM images, see Appendix B, Figure B.1), and m is a scaling exponent. However, C is a scaling factor directly related to the height of the Q^* peak

and can be used to quantify the solvent segregation into PS and PI domains. The fit parameter values from the model are summarized in Table 1, and plots of the broad peak model fits are shown in Appendix B, Figure B.13. By using the known $(\Delta\rho)^2$ between solvent-free PS and PI, the fit C value for the as-cast film, and the assumption that $(\Delta\rho)^2 = 0$ would result in a C of zero, a linear relationship between $(\Delta\rho)^2$ and C was generated. This relationship was used to extrapolate $(\Delta\rho)^2$ between PS and PI domains in swollen films and to calculate the partitioning of solvent in each domain as a function of p/p_{sat} . The models, calculations, and assumptions used in this analysis are described in more detail in the Appendix B, Section B.1.

Table 4.1: Broad peak model fit parameters for SIS thin films swollen with *d*-benzene

p/p_{sat}	Q^* (\AA^{-1})	B (cm^{-1})	ζ (\AA)	m	C
0.93	0.0201 ± 0.0001	29.3 ± 0.1	216 ± 4	2.9 ± 0.1	40.4 ± 0.6
0.84	0.0203 ± 0.0001	29.2 ± 0.1	221 ± 4	2.9 ± 0.1	39.1 ± 0.6
0.59	0.0205 ± 0.0001	29.4 ± 0.1	216 ± 4	3.0 ± 0.1	35.9 ± 0.6
0.43	0.0205 ± 0.0001	29.3 ± 0.1	219 ± 5	3.0 ± 0.1	33.5 ± 0.6
0 (as-cast)	0.0204 ± 0.0001	28.9 ± 0.1	207 ± 5	3.1 ± 0.1	24.9 ± 0.5

From the measured SANS profiles, the total segregation of solvent (moles of solvent in each domain divided by the total moles of solvent in the film) into the PS (41 mol%) and PI (59 mol%) domains was calculated within ± 1 mol% for all p/p_{sat} , which supported the robustness of this approach for determining the solvent segregation in the film. The larger percentage of the solvent in the PI domain was due to PI representing the majority component in the SIS film ($f_{PI} = 0.732$). However, the normalized or relative concentration of solvent in each polymer domain (moles of

solvent in each domain divided by total moles of solvent and polymer in that domain, moles polymer obtained from neat volume fractions of BP) was calculated as a function of p/p_{sat} as shown in Figure 4.2. The higher concentration of *d*-benzene in PS domains in all cases quantitatively indicates that the *d*-benzene was preferential to the PS domains, also in agreement with literature.⁴⁵

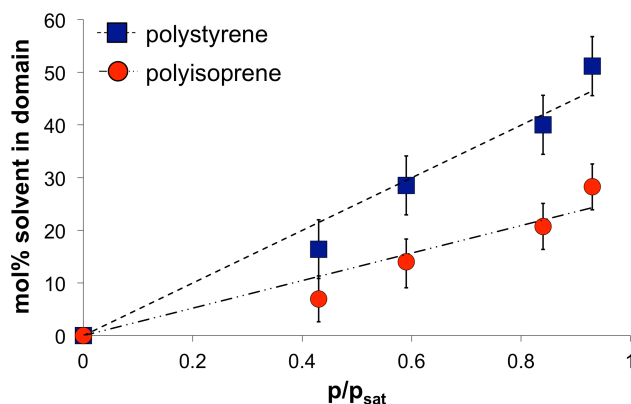


Figure 4.2: Solvent content in PS and PI domains calculated from broad peak model fits to azimuthally averaged SANS intensity profiles indicated that the normalized *d*-benzene mol% (moles *d*-benzene in PS [or PI] divided by moles *d*-benzene plus PS [or PI]) was always higher in the PS domains compared to the PI domains (*i.e.*, the solvent was PS-preferential). Additionally, the ratio of solvent to polymer within a particular domain increased with p/p_{sat} . Error bars were calculated by propagating differences of ± 5 vol% total solvent in the film through the calculations. Reprinted with permission from Shelton, C. K. *et al. Macromolecules* **2016**, 49, 7525-7534, Copyright 2016 American Chemical Society.⁴¹

$\chi_{poly-sol}$ was calculated from the SANS, using Equation 4.2,⁴⁶

$$\ln\left(\frac{P}{P_{sat}}\right) = \chi_{poly-sol} \phi_{poly}^2 + \ln(1 - \phi_{poly}) + \left(1 - \frac{V_{sol}}{V_{poly}}\right) \phi_{poly} \quad (4.2)$$

In Equation 4.2, ϕ_{poly} is the volume fraction of polymer in the film, and V_{sol} and V_{poly} are the molar volume of the solvent and polymer, respectively. From Equation 4.2, a $\chi_{poly-sol}$ of 0.49 ± 0.14 was measured for PS and *d*-benzene, and a $\chi_{poly-sol}$ of 0.86 ± 0.25 was measured for PI and *d*-benzene. Although the $\chi_{poly-sol}$ values are higher than those reported in literature for PS (0.37) and PI (0.44) with benzene,^{38, 39} the thin film geometry, covalent bonds between PS and PI, and polymer-polymer interactions between the individual blocks likely limited the polymer chains' ability to stretch, resulting in less solvent uptake in comparison to homopolymer analogues.⁴⁷ Therefore, the more constrained middle block in the ABA block polymer (PI in SIS) was expected to swell less than the end blocks (PS in SIS) in relation to their homopolymer constituents, which is indicated in these results; the $\chi_{poly-sol}$ value for PS is similar to the literature value within error, but the $\chi_{poly-sol}$ value for PI is higher than values reported in literature. Also, isotopic differences between benzene and *d*-benzene could possibly impact the Flory-Huggins interaction parameter.⁴⁸⁻⁵⁰ Thus, polymer-solvent contrast introduced by neutron scattering experiments helped glean the importance of these additional thin film parameters on swelling.

4.3.1.2 Nanostructure Reorganization Effects

NR profiles from SIS films during SVA at different equilibrated *d*-benzene concentrations are shown in Figure 4.3 (temporal NR profiles during swelling and deswelling are shown in Appendix B, Figures B.14 to B.18). A visual analysis of the scattering patterns revealed three main features. First, the decrease in distance between subsequent Kiessig fringes with increasing p/p_{sat} indicated the film was getting thicker as the solvent partial pressure increased. Second, a distinct Bragg peak appeared after annealing the SIS film with *d*-benzene. The Bragg peak was not

present in the as-cast profile, which indicated the development of a domain structure that had a periodic composition modulation perpendicular to the substrate (parallel cylinder layers) as a result of solvent exposure. Finally, the Bragg peak position (Q_z^*) decreased going from the first ($p/p_{sat} = 0.93$) to second ($p/p_{sat} = 0.84$) solvent concentration and increased thereafter. This characteristic signified a change in the vertical L_z brought about by solvent swelling/deswelling and polymer domain reorganization.

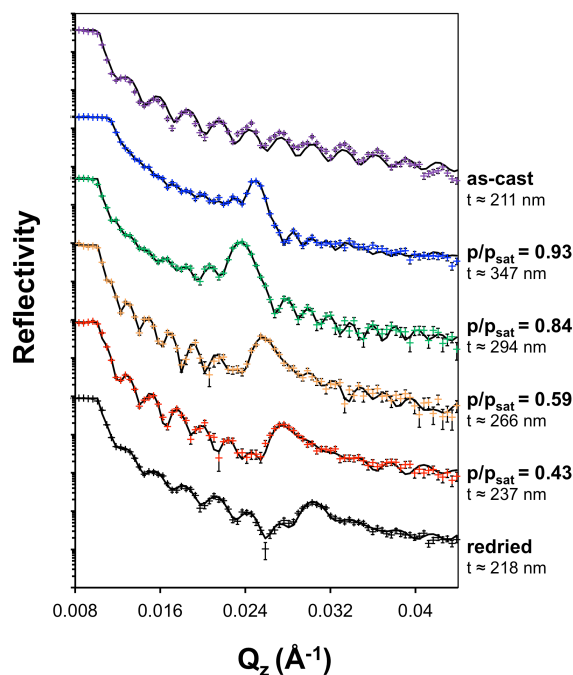


Figure 4.3: NR profiles (data points) and model fits (black lines) for *d*-benzene swollen SIS films at different p/p_{sat} in the order that they were run from top to bottom. Upon exposure to solvent vapor, the film increased in thickness (t) due to solvent swelling and developed repeating parallel cylinder layers as evidenced by the narrowing of Kiessig fringes and the formation of a Bragg peak, respectively. In general, L_z decreased with the value of p/p_{sat} . However, L_z increased slightly from $p/p_{sat} = 0.93$ to $p/p_{sat} = 0.84$. The NR profiles have been vertically offset for clarity. Reprinted with permission from Shelton, C. K. *et al. Macromolecules* **2016**, 49, 7525-7534, Copyright 2016 American Chemical Society.⁴¹

Although literature typically reports a decrease in L_z with reducing solvent partial pressure,^{51, 52} the Q_z shift of the Bragg peak in Figure 4.3 indicated an initial increase in L_z from 27 nm to 29 nm as partial pressure changed from $p/p_{sat} = 0.93$ to $p/p_{sat} = 0.84$, followed by decreases in L_z thereafter. Similar L_z increases in literature have been suggested for cylindrical systems and were attributed to the coalescence of cylindrical layers as solvent concentration in the film decreased.^{13, 53} In the highly

swollen films, enough solvent is present to impart polymer chain mobility, such that the decreases in swollen film thickness (*i.e.*, going from $p/p_{sat} = 0.93$ to $p/p_{sat} = 0.84$) allows changes in the number of layers rather than only the thickness of each layer. As the film thickness decreased with solvent content, this process permitted the nanostructures to maintain an energetically favorable L_z as determined by the interplay of polymer-polymer interactions and polymer chain lengths.

The full mechanism describing the increase/decrease in the number of layers (n) and the L_z is detailed in Figure 4.4. For solvent concentrations of $p/p_{sat} = 0.93$ and $p/p_{sat} = 0.84$, the *d*-benzene concentration in the glassy PS domain (x_{PS-sol}) was 51 mol% and 40 mol% according to SANS results (Figure 4.2). Both concentrations of *d*-benzene were sufficient to lower the T_g of PS below 25 °C and impart chain mobility according to literature.^{54, 55} Therefore, the polymer chains had enough mobility to decrease n and maintain a favorable L_z (approximately 27-29 nm as measured by Luo *et al.*)⁵⁶ at a reduced film thickness. *Note: The minor incommensurability between the number of layers ($n = 12$) and the film thickness ($t = 347$ nm) at $p/p_{sat} = 0.93$ resulted from roughened domain and free-surface interfaces, as indicated by the lower amplitude Kiessig fringes in Figure 4.3, in the highly swollen film (see Appendix B, Section B.2 for further details).*⁵⁷ At the new $n = 10$ (for $p/p_{sat} = 0.84$), the layers were stretched slightly from 27 nm to 29 nm to achieve commensurability between the film thickness and L_z and to account for the slight increase in χ_{PS-PI} when the solvent concentration in the film was reduced.^{57, 58} Additionally, for hexagonally-packed cylinder morphologies, the in-plane and out-of-plane periodicity is expected to change by a factor of approximately $\sqrt{3}/2$ ($L_z \approx 0.87L_0$). The large decrease in the measured L_z , (from NR) compared to the measured

L_0 (from SANS) was likely the result of this effect and incommensurability between the swollen film thickness and equilibrium L_z .

For subsequent deswelling ($p/p_{sat} = 0.59$ [$x_{PS-sol} = 28$ mol%], $p/p_{sat} = 0.43$ [$x_{PS-sol} = 16$ mol%], and $p/p_{sat} = 0$ [redried film]) the L_z decreased in proportion to overall film thickness because there was not enough solvent present in the film to promote layer restructuring as the film thickness decreased (the minimum solvent concentration required to reduce the T_g of PS below 25 °C is approximately 25-30 mol%).^{54, 55} Although, the x_{PS-sol} from the $p/p_{sat} = 0.59$ run falls in this range, it is likely there was not a sufficient reduction in glassy behavior or polymer-polymer segregation ($\chi_{poly-poly}$) to promote a further decrease in n .^{57, 58} Thus, these results demonstrate how solvent conditions above or below the critical p/p_{sat} value change the interplay between thermodynamic and kinetic effects, which can have significant implications for the morphological development (*i.e.*, domain size, degree of ordering, and interfacial roughness) of nanostructured films.

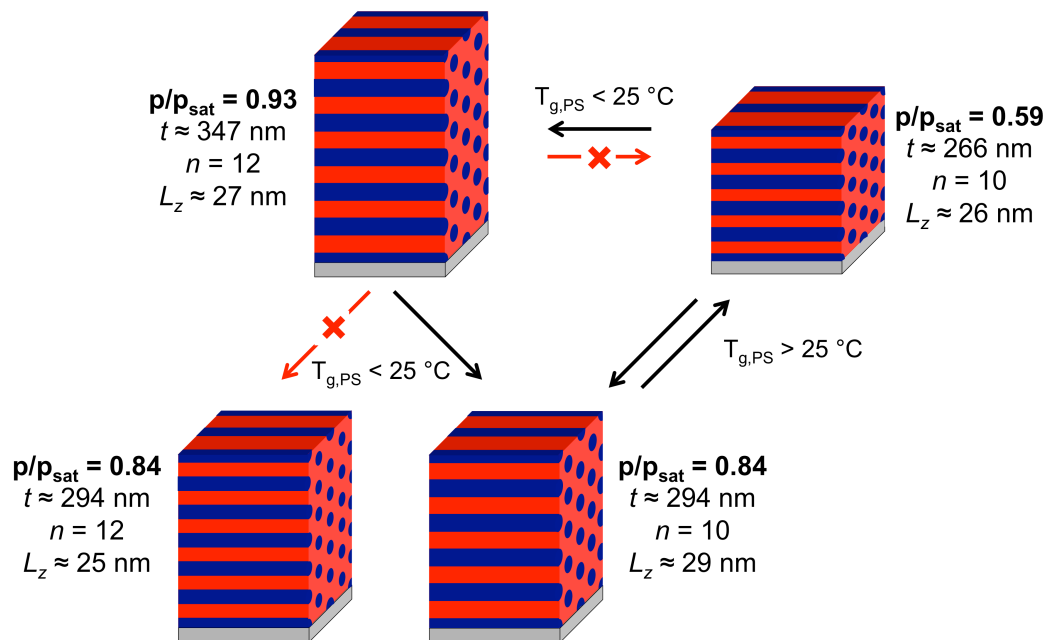


Figure 4.4: Schematic detailing the process by which SIS nanostructures restructured during SVA. SVA promoted layering of parallel cylinders by swelling the film to impart chain mobility *via* reduction of the T_g of the glassy PS domains below the annealing temperature (25 °C). To account for the film thickness (t) reduction during solvent removal from $p/p_{sat} = 0.93$ to $p/p_{sat} = 0.84$, n decreased, rather than L_z , to prevent unfavorable compression of the polymer chains. However, commensurability conditions from mismatches in t and n and an increased χ_{PS-PI} led to slightly stretched layers ($L_z = 27$ to $L_z = 29$). When there was not enough solvent in the film to lower the PS T_g below 25 °C ($p/p_{sat} \leq 0.59$), n could no longer adjust to account for thickness changes; instead, the average L_z decreased with the value of p/p_{sat} to account for the change in t . The error in t was recorded as ± 10 nm to account for roughness at the free surface that limited the accuracy of film thickness measurements. Although the SANS and NR profiles suggest the in-plane and out-of-plane structure is not perfectly-ordered, the schematic depicts uniform parallel cylinder morphology for clarity in describing the mechanisms for domain restructuring. Reprinted with permission from Shelton, C. K. *et al. Macromolecules* **2016**, 49, 7525-7534, Copyright 2016 American Chemical Society.⁴¹

4.3.1.3 Substrate to Free Surface Solvent Profiles

NR profiles were fit to multilayer models using reflfit and refl1D software.³⁵ (Fits are shown in Figure 4.3 and Appendix B, Figure B.19) The model schematic and model fit to the $p/p_{sat} = 0.93$ NR data are illustrated in Figure 4.5. The model incorporated a series of $n-1$ repeating layers with the polymer contents consisting of cylindrical PS nanostructures in PI matrix and pure PI (between cylindrical layers). The final layer (n) was composed of half-cylinder wetting layers at both the substrate and the free surface, as the end block PS was preferential for both the silicon oxide (SiO_2) at the substrate surface and the solvent-rich atmosphere at the free surface. The presence of half-cylinders at the substrate and free surface was assumed on the basis of previous work that measured half-cylinder wetting layers in SIS at each interface after SVA and thermal annealing.^{31,56} Each layer was modeled individually to account for changes in ρ and layer thickness through the film. The ρ profile in Figure 4.5 indicated an oscillatory behavior through the film resulting from pure PI layers that had a lower ρ than PS/PI layers ($\rho_{\text{PS/PI}} > \rho_{\text{PI}}$). Additionally, the fits mirrored the proposed mechanism from Figure 4.4 as n decreased from 12 to 10 for $p/p_{sat} = 0.93$ to $p/p_{sat} = 0.84$ and remained constant at 10 for any further reduction in solvent content (*i.e.*, additional deswelling). As further evidence of a change in n during removal of solvent, a comparison of fits for $p/p_{sat} = 0.84$ data using multilayer models with $n = 10$ and $n = 12$ is shown in Appendix B, Figure B.20. Although the $n = 12$ model produces the same film thickness as the $n = 10$ model, the Bragg peak location (related to L_z) and number/location of Kiessig fringes before the Bragg peak (related to n) do not match the measured NR profile for $n = 12$. These differences result in a significantly higher χ^2 for the $n = 12$ model ($\chi^2 = 442$) in comparison to the

$n = 10$ ($\chi^2 = 1.47$) model and further supports the conclusion that n decreased upon deswelling.

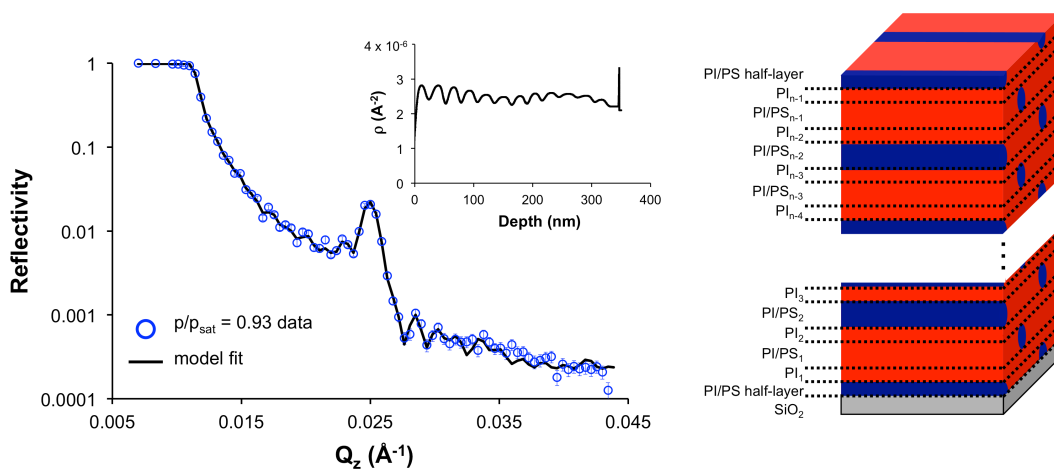


Figure 4.5: NR data (open blue circles) and multilayer model fit (black line) for $p/p_{\text{sat}} = 0.93$. The inset plot details the free surface (depth = 0) to substrate ρ profile from the model fit. The oscillating ρ with depth resulted from the layer model incorporating pure PI (lower initial ρ and less solvent) and PS/PI mixture layers (higher initial ρ and more solvent). As shown in the illustration, PS/PI layers contained cylindrical domains, and pure PI layers represented the space between nearest neighbor cylindrical layers. Reprinted with permission from Shelton, C. K. *et al. Macromolecules* **2016**, 49, 7525-7534, Copyright 2016 American Chemical Society.⁴¹

By modeling the profile as a series of independent domains of repeating PS cylinders in PI matrix and pure PI matrix layers with changing ρ values (from solvent content in each domain), the substrate-to-free surface solvent distribution was mapped. In Figure 4.6, the resulting substrate-to-free surface solvent profiles from model fits to the data for d -benzene in SIS at different values of p/p_{sat} is detailed. From the solvent

profiles, several key aspects were noted. First, layer-to-layer fluctuations of ρ in the z -profile were the result of differences in ρ for PS and PI, which were enhanced by the preferential solvent segregation in PS domains as calculated from SANS results shown in Figure 4.2. Second, $p/p_{sat} = 0.84$ and $p/p_{sat} = 0.59$ profiles had a statistically significant increase in solvent concentration from the free surface to substrate. Although the average solvent concentration in the film appears to be higher towards the substrate at all p/p_{sat} values, the significantly larger solvent concentration at the substrate in moderate solvent partial pressure profiles likely indicates some solvent is being trapped in the film during deswelling as has been reported in literature.⁵⁹ Furthermore, it is possible that this result is a thermodynamic effect (*e.g.*, increased substrate-solvent preference at mid-range p/p_{sat} values due to parameters such as the Hamaker constant); however, literature suggests that if there was a substantial thermodynamic preference for the solvent to reside at the substrate surface, the film would have a tendency to dewet.^{60, 61} Third, deviations from a uniform solvent concentration in PI/PS domains and PI domains through the film increased from approximately ± 5 vol% to ± 10 vol% at $p/p_{sat} \leq 0.59$. This behavior was likely the result of a lack of solvent needed to reduce the T_g below room temperature as discussed previously. Because the PS chains were still glassy, solvent could not diffuse easily through the film resulting in the formation of trapped solvent. Additionally, AFM images of the SIS film before and after *in situ* NR (see Appendix B, Figure B.1) indicate areas of short cylinders and perforated structures (perpendicular alignment to the substrate) in the annealed nanostructure, which likely contribute to the roughness between layers noted in through-film ρ and solvent composition profiles. Finally, the average solvent concentration in the film matched

well with those calculated from SANS results in Figure 4.2 (dashed lines in Figure 4.6) and known polymer volume fractions in the film. The agreement between the results indicates the chosen models for NR profiles accurately describe the solvent's presence in the film.

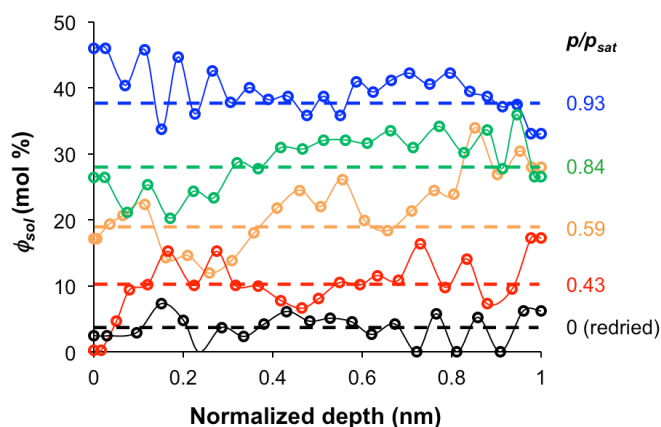


Figure 4.6: Solvent profiles of *d*-benzene in SIS films from the free surface (depth = 0) to substrate (depth = 1). At $p/p_{sat} \leq 0.59$, large deviations from through-film solvent uniformity were noted. The average solvent concentration in the film at each p/p_{sat} was in reasonable agreement with the values determined by SANS at the same p/p_{sat} values (dashed lines). The lines between data points are to guide the eye. Reprinted with permission from Shelton, C. K. *et al. Macromolecules* **2016**, 49, 7525-7534, Copyright 2016 American Chemical Society.⁴¹

Using the $\chi_{poly-sol}$ parameters determined from Figures 4.1 and 4.2, the measured restructuring of polymer domains was related to calculated polymer-solvent interactions. From the $\chi_{poly-sol}$ values for the individual polymer blocks, the ratio of solvent segregation in individual polymer domains can be calculated with Equation 4.2. Additionally, because the solvent concentration in each layer remains

relatively constant through the film thickness, as indicated by through-film solvent profiles (Figure 4.6), the $\chi_{poly-sol}$ values can forecast the through-film solvent concentration and film thickness as a function of p/p_{sat} . Provided this value is above the threshold of solvent required to lower the T_g below room temperature and impart chain mobility, the restructuring of polymer domains can be predicted with knowledge of the energetically favorable vertical L_z in the film from *ex situ* studies to calculate the number of layers in the film, as well as whether the layers will be stretched or compressed.

4.3.2 Highly Selective Solvents

Highly selective solvents for PS (*d*-acetone) and PI (*d*-hexane) were used to examine polymer-solvent interactions further. At 25 °C, the solubility parameter of acetone ($\delta_{acetone} = 20.3 \text{ MPa}^{1/2}$) and hexane ($\delta_{hexane} = 14.9 \text{ MPa}^{1/2}$) in comparison to PS ($\delta_{PS} = 18.6 \text{ MPa}^{1/2}$) and PI ($\delta_{PI} = 16.4 \text{ MPa}^{1/2}$) indicate these solvents should only swell one domain significantly.³⁶ *In situ* NR was used to investigate the response of the nanostructure reorganization during swelling and swelling with these solvents.

NR profiles from SIS films during SVA at different equilibrated *d*-acetone concentrations are shown in Figure 4.7. From top to bottom, the *d*-acetone-rich nitrogen to diluent nitrogen ratios (mL/min:mL/min) of 0:0 (as-cast), 10:0, 8:2, 6:4, 4:6, and 0:10 (redried) were exposed to the films in order. Two broad Bragg peaks appeared at Q_z values of 0.021 \AA^{-1} and 0.040 \AA^{-1} in the fully swollen films and shifted to higher Q_z values (decrease in L_z) as the film was deswelled. The broadness of the Bragg peaks indicated a consistent layering structure never developed in the film. This effect likely was the result of *d*-acetone being a poor, albeit preferential, solvent for PS. The amount of *d*-acetone in the PS domain was sufficient to promote partial

restructuring but a higher solvent concentration and longer annealing times would be needed to promote complete restructuring into uniform cylindrical layers for analysis.

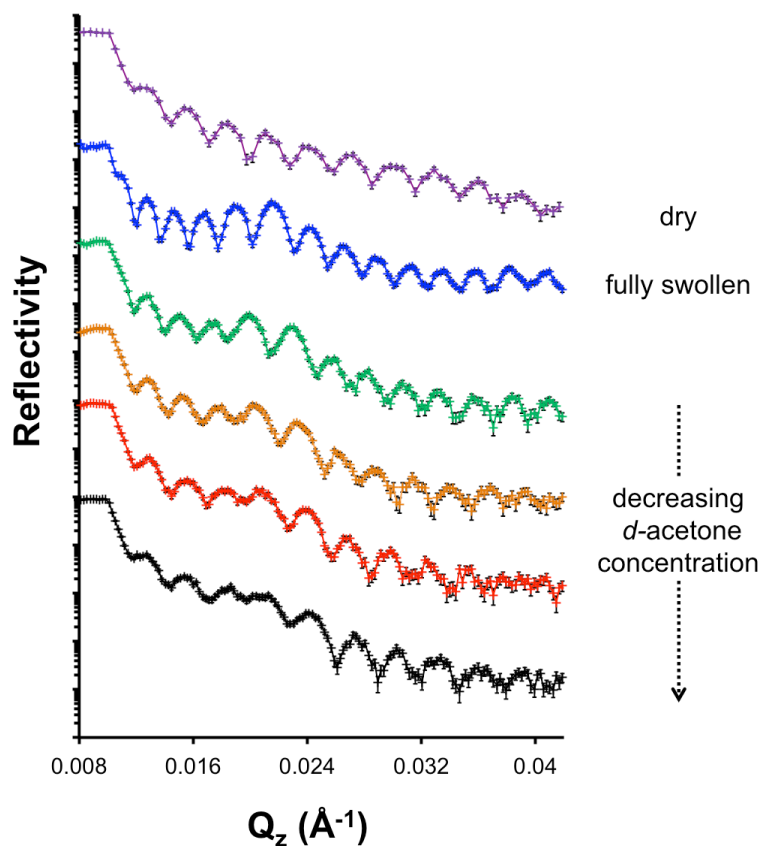


Figure 4.7: NR profiles of dry SIS films (top profile), fully swollen SIS films (second profile; swollen with 10 mL/min *d*-acetone-rich nitrogen), and SIS films dried to nitrogen/*d*-acetone to diluent nitrogen ratios of 8:2, 6:4, 4:6, and 0:10 (third profile to bottom). Broad Bragg peaks developed at $Q_z = 0.021 \text{ \AA}^{-1}$ and $Q_z = 0.040 \text{ \AA}^{-1}$ after exposure to *d*-acetone. The Bragg peaks shifted to higher Q_z values as the film was deswelled.

NR profiles from *d*SI*d*S films during SVA at different equilibrated *d*-hexane concentrations are shown in Figure 4.8. From top to bottom, the *d*-hexane-rich nitrogen to diluent nitrogen ratios (mL/min:mL/min) of 0:0 (as-cast), 10:0, 8:2, 6:4, 4:6, and 0:10 (redried) were exposed to the films in order. A broad Bragg peak was recorded in dry film profiles at high Q_z , which likely indicated the presence of some layering in the as-cast state with a range of L_z values. The Bragg peak disappeared in films swelled with *d*-hexane due to the solvent preference to the PI domain and subsequent nanostructure reorientation. The *d*-hexane vapor above the film drove the PI domain to the free surface; however, because the PI is the middle block in the triblock copolymer, the polymer chain must fold in half, resulting in an entropic penalty.⁶² To avoid the entropic penalty, the nanostructures reorient perpendicular to the substrate, which eliminates an out-of-plane layering and Bragg peaks scattering.^{56,}
⁶² Therefore, neutron scattering geometries that permit the simultaneous investigation of in-plane and out-of-plane features in BP thin films, such as GISANS, are needed to better analyze this system (see Chapter 7, Section 7.2.5).

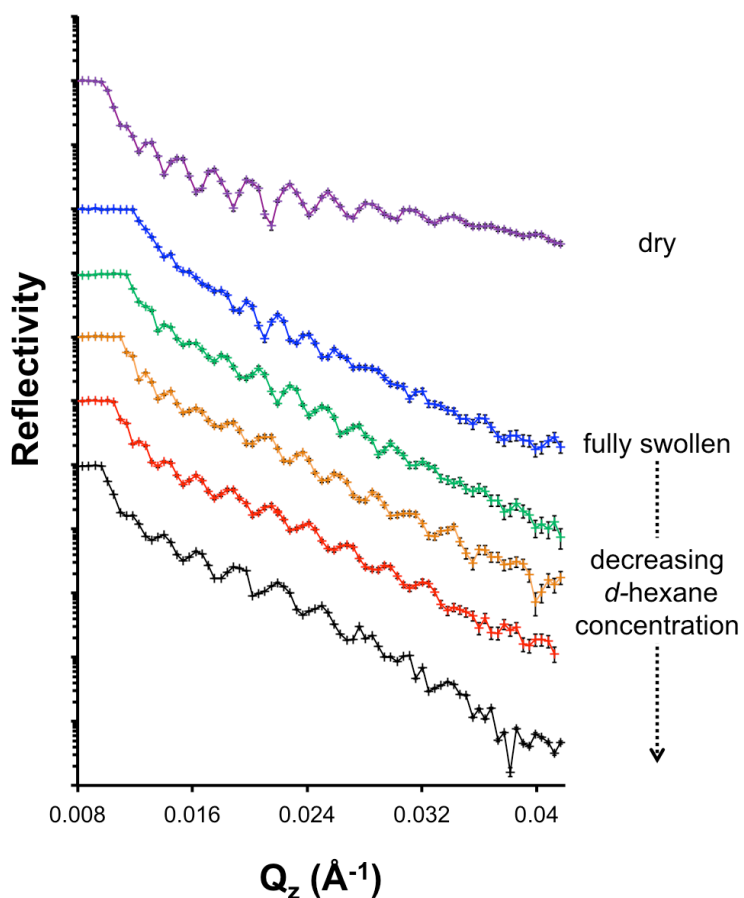


Figure 4.8: NR profiles of dry *dSI/dS* films (top profile), fully swollen *dSI/dS* films (second profile; swollen with 10 mL/min *d*-hexane-rich nitrogen), and dried to nitrogen/*d*-hexane to diluent nitrogen/*d*-hexane ratios (mL/min:mL/min) of 8:2, 6:4, 4:6, and 0:10 (third profile to bottom). A broad Bragg peak in the dry film disappeared after swelling and deswelling with *d*-hexane.

4.4 Conclusions

In this chapter, the distribution of *d*-benzene was tracked into individual PS and PI domains of an SIS BP as a function of solvent partial pressure (p/p_{sat}) using *in situ* SANS and NR. Measurable differences in polymer domain sizes (L_0 and L_z), number of layers (n), and film thickness (t) were related to in-plane and out-of-plane

solvent profiles determined with SANS and NR, respectively. Furthermore, a preferential segregation of *d*-benzene into PS domains was measured and used the results to calculate $\chi_{poly-sol}$ parameters that were in qualitative agreement with literature. More selective solvents (*d*-acetone and *d*-hexane) also were studied to explore how nanostructure reorganization changes as a function of solvent preference. The ability to add polymer-solvent contrast (*via* deuterated solvents), not easily obtained in X-ray scattering, permitted the relation of both polymer-polymer and polymer-solvent interactions to the reorganization of nanostructures during SVA. Thus, these results define how solvent preferentially diffuses into individual domains, how solvent diffusion effects nanostructure reorganization as a function of p/p_{sat} , and how domains become kinetically trapped during solvent removal. Additionally, L_z can be controlled by manipulating the solvent content in the film and the swelling/drying pathway, as demonstrated in this chapter. These outcomes help define several of the underlying mechanisms that govern the morphological evolution in BP thin films subjected to SVA, such as the mobility required to restructure the domain lattice, the impact of surface and interfacial roughness on commensurability constraints, the trapping of solvent in the film as a function of polymer mobility, and the selectivity of polymer and solvent at the free and substrate surfaces. Finally, this work provides an approach for predicting the solvent p/p_{sat} threshold necessary to effect morphological rearrangement on the basis of changes in T_g due to solvent uptake.

REFERENCES

1. Sinturel, C.; Vayer, M.; Morris, M.; Hillmyer, M. A. *Macromolecules* **2013**, *46*, 5399-5415.
2. Cavicchi, K. A.; Berthiaume, K. J.; Russell, T. P. *Polymer* **2005**, *46*, 11635-11639.
3. Zhang, J.; Posselt, D.; Sepe, A.; Shen, X.; Perlich, J.; Smilgies, D.-M.; Papadakis, C. M. *Macromol. Rapid Commun.* **2013**, *34*, 1289-1295.
4. Gowd, E. B.; Marcus, B.; Manfred, S. *IOP Conf. Ser.: Mater. Sci. Eng.* **2010**, *14*, 012015.
5. Di, Z.; Posselt, D.; Smilgies, D.-M.; Papadakis, C. M. *Macromolecules* **2010**, *43*, 418-427.
6. Mahadevapuram, N.; Strzalka, J.; Stein, G. E. *J. Polym. Sci., Part B: Polym. Phys.* **2013**, *51*, 602-610.
7. Gowd, E. B.; Koga, T.; Endoh, M. K.; Kumar, K.; Stamm, M. *Soft Matter* **2014**, *10*, 7753-7761.
8. Kao, J.; Thorkelsson, K.; Bai, P.; Zhang, Z.; Sun, C.; Xu, T. *Nat. Commun.* **2014**, *5*, 1-8.
9. Gunkel, I.; Gu, X.; Sun, Z.; Schaible, E.; Hexemer, A.; Russell, T. P. *J. Polym. Sci., Part B: Polym. Phys.* **2015**, 331-338.
10. Paik, M. Y.; Bosworth, J. K.; Smilgies, D.-M.; Schwartz, E. L.; Andre, X.; Ober, C. K. *Macromolecules* **2010**, *43*, 4253-4260.
11. Di, Z.; Posselt, D.; Smilgies, D.-M.; Li, R.; Rauscher, M.; Potemkin, I. I.; Papadakis, C. M. *Macromolecules* **2012**, *45*, 5185-5195.
12. Chavis, M. A.; Smilgies, D.-M.; Wiesner, U. B.; Ober, C. K. *Adv. Funct. Mater.* **2015**, *25*, 3057-3065.
13. Bai, W.; Yager, K. G.; Ross, C. A. *Macromolecules* **2015**, *48*, 8574-8584.

14. Gu, X.; Gunkel, I.; Hexemer, A.; Gu, W.; Russell, T. P. *Adv. Mater.* **2014**, *26*, 273-281.
15. Hamley, I. W. *Prog. Polym. Sci.* **2009**, *34*, 1161-1210.
16. Vaselabadi, S. A.; Shakarisaz, D.; Ruchhoeft, P.; Strzalka, J.; Stein, G. E. *J. Polym. Sci., Part B: Polym. Phys.* **2016**, 1074-1086.
17. Virgili, J. M.; Tao, Y.; Kortright, J. B.; Balsara, N. P.; Segalman, R. A. *Macromolecules* **2007**, *40*, 2092-2099.
18. Pavlopoulou, E.; Anastasiadis, S. H.; Kortright, J. B.; Bras, W.; Portale, G. *IOP Conf. Ser.: Mater. Sci. Eng.* **2010**, *14*, 012017.
19. Shelton, C. K.; Epps, T. H., III *Polymer* **2016**, *105*, 545-561.
20. Stamm, M.; Schubert, D. W. *Annu. Rev. Mater. Sci.* **1995**, *25*, 325-356.
21. Zhang, X. H.; Berry, B. C.; Yager, K. G.; Kim, S.; Jones, R. L.; Satija, S.; Pickel, D. L.; Douglas, J. F.; Karim, A. *ACS Nano* **2008**, *2*, 2331-2341.
22. Muller-Buschbaum, P. *Polym. J.* **2013**, *45*, 34-42.
23. Müller-Buschbaum, P.; Cubitt, R.; Petry, W. *Langmuir* **2003**, *19*, 7778-7782.
24. Kim, S. Y.; Park, M. J.; Balsara, N. P.; Jackson, A. *Macromolecules* **2010**, *43*, 8128-8135.
25. Zhong, Q.; Metwalli, E.; Rawolle, M.; Kaune, G.; Bivigou-Koumba, A. M.; Laschewsky, A.; Papadakis, C. M.; Cubitt, R.; Wang, J.; Müller-Buschbaum, P. *Macromolecules* **2016**, *49*, 317-326.
26. Wang, W.; Metwalli, E.; Perlich, J.; Papadakis, C. M.; Cubitt, R.; Müller-Buschbaum, P. *Macromolecules* **2009**, *42*, 9041-9051.
27. Kamata, Y.; Parnell, A. J.; Gutfreund, P.; Skoda, M. W. A.; Dennison, A. J. C.; Barker, R.; Mai, S.; Howse, J. R.; Ryan, A. J.; Torikai, N.; Kawaguchi, M.; Jones, R. A. L. *Macromolecules* **2014**, *47*, 8682-8690.
28. Dura, J. A.; Murthi, V. S.; Hartman, M.; Satija, S. K.; Majkrzak, C. F. *Macromolecules* **2009**, *42*, 4769-4774.
29. DeCaluwe, S. C.; Kienzle, P. A.; Bhargava, P.; Baker, A. M.; Dura, J. A. *Soft Matter* **2014**, *10*, 5763-5776.

30. Wang, W.; Metwalli, E.; Perlich, J.; Troll, K.; Papadakis, C. M.; Cubitt, R.; Müller-Buschbaum, P. *Macromol. Rapid Commun.* **2009**, 30, 114-119.
31. Albert, J. N. L.; Young, W.-S.; Lewis, R. L.; Bogart, T. D.; Smith, J. R.; Epps, T. H., III. *ACS Nano* **2012**, 6, 459-466.
32. Stafford, C. M.; Roskov, K. E.; Epps, T. H., III; Fasolka, M. J. *Rev. Sci. Instrum.* **2006**, 77, 023908.
33. Stein, S. E., Mass Spectra. In *NIST Chemistry WebBook*, National Institute of Standards and Technology: Gaithersburg, MD.
34. Kline, S. *J. Appl. Crystallogr.* **2006**, 39, 895-900.
35. Kienzle, P. A.; O'Donovan, K. V.; Ankner, J. F.; Berk, N. F.; Majkrzak, C. F. <http://www.ncnr.nist.gov/reflpak> **2000-2006**.
36. Brandrup, J.; Immergut, E. H.; Grulke, E. A., *Polymer handbook*; 4th Ed.; Wiley: New York ; Chichester, 2004.
37. Sears, V. F. *Neutron News* **1992**, 3, 26-37.
38. Noda, I.; Higo, Y.; Ueno, N.; Fujimoto, T. *Macromolecules* **1984**, 17, 1055-1059.
39. Rodriguez, F.; Cohen, C.; Ober, C. K.; Archer, L., *Principles of Polymer Systems*; 6th ed.; CRC Press: 2014.
40. Davis, R. T.; Schiessler, R. W. *J. Phys. Chem.* **1953**, 57, 966-968.
41. Shelton, C. K.; Jones, R. L.; Dura, J. A.; Epps, T. H., III *Macromolecules* **2016**, 49, 7525-7534.
42. Hammouda, B., Probing Nanoscale Structures: The SANS Toolbox. NIST: 2008.
43. Horkay, F.; Hammouda, B. *Colloid. Polym. Sci.* **2008**, 286, 611-620.
44. Wadsater, M.; Barauskas, J.; Rogers, S.; Skoda, M. W. A.; Thomas, R. K.; Tiberg, F.; Nylander, T. *Soft Matter* **2015**, 11, 1140-1150.
45. Huang, C.-I.; Chapman, B. R.; Lodge, T. P.; Balsara, N. P. *Macromolecules* **1998**, 31, 9384-9386.

46. Flory, P. J., *Principles of Polymer Chemistry*. Cornell University Press: Ithaca, United States, 1953.
47. Elbs, H.; Krausch, G. *Polymer* **2004**, *45*, 7935-7942.
48. Virgili, J. M.; Nedoma, A. J.; Segalman, R. A.; Balsara, N. P. *Macromolecules* **2010**, *43*, 3750-3756.
49. Russell, T. P. *Macromolecules* **1993**, *26*, 5819-5819.
50. Lodge, T. P.; Hamersky, M. W.; Hanley, K. J.; Huang, C.-I. *Macromolecules* **1997**, *30*, 6139-6149.
51. Hamley, I. W., *Block Copolymers in Solution: Fundamentals and Applications*. John Wiley & Sons Ltd.: West Sussex, England, 2005.
52. Hannon, A. F.; Bai, W.; Alexander-Katz, A.; Ross, C. A. *Soft Matter* **2015**, *11*, 3794-3805.
53. Knoll, A.; Tsarkova, L.; Krausch, G. *Nano Lett.* **2007**, *7*, 843-846.
54. Jenckel, E.; Heusch, R. *Kolloid-Zeitschrift* **130**, 89-105.
55. Mark, J. E., *Physical Properties of Polymers Handbook*. Springer Science & Business Media, LLC: New York, NY, 2007.
56. Luo, M.; Seppala, J. E.; Albert, J. N. L.; Lewis, R. L.; Mahadevapuram, N.; Stein, G. E.; Epps, T. H., III. *Macromolecules* **2013**, *46*, 1803-1811.
57. Papadakis, C. M.; Di, Z.; Posselt, D.; Smilgies, D.-M. *Langmuir* **2008**, *24*, 13815-13818.
58. Heinzer, M. J.; Han, S.; Pople, J. A.; Baird, D. G.; Martin, S. M. *Macromolecules* **2012**, *45*, 3480-3486.
59. Kim, S.; Briber, R. M.; Karim, A.; Jones, R. L.; Kim, H. C. *Macromolecules* **2007**, *40*, 4102-4105.
60. Albert, J. N. L.; Bogart, T. D.; Lewis, R. L.; Beers, K. L.; Fasolka, M. J.; Hutchison, J. B.; Vogt, B. D.; Epps, T. H., III. *Nano Lett.* **2011**, *11*, 1351-1357.
61. Epps, T. H., III; DeLongchamp, D. M.; Fasolka, M. J.; Fischer, D. A.; Jablonski, E. L. *Langmuir* **2007**, *23*, 3355-3362.

62. Vu, T.; Mahadevapuram, N.; Perera, G. M.; Stein, G. E. *Macromolecules* **2011**, *44*, 6121-6127.

Chapter 5

MANIPULATION OF SHEAR-ALIGNMENT EFFECTS IN BLOCK POLYMER THIN FILMS

In this chapter, small-angle neutron scattering (SANS) was used to identify the kinetic pathways between disordered and ordered states in block polymer (BP) thin films subjected to solvent vapor annealing with soft shear (SVA-SS), which enabled the optimization of large-scale nanostructure ordering and alignment. The judicious incorporation of deuteration in poly(deuterated styrene-*b*-isoprene-*b*-deuterated styrene) (*dSIIdS*) films (≈ 200 nm thick) provided sufficient contrast in the SANS experiments to overcome the diffuse scattering as a result of scattering through thicker (non-deuterated) polydimethylsiloxane (PDMS) pads (≈ 500 μm thick), permitting the *in situ* tracking of BP nanostructure responses to swelling, deswelling, and shear forces. Through these experiments, a robust and ‘hands-off’ approach using gradient thickness PDMS pads to create large and controllable shear forces that direct BP thin film self-assembly was developed. Furthermore, insight gleaned from these experiments was applied to the creation of a novel film casting technique that produces shear-aligned BP thin film nanostructures in a high-throughput, continuous process. The methods highlighted in this chapter can be applied to quickly and reliably generate cost-effective, low defect density, microscopic patterns over macroscopic areas for both nanotechnology research and industrial applications. Text and figures are reproduced or adapted with permission from Shelton, C. K., Jones, R. L., and Epps, T. H., III, *in preparation*.

5.1 Introduction

Unlocking the potential of BP thin films for nanolithography and templating applications rests in the ability to direct self-assembly (*i.e.*, morphology, ordering, orientation) precisely, a task that becomes more difficult as size scales continue to shrink.¹⁻¹⁰ As discussed in a recent report that examined the use of BP thin films for templating and lithography, “the biggest problem is defectivity, followed in order by pattern roughness/uniformity, placement accuracy, and material quality control.”¹¹ Specifically, the thermodynamics of BP thin film self-assembly allows for a high probability of generating low-energy, kinetically trapped defects.^{12, 13} This issue has hindered the mainstream use of BP thin films in nanotechnology and forced industry to invest in high-cost lithography techniques such as extreme ultraviolet ozone lithography for the production of nanometer-scale patterned features.¹¹ Although BP thin films have the potential to reduce current lithographic feature sizes, and the associated expenses, key challenges must be overcome including the development of rapid, cost-effective, and scalable methods to align nanostructures with low defect densities over macroscopic areas.

Although a variety of directed self-assembly techniques exist (see Chapter 1, Section 1.5), shear-alignment has garnered substantial consideration in recent years due to its high-degree of ordering, low cost, and relative universality among BP thin film systems. Seminal work by Register and coworkers discussed how manual displacement of PDMS pads across thermally annealed BP thin films induced a directional shear force that aligned the domains.¹⁴ Heating the BP above the glass transition temperature (T_g) of the individual blocks provided sufficient mobility to the polymer chains to promote domain alignment during shear. Although well-ordered and aligned nanostructures in many BP thin film chemistries and morphologies have

been achieved with this technique,¹⁴⁻¹⁹ the time-scales for alignment are on the order of several minutes to hours, and the restructuring effects are limited to film thicknesses of one or two domains.^{14, 20} To address these concerns, Jeong *et al.* used SVA rather than high temperatures to impart mobility to the polymer chains.²¹ The exposure to solvent vapor plasticized the polymer chains and effectively reduced the polymer T_g s to below room temperature.^{2, 22, 23} The researchers demonstrated that a solvent-swollen PDMS pad in direct contact with a BP thin film could be drawn across the free surface in the desired alignment direction to impart the same degree of ordering and directionality achieved *via* thermal annealing but over time-scales on the order of 5 s to 30 s.²¹

In contrast to physically displacing a PDMS pad on a film (*i.e.*, hard shear), material property differences can induce shear forces between the BP and a PDMS pad (*i.e.*, soft shear).^{24, 25} Two commonly exploited phenomena to produce soft shear are thermal expansion and solvent swelling. Singh *et al.* demonstrated that PDMS pads placed on poly(styrene-*b*-methyl methacrylate) (PS-PMMA) films and subjected to thermal gradients in a cold zone annealing (CZA) process generated a shear force from differences in the thermal expansion of the film (thermal expansion coefficients: $\alpha_{PS} = 80 \times 10^{-6}/^{\circ}\text{C}$ and $\alpha_{PMMA} = 50 \times 10^{-6}/^{\circ}\text{C}$) versus PDMS ($\alpha_{PDMS} = 325 \times 10^{-6}/^{\circ}\text{C}$).²⁴ The shear force directed the alignment of nanostructures and reduced the defect density in the film in comparison to CZA alone.^{26, 27} Similarly, Majewski and Yager developed soft shear laser zone annealing (LZA), which used a high-intensity laser and light-absorbing germanium monolayer to localize the shear direction and intensify the thermal gradient, allowing for faster annealing times.²⁸ However, CZA and LZA subject the films to high temperatures that can cause chemical or morphological

changes in thermally-responsive BPs, as well as polymer degradation.^{29, 30} Swelling and deswelling of the PDMS from exposure to solvent vapor during SVA-SS can create shear fields to align BP thin film nanostructures at room temperature.^{25, 31, 32} Qiang *et al.* used SVA-SS to align cylindrical poly(styrene-*b*-isoprene-*b*-styrene) (SIS) nanostructures with this technique.^{25, 31} The lateral swelling and deswelling of PDMS in contact with an SIS thin film generated a shear field that aligned the solvent-swollen domains. Luo *et al.* improved the patterning ability of SVA-SS using raster solvent vapor annealing with soft shear (RSVA-SS) to localize swelling and deswelling in SIS films for controlled shear field directionality and nanostructure alignment.³² Annealing times in the range of seconds to minutes were achieved with SVA-SS and RSVA-SS without complications associated with thermal degradation; however, the actual mechanics of the domain restructuring process have not been explored, which limits the ability to design universal approaches to produce the desired assemblies.³³

In this chapter, the kinetics of toluene SVA-SS in cylinder-forming *dSI/dS* thin films were studied using *in situ* SANS experiments. By systematically testing the effects of several key parameters (PDMS elasticity, swelling ratio, and deswell rate), the best conditions to produce highly-ordered, well-aligned nanostructures over macroscopic film areas with SVA-SS were determined. The deuteration of the polystyrene blocks in the copolymer films significantly enhanced the contrast between the polymer domains, which overcame the large diffuse scattering contribution (background) from PDMS pads and also reduced SANS data collection times to 15 min. This experimental method provided fundamental and actionable insights into the mechanisms of shear-alignment during SVA-SS. From the analysis, more

reproducible spatial control over nanostructure alignment was developed using gradient thickness PDMS pads that directed drying fronts and shear directions in thin films. Furthermore, the insight from SVA-SS experiments was applied in the development of a novel thin film coating technique (termed shear casting) to cast and shear-align BP thin film nanostructures simultaneously in a single-step process through the incorporation of a flexible PDMS blade proceeding the rigid casting blade in a typical flow coating process. Overall, this chapter details translatable approaches to produce highly ordered and ‘programmable’ patterns across macroscopic areas in hierarchical materials with as few processing steps as possible to access new avenues of applied nanotechnology research and make industrial-scale BP thin film nanostructure generation more feasible and cost-effective.

5.2 Materials and Methods

5.2.1 Thin Film Casting and Characterization

The *dSIIdS* triblock copolymer ($M_n = 160$ kg/mol; $\mathfrak{D} = 1.07$; block volume fractions: $f_S = 0.10$, $f_I = 0.78$, $f_S = 0.12$; cylindrical nanostructure) was synthesized (courtesy of Maëva Tureau) *via* sequential anionic polymerization of perdeuterated styrene (Acros, stabilized, 98+ atom% D) and isoprene (Acros, 98% stabilized) as described in the literature.³⁴ The SIS triblock copolymer ($M_n = 118$ kg/mol; $\mathfrak{D} = 1.09$; block volume fractions: $f_S = 0.134$, $f_I = 0.732$, $f_S = 0.134$; cylindrical nanostructure) for shear casting was obtained from DEXCO (V4211) and used as received. Both polymers were characterized by size exclusion chromatography (Viscotek, GPCmax WE-2001), proton nuclear magnetic resonance spectroscopy (Bruker, AVX400), and atomic force microscopy (AFM; Veeco Dimension 3100).

dSiDS films were flow coated³⁵ onto silicon wafers (Wafer World Inc.) from 2.1 wt% polymer in tetrahydrofuran (Optima) solutions. SIS films were shear cast³⁶ onto silicon wafers from 2.1 wt% polymer in 5:95 *o*-xylene:THF (mass%:mass%) solutions. *o*-Xylene was purchased from Sigma Aldrich (puriss. p.a., $\geq 99.0\%$ [GC]) and used as received. Prior to casting, the silicon wafers were triple rinsed with toluene, dried with compressed nitrogen gas (Keen Compressed Gas Co.), processed in an ultraviolet ozone cleaner (model 342, Jelight Co., Inc.) for ≈ 1 h, and re-rinsed with toluene. *dSiDS* films were cast at uniform thickness (200 ± 5 nm) as determined by a spectral reflectometer (Filmetrics, F20-UV) taking measurements every 5 mm along the length of 25 mm films. The casting of SIS films was more varied, as described in Section 5.4. The free surface morphologies of as-cast and processed (SVA-SS or shear casting) films were examined by tapping mode AFM with silicon probes (Tap150G, BudgetSensors) at a typical setpoint ratio of 0.65. After shear casting and AFM imaging, SIS films were subjected to dynamic vacuum (20 mTorr) at room temperature to remove residual solvent before thermal annealing under vacuum at 130 °C for 2 h to promote polymer chain mobility and nanostructure coalescence into larger grains. After 2 h, films were removed from the vacuum oven and quenched on a metal plate to bring the films to room temperature and kinetically trap the microstructures, and the free surface morphology was reimaged with AFM.

5.2.2 Polydimethylsiloxane Pad Preparation

Elastomeric pads and flexible blades were generated from a PDMS kit (Dow Corning Sylgard 184). PDMS pads were fabricated at 5:1, 10:1, 15:1, or 20:1 wt:wt ratio of elastomer base to curing agent. Flexible PDMS blades for shear coating were made at 10:1 ratios. The mixtures were combined in a glass beaker *via* stirring, and

dynamic vacuum was pulled for 30 min to degas the blend prior to curing at 65 °C for 3 h. The thickness of each pad was ≈ 0.3 mm, and the thickness of each flexible blade was ≈ 2 mm. For gradient thickness PDMS pads, the Petri dishes were angled $\approx 2^\circ$ by placing two glass microscope slides (1 mm-thick each) under one side of the dish. The PDMS spread at this angle during degassing in the vacuum oven, and it was cured for the same temperature and time as uniform thickness pads. Cured and cooled PDMS pads were slowly placed onto the *dSI₂S* films to ensure no air bubbles were trapped between the pads and films before SVA-SS. PDMS pads were angled slightly on the film in relation to the input vapor stream of the SVA chamber to control the location of the initial drying front (and domain alignment) in all samples; drying fronts propagate from the corner of the pads.²⁵

5.2.3 Small-Angle Neutron Scattering during Solvent Vapor Annealing with Soft Shear

SANS experiments were conducted using the 10 m SANS (NGB) instrument at the National Institute of Standards and Technology (NIST) Center for Neutron Research (NCNR). A 12.7 mm diameter neutron beam, 10 Å incident wavelength (λ), 5.2 m sample to detector distance, and 25.4 mm diameter beamstop were used for all runs. These specifications resulted in a measured Q range of $0.0007 \text{ \AA}^{-1} \leq Q \leq 0.0536 \text{ \AA}^{-1}$. A specially designed SVA flow chamber was employed as detailed in Section 4.2.3 and the literature.²³ The SVA chamber housed a single 200 ± 5 nm thick *dSI₂S* film (with or without PDMS), and the temperature was maintained at 25 °C using continuous circulating water baths. SANS measurements were recorded every 15 min to collect kinetic data during swelling and deswelling of films. Additionally, SANS profiles were recorded before (as-cast) and after (annealed) solvent exposure.

PDMS pads were removed from the film for these two measurements to improve resolution. SANS scattering data were reduced using Igor Pro (WaveMetrics) software with NCNR SANS reduction macros.³⁷

dSIaS films were annealed with toluene (Taylor Scientific, Reagent A.C.S.) vapor by bubbling nitrogen gas through a toluene reservoir to produce a solvent-rich vapor stream. To manipulate the vapor composition, a pure nitrogen stream was mixed with the solvent-rich stream several feet before reaching the inlet of the sample chamber to ensure that the flow was well-mixed. The flow rate of nitrogen bubbled through the toluene reservoir was modulated with two separate mass flow controllers (MKS Instruments Type 146C Cluster Gauge) with 0 – 10 mL/min set points. Three different solvent-rich to diluent nitrogen ratios were used to swell the *dSIaS* films: 10:0 (most swollen), 8:2, and 6:4 (least swollen). *dSIaS* films were deswelled by setting the solvent-rich stream mass flow rate to 0 mL/min and the diluent nitrogen flow rate to either 3 mL/min (slowest deswell), 5 mL/min, or 7 mL/min (fastest deswell). These flow rates corresponded to characteristic continuous stirred-tank reactor (CSTR) mean residence times (τ_{CSTR}) of 0.51 min, 0.30 min, and 0.22 min, respectively. τ_{CSTR} values were calculated by dividing the diluent nitrogen flow rate by the volume of the cylindrical SVA chamber (chamber internal radius = 1.27 cm and internal height = 3 mm) and assuming there were no stagnant flow regions in the chamber.³⁸ *Note: literature has demonstrated that SVA chambers reach steady state exponentially, which is characteristic of a CSTR.*^{39, 40}

5.3 Results and Discussion

5.3.1 Kinetics of Solvent Vapor Annealing with Soft Shear

SANS profiles recorded every 15 min during SVA-SS (10 mL/min solvent-rich flow rate, 10:1 elastomer-to-curing agent PDMS, 3 mL/min diluent nitrogen deswell flow rate) revealed the disappearance of the diffraction primary peak during SVA-SS swelling and reappearance during deswelling (Figure 5.1a). The initial peak intensity was due to self-assembled nanostructures and the scattering contrast between *d*PS and PI domains. The peak intensity of the fully swollen state during SVA-SS (Figure 5.1a) was approximately one order of magnitude less than the initial (pre SVA-SS) or post SVA-SS peak intensities obtained *via* SANS. The primary peak remained relatively unchanged during SVA (Figure 5.1b) conducted at the same conditions (*i.e.*, swollen film thickness, annealing time, swell and deswell rate). A direct comparison between the two-dimensional scattering patterns obtained from the initial and final states of *d*SI*d*S films exposed to SVA or SVA-SS is shown in Appendix C, Figure C.1. *Note: the overall scattering intensity was higher for SVA-SS than SVA due to the diffuse scattering contribution from the PDMS pad (SVA-SS background \approx 400, SVA background \approx 10 in arbitrary units).*

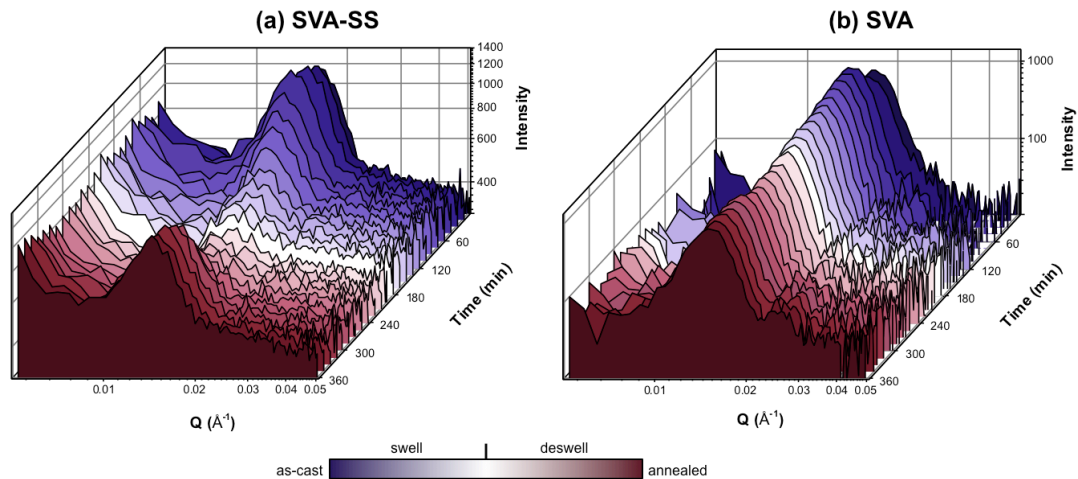


Figure 5.1: Temporal series of SANS profiles that track BP and PDMS swelling and deswelling during (a) SVA-SS or (b) SVA. An order of magnitude drop in the primary peak scattering intensity was recorded during SVA-SS processing; a similar intensity drop was not noted during SVA processing. However, the primary peak scattering intensity for the SVA-SS sample returned to initial levels as the film was deswelled. *Note: the SVA-SS profiles have higher absolute scattering intensities in comparison to SVA profiles due to increased background scattering from the PDMS pads.*⁴¹

The order of magnitude drop in scattering intensity during SVA-SS likely indicated that the shear generated from swelling the PDMS pad across the film induced chain mixing and nanostructure disordering. This disordering reduced scattering significantly and led to the destruction of grain structure in the film.⁴² As solvent was removed from the film and the shear forces reversed directions, the increase in scattering intensity at the primary peak suggested that phase separation into small grains occurred. These smaller grains were easier to align than larger grains due to decreased energetic penalties for domain restructuring.^{43,44} Therefore, the reorientation and alignment of smaller grains helped prevent the kinetic trapping of defects in the assemblies that limit domain ordering and directionality. Similar

“intermediate states” that relieve entropic barriers for aligning large BP grains are discussed in literature.⁴³⁻⁴⁶

Anisotropic SANS patterns were recorded after SVA-SS (Figure 5.2a; higher-intensity points highlighted with dashed white circles), which suggest well-ordered and aligned parallel cylinders in the films. AFM images (Figure 5.2b) supported the suspected nanostructure formations and directionality in the film as denoted by first and second order peaks in the corresponding fast Fourier transformation (FFT; Figure 2c) and a Herman’s orientation factor (S) of 0.89. Herman’s orientation parameters were calculated from AFM images using annularly averaged intensity profiles at azimuthal angles associated with the primary peak and Equation 1.⁴⁷

$$S = \frac{3\langle \cos^2 \phi \rangle - 1}{2} \quad (5.1)$$

In Equation 5.1, ϕ is the annular angle and $\langle \cos^2 \phi \rangle$ is the average of $\cos^2 \phi$ as a function of the intensity of the FFT at a given annular angle, $I(\phi)$, calculated with Equation 5.2.

$$\langle \cos^2 \phi \rangle = \frac{\sum_{\phi=0}^{2\pi} I(\phi) \sin \phi \cos^2 \phi}{\sum_{\phi=0}^{2\pi} I(\phi) \sin \phi} \quad (5.2)$$

AFM FFTs contained dot patterns rather than the crescent patterns noted in the SANS scattering data as a result of the smaller area (μm^2) of analysis in AFM. More specifically, the single-image AFM data did not capture the full nanostructure orientation or the complete ordering and alignment of the domains demonstrated over the SANS scattering sampling area (mm^2). Furthermore, AFM only examined the free surface (x-y plane), but SANS measured information in all three dimensions (x, y, and

z). The use of neutron scattering provided the improved statistical capabilities necessary to elucidate key details about the SVA-SS process. SVA without soft shear did not generate aligned nanostructures as evidenced by isotropic SANS patterns, mixed orientations in AFM images, and an S of 0.25 from AFM-generated FFTs (Figure 5.2d, e, and f, respectively). AFM images from portions of the SVA-SS film that did not experience shear-alignment detailed a similar mixed morphology of parallel and perpendicular cylinders and featureless areas as shown in films exposed to SVA without soft shear. This similarity implied there was no difference in the swelling conditions between the two samples that influenced the ordering and orientation behavior in the SVA vs. SVA-SS specimens (see Appendix C, Figure C.2). The alignment of domains depicted in Figure 5.2 SANS and AFM images post SVA-SS suggested that the small grains produced from shear forces during PDMS swelling had sufficient mobility to reorient and coalesce in the direction of the drying front as solvent was removed from the film.⁴⁸ Therefore, larger shear fields and degrees of grain breakup are essential to improve nanostructure ordering and alignment.

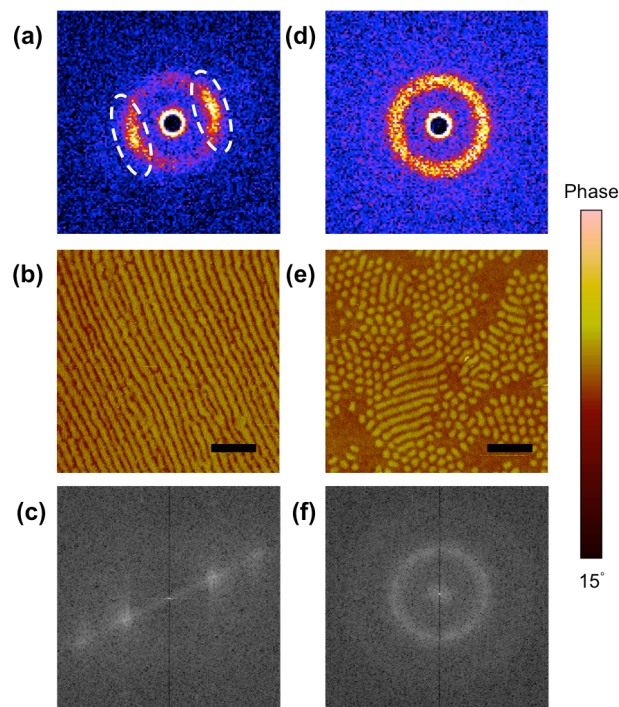


Figure 5.2: SANS scattering data and representative AFM phase images with FFTs of *dSIIdS* films after SVA-SS (a, b, c) or SVA (d, e, f), respectively. SANS data and AFM images of films subjected to SVA-SS had anisotropic rings (anisotropy highlighted with dashed white circles) and displayed well-ordered nanostructures, respectively, in contrast to the isotropic rings and mixed nanostructure orientations noted in the analysis of films exposed to SVA alone. SVA-SS FFTs from AFM were dot patterns rather than crescent patterns as obtained from the SANS data on similar samples, as the smaller AFM scan area (μm^2) was not able to capture the full film behavior in a manner similar to the SANS studies (mm^2). The scale bars in both AFM images represent 250 nm.⁴¹

The effect of solvent concentration, and subsequent PDMS swelling, on the induced shear force that promoted chain mixing and grain breakup was examined, as shown in Figure 5.3. The four data sets in Figure 5.3 represent the as-cast (with PDMS) SANS profile and steady-state SVA-SS SANS profiles after swelling *dSIIdS* films using three different solvent-rich to diluent stream flow rate ratios: 10:0, 8:2, and

6:4 (mL/min:mL/min) and 10:1 elastomer-to-curing agent PDMS pads. The solvent-rich stream was a nitrogen stream saturated with toluene vapor, and the diluent stream was pure nitrogen. The larger ratios of solvent-rich to diluent flow rates increased PDMS and film swelling, as well as reduced the scattering at the primary peak ($Q = 0.015 \text{ \AA}^{-1}$) in comparison to smaller ratios. The scattering intensity of the primary peak is lower in the as-cast profile than the 8:2 and 6:4 profiles due to increased scattering from the solvent and swollen film and PDMS. The primary peak location shifted to smaller Q , and the scattering intensity increased, in as-cast samples in the first 30 min of swelling as shown in Figure 5.1. The increased degree of swelling was noted by the increase in background scattering, in relation to the as-cast state, as the solvent partial pressure was raised. The increase in diffuse scattering did not obscure the primary peak needed for structural analysis.

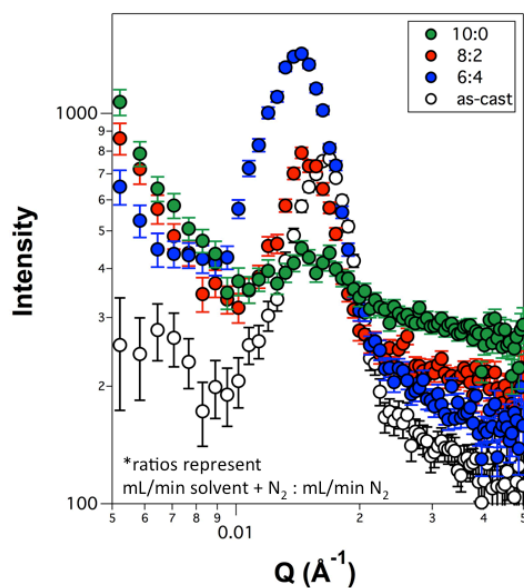


Figure 5.3: Azimuthally averaged SANS profiles for as-cast and fully swollen *dSI/dS* films at different solvent-rich stream to diluent stream flow rates (10:0, 8:2, and 6:4 - mL/min:mL/min). The scattering intensity of the primary peak (at $Q = 0.015 \text{ \AA}^{-1}$) decreased as solvent concentration increased (10:0 > 8:2 > 6:4). The as-cast profile had a less intense primary peak than the 8:2 and 6:4 samples due to the lack of solvent swelling. The primary peak intensity increased within the first 30 minutes of solvent swelling as shown in Figure 5.1. The degree of PDMS swelling increased with increasing solvent concentration as indicated by the rise in background scattering, in comparison to as-cast samples, primarily as a result of larger PDMS (diffuse) scattering volumes. Error bars represent one standard deviation from the measured intensity and were calculated during data reduction.⁴¹

At the lowest toluene concentration (6:4 ratio; least PDMS swelling), less scattering loss at the primary peak was noticed during swelling in comparison to 8:2 and 10:0 samples, which indicated less disordering from a combination of smaller shear forces (primary effect) and reduced swelling (secondary effect). Higher toluene concentrations (8:2 ratio and 10:0 ratio [most PDMS swelling]) led to greater shear forces and larger degrees of chain mixing and disordering. During swelling, the

correlation between the reduction in primary peak scattering intensity and PDMS swelling signified that the larger shear forces disordered a greater fraction of the film area, and upon deswelling, promoted the formation of small grains that were easier to align. AFM images of films after SVA-SS at the different flow rate ratios (*i.e.*, solvent concentrations) provide details regarding the impact of shear on the final nanostructure ordering (see Appendix C, Figure C.3). Notably, only films subjected to the highest solvent concentrations (10:0 ratio) developed directional alignment and low defect densities during drying. Films processed at an 8:2 ratio had aligned domains but contained a relatively high density of trapped defects. Films annealed at a 6:4 ratio appear to not have swelled sufficiently to plasticize the polymer chains and promote restructuring during SVA-SS.

5.3.2 Tuning Polydimethylsiloxane Swelling/Shear *via* Elasticity

From the kinetic analysis, grain breakup and reformation during swelling and deswelling was hypothesized to be responsible for nanostructure directionality and ordering. To induce larger shear forces and produce nanostructure arrays with greater degrees of ordering and alignment, the elastomer-to-curing agent ratio in the PDMS pad was altered; higher elastomer ratio PDMS is less elastic and swells more readily. The SANS data, azimuthally and annularly averaged profiles, and AFM images from four different ratios (5:1 [most elastic], 10:1, 15:1, or 20:1 [least elastic] wt:wt elastomer/curing agent) are shown in Figure 5.4. All samples were swollen with a 10 mL/min toluene-rich nitrogen stream for 2.5 h and then deswelled with 3 mL/min pure nitrogen until dry (3 – 6 h).

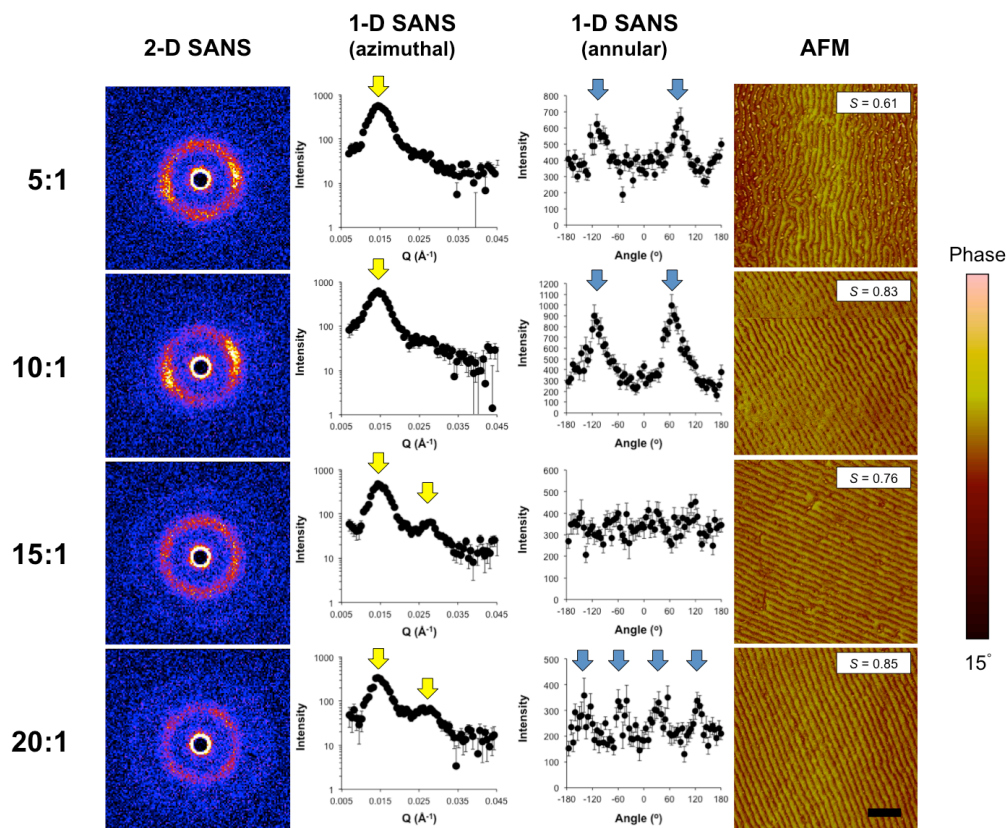


Figure 5.4: SANS data and representative AFM images for *dSI/dS* films subjected to SVA-SS from PDMS pads with elastomer-to-curing agent ratios (wt:wt) of 5:1 [most elastic, least swelling], 10:1, 15:1, or 20:1 [least elastic, most swelling]. SANS scattering data are shown in the first column as a function of elastomer-to-curing agent ratio. Azimuthally averaged profiles are presented in the second column, in which the diffraction peaks are marked by yellow arrows. Annularly averaged profiles are displayed in the third column, in which blue arrows mark the peak locations and are used to highlight changes in alignment direction from single direction (5:1 and 10:1; 2 peaks), to poorly-aligned (15:1; no high-intensity peaks), to multiple direction (20:1; 4 peaks). AFM phase images and corresponding orientation parameter values (S ; calculated from FFTs of the micrographs) are shown in the fourth column. The scale bar for the AFM images represents 250 nm and applies to all micrographs. Error bars in plots represent one standard deviation from the measured intensity and were calculated during data reduction.⁴¹

Distinct nanostructure assemblies were created from PDMS pads with different elastomer-to-curing agent ratios, as shown in Figure 5.4. Lower ratios (5:1 or 10:1) promoted nanostructure alignment with high directionality (two high-intensity peaks [blue arrows] confirmed with annularly averaged profiles) but limited ordering (no second order SANS peak [yellow arrows] in azimuthally averaged patterns). Larger degrees of ordering were achieved with less elastic PDMS pads (15:1 or 20:1), but the annular averages suggested a change from a single alignment direction (two high-intensity peaks) to poor alignment (15:1; no high-intensity peaks) or multiple alignment directions (20:1; four high-intensity peaks). These results were in contrast to a similar study conducted by Qiang *et al.* in which higher elastomer-to-curing agent ratios produced both better alignment and higher degrees of order in AFM images of films subjected to SVA-SS.³¹ The inconsistency likely was a result of the differences in analysis area between neutron scattering and AFM. A single alignment direction and limited defects ($S > 0.75$ for all samples) were suggested from AFM images in Figure 5.4 (2 $\mu\text{m} \times 2 \mu\text{m}$ images captured after SVA-SS with 10:1, 15:1, or 20:1). However, with the larger, more representative area analyzed with SANS, it was determined that drying fronts developed at each corner of the 15:1 and 20:1 PDMS pads. These drying fronts propagated inward and competed to create multiple orientation directions throughout the film. PDMS pads at 5:1 and 10:1 ratios had one drying front that propagated from one corner in the direction of the opposite corner to generate a single alignment direction across the film.

To demonstrate the effect of multiple drying fronts, an AFM analysis of the films subjected to SVA-SS with a 20:1 PDMS pad is presented in Figure 5.5. Images from each corner of the film revealed one of two competing directions as suggested by

the SANS analysis. The middle of the film had limited directionality or ordering. The orthogonal alignment directions indicated that a drying front propagated from each corner of the PDMS, as expected from mass transfer principles, highly swollen films, and slow deswell rates.²⁵ In the middle of the PDMS, opposing shear directions created a zero shear field that inhibited nanostructure alignment.

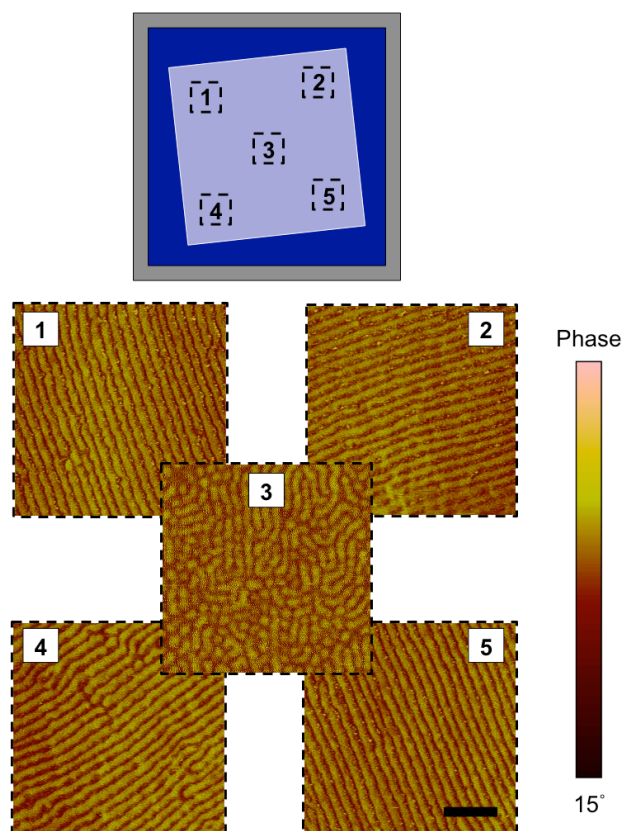


Figure 5.5: AFM phase images captured at each corner and the middle of the *dSI/dS* film, which visually indicated the direction of nanostructure alignment throughout the film after SVA-SS with a 20:1 elastomer-to-curing agent PDMS pad. No alignment was detected in the middle of the film. The scale bar represents 250 nm and applies to all AFM images.⁴¹

5.3.3 Controlling Alignment Drying Fronts

Although the higher elastomeric ratios were more beneficial because they were associated with better domain ordering, the creation of multiple drying fronts eliminates the desirable domain directionality across the film. Therefore, methods to control the propagation of drying fronts in highly swollen PDMS pads (15:1 and 20:1 elastomer-to-curing agent ratios) were investigated.

5.3.3.1 Drying Rate Effects

The influences of changes to the drying front propagation by altering the deswell nitrogen flow rates from 3 mL/min (slowest deswell) to 5 mL/min to 7 mL/min (fastest deswell) were examined. Key results are displayed in Figure 5.6. Azimuthally averaged profiles at all deswell conditions had second order peaks (peaks marked by yellow arrows); however, the annularly averaged profiles indicated significant differences between the samples. More specifically, at 3 mL/min, 5 mL/min, and 7 mL/min, four-peak, two-peak, and zero-peak annular patterns, respectively, were present in the SANS data (see peaks marked by blue arrows in Figure 5.6).

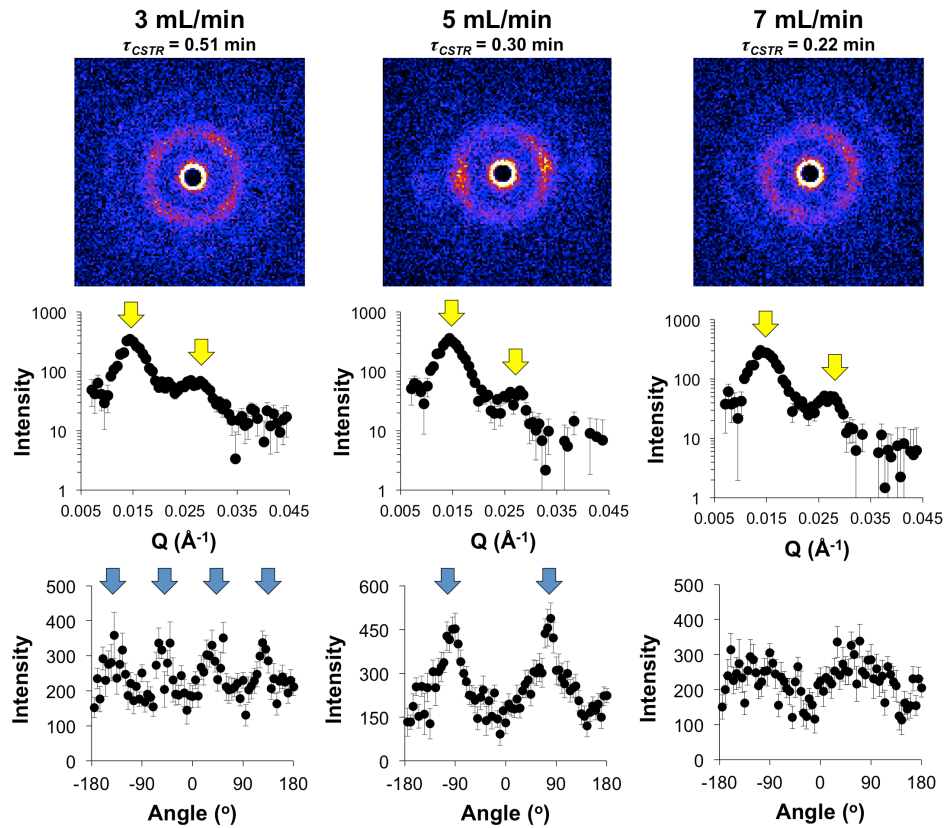


Figure 5.6: SANS scattering data (first row) of *dSI/dS* films after SVA-SS with different nitrogen flow rates used to deswell the film (3 mL/min [slowest deswell], 5 mL/min, and 7 mL/min [fastest deswell]). A second order peak in azimuthally averaged SANS patterns (second row) was present at all nitrogen flow rates (peaks marked by yellow arrows). However, an increase in the nitrogen flow (from 3 mL/min to 5 mL/min) led to a change from two alignment directions (four-peak annular pattern [third row]; peaks marked by blue arrows) to a single alignment direction (two-peak annular pattern). With a 7 mL/min nitrogen flow during deswell, only low-intensity annular peaks were measured. The 3 mL/min, 5 mL/min, and 7 mL/min flow rates and dimensions of the SVA chamber were used to calculate τ_{CSTR} values of 0.51 min, 0.30 min, and 0.22 min, respectively. Error bars represent one standard deviation from the measured intensity and were calculated during data reduction.⁴¹

The presence of second order peaks at all nitrogen flow rates suggested that the change in deswell rate had little effect on the domain ordering. However, the change in annular peaks indicated the alignment direction(s) of domains was the result of shear fields during drying. Slow deswell rates (3 mL/min) generated multiple, competing alignment directions (four-peak annular pattern) as discussed previously. Fast deswell rates (7 mL/min) produced significantly less defined domain directions (zero-peak annular pattern). The faster removal of solvent from the film limited reorientation times and kinetically trapped the nanostructures, which prevented the alignment of domains.³¹ At 5 mL/min, a single drying front aligned nanostructures (two-peak pattern) before a second front was created. Characteristic τ_{CSTR} values for the SVA chamber and the three diluent nitrogen flow rates were calculated as 0.51 min (3 mL/min), 0.30 min (5 mL/min), and 0.22 min (7 mL/min). The residence times provided a relative estimate of the time needed to deswell the film. Notably, the change in τ_{CSTR} for the 5 mL/min and 7 mL/min nitrogen flow rates was only 0.08 min. This small difference suggested that modulating deswell speeds is not a robust method to control domain directionality.

5.3.3.2 Gradient Thickness Polydimethylsiloxane Pads

Using the information above, gradient thickness PDMS pads were created for ‘hands-off’ shear control, which regulated the drying rate and the alignment of the nanostructures. SANS scattering data obtained from SVA-SS processed with uniform thickness and 2° gradient thickness PDMS pads are compared in Figure 5.7. The films and PDMS pads were swollen for 6 h with a 10 mL/min toluene-rich nitrogen stream before deswelling with a 3 mL/min diluent nitrogen stream.

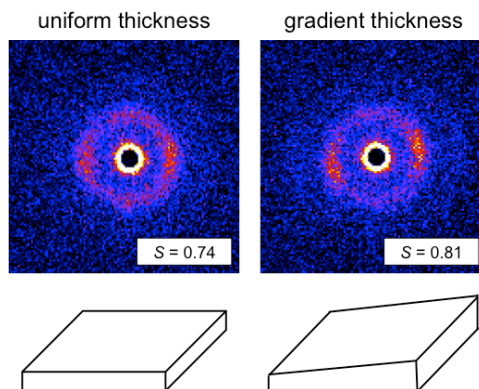


Figure 5.7: Comparison of SANS scattering data for *dSI/dS* films exposed to the same SVA-SS conditions but with uniform thickness or 2° gradient thickness 20:1 elastomer-to-curing agent ratio PDMS pads. SANS data obtained post SVA-SS after the PDMS pad was removed. *S* values of 0.74 and 0.81 were calculated from annularly averaged intensity profiles (not shown) with uniform and gradient thickness PDMS pads, respectively.⁴¹

The thickness gradient of the PDMS pads across the sample directed the drying front from the thin side to the thick side and reduced the development of multiple drying fronts in more swollen PDMS pads (see also Figures 5.5 and 5.6). This effect resulted in a 10% increase in *S* calculated from annularly averaged intensity profiles from 0.74 (uniform thickness PDMS) to 0.81 (gradient thickness PDMS), and domains oriented in a single direction across the film as noted in complementary AFM images of the shear-aligned nanostructures (see Appendix C, Figure C.4). Furthermore, the use of low elasticity PDMS (20:1 ratio) generated significant shear forces that induced chain mixing and nanostructure disordering to maximize domain ordering upon solvent removal and nanostructure coalescence (see also Figures 5.1, 5.2, and 5.3). Therefore, both domain ordering and directionality, which are competing processes according to Figure 5.4, were improved with gradient thickness PDMS. Hence, the

use of gradient thickness PDMS pads adds new avenues for directing BP thin film self-assembly with SVA-SS that can be exploited to generate domain patterns with high directionality and low defect densities in a more robust manner.

5.4 Shear-Alignment during Casting

Although the alignment times of SVA-SS (s – min) are considered reasonable for industrial application, the alignment, and any post-thermal annealing, adds processing steps to film production (*i.e.*, casting, annealing, aligning, post-processing). Ideally, different steps should be combined to reduce production times and resources. Therefore, casting and shear-alignment procedures were combined into a technique called shear casting to create a continuous, high-throughput method to generate aligned domains in nanostructured thin films.³⁶ Experimentation with different casting conditions (*e.g.*, casting solutions, casting speeds, post-processing methods) and shear casting setups discussed in this section was accomplished with assistance from John Saltwick.

Shear casting was conducted using the setup shown in Figure 5.8. The shear casting procedure started with a traditional flow coater motor stage³⁵ (substrate placed on top) and rigid casting blade (*e.g.*, glass). Then, a flexible blade (*e.g.*, PDMS) was added to the process. The flexible blade trailed the casting blade during movement of the motor stage and was angled such that it contacted the substrate with a downward force that mirrored the force provided by weights in the literature.¹⁴ During shear casting, a polymer solution was deposited between the rigid blade and substrate surface, and the motor stage was drawn under the rigid blade to cast the film. A solvent evaporation front developed as the polymer solution was deposited on the substrate. The flexible blade dragged across the film surface to generate a shear force

that aligned the nanostructures in the direction of casting provided there was sufficient solvent in the film to promote chain mobility. Although the components in the shear casting setup (*i.e.*, moving stage/substrate, rigid casting blade, flexible shearing blade, polymer solution) are consistent, specifics of the setup can vary, which makes this process adaptable for industrial needs. Examples of different shear casting setups are shown in Appendix C, Figures C.5 to C.7.

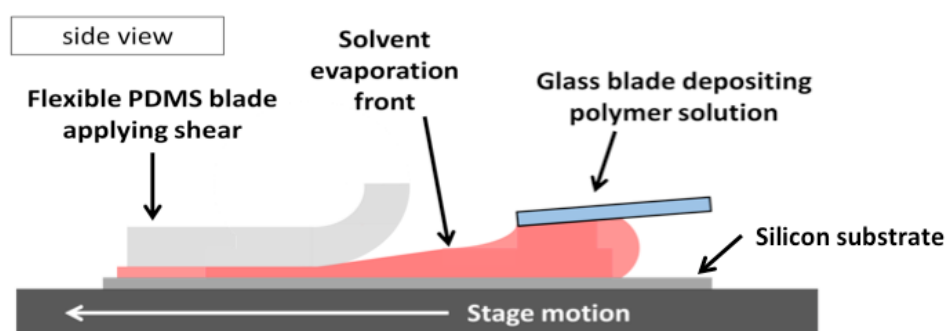


Figure 5.8: Illustration of shear casting setup (side view) with motorized stage (substrate placed on top of stage), glass casting blade, and flexible PDMS blade. The polymer solution is deposited on the substrate as the substrate is drawn beneath the glass blade. A solvent evaporation front develops as the polymer solution is deposited. To induce a shear force, the flexible blade drags across the drying film at a distance at which there is enough solvent to promote chain mobility. Image courtesy of John Saltwick.

Shear casting exploited a combination of hard and soft shear strategies to generate aligned nanostructures in a single step. The flexible blade manually displaced across the film in direct contact with the cast film produced a shear force (hard shear) that directed alignment and ordering. However, solvent swelling of the film (commonly employed in soft shear)^{25, 31} produced the necessary chain mobility to align the nanostructures. The combination of manual displacement to generate shear

and solvent swelling to provide chain mobility required precise control over the concentration of solvent in the film (decreased with time from solvent evaporation) during shearing. If too little solvent was present, the polymer chains did not have the mobility to realign nanostructures. If too much solvent was present, the film was lifted from the substrate surface by the flexible blade, as shown in Appendix C, Figure C.8.

To adjust the concentration of solvent in the film at the point when the flexible blade comes in contact with the film, two parameters were varied: the solvent evaporation rate and the casting speed. Slowing the evaporation rate of the solvent broadened the window of time in which the flexible blade could shear the film at the appropriate solvent concentration, but decreasing the evaporation rate too much slowed the overall process to the point that it was no longer advantageous to combine the casting and alignment steps. Therefore, the drying times of mixtures of THF (boiling point [T_{BP}] = 66 °C)⁴⁹ and *o*-xylene (T_{BP} = 144 °C)⁵⁰ were tested, as shown in Appendix C, Figure C.9, and a 5:95 *o*-xylene:THF (mass%:mass%) solution composition was selected. The fast-drying THF evaporated before the flexible blade dragged across the film, and the slow-drying *o*-xylene remained at a concentration sufficient to promote chain ordering with more limited film removal. Different casting speeds were tested with this solvent mixture to find the window in which domains were aligned with limited film damage. AFM images of SIS thin films flow coated (no shear) and shear cast from 5:95 *o*-xylene:THF solutions at different casting speeds are shown in Figure 5.9. Films produced *via* shear casting were thermally annealed at 130 °C for 2 h to improve the ordering of domains as discussed in recent literature.⁴³

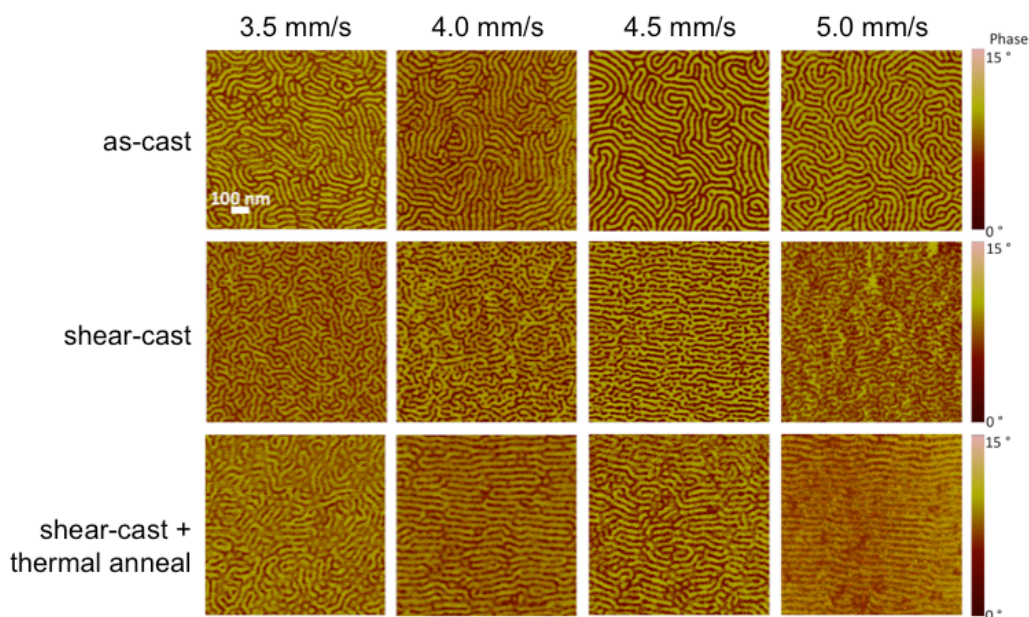


Figure 5.9: AFM images of SIS thin films flow coated (as cast; top row) and shear cast (middle row) from polymer solutions with 5:95 *o*-xylene:THF (mass%:mass%) solvent mixtures. Shear cast films were thermally annealed after casting (bottom row) to improve nanostructure ordering and increase grain sizes. Image courtesy of John Saltwick.

From Figure 5.9, shear casting resulted in more aligned domains than flow coated (as-cast) films at the same casting conditions when the speed was greater than 3.5 mm/s. The alignment of domains appeared to improve with casting speed, but higher speeds also produced more film damage. Notably, shear casting did not always create continuous grains in the films; trapped defects were present in AFM images that decreased grain sizes. Thermal annealing after shear casting appeared to improve grain sizes and help remove trapped defects; the average S for shear-cast samples was ≈ 0.40 , which improved to ≈ 0.88 after thermal annealing. This effect likely was the result of latent shear forces in the film that induced an alignment direction but did not have the time to orient all the domains.⁴³ Although promising results have been

achieved with shear casting, significant future work will be needed to improve alignment and ordering parameters, increase grain sizes, and reduce film damage as discussed in Chapter 7, Section 7.2.2.

5.5 Conclusions

In this chapter, *in situ* SANS during toluene SVA-SS was used to monitor kinetic pathways of nanostructure alignment in BP thin films. It was determined that as PDMS pad swelled above the film in the presence of solvent vapor, chain mixing and nanostructure disordering induced by shear fields reduced scattering intensities of the primary peak. Deswelling of the PDMS pad precipitated the formation of small grains, with reduced entropic penalties for alignment, which induced nanostructure orientation in the direction of the drying front and coalescence into large grains as solvent was removed, without the kinetic trapping of a large number of defects. Well-ordered and aligned nanostructures did not develop if sufficient chain mixing and domain disordering were not achieved during solvent swelling. Furthermore, more swollen PDMS pads, which produced larger shear forces, generated more ordered structures but reduced directional uniformity unless the drying front was controlled through careful tuning of the drying rate. To overcome this challenge, gradient thickness PDMS pads were incorporated to dictate the drying front propagation direction in a ‘hands-off’ manner, thus producing films with enhanced nanostructure directionality and ordering. The insight gained from these experiments was applied to the development of a novel film casting technique that simultaneously cast and shear-aligned domains in a continuous process amenable to high-throughput film production. Overall, the work in this chapter has helped develop translatable strategies to align nanostructures and maintain domain ordering with SVA-SS, and has advanced

understanding of universal, ‘programmable’, and high-throughput patterning methods for nanostructured thin films.

REFERENCES

1. Bates, F. S.; Fredrickson, G. H. *Phys. Today* **1999**, 52, 32-38.
2. Albert, J. N. L.; Epps, T. H., III. *Mater. Today* **2010**, 13, 24-33.
3. Fasolka, M. J.; Mayes, A. M. *Annu. Rev. Mater. Sci.* **2001**, 31, 323-355.
4. Segalman, R. A. *Mater. Sci. Eng., R* **2005**, 48, 191-226.
5. Epps, T. H., III; O'Reilly, R. K. *Chem. Sci.* **2016**, 7, 1674-1689.
6. Hamley, I. W. *Prog. Polym. Sci.* **2009**, 34, 1161-1210.
7. Hamley, I. W. *Nanotechnology* **2003**, 14, R39.
8. Bates, C. M.; Maher, M. J.; Janes, D. W.; Ellison, C. J.; Willson, C. G. *Macromolecules* **2013**, 47, 2-12.
9. Liddle, J. A.; Gallatin, G. M. *ACS Nano* **2016**, 10, 2995-3014.
10. Majewski, P. W.; Yager, K. G. *J. Phys.: Condens. Matter* **2016**, 28, 403002.
11. Lapedus, M., What Happened to DSA? In *Semiconductor Engineering* [online], 2016, <http://semiengineering.com/what-happened-to-dsa/>.
12. Ruiz, R.; Kang, H.; Detcheverry, F. A.; Dobisz, E.; Kercher, D. S.; Albrecht, T. R.; de Pablo, J. J.; Nealey, P. F. *Science* **2008**, 321, 936-939.
13. Bates, F. S.; Fredrickson, G. H. *Annu. Rev. Phys. Chem.* **1990**, 41, 525-557.
14. Angelescu, D. E.; Waller, J. H.; Adamson, D. H.; Deshpande, P.; Chou, S. Y.; Register, R. A.; Chaikin, P. M. *Adv. Mater.* **2004**, 16, 1736-1740.
15. Chremos, A.; Chaikin, P. M.; Register, R. A.; Panagiotopoulos, A. Z. *Soft Matter* **2012**, 8, 7803-7811.

16. Davis, R. L.; Chaikin, P. M.; Register, R. A. *Macromolecules* **2014**, *47*, 5277-5285.
17. Davis, R. L.; Michal, B. T.; Chaikin, P. M.; Register, R. A. *Macromolecules* **2015**, *48*, 5339-5347.
18. Kim, S. Y.; Nunns, A.; Gwyther, J.; Davis, R. L.; Manners, I.; Chaikin, P. M.; Register, R. A. *Nano Lett.* **2014**, *14*, 5698-5705.
19. Marencic, A. P.; Wu, M. W.; Register, R. A.; Chaikin, P. M. *Macromolecules* **2007**, *40*, 7299-7305.
20. Luo, M.; Epps, T. H., III. *Macromolecules* **2013**, *46*, 7567-7579.
21. Jeong, J. W.; Hur, Y. H.; Kim, H.-J.; Kim, J. M.; Park, W. I.; Kim, M. J.; Kim, B. J.; Jung, Y. S. *ACS Nano* **2013**, *7*, 6747-6757.
22. Sinturel, C.; Vayer, M.; Morris, M.; Hillmyer, M. A. *Macromolecules* **2013**, *46*, 5399-5415.
23. Shelton, C. K.; Jones, R. L.; Dura, J. A.; Epps, T. H., III *Macromolecules* **2016**, *49*, 7525-7534.
24. Singh, G.; Yager, K. G.; Berry, B.; Kim, H.-C.; Karim, A. *ACS Nano* **2012**, *6*, 10335-10342.
25. Qiang, Z.; Zhang, L.; Stein, G. E.; Cavicchi, K. A.; Vogt, B. D. *Macromolecules* **2014**, *47*, 1109-1116.
26. Berry, B. C.; Bosse, A. W.; Douglas, J. F.; Jones, R. L.; Karim, A. *Nano Lett.* **2007**, *7*, 2789-2794.
27. Singh, G.; Yager, K. G.; Smilgies, D.-M.; Kulkarni, M. M.; Bucknall, D. G.; Karim, A. *Macromolecules* **2012**, *45*, 7107-7117.
28. Majewski, P. W.; Yager, K. G. *ACS Nano* **2015**, *9*, 3896-3906.
29. Kelly, J. Y.; Albert, J. N. L.; Howarter, J. A.; Kang, S.; Stafford, C. M.; Epps, T. H., III; Faselka, M. J. *ACS Appl. Mater. Interfaces* **2010**, *2*, 3241-3248.
30. Kelly, J. Y.; Albert, J. N. L.; Howarter, J. A.; Stafford, C. M.; Epps, T. H., III; Faselka, M. J. *J. Polym. Sci., Part B: Polym. Phys.* **2012**, *50*, 263-271.

31. Qiang, Z.; Zhang, Y.; Groff, J. A.; Cavicchi, K. A.; Vogt, B. D. *Soft Matter* **2014**, 10, 6068-6076.
32. Luo, M.; Scott, D. M.; Epps, T. H., III. *ACS Macro Lett.* **2015**, 4, 516-520.
33. Shelton, C. K.; Epps, T. H., III *Polymer* **2016**, 105, 545-561.
34. Albert, J. N. L.; Young, W.-S.; Lewis, R. L.; Bogart, T. D.; Smith, J. R.; Epps, T. H., III. *ACS Nano* **2012**, 6, 459-466.
35. Stafford, C. M.; Roskov, K. E.; Epps, T. H., III; Fasolka, M. J. *Rev. Sci. Instrum.* **2006**, 77, 023908.
36. Shelton, C. K.; Epps, T. H., III *Device and Method for Making Shear-Aligned, Solvent-Cast Films*. U.S. Prov. Pat. Appl. 62/264986, filed Dec. 9, 2015. U.S. Pat. Appl. Filed on Dec. 8, 2016.
37. Kline, S. *J. Appl. Crystallogr.* **2006**, 39, 895-900.
38. Rawlings, J. B.; Ekerdt, J. G., *Chemical Reactor Analysis and Design Fundamentals*. Nob Hill Publishing: 2012.
39. Emerson, J. A.; Toolan, D. T. W.; Howse, J. R.; Furst, E. M.; Epps, T. H., III *Macromolecules* **2013**, 46, 6533-6540.
40. Elbs, H.; Krausch, G. *Polymer* **2004**, 45, 7935-7942.
41. Shelton, C. K.; Jones, R. L.; Epps, T. H., III. *in preparation*.
42. Hu, H.; Gopinadhan, M.; Osuji, C. O. *Soft Matter* **2014**, 10, 3867-3889.
43. Majewski, P. W.; Yager, K. G. *Nano Lett.* **2015**, 15, 5221-5228.
44. Schmidt, K.; Böker, A.; Zettl, H.; Schubert, F.; Hänsel, H.; Fischer, F.; Weiss, T. M.; Abetz, V.; Zvelindovsky, A. V.; Sevink, G. J. A.; Krausch, G. *Langmuir* **2005**, 21, 11974-11980.
45. DeRouchey, J.; Thurn-Albrecht, T.; Russell, T. P.; Kolb, R. *Macromolecules* **2004**, 37, 2538-2543.
46. Olszowka, V.; Hund, M.; Kuntermann, V.; Scherdel, S.; Tsarkova, L.; Böker, A. *ACS Nano* **2009**, 3, 1091-1096.
47. Choi, K.-J.; Spruiell, J. E.; White, J. L. *J. Polym. Sci., Part B: Polym. Phys.* **1982**, 20, 27-47.

48. Xu, T.; Zvelindovsky, A. V.; Sevink, G. J. A.; Lyakhova, K. S.; Jinnai, H.; Russell, T. P. *Macromolecules* **2005**, 38, 10788-10798.
49. Tetrahydrofuran. In *NIST Chemistry WebBook*, National Institute of Standards and Technology: Gaithersburg, MD, 2016.
50. o-Xylene. In *NIST Chemistry WebBook*, National Institute of Standards and Technology: Gaithersburg, MD, 2016.

Chapter 6

QUANTIFICATION OF SALT DISTRIBUTIONS IN BLOCK POLYMER ELECTROLYTE THIN FILMS

The use of neutron reflectometry (NR) to investigate the distribution of lithium salts in ion-conducting poly(styrene-*b*-oligo[oxyethylene] methacrylate) (PS-POEM) block polymer (BP) thin films in a high-resolution, non-destructive manner is discussed in this chapter. The quantification of lithium salt distributions within BP domains is considered challenging by conventional X-ray scattering or electron microscopy techniques, but neutron scattering contrast between PS, POEM, and three different lithium salts of interest, lithium trifluoromethanesulfonate (Li triflate), lithium bistrifluoromethanesulfonimide (LiTFSI), and lithium perchlorate (Li perchlorate), was ideal to determine that the salt mixed evenly within the POEM layers (*i.e.*, the salt to POEM concentration was constant through the POEM layers). The results from this section provide details of ion-mobility pathways through BP lithium ion battery membranes that can be used to improve future BP electrolyte membrane systems. Furthermore, the techniques demonstrated in this chapter can be applied to study a variety of additive distribution profiles (*i.e.*, salts, nanoparticles, homopolymer, metal precursors) in nanostructured thin films to progress research and expand applications of hierarchical materials. Text and figures are reproduced or adapted with permission from Gartner, T. E., III, Morris, M. A., Shelton, C. K., Dura, J. A., and Epps, T. H., III, *in preparation*.

6.1 Introduction

BP thin films composed of one ion-solvating block (*e.g.* poly[ethylene oxide] [PEO]) and one rigid, non-conducting block (*e.g.* polystyrene [PS]) have received significant attention for rechargeable battery membrane applications due to high thermal, mechanical, and electrochemical stabilities in comparison to traditional electrolyte systems.¹ The ion-conducting block typically is complexed with a metal salt to develop conducting pathways, while the non-conducting block provides stability and resists dendrite formations.²⁻⁴ To design battery systems with BPs that improve ion conductivity and mechanical properties simultaneously, studies have focused on the relationship between these properties and morphological effects.⁵⁻⁹ Although the correlation between mechanical properties and morphological effects is well-understood,^{10, 11} the link between ionic conductivities and morphology is more complicated.¹² For example, Panday *et al.* investigated PS-PEO lamellar systems doped with lithium salt and determined that ion conductivity increased with increasing molecular weight of the PEO block ($M_{n,PEO} = 7 - 98$ kg/mol).⁴ However, this result is in contrast to homopolymer electrolyte and low molecular weight BP ($M_{n,PEO} = 1.5 - 7$ kg/mol) systems in which a decrease in ion conductivity with increasing $M_{n,PEO}$ is measured.^{13, 14} The difference in ion conductivity trends suggests there are variations in the local ion distributions within polymer systems that must be understood to improve BP battery designs.

The distribution of lithium salts within ion-conducting BP thin films has been measured with energy-filtered transmission electron microscopy (EFTEM) and X-ray photoelectron spectroscopy (XPS) with conflicting results.^{12, 15} Using EFTEM, Gomez *et al.* determined LiTFSI was localized in the middle of PEO domains within a PS-PEO BP due to local stress fields, modeled with self-consistent field theory

(SCFT) in salt free systems, that prevented PEO chains from coordinating with lithium cations near PS-PEO interfaces.¹⁵ However, quantifying salt distribution was difficult with EFTEM as the small concentrations of lithium in the domains generated minimal contrast for analysis. To probe lithium ion distribution in a more robust manner, Gilbert *et al.* conducted XPS investigations and identified an even distribution of lithium salt throughout the ion-conducting domains in PS-POEM thin films (*i.e.*, the concentration of lithium salt was correlated directly to the concentration of POEM).¹² This work was in agreement with salt-doping SCFT models produced by Nakamura and Wang that calculated uniform distributions of salt within PEO domains, which suggested that factors such as electrostatic potential and local solvation energy also effect lithium salt distributions and ion-mobility pathways.¹⁶ However, the destruction of PS and POEM layers during XPS also limited salt distribution resolution, especially as more layers were removed.

To overcome inherent limitations in previous lithium salt distribution studies, this chapter describes NR experiments conducted to probe lamellar-forming PS-POEM diblock copolymer thin films doped with three different lithium salts (LiTFSI, Li triflate, and Li perchlorate) at varying concentrations. This chapter provides the first high-resolution, non-destructive analysis of salt segregation profiles in ion-conducting BPs by exploiting contrast from PS, POEM, and each lithium salt. The natural contrast between PS ($\rho_{PS} = 1.41 \times 10^{-6} \text{ \AA}^{-2}$) and POEM ($\rho_{POEM} = 0.78 \times 10^{-6} \text{ \AA}^{-2}$) paired with higher scattering length densities from each lithium salt ($\rho_{LiTFSI} = 3.55 \times 10^{-6} \text{ \AA}^{-2}$; $\rho_{Li\ triflate} = 3.08 \times 10^{-6} \text{ \AA}^{-2}$; $\rho_{Li\ perchlorate} = 4.23 \times 10^{-6} \text{ \AA}^{-2}$) in comparison to the BP domains permitted a quantitative and robust analysis described in this chapter.¹⁷ NR measurements of neat and salt-doped PS-POEM films indicated lithium

ions were distributed evenly (*i.e.*, salt concentrations were correlated evenly with POEM concentrations) throughout the POEM domains, which has significant implications on ion-mobility pathways during charge and discharge cycles and the design of next-generation lithium ion BP battery membranes.

6.2 Materials and Methods

6.2.1 Preparation of Salt-Doped Polymer Electrolyte Solutions and Films

The PS-POEM diblock copolymer used in this chapter ($M_n = 54$ kg/mol; block volume fractions: $f_S = 0.50$, $f_{OEM} = 0.50$; 8.5 PEO repeats in monomer side-chain, lamellae nanostructure) was synthesized (courtesy of Melody Morris) *via* an atom transfer radical polymerization method described in the literature.¹² The polymer was characterized by size exclusion chromatography (Viscotek, GPCmax WE-2001) and proton nuclear magnetic resonance spectroscopy (Bruker, AVX400). The dry PS-POEM was synthesized under an argon atmosphere and stored in an argon glovebox to limit exposure to water vapor. The three lithium salts (LiTFSI, Li triflate, and Li perchlorate) were purchased from Sigma Aldrich. Due to the hygroscopic nature of the lithium salts, each salt was sealed in a vacuum chamber, dried under dynamic vacuum for a minimum of 24 h, and transferred, under static vacuum, to an argon glove box for storage.

Tetrahydrofuran (THF; argon-purged and further dried by passage through two neutral alumina columns) solutions of neat PS-POEM and lithium salt-doped PS-POEM were made in an argon glovebox. Lithium salt concentrations (ether oxygen to lithium cation molar ratios [EO]:[Li]) of 45:1, 22:1, and 11:1 were used in this chapter. Anhydrous methanol (99.8%, Sigma Aldrich) was added to the salt-doped

solutions (≈ 30 wt% total solution) to help dissolve the polymer-salt complex prior to film casting.

Uniform and gradient thickness PS-POEM films (with and without lithium salt) were fabricated *via* flow coating¹⁸ onto toluene-rinsed and ultraviolet ozone treated silicon wafers. Films were thermally annealed under vacuum at 135 °C for 6 h to promote the formation of parallel lamellae nanostructures, as illustrated in Figure 6.1.¹² After annealing, film thickness was measured every 5 mm along the length of the film (total of 13 measurements across a 70 mm film) using a spectral reflectometer (Filmetrics, F20-UV). Commensurate thicknesses (*i.e.*, thicknesses at which island and hole formations did not develop) were noted on gradient thickness films to determine how thick to cast uniform thickness films. For the neat and salt-doped films, uniform thickness films for NR were cast at commensurate thicknesses equal to 3.5 domain spacings (L_0 ; asymmetric wetting behavior).

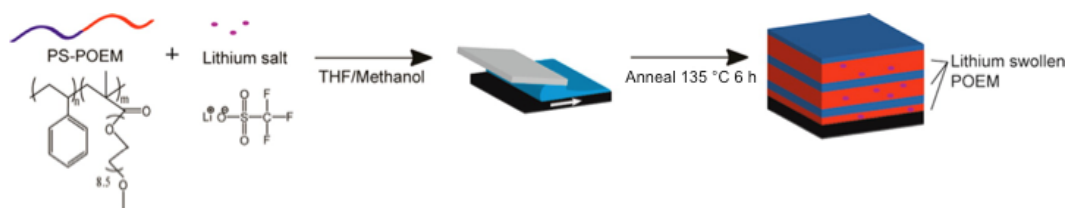


Figure 6.1: Schematic of the procedure to generate lamellar-forming, salt-doped PS-POEM thin films. Reprinted with permission from Gilbert, J. B. *et al.* *ACS Nano* **2014**, 9, 512-520, Copyright 2014 American Chemical Society.¹²

6.2.2 Neutron Reflectometry of Salt-Doped Polymer Films

NR experiments were conducted using the multi-angle grazing-incidence k-vector (MAGIK) instrument at the National Institute of Standards and Technology

(NIST) Center for Neutron Research (NCNR). Neutrons with an incident wavelength of 5 Å were directed at 64 mm long, 25 mm wide PS-POEM films with uniform thicknesses (ranging from 100 nm to 180 nm depending on the salt and salt concentration; $3.5 L_0$ total for all samples). For each sample, Q_z scans from 0 Å⁻¹ to 0.0877 Å⁻¹ with a step size of 0.0004 Å⁻¹ were recorded. Resulting reflectometry profiles were reduced using reflred software and analyzed with repeating lamellae models in reflfit and refl1D software programs.¹⁹ These modeling programs also were used to generate predictive fits prior to NR. Films were held in the neutron beam at reflectivity geometries using an aluminum sample holder and elastic clamps, as shown in Figure 6.2. The elastic clamps secured the film with minimal force in comparison to metal clamps to reduce warping of the silicon substrates. A borated aluminum mask was placed between the neutron source and films to prevent neutrons from scattering off the holder, clamp, and portions of the silicon wafers not coated with films.

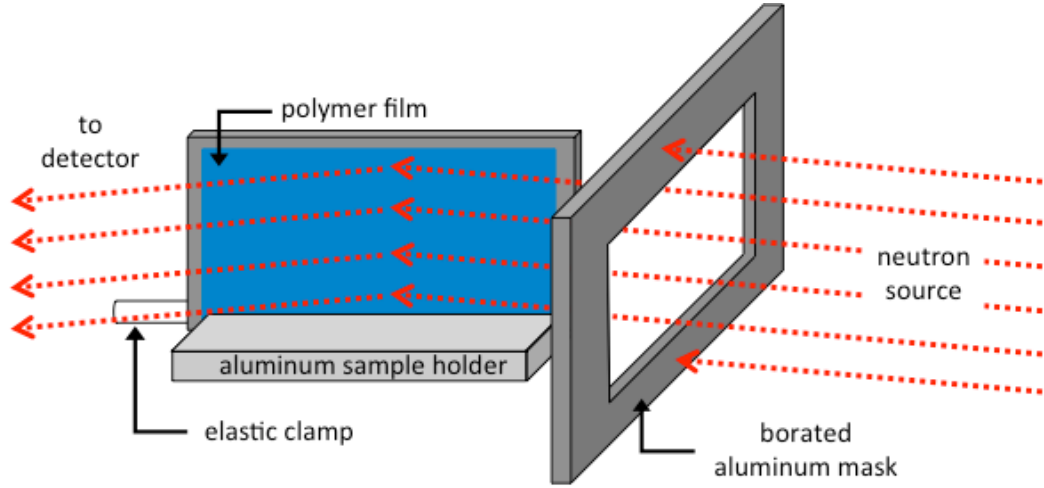


Figure 6.2: Illustration of NR setup for measuring lithium salt distributions in PS-POEM films. Neutrons were directed at PS-POEM films held in reflectivity geometries *via* an aluminum sample holder and elastic clamps. Scattering from the uncoated silicon wafers, sample holder, and clamp was prevented through the addition of a borated aluminum mask between the neutron source and the samples.²⁰

6.3 Lithium Salt Distribution from Neutron Reflectometry

The higher ρ values of the LiTFSI ($\rho_{LiTFSI} = 3.55 \times 10^{-6} \text{ \AA}^{-2}$), Li triflate ($\rho_{Li\ triflate} = 3.08 \times 10^{-6} \text{ \AA}^{-2}$), and Li perchlorate ($\rho_{Li\ perchlorate} = 4.23 \times 10^{-6} \text{ \AA}^{-2}$) in comparison to PS ($\rho_{PS} = 1.41 \times 10^{-6} \text{ \AA}^{-2}$) and POEM ($\rho_{POEM} = 0.78 \times 10^{-6} \text{ \AA}^{-2}$) was exploited to track the salt distributions in the film at four different salt ratios (neat and [EO]:[Li] = 45:1, 22:1, or 11:1).¹⁷ The diffusion of each lithium salt into the POEM domain increased the $\rho_{POEM/salt}$ of that layer in a predictable manner, as shown in Figure 6.3. The $\rho_{POEM/salt}$ values were calculated using salt concentration (ϕ_{salt} [vol%]), the ideal mixing assumption, and Equation 6.1.

$$\rho_{POEM/salt} = \rho_{POEM} \left(1 - \frac{\phi_{salt}}{100}\right) + \rho_{salt} \left(\frac{\phi_{salt}}{100}\right) \quad (6.1)$$

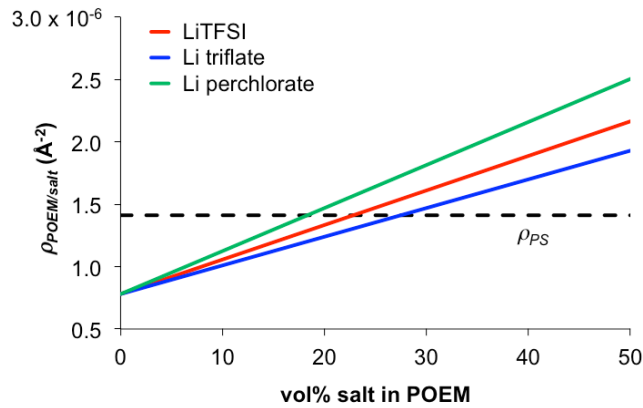


Figure 6.3: Plot of POEM domain ρ values ($\rho_{POEM/salt}$) at different salt concentrations (vol%) with LiTFSI, Li triflate, and Li perchlorate salts. At salt concentrations of 23 vol% (LiTFSI), 28 vol% (Li triflate), and 18 vol% (Li perchlorate), the POEM domain is contrast matched with the PS domain ($\rho_{PS} = 1.41 \times 10^{-6} \text{ \AA}^{-2}$; black dotted line).²⁰

At a specific concentration of salt (intersection between each salt line with the horizontal ρ_{PS} line), the $\rho_{POEM/salt}$ is equal to the ρ_{PS} and contrast matching is achieved. The neutrons are unable to distinguish between PS and POEM layers at the contrast match point, which results in two possible scattering profiles that define the salt distribution within the film, as shown in Figure 6.4. If the salt is evenly distributed within the POEM layers (Figure 6.4a), neutrons will reflect off the top of the film and the substrate only (*i.e.*, no multilayer structure will be measured). The resulting NR profile will contain Kiessig fringes (related to film thickness) but no Bragg peaks (related to the presence of multilayers). If the salt is localized to the middle of the POEM layers (Figure 6.4b), neutrons will reflect off the top of the film, the substrate, each PS/POEM interface, and at the regions of high vs. low salt concentrations in the middle of the POEM domains. The resulting NR profile will contain Kiessig fringes and Bragg peaks. Furthermore, the Bragg peaks are different than neat samples

(Appendix D, Figure D.1) due to the high $\rho_{POEM/salt}$ layer at the middle of POEM domains that changes the multilayer profile. Similar reflectivity profiles with large differences in Bragg peak size and location are not achievable with X-rays and demonstrate the advantage of neutron scattering to measure additive distributions in thin films.

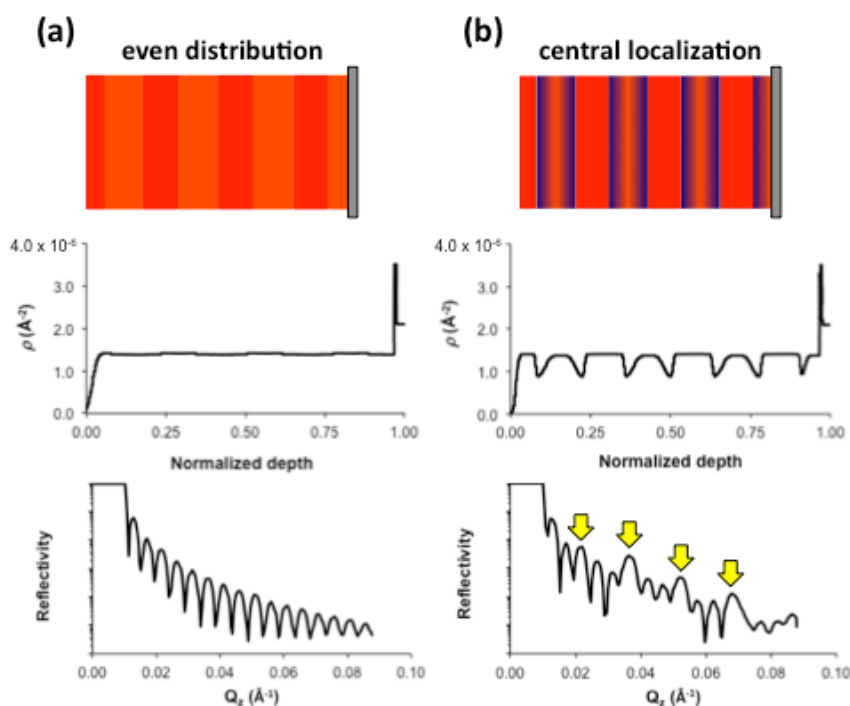


Figure 6.4: PS-POEM films doped with lithium salt as viewed by neutrons at the PS-POEM contrast match point (top row; blue = ρ of POEM; red = ρ of PS) along with predictive ρ (middle row) and reflectometry (bottom row) profiles. Even distributions of salt within the POEM layers (a) resulted in reflectivity profiles with no Bragg peaks. Central localization of the salt within the POEM layers (b) resulted in multiple Bragg peaks (highlighted by yellow arrows). Depths were normalized such that 0.00 was the free surface and 1.00 was the substrate surface.²⁰

Measured NR profiles of PS-POEM films without salt (neat) and doped with [EO]:[Li] ratios of 45:1, 22:1, and 11:1 (black data points) were collected on the MAGIK reflectometer, as shown in Figure 6.5. As the salt concentration increased, the Bragg peak locations shifted to lower Q_z and the space between Bragg peaks decreased. Furthermore, the intensity of the Bragg peaks relative to the Kiessig fringes decreased as salt concentration increased. Bragg peaks were not present in PS-POEM films doped with an [EO]:[LiTFSI] ratio of 11:1. Each profile was fit with a multilayer model (red lines) developed with NCNR fitting software.¹⁹ A more in-depth analysis of the model fits for Li triflate and Li perchlorate systems is shown in Appendix D, Figures D.2-D.3.

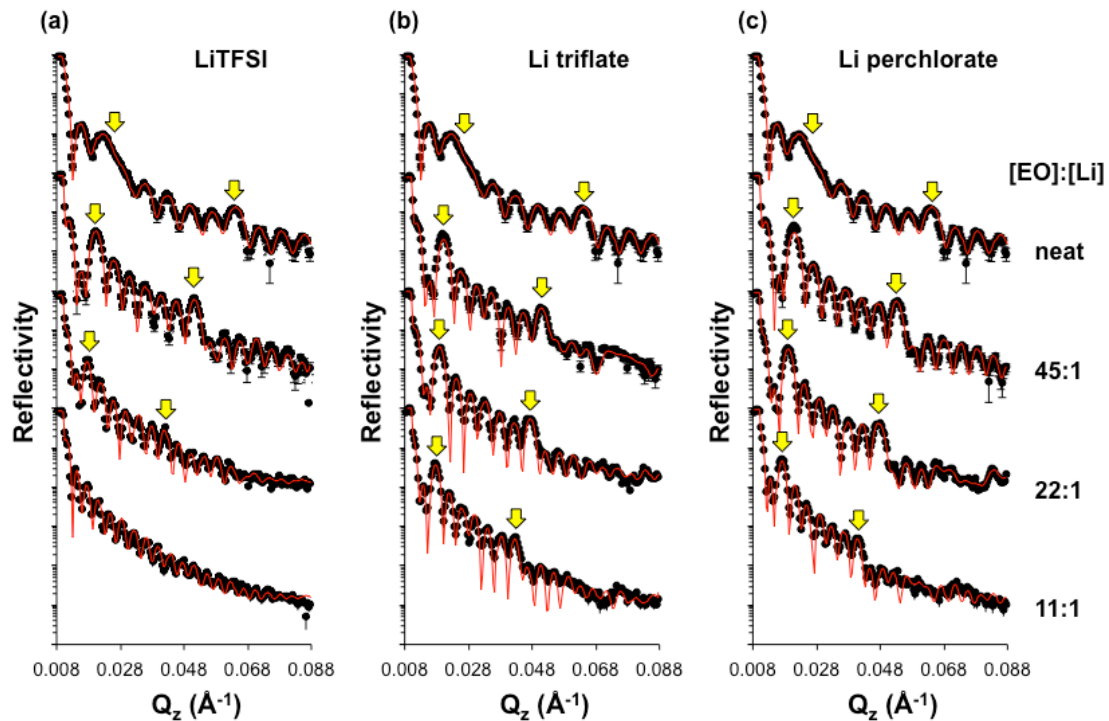


Figure 6.5: NR profiles (black data points) and model fits (red lines) of neat PS-POEM films (top profiles) and films doped with (a) LiTFSI, (b) Li triflate, and (c) Li perchlorate salts at [EO]:[Li] ratios of 45:1, 22:1, and 11:1. Bragg peaks (highlighted with yellow arrows) shifted to smaller Q_z values and decreased in intensity relative to the rest of the NR profile as salt concentration increased (from top to bottom profiles). Bragg peaks were not present in films doped with an 11:1 [EO]:[LiTFSI] ratio. Error bars represent one standard deviation from the measured intensity and were calculated during data reduction.²⁰

The shifting Bragg peak locations and intensities in NR profiles indicated that the salt segregated into the ion-solvating POEM block preferentially, which swelled the POEM layers and decreased the contrast between PS and POEM domains in the film. Evidence of an even distribution of salt in all samples was noted with the lack of secondary Bragg peaks related to lower ρ values at PS-POEM interfaces if the salt localized in the center of the POEM layers as shown in Figure 6.4b. Furthermore, the

lack of Bragg peaks in the 11:1 LiTFSI sample strongly suggested that the salt distributed evenly within the POEM domains as shown in Figure 6.4a. Contrast match points were not reached with Li triflate and Li perchlorate samples for two reasons: (1) the Li triflate had a lower ρ value than LiTFSI, so higher salt doping levels would be needed, and (2) the Li perchlorate is smaller (by volume) than LiTFSI, so POEM domains at the same [EO]:[Li] ratio contained less Li perchlorate by volume (*i.e.*, less influence on scattering). From $\rho_{POEM/salt}$ calculations (see Appendix D, Section D.1), the contrast match point was expected at LiTFSI, Li triflate, and Li perchlorate [EO]:[Li] ratios of 13:1, 6:1, and 5:1, respectively. Fit and calculated $\rho_{POEM/salt}$ values for the different salts and salt concentrations are shown in Figure 6.6. Ideal mixing was assumed for the calculated $\rho_{POEM/salt}$ values. Good agreement between the $\rho_{POEM/salt}$ values was noted for all samples, which helped validate the models used to fit to the data and extract the salt distribution profiles.

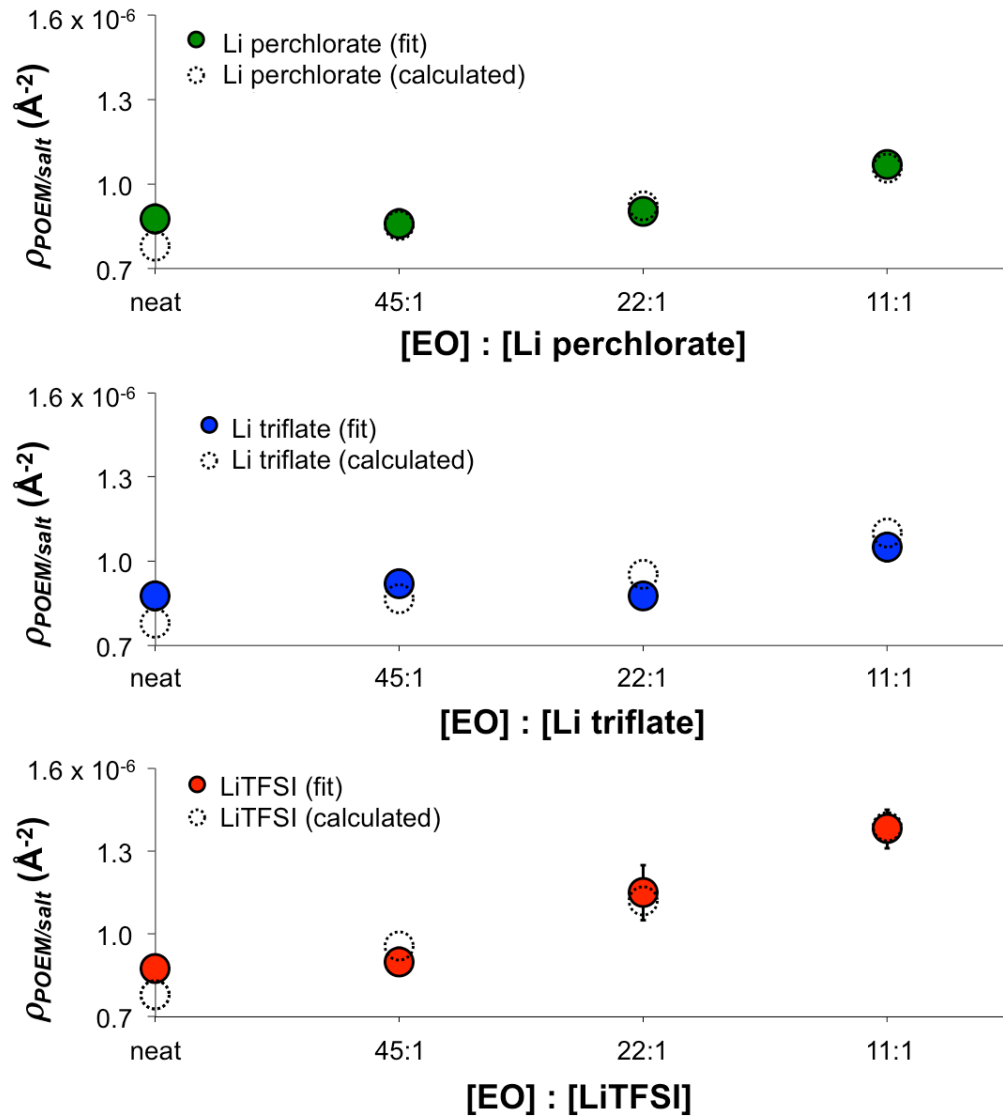


Figure 6.6: Fit (solid circles) vs. calculated (empty circles) $\rho_{POEM/salt}$ values for POEM domains doped with Li perchlorate (top row), Li triflate (middle row), and LiTFSI (bottom row). Calculated $\rho_{POEM/salt}$ values were determined with the ideal mixing assumption. Error bars were calculated as the standard deviation between every $\rho_{POEM/salt}$ value (*i.e.*, each layer) in the film.²⁰

To examine the distribution of salt within the films further, lamellar model fits to the PS-POEM films doped with LiTFSI were tested, as shown in Figure 6.7. The film depth was normalized from 0.0 (free surface) to 1.0 (substrate surface) to account for the change in total film thickness to accommodate $3.5L_0$ at each salt concentration as the POEM domains swelled with salt. In the ρ profiles, the ρ_{PS} values were maintained at the approximate value of neat PS (*i.e.*, the salt does not penetrate the PS domains). However, the $\rho_{POEM/salt}$ values increased with salt concentration due to solvation with the lithium ions. At an [EO]:[Li] of 11:1, the model fits indicated that the salt concentration was sufficient to raise the $\rho_{POEM/salt}$ values to ρ_{PS} , which resulted in the disappearance of Bragg peaks in the NR profiles. Therefore, the model fits match the predicted profiles for an even distribution of salt within the POEM domains. Notably, the salt concentration also appeared to deviate between POEM layers from the substrate surface to the free surface. Higher $\rho_{POEM/salt}$ values were modeled for POEM layers closer to the substrate surface, and a higher free surface ρ value was measured in many samples. The increase in salt concentration from the free to substrate surface was likely caused by the hydrophilicity of the silicon substrate. The lithium salts were highly hygroscopic and possibly segregated preferentially towards the polar silicon substrate, which resulted in a gradient in salt concentration through the film. The higher ρ value at the free surface was likely caused by lithium salt diffusing out of the film during thermal annealing to relieve polymer chain stresses when too much salt is present. Similar effects have been discussed in literature for PS-PEO films.²¹

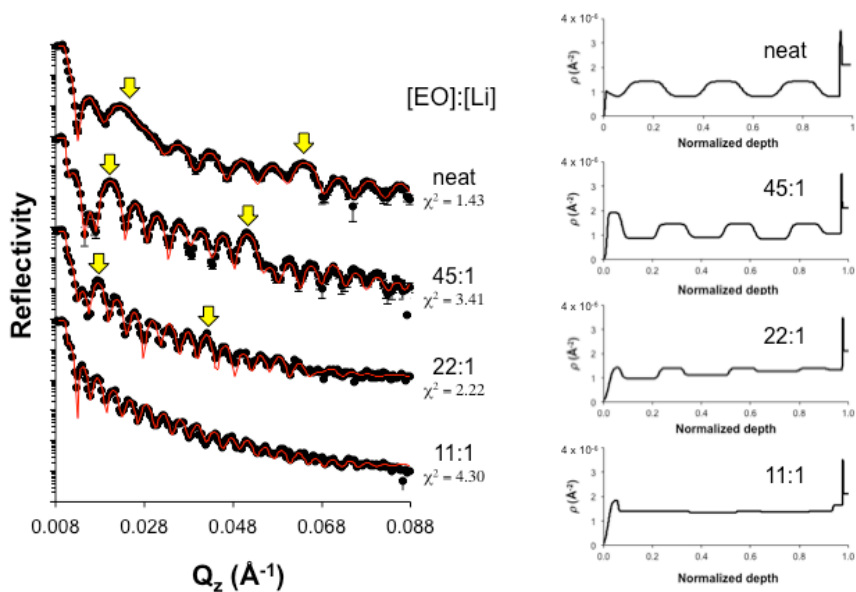


Figure 6.7: NR profiles (black data points) and model fits (red lines) for neat PS-POEM films and films doped with LiTFSI at 45:1, 22:1, and 11:1 [EO]:[Li] ratios (left side; profiles from Figure 6.5), and ρ profiles as a function of film depth (right side; normalized from 0.0 [free surface] to 1.0 [substrate surface]). As the salt concentration in the film was increased, the $\rho_{POEM/salt}$ values increased towards ρ_{PS} until a contrast match point ($\rho_{POEM/salt} = \rho_{PS}$) was achieved at approximately [EO]:[Li] = 11:1. Bragg peaks (highlighted by yellow arrows) in the NR profiles were not present at an 11:1 ratio. Furthermore, ρ models indicated a change in salt concentration in POEM layers from the free to substrate surface. Error bars in NR profiles represent one standard deviation from the measured intensity and were calculated during data reduction.²⁰

6.4 Conclusions

In this chapter, a quantitative analysis of lithium salt distribution in PS-POEM films was conducted with NR. The agreement between measured NR and fit ρ profiles of lithium salt-doped PS-POEM films strongly suggested the lithium salts studied (LiTFSI, Li triflate, and Li perchlorate) all distributed evenly within POEM domains throughout the film. Furthermore, the measured results matched well with

predictive model profiles for uniform distributions of lithium salts; namely, Bragg peaks disappeared or secondary Bragg peaks related to the lower ρ values at the PS-POEM interfaces were not present in all samples tested. Although an even distribution of LiTFSI within PS-POEM domains is in contrast to the EFTEM work on PS-PEO of Gomez *et al.* discussed in Section 6.1, the difference is likely the result of increased resolution achieved with NR. The NR profiles were the result of ρ profiles in the film rather than concentration profiles, so even though the salt and polymer concentration decreased at the interface (and significant contrast was not achievable with EFTEM), NR measured the relative concentration, which remained constant through the POEM domains. The ρ profiles also identified an increase in salt concentration at the free and substrate surfaces, which suggested thin film confinement effects must be accounted for to understand BP thin films for battery membrane applications. Furthermore, the use of NR improved upon more recent measurements conducted with XPS by incorporating a nondestructive technique in the measurement process. Thus, this chapter provides the first high-resolution, non-destructive analysis of lithium ion distributions in BP electrolyte thin films, which cannot be achieved easily with X-ray or microscopy tools. The results from this chapter have immediate impact in energy research as they help define ion mobility pathways through ion-conducting domains in BPs, which must be understood to develop more efficient lithium ion batteries, and provide a more robust analysis tool to measure additive distributions (*e.g.*, salts, homopolymers, nanoparticles, metal precursors) in nanostructured thin films for emerging research and applications.

REFERENCES

1. Young, W.-S.; Kuan, W.-F.; Epps, T. H., III *J. Polym. Sci., Part B: Polym. Phys.* **2014**, *52*, 1-16.
2. Singh, M.; Odusanya, O.; Wilmes, G. M.; Eitouni, H. B.; Gomez, E. D.; Patel, A. J.; Chen, V. L.; Park, M. J.; Fragouli, P.; Iatrou, H.; Hadjichristidis, N.; Cookson, D.; Balsara, N. P. *Macromolecules* **2007**, *40*, 4578-4585.
3. Wang, C.; Sakai, T.; Watanabe, O.; Hirahara, K.; Nakanishi, T. *J. Electrochem. Soc.* **2003**, *150*, A1166-A1170.
4. Panday, A.; Mullin, S.; Gomez, E. D.; Wanakule, N.; Chen, V. L.; Hexemer, A.; Pople, J.; Balsara, N. P. *Macromolecules* **2009**, *42*, 4632-4637.
5. Qin, J.; de Pablo, J. J. *Macromolecules* **2016**, *49*, 3630-3638.
6. Young, W.-S.; Epps, T. H., III *Macromolecules* **2012**, *45*, 4689-4697.
7. Majewski, P. W.; Gopinadhan, M.; Osuji, C. O. *Soft Matter* **2013**, *9*, 7106-7116.
8. Weber, R. L.; Ye, Y.; Schmitt, A. L.; Banik, S. M.; Elabd, Y. A.; Mahanthappa, M. K. *Macromolecules* **2011**, *44*, 5727-5735.
9. Wanakule, N. S.; Panday, A.; Mullin, S. A.; Gann, E.; Hexemer, A.; Balsara, N. P. *Macromolecules* **2009**, *42*, 5642-5651.
10. Khandpur, A. K.; Foerster, S.; Bates, F. S.; Hamley, I. W.; Ryan, A. J.; Bras, W.; Almdal, K.; Mortensen, K. *Macromolecules* **1995**, *28*, 8796-8806.
11. Dair, B. J.; Honeker, C. C.; Alward, D. B.; Avgeropoulos, A.; Hadjichristidis, N.; Fetters, L. J.; Capel, M.; Thomas, E. L. *Macromolecules* **1999**, *32*, 8145-8152.

12. Gilbert, J. B.; Luo, M.; Shelton, C. K.; Rubner, M. F.; Cohen, R. E.; Epps, T. H., III *ACS Nano* **2015**, 9, 512-520.
13. Yuan, R.; Teran, A. A.; Gurevitch, I.; Mullin, S. A.; Wanakule, N. S.; Balsara, N. P. *Macromolecules* **2013**, 46, 914-921.
14. Shi, J.; Vincent, C. A. *Solid State Ionics* **1993**, 60, 11-17.
15. Gomez, E. D.; Panday, A.; Feng, E. H.; Chen, V.; Stone, G. M.; Minor, A. M.; Kisielowski, C.; Downing, K. H.; Borodin, O.; Smith, G. D.; Balsara, N. P. *Nano Lett.* **2009**, 9, 1212-1216.
16. Nakamura, I.; Wang, Z.-G. *Soft Matter* **2012**, 8, 9356-9367.
17. Sears, V. F. *Neutron News* **1992**, 3, 26-37.
18. Stafford, C. M.; Roskov, K. E.; Epps, T. H., III; Fasolka, M. J. *Rev. Sci. Instrum.* **2006**, 77, 023908.
19. Kienzle, P. A.; O'Donovan, K. V.; Ankner, J. F.; Berk, N. F.; Majkrzak, C. F. <http://www.ncnr.nist.gov/reflpak> **2000-2006**.
20. Gartner, T. E., III; Morris, M. A.; Shelton, C. K.; Dura, J. A.; Epps, T. H., III. *in preparation*.
21. Metwalli, E.; Nie, M.; Körstgens, V.; Perlich, J.; Roth, S. V.; Müller-Buschbaum, P. *Macromol. Chem. Phys.* **2011**, 212, 1742-1750.

Chapter 7

CONCLUSIONS AND FUTURE WORK

7.1 Dissertation Summary

The potential use of block polymer (BP) thin films for next-generation nanolithography, nanotemplating, nanoporous membrane, organic optoelectronics, and electrolyte battery membranes applications has garnered significant attention in recent years.¹⁻⁵ The self-assembly of BP nanostructures into periodic arrays combined with the diverse and tunable chemistries, architectures, size-scales, and morphologies provides enormous potential for emerging nanotechnologies.⁶ However, the universal directed self-assembly of BP nanostructures into patterned arrays with low defect densities continues to be plagued by limited understanding of self-assembly kinetics and thermodynamics, high cost (both monetary and time) annealing procedures, and narrow efficacy among BP systems.⁷⁻⁹ In this dissertation, noteworthy efforts to predict and manipulate thin film confinement interactions to control nanostructure orientation and ordering (Chapter 3), understand the interplay between kinetics and thermodynamics of solvent vapor annealing (SVA), with and without shear-alignment, parameters to develop optimized annealing protocols and techniques (Chapters 4 and 5), and probe the influence of lithium ion distributions in BP electrolyte films (Chapter 6) were discussed to enhance the feasibility of industrial-scale use of BP thin films.

7.1.1 Substrate Modification for Through-Film Order and Orientation Control

BP thin film self-assembly is influenced strongly by substrate surface interactions that can dictate substrate-polymer wetting behavior and commensurability conditions,^{1, 10, 11} domain orientation,¹²⁻¹⁴ nanostructure ordering,^{10, 15, 16} morphology,¹⁷ and through-film uniformity.¹⁸⁻²¹ In Chapter 3, surface modification with a suite of chlorosilanes was used to determine how the substrate-polymer interactions can be manipulated to direct self-assembly for the desired applications. Specific focus was given to the interplay between individual dispersive and polar interactions of the total surface energy and whether or not the total surface energy needed to be decoupled to predict the substrate effects on self-assembly accurately. The different functionalities of the chlorosilane monolayers (*e.g.*, aromatic ring, methacrylate group, hydrocarbon chain, acetyl group) produced a variety of total surface energies and dispersive and polar components for improved investigation of surface energy effects. Studying the difference between total and decoupled surface energy equations was made possible by judicious choice of the poly(methyl methacrylate-*b-n*-butyl methacrylate) (PMMA-*Pn*BA) BP, which had two blocks with similar dispersive and different total and polar interactions.

Island and hole formations caused by energetically unfavorable chain stretching and compression at incommensurate film thicknesses were studied with optical microscopy (OM) for high-throughput analysis. Although OM could not provide nanoscale details of the response in self-assembly to different surface interactions, OM was used to monitor and measure the surface features easier and faster than atomic force microscopy (AFM). From OM, the thicknesses at which island and hole formations were and were not present and the size of the features indicated which polymer block was preferential for the substrate surface (*i.e.*, wetting

behavior), how far the substrate-polymer interaction effects propagated through the film thickness, and the strength of the substrate-polymer interactions. Each of these effects regulates self-assembly factors that dictate domain orientation and ordering in the film, and each must be controlled to produce the desired self-assembly for different applications.

Predictive formalisms were developed to capture the effect of total, dispersive, and polar surface energy components of the substrate-polymer interactions on the resulting self-assembly.^{10, 18} Wetting behavior was predicted from short-range, repulsive total surface interactions. The polymer block with the smallest interfacial energy with the substrate mitigated these repulsive interactions and segregated to the substrate surface. The Hamaker constant was included in this analysis to ensure these repulsive interactions did not propagate through the film and destabilize the interface. The strength of the substrate-polymer influence on self-assembly, which can affect defect density, was dependent on total and decoupled surface energy components as both short-range, repulsive and long-range, attractive interactions are experienced beyond the substrate-polymer interface. Larger interfacial energy differences created larger driving forces for self-assembly and more ordered structures in the film. The propagation distance of the substrate surface effects was dependent solely on the long-range, attractive interactions described by the decoupled surface energy components. Larger interfacial energy differences from dispersive and polar substrate-polymer interactions dominated competing free surface-polymer interactions at further film thicknesses and can be used to maintain a single orientation direction of domains through the film thickness. Understanding how all these surface energy components

affect BP thin film self-assembly provides a more translatable approach to tune nanostructure ordering and orientation with chemically-tailored substrate surfaces.

7.1.2 Nanostructure Reorganization Pathways during Solvent Vapor Annealing and Solvent Vapor Annealing with Soft Shear

SVA is a powerful annealing technique that can manipulate polymer-polymer and surface-polymer interactions to regulate self-assembly without potential film damage from high annealing temperatures.²² The tunability afforded with SVA can be exploited to alter commensurability conditions,²³⁻²⁷ nanostructure morphology and characteristic length scales,^{23, 24, 28-34} and wetting behavior in industrially-feasible time scales (s – min).³⁵⁻³⁷ However, understanding how different solvent choices and annealing conditions affect the interplay between kinetics and thermodynamics of nanostructure reorganization is crucial to develop optimized annealing protocols universally among BP thin film systems.

In Chapter 4, the swelling and deswelling of polymer domains in cylinder-forming poly(styrene-*b*-isoprene-*b*-styrene) (SIS) films was tracked with neutron scattering to elucidate the importance of polymer-solvent interactions and kinetic trapping on morphological development during SVA. The use of deuterated solvents in combination with non-deuterated polymer films permitted simultaneous monitoring of solvent diffusion and domain restructuring. The change in scattering contrast at different swelling conditions indicated the solvent was segregating preferentially into the individual domains. The quantified distribution of solvent was extracted from small-angle neutron scattering (SANS) experiments and was paired with changes to the BP thin film characteristic lengths obtained from neutron reflectometry (NR). As the film swelled and deswelled, the number of cylindrical layers and the out-of-plane

layer spacing (L_z) adjusted to accommodate increases and decreases in film thickness. If the glassy polystyrene domains were swollen with enough solvent to lower the glass transition temperature (T_g) below room temperature, the number of layers changed and L_z stayed relatively constant. The opposite was true if the T_g of the polystyrene was above room temperature, as the kinetically trapped polymer chains did not have mobility to alter the number of layers. Instead, the individual layers were stretched or compressed to account for changes in film thickness from solvent addition and removal, respectively. This analysis demonstrated the importance of controlled annealing conditions, which have significant implications on the size of domains, degree of ordering, and interfacial roughness.²⁴

More recently, SVA with soft shear (SVA-SS) has been used to direct domain restructuring in specific alignments.³⁸⁻⁴⁰ Polydimethylsiloxane (PDMS) pads placed on BP films induce shear forces during isotropic swelling and deswelling across the pinned film. These shear forces align nanostructures in specific directions across large film areas with limited defects. Furthermore, localized swelling and deswelling can be incorporated to control the alignment direction.⁴¹ SVA-SS has several advantages over current directed self-assembly strategies such as fewer and less expensive (*i.e.*, lower capital costs) processing steps, shorter annealing times, and more universal BP system effectiveness.

In Chapter 5, the SVA and shear mechanisms during SVA-SS were tuned to optimize directional alignment and defect annihilation by studying the kinetic pathways for nanostructure rearrangement with *in situ* SANS. The PDMS pad was found to induce chain mixing and nanostructure disordering during swelling and the formation of small grains upon deswelling; small grains reduced the entropic penalties

for domains to coalesce into large grains.⁴² Therefore, higher degrees of swelling were ideal to produce the fewest entropic barriers for alignment. The degree of swelling was manipulated by changing the solvent concentration exposed to the film and the elasticity of the PDMS. More elastic PDMS did not swell as much as less elastic PDMS. The deswell portion of the process required more control to achieve highly-aligned structures. For very swollen films, longer deswell times induced multiple drying fronts in competing directions, and shorter deswell times did not provide sufficient shear forces for alignment. Alignment in one direction occurred only if the drying rate was fast enough to prevent multiple drying fronts but slow enough to allow the shear forces to align domains. This analysis led to the development of new SVA-SS annealing protocols that exploit gradient thickness PDMS pads to direct the drying front propagation across the PDMS in a more controlled fashion while maintaining the ordering achieved with high degrees of swelling.⁴²

Insight gained from this chapter was incorporated into the development of a single-step, continuous process to cast and shear-align BP thin film nanostructures. BP solutions were cast onto substrate surfaces and allowed to dry to generate BP thin films, but the domains were poorly ordered and the grain size was small in the as-cast film since kinetic trapping occurs quickly. Therefore, shear forces across slightly solvent-swollen films immediately after casting were used to align domains in the direction of the shear force and increase grain sizes. This technique was demonstrated with PDMS pads following glass casting blades in Chapter 5 and is translatable to industrial roll-to-roll processing for high-throughput generation of aligned nanostructures in BP thin films.⁴³

7.1.3 Determination of Lithium Salt Distribution in Block Polymer Electrolyte Films

One highly investigated application for BP thin films is electrolyte membranes for lithium ion battery applications due to their high mechanical, thermal, and electrochemical stability in comparison to traditional liquid or gel-like electrolyte systems.⁴⁴ In these BP systems, one block in the BP is ion-conducting and complexed with a lithium salt, and the other block is mechanically stable to prevent dendrite formations that can lead to short circuits and explosions. However, the conductivities of BP electrolyte membranes are significantly smaller than pure ion-conducting membranes. Recent research has focused on increasing BP electrolyte conductivity by improving ion mobility pathways in the films through different chemistries, morphologies, and polymer-polymer interfacial interactions.⁴⁵ One heavily debated topic related to these ion mobility pathways is how the salt distributes within the film, which affects how the lithium ions move through the film during charge and discharge cycles. Previous literature investigating this topic has produced conflicting results and used destructive X-ray photoelectron spectroscopy (XPS) or low-resolution energy-filtered transmission electron microscopy to measure the distribution.^{44, 46}

In Chapter 6, the first high-resolution, non-destructive analysis of lithium salt distribution in BP electrolyte films was presented. NR was leveraged to measure scattering contrast between polystyrene (PS) domains, poly(oligo[oxyethylene] methacrylate) (POEM) domains, and three common lithium salts (lithium triflate, lithium bistrifluoromethanesulfonimide, and lithium perchlorate).⁴⁷ The scattering from the POEM was recorded as a function of salt concentration and film thickness to determine where the salt was localized in the film. The results were more conclusive than previous measurements with energy filtered transmission electron microscopy

and X-ray photoelectron spectroscopy due to the significant scattering contrast between the lithium salts and BP domains, and they indicated an even distribution of salt in the film for all lithium salts and salt concentrations. Thus, this analysis provided useful insights in the design of future BP electrolyte membranes with optimized parameters to exploit the ion mobility pathways throughout the entire ion-conducting domains.

7.1.4 Concluding Remarks

Overall, several investigations were conducted in this dissertation to determine how BP thin film nanostructures self-assemble when subjected to different processing conditions and how that knowledge can be applied to generate more universal annealing strategies, direct the self-assembly of nanostructures, and create nanotechnology with more feasible time-scales, costs, and performance outputs. The high-throughput substrate surface energy analysis in Chapter 3 indicated that substrate-polymer interactions can have large influences on BP thin film self-assembly. The development of predictive formalisms to control these interactions provides a promising approach to match the desired self-assembly with chemically-tailored substrate modification. The SVA study conducted in Chapter 4 clarified the interplay between the kinetic and thermodynamics effects that can regulate self-assembly and through-film periodicity of nanostructured thin films. The SVA-SS investigation in Chapter 5 provided unparalleled kinetic information about the alignment pathways of polymer domains during exposure to shear. The level of understanding gained from this analysis led to more controlled shear-alignment strategies for directed self-assembly and a one-step casting and shear-alignment technique for faster film processing in roll-to-roll assemblies. The salt-doped BP

electrolyte film analysis in Chapter 6 helped determine how lithium salt segregates in the ion-conducting domains to affect conductivity pathways through the film for battery applications and is the only investigation of its kind conducted with a high-resolution, non-destructive characterization tool. The experimental methods and information gleaned from these chapters will be beneficial for advancing BP thin film annealing techniques, optimizing directed self-assembly, and designing next-generation battery membranes.

7.2 Future Directions

Although significant progress in the field of BP thin film directed self-assembly was achieved through the work discussed in this dissertation, there are still many opportunities to advance the field. The ideas in this section represent follow-up projects to current results, next-generation annealing strategies and characterization tools to improve nanostructure ordering and orientation, and an expansion into more diverse BP architectures with promising properties. Each of these potential projects would have a significant impact on the field and would make large-scale use of BP thin films in commercial applications more feasible.

7.2.1 Patterned Polydimethylsiloxane Thickness/Elasticity

SVA-SS with PDMS pads is an effective and relatively universal strategy to control the alignment of BP thin film domains into desired pathways for templating and lithography applications.^{9, 38, 48, 49} Previous work with SVA-SS has demonstrated that the shear fields can be directed with localized swelling and deswelling to dictate the alignment pathways.⁴¹ However, these methods to “write” the desired patterns into the film typically require longer length scales than are ideal for industry (≈ 1 h per

50 mm film) and do not work for sharp changes in directions (*i.e.*, T-junctions). Developing advancements to SVA-SS that can provide more control over pattern definition in seconds rather than minutes would be a marked improvement over current standards. One possible approach to overcome this limitation is to incorporate gradients in the PDMS pads (*i.e.*, thickness or elasticity gradients) that direct the solvent drying front and the shear direction.⁴²

In Chapter 5, linear gradient thickness PDMS pads were used to maintain the nanostructure alignment throughout the film by imposing a single drying front; even-thickness pads led to the generation of uncontrollable drying fronts and competing alignment directions. Engineering more complex thickness gradients that incorporate multiple alignment directions could be useful for defining the drying front and shear direction into multiple, controlled directions. For example, in Figure 7.1 two Teflon molds with different gradient patterns are described: (a) a bend for sharp directional changes and (b) a spiral for circular pathways. PDMS pads can be cured in these molds to create gradient thickness PDMS pads for SVA-SS. The drying front, and induced shear force, should propagate in the direction of the gradient to create the desired patterns as the films and pads are deswelled.

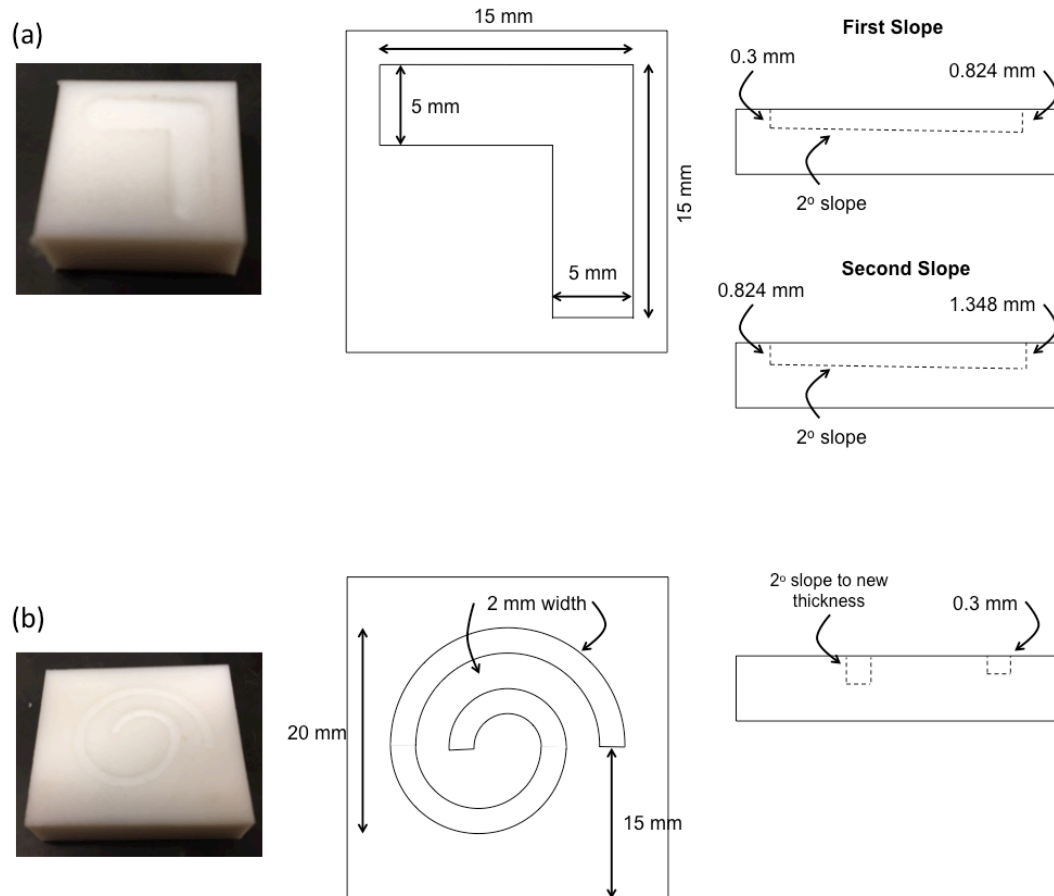


Figure 7.1: Images and schematics of Teflon molds with machined patterns for preparing PDMS pads with 2° gradients in thickness that can direct the drying front propagation during SVA-SS in (a) bends or (b) spirals.

Elasticity gradients also can control PDMS drying across the film since PDMS elasticity and swelling are inversely related. Elasticity gradients can be incorporated in PDMS pads with temperature gradients or photocurable PDMS and UV masks to direct the drying front.^{50, 51} This method also could be used to prevent shear-alignment in portions of the film by introducing areas of very high elasticity that will not swell or generate shear forces. A controlled drying front approach offers a potentially high-throughput and reproducible method to produce patterned BP thin

film nanostructures for templating and lithography applications. The time-scales and cost to achieve the same degrees of ordering and pattern specificity also represent a large improvement of current industry standards such as extreme ultraviolet lithography.⁵²

7.2.2 Shear-Alignment during Film Casting

Directed self-assembly with shear-alignment has been demonstrated in literature for a variety of BP thin film systems.⁷⁻⁹ Recent additions to the field using soft shear approaches have improved shear-alignment capabilities by shortening time scales for nanostructure rearrangement, permitting more universal annealing pathways, and increasing the effective distance of shear fields through the film.^{38-42, 49, 53, 54} However, many of these methods use multiple steps to achieve the desired ordering, which increases processing times or limits high-throughput generation of aligned nanostructures. Combining the advantages of hard and soft shear by exploiting residual solvent as the film dries during flow coating with a flexible PDMS blade, as demonstrated in Chapter 5, can be an effective strategy to cast and align nanostructures in a single step process, but defining optimal conditions without damaging the film is difficult. If too much solvent is in the film when the flexible blade shears the film, the polymer will not wet the substrate resulting in non-uniform films. If too little solvent is present, the domains do not have the necessary mobility to realign. Exploring different casting speeds, solution properties, and shear forces with this process could produce predictive controls to achieve the desired films. Furthermore, the effective solvent concentration window can be expanded with the help of mixtures of fast and slow drying solvents. The fast drying solvent would evaporate before the flexible blade shears the film, and the slow drying solvent would

maintain polymer chain mobility at the lowest possible solvent concentrations. Once the casting conditions are optimized, novel flexible blades with patterned structures or varying elasticities can be tested to explore the potential of this single step technique and how it can be modified for further self-assembly control.

Although flow coating is more amenable to industrial scale roll-to-roll processing,⁵⁵ single-step spin coating and alignment techniques could be useful for lab-scale experimentation and have more potential for domain patterning. A PDMS oil deposited on a drying film during spin coating potentially could create a shear force to align nanostructures as it is spun-off radially during spin coating. The shear forces would align the nanostructures either outward from the center or in spiral patterns depending on the viscosity of the fluid (*i.e.*, its spin-off pathway) if the same residual solvent conditions that were present with flow coating are maintained with spin coating. Davis *et al.* demonstrated a similar approach on pre-cast BP films that were thermally annealed and subjected to shear-alignment with PDMS oils in a rheometer (Figure 7.2).^{56, 57} Leveraging the residual solvent rather than thermal annealing could make the process single-step for high-throughput lab-scale generation of aligned nanostructures. Also, controlling spin-off pathways of the PDMS oil with patterned sluices offers the potential for directing the self-assembly in multiple directions. Devising methods to dictate the alignment pathways would require significant improvements of current flow and spin coating techniques but would greatly advance the production of BP thin films with directed self-assembly.

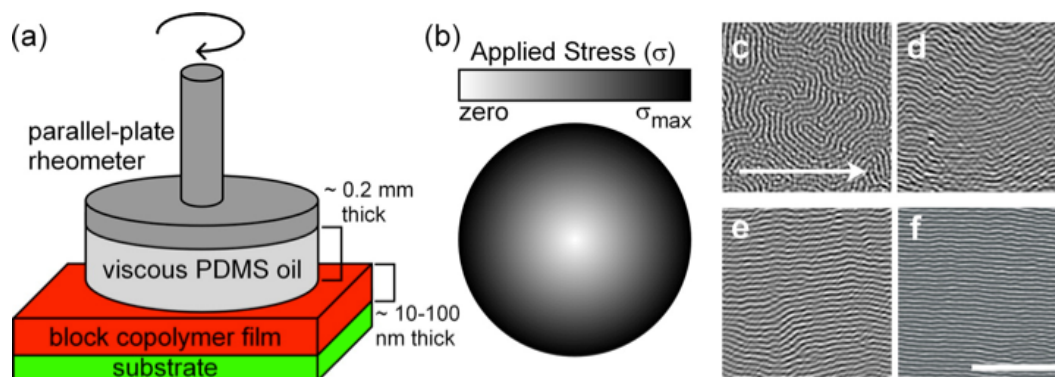


Figure 7.2: (a) Schematic of parallel-plate rheometer used to induce shear-alignment of a BP thin film with a viscous PDMS oil. (b) The applied stress was larger farther away from the center of the rheometer, and longer shear times (c \rightarrow d \rightarrow e \rightarrow f) improved in the ordering of the nanostructures. Reprinted with permission from Davis, R. L. *et al. Macromolecules* **2015**, 48, 5339-5347, Copyright 2015 American Chemical Society.⁵⁶

7.2.3 Reversible Roughening of Substrate Surfaces

Nanostructure domains that extend from the substrate to free surface are needed in many of the previously mentioned applications for BP thin films. For example, nanolithography and nanotemplating masks require holes in the film so the light or metal precursors can reach the substrate surface when introduced at the free surface, so lamellar and cylindrical nanostructures must be oriented perpendicular to the substrate.^{3, 58} Perpendicular orientations occur if the substrate surface is non-preferential to each of the polymer blocks in the BP.^{12, 59} Various strategies incorporating substrate modification,⁶⁰⁻⁶⁴ thermal annealing,^{12, 65} and SVA have been developed to induce neutral substrate-polymer interactions,^{28, 66-69} but tuning the effects precisely can be difficult and time-consuming for universal applicability among BP thin film systems.

One strategy to control the orientation of domains has been to cast BP films on roughened substrates.⁷⁰⁻⁷⁴ The rough surfaces increase the entropic penalties for

having a single polymer block wet the substrate as described in Figure 7.3.^{70, 75} The nanostructures orient perpendicular to the substrate to create more potential configurations for the chains to arrange the microdomain interfaces and reduce free energy. Kulkarni *et al.* demonstrated this technique using tunable rough surfaces of silica nanoparticle gels to achieve perpendicular lamellae structures in poly(styrene-*b*-methyl methacrylate) (PS-PMMA) thin films.⁷⁰ The researchers found that higher degrees of roughness generated more perpendicular structures; however more roughened substrates create coarser substrate-polymer interfaces, which limits the BP film's application as a high-precision lithographic mask or template.

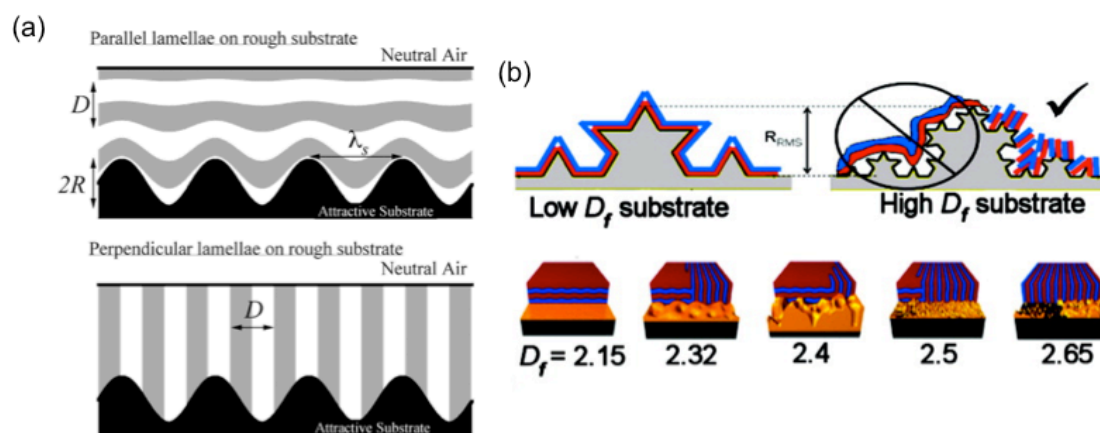


Figure 7.3: (a) A visual depiction of parallel and perpendicular nanostructures on roughened substrates is shown. Preferential (*i.e.*, attractive) surfaces typically orient domains parallel to the substrate, but maintaining the wetting of one domain on the rough substrate induces energetic penalties that are mitigated when domains orient perpendicular to the substrate. (b) As the roughness of the substrate (D_f) is increased, the likelihood of perpendicular orientations increases due to increasing entropic penalties. Left image adapted with permission from Sivaniah, E. *et al. Macromolecules* **2005**, 38, 1837-1849, Copyright 2005 American Chemical Society.⁷⁵ Right image reprinted with permission from Kulkarni, M. M. *et al. Macromolecules* **2012**, 45, 4303-4314, Copyright 2012 American Chemical Society.⁷⁰

Reversible roughening of the substrate surface would provide a novel route to exploit the benefits of high entropic penalties that reorient domains but maintain smooth interfaces for pattern transfer. The premise of this idea is to thermally anneal the BP films while the substrate surface is roughened to induce perpendicular orientation of the domains. The substrate roughening would be triggered by a response to heat, ultraviolet light, or an electric/magnetic field. Then, quenching the film on the roughened substrate would kinetically trap the domains before removing the stimulus that roughened the substrate. Over time, the substrate would become smooth and pull the pinned polymer to form an even interface. Low temperature or short time anneals might be required to pull the film to the interface as the roughening is removed, but these conditions should not result in complete restructuring of the assembly. The film then could be removed and used as a mask or template without sacrificing the pattern definition at one interface.

There are a variety of methods that can be explored to induce reversible substrate roughening such as shape-memory materials,⁷⁶⁻⁷⁹ ferrofluids,^{80, 81} and liquid crystal elastomers (LCEs) that respond to different stimuli (*e.g.*, light, temperature, magnetic fields, *etc.*) by changing structure.^{82, 83} When the stimulus is removed, the material returns to its original state. LCEs offer intriguing functionality within this group with their ability to respond to changes in temperature. For example, Ware *et al.* demonstrated how specially-designed LCEs capable of programmable shape changes when heated and cooled could be used to generate mechanical responses as shown in Figure 7.4.⁸² Layering BP films on LCEs would provide a one-step process to anneal polymer domains and roughen substrate surfaces by heating the assembly in a vacuum oven. Quenching the assembly would kinetically trap the domains and

smooth the substrate-polymer interface simultaneously. One potential downside is that the size scale of the surface features formed with temperature-responsive LCEs typically is on the order of μm to mm .⁸³ Shape-responsive polymers can form significantly smaller size scales than LCEs if a replacement is needed.⁸⁴

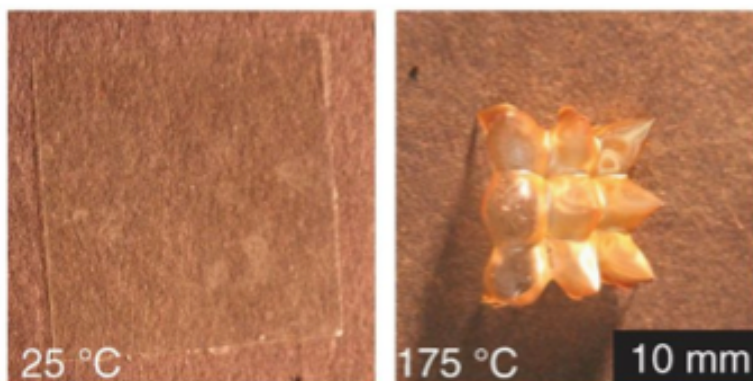


Figure 7.4: Photographs of LCE films at room temperature (25 °C) and after heating to 175 °C. A nine-peak roughness pattern appears in the film at higher temperatures and reversibly flattens when the temperature is decreased. Reprinted with permission from Ware, T. H. *et al. Science* **2015**, 347, 982-984, Copyright 2016 by the American Association for the Advancement of Science.⁸²

Reversible roughening of substrates would solve two key issues with block polymer thin film self-assembly. First, a facile and universal route to align domains perpendicular to the substrate would be achieved. This accomplishment would eliminate the need to investigate how to tune substrate surface energy and annealing conditions for an ever-expanding list of BP systems. Second, substrate surface area and substrate-polymer interface definition would not be sacrificed to produce better ordering. Techniques such as graphoepitaxy and non-reversible roughening work well

to direct nanostructure ordering but have inherent flaws by sacrificing the substrate-polymer interface.^{7,41} Layering BP thin films on substrates with the ability to coarsen and smooth when exposed to different stimuli would be attractive directed self-assembly methods for the generation of nanolithographic masks, material deposition templates, and nanoporous membranes.

7.2.4 Directing Designer Block Polymer Self-Assembly

The directed self-assembly of BP thin films for next-generation nanotechnology is dependent on the ability of BPs to form nanostructures with continually decreasing sizes.⁸⁵⁻⁸⁸ The current target for BP thin films is sub-10 nm to extend optical lithography beyond its current limits.^{89,90} However, the size scales of BP thin film nanostructures are limited by the interplay between the Flory-Huggins interaction parameter (χ), the length of polymer chains (*i.e.*, degree of polymerization [N]), and the order-disorder transition (ODT).⁸⁵ Smaller domains are created by decreasing N , but chains that are too small cannot phase separate unless χ is increased. Specifically, values of χN below 10.495 lead to chain mixing and disordered morphologies.⁹¹ High- χ polymers taking advantage of novel chemistries with highly repulsive polymer-polymer interactions have received significant attention in recent years as a method to reduce feature sizes and have led to the production of assemblies with pitches of ≈ 5 nm.⁹²⁻⁹⁵

Another interesting method to increase χ is to change the BP architecture. Literature has described how star BPs, with each arm as a different block or each arm representing a BP chain, have higher χ values than linear counterparts; attaching the individual polymer chains to one point creates additional entropic penalties and repulsive polymer-polymer interactions.^{91,96-99} Furthermore, the size of the

nanostructures formed with star BPs is dependent on the length of each arm, not the total molecular weight. This effect can shift the ODT of the phase diagram to lower segregation strengths and permit smaller N values without disordering the morphology.^{100, 101} The additional entropic interactions also can ease the formation of perpendicular nanostructures for lithography and templating applications.¹⁰²

The Epps Research Group has experimented with high- χ star BPs recently to investigate how to achieve smaller domains in thin films. The poly(styrene-*b*-octafluoropentyl methacrylate) (PS-POFPMA) BPs were cast on neutral substrate layers and exposed to SVA with a neutral solvent to reorient the lamellar domains perpendicular to the substrate as shown in Figure 7.5. The next step in this work is to shear-align the perpendicular lamellae to demonstrate directional alignment with different polymer architectures. Shear-alignment can be induced with SVA-SS. If star BP self-assembly can be directed with high degrees of ordering, their substantial benefits might warrant a change in the standard linear architecture to access and align sub-10 nm morphologies.

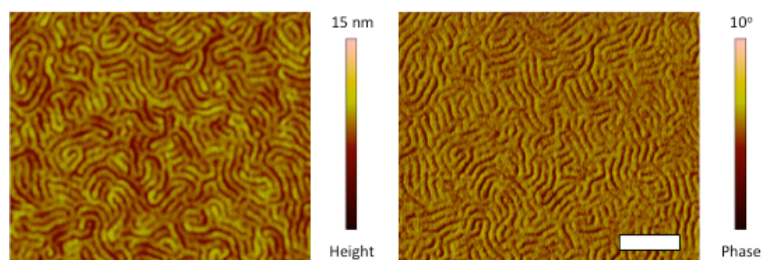


Figure 7.5: Height (left) and phase (right) atomic force micrographs of PS-POFPMA films with perpendicular lamellae structures after SVA with a neutral solvent. The scale bar represents 200 nm and applies to both images.

Star BPs are just one of several potential architectures to improve BP thin film self-assembly. Cyclic and figure-8 architectures can affect polymer-polymer interactions and alter size scales and interfacial mixing in comparison to linear counterparts.^{103, 104} Multiple blocks and chemistries also can be incorporated with different architectures to increase the phase space of designer morphologies.^{6, 105, 106} The key in choosing new chemistries and architectures should be to tune the desired properties. For example, star BPs with each arm composed of a linear ABA triblock chain might prove useful for generating perpendicular structures with smaller feature sizes. Nanostructures in ABA triblocks are easier to orient perpendicular than AB diblocks, as has been discussed in the literature.^{17, 107} Making substrate and free surface interactions preferential for the middle component in the ABA triblock leads to folding of the chains, which is energetically unfavorable and causes domains to reorient perpendicular to the substrate. Creating preferential surface interactions is easier than finding neutral conditions for a given BP system, so incorporating ABA triblocks in the star arms could prove beneficial for processing BP thin films.¹⁰⁸ As one example, PS-POFPMA star BPs with triblock arms rather than diblock arms have the potential to have smaller features than linear BP systems, orient perpendicular to the substrate without substrate modification, and be processed as nanotemplates with easy removal of the POFPMA domain with plasma etching. Understanding the key features needed for a given application and designing a BP thin film system around those parameters would be more efficient than the traditional approach of forcing a simple BP system (*e.g.*, PS-PMMA) to conform to the desired nanostructure arrangements. Moving forward, similar strategies to design BP systems for a given

application should be used, a process that requires additional information about how different chemistries and architectures affect inherent BP thin film properties.

7.2.5 Advancing Neutron Scattering of Block Polymer Thin Films

Neutron scattering of BP thin films has been used extensively to study annealing kinetics, characterize through-film morphologies, and quantify additive distributions in the individual domains.¹⁰⁹ The resolution capabilities of neutron scattering for organic materials, especially with the benefits of contrast variation and deuteration, provides enormous potential for investigating the self-assembly, restructuring, and application of future BP thin film systems.¹¹⁰⁻¹¹³ Chapters 4, 5, and 6 demonstrated how neutron scattering can be leveraged to gather key information about particular BP systems to predict how the domains will respond to various SVA conditions, to optimize SVA-SS procedures for improved nanostructure alignment and ordering, and to quantify lithium salt distributions in polymer electrolyte membranes. Although each of these projects progressed the field of BP thin film neutron scattering, the use of multi-dimensional neutron scattering techniques that capture both in-plane and out-of-plane information simultaneously would provide unprecedented levels of understanding if three criteria are met: data collection times improve, new *in situ* neutron scattering chambers are designed, and advanced computational modeling tools are developed.¹⁰⁹

Multidimensional neutron scattering tools can provide information from both the in-plane and out-of-plane directions simultaneously unlike the neutron scattering techniques covered in this dissertation, SANS and NR, which only capture details in one plane. Off-specular NR, grazing-incidence small-angle neutron scattering (GISANS), and rotational small-angle neutron scattering (RSANS) all can generate the

same information as SANS and NR but in one continuous experiment to ensure the same interactions are being monitored.^{70-72, 114-118} For example, Zhang *et al.* used RSANS to track the concentration of parallel (in-plane direction) vs. perpendicular (out-of-plane direction) orientations of cylindrical domains in BP thin films as a function of film thickness and annealing temperature (Figure 7.6). Pairing SANS and NR to get the same analysis would assume that different films were annealed the exact same or would require complex modeling to extract the desired information. Although these techniques are useful, they suffer from three key flaws. First, the time scales to achieve the necessary statistical information (several hours) are impractical for studying the kinetics of domain restructuring.^{119, 120} Designing novel methods to slow restructuring kinetics or improve resolution over shorter times (*e.g.*, introducing deuteration, increasing sample thickness, focusing on larger size scales [*Note: larger size scales are measured with smaller sample to detector distances, which leads to the collection of more scattered neutrons over the same scattering time*]) can help condense data collection times; additionally, as neutron fluxes continue to improve and next-generation neutron scattering tools, such as chromatic analysis neutron diffractometer or reflectometer (CANDOR), are built, data collection times should decrease.¹²¹⁻¹²³ Second, engineering new sample chambers that work in the multidimensional geometries are needed to pair with the scattering tools. The complex nature of the scattering geometries requires keen insight to develop sample environments without sacrificing scattering resolution or structural information.¹⁰⁹ For example, *in situ* RSANS during SVA would be a valuable investigation to obtain a 3-D solvent distribution profile for advanced SVA analysis but would require the construction of an SVA chamber that could rotate in the neutron beam without

affecting the scattering intensity from the empty cell (*i.e.*, the path length for the neutrons through the chamber has to be consistent). One approach to overcome this challenge is to design a spherical SVA chamber, likely out of titanium to minimize chamber scattering, which encloses the sample and rotates within the neutron beam. New scattering chambers for SANS and NR exploration of other directed self assembly techniques such as magnetic field alignment, microwave-assisted SVA, and solvothermal annealing also would be beneficial. Lastly, modeling data obtained from multidimensional scattering methods can be convoluted, especially if the system is changing over time.¹⁰⁹ The development of procedures and models to process the data and extract the desired information is vital to the widespread use of these tools. To achieve this goal, model systems that are easy to define (*e.g.*, diblock, lamellar-forming BP) should be tested first to create simple, multidimensional models. From there, the complexity should be increased (*e.g.*, lamellar to cylinders or diblock to triblock) to progress the models until they are more robust for different BP systems. Projects focused on one or more of these goals would greatly benefit the field of BP thin films by providing unmatched characterization tools for improved understanding of self-assembly phenomena.

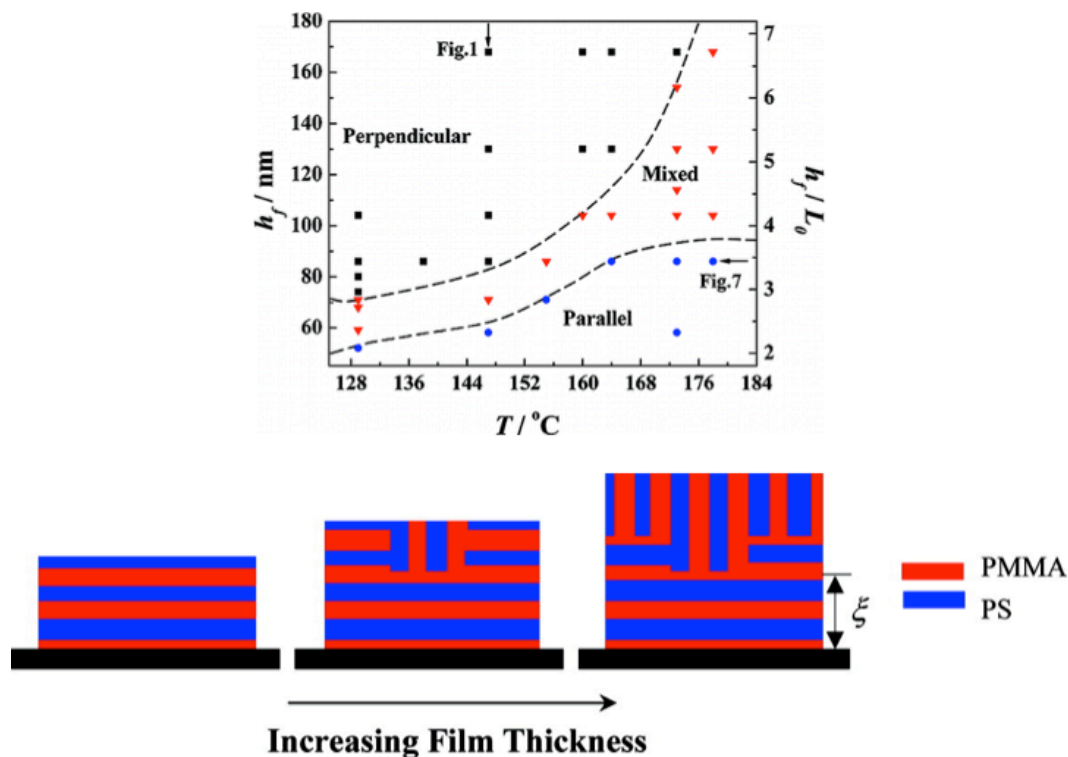


Figure 7.6: Through-film phase diagram for a cylindrical-forming BP thin film generated from RSANS. RSANS was used to probe the in-plane and out-of-plane features simultaneously to determine at what film thicknesses the substrate and free surface interactions competed to reorient domains. Adapted with permission from Zhang, *et al. ACS Nano* **2008**, 2, 2331-2341, Copyright 2008 American Chemical Society.¹¹⁸

REFERENCES

1. Albert, J. N. L.; Epps, T. H., III. *Mater. Today* **2010**, 13, 24-33.
2. Epps, T. H., III; O'Reilly, R. K. *Chem. Sci.* **2016**, 7, 1674-1689.
3. Bates, C. M.; Maher, M. J.; Janes, D. W.; Ellison, C. J.; Willson, C. G. *Macromolecules* **2013**, 47, 2-12.
4. Fasolka, M. J.; Mayes, A. M. *Annu. Rev. Mater. Sci.* **2001**, 31, 323-355.
5. Segalman, R. A. *Mater. Sci. Eng., R* **2005**, 48, 191-226.
6. Bates, F. S.; Hillmyer, M. A.; Lodge, T. P.; Bates, C. M.; Delaney, K. T.; Fredrickson, G. H. *Science* **2012**, 336, 434-440.
7. Luo, M.; Epps, T. H., III. *Macromolecules* **2013**, 46, 7567-7579.
8. Hu, H.; Gopinadhan, M.; Osuji, C. O. *Soft Matter* **2014**, 10, 3867-3889.
9. Majewski, P. W.; Yager, K. G. *J. Phys.: Condens. Matter* **2016**, 28, 403002.
10. Shelton, C. K.; Epps, T. H., III. *Macromolecules* **2015**, 48, 4572-4580.
11. Epps, T. H., III; DeLongchamp, D. M.; Fasolka, M. J.; Fischer, D. A.; Jablonski, E. L. *Langmuir* **2007**, 23, 3355-3362.
12. Han, E.; Stuen, K. O.; Leolukman, M.; Liu, C.-C.; Nealey, P. F.; Gopalan, P. *Macromolecules* **2009**, 42, 4896-4901.
13. Khanna, V.; Cochran, E. W.; Hexemer, A.; Stein, G. E.; Fredrickson, G. H.; Kramer, E. J.; Li, X.; Wang, J.; Hahn, S. F. *Macromolecules* **2006**, 39, 9346-9356.
14. Khaira, G. S.; Qin, J.; Garner, G. P.; Xiong, S.; Wan, L.; Ruiz, R.; Jaeger, H. M.; Nealey, P. F.; de Pablo, J. J. *ACS Macro Lett.* **2014**, 3, 747-752.

15. Nagpal, U.; Müller, M.; Nealey, P. F.; de Pablo, J. J. *ACS Macro Lett.* **2012**, 1, 418-422.
16. Edwards, E. W.; Stoykovich, M. P.; Müller, M.; Solak, H. H.; de Pablo, J. J.; Nealey, P. F. *J. Polym. Sci., Part B: Polym. Phys.* **2005**, 43, 3444-3459.
17. Luo, M.; Seppala, J. E.; Albert, J. N. L.; Lewis, R. L.; Mahadevapuram, N.; Stein, G. E.; Epps, T. H., III. *Macromolecules* **2013**, 46, 1803-1811.
18. Shelton, C. K.; Epps, T. H., III. *Macromolecules* **2016**, 49, 574-580.
19. Xu, T.; Hawker, C. J.; Russell, T. P. *Macromolecules* **2005**, 38, 2802-2805.
20. Ji, S.; Liu, C.-C.; Liao, W.; Fenske, A. L.; Craig, G. S. W.; Nealey, P. F. *Macromolecules* **2011**, 44, 4291-4300.
21. Welander, A. M.; Craig, G. S. W.; Tada, Y.; Yoshida, H.; Nealey, P. F. *Macromolecules* **2013**, 46, 3915-3921.
22. Sinturel, C.; Vayer, M.; Morris, M.; Hillmyer, M. A. *Macromolecules* **2013**, 46, 5399-5415.
23. Di, Z.; Posselt, D.; Smilgies, D.-M.; Papadakis, C. M. *Macromolecules* **2010**, 43, 418-427.
24. Shelton, C. K.; Jones, R. L.; Dura, J. A.; Epps, T. H., III. *Macromolecules* **2016**, 49, 7525-7534.
25. Knoll, A.; Tsarkova, L.; Krausch, G. *Nano Lett.* **2007**, 7, 843-846.
26. Hannon, A. F.; Bai, W.; Alexander-Katz, A.; Ross, C. A. *Soft Matter* **2015**, 11, 3794-3805.
27. Bai, W.; Yager, K. G.; Ross, C. A. *Macromolecules* **2015**, 48, 8574-8584.
28. Jung, Y. S.; Ross, C. A. *Adv. Mater.* **2009**, 21, 2540-2545.
29. Zettl, U.; Knoll, A.; Tsarkova, L. *Langmuir* **2010**, 26, 6610-6617.
30. Chen, Y.; Huang, H.; Hu, Z.; He, T. *Langmuir* **2004**, 20, 3805-3808.
31. Li, Y.; Huang, H.; He, T.; Gong, Y. *J. Phys. Chem. B* **2010**, 114, 1264-1270.

32. Bang, J.; Kim, B. J.; Stein, G. E.; Russell, T. P.; Li, X.; Wang, J.; Kramer, E. J.; Hawker, C. J. *Macromolecules* **2007**, *40*, 7019-7025.
33. Hsieh, I. F.; Sun, H.-J.; Fu, Q.; Lotz, B.; Cavicchi, K. A.; Cheng, S. Z. D. *Soft Matter* **2012**, *8*, 7937-7944.
34. Paik, M. Y.; Bosworth, J. K.; Smilges, D.-M.; Schwartz, E. L.; Andre, X.; Ober, C. K. *Macromolecules* **2010**, *43*, 4253-4260.
35. Cavicchi, K. A.; Berthiaume, K. J.; Russell, T. P. *Polymer* **2005**, *46*, 11635-11639.
36. Xuan, Y.; Peng, J.; Cui, L.; Wang, H.; Li, B.; Han, Y. *Macromolecules* **2004**, *37*, 7301-7307.
37. Lin, Z. Q.; Kim, D. H.; Wu, X. D.; Boosahda, L.; Stone, D.; LaRose, L.; Russell, T. P. *Adv. Mater.* **2002**, *14*, 1373-1376.
38. Qiang, Z.; Zhang, L.; Stein, G. E.; Cavicchi, K. A.; Vogt, B. D. *Macromolecules* **2014**, *47*, 1109-1116.
39. Qiang, Z.; Zhang, Y.; Groff, J. A.; Cavicchi, K. A.; Vogt, B. D. *Soft Matter* **2014**, *10*, 6068-6076.
40. Qiang, Z.; Zhang, Y.; Wang, Y.; Bhaway, S. M.; Cavicchi, K. A.; Vogt, B. D. *Carbon* **2015**, *82*, 51-59.
41. Luo, M.; Scott, D. M.; Epps, T. H., III. *ACS Macro Lett.* **2015**, *4*, 516-520.
42. Shelton, C. K.; Jones, R. L.; Epps, T. H., III. *in preparation*.
43. Shelton, C. K.; Epps, T. H., III *Device and Method for Making Shear-Aligned, Solvent-Cast Films*. U.S. Prov. Pat. Appl. 62/264986, filed Dec. 9, 2015. U.S. Pat. Appl. filed on Dec. 8, 2016.
44. Gilbert, J. B.; Luo, M.; Shelton, C. K.; Rubner, M. F.; Cohen, R. E.; Epps, T. H., III *ACS Nano* **2015**, *9*, 512-520.
45. Young, W.-S.; Kuan, W.-F.; Epps, T. H., III *J. Polym. Sci., Part B: Polym. Phys.* **2014**, *52*, 1-16.
46. Gomez, E. D.; Panday, A.; Feng, E. H.; Chen, V.; Stone, G. M.; Minor, A. M.; Kisielowski, C.; Downing, K. H.; Borodin, O.; Smith, G. D.; Balsara, N. P. *Nano Lett.* **2009**, *9*, 1212-1216.

47. Gartner, T. E., III; Morris, M. A.; Shelton, C. K.; Dura, J. A.; Epps, T. H., III. *in preparation*.
48. Singh, G.; Yager, K. G.; Berry, B.; Kim, H.-C.; Karim, A. *ACS Nano* **2012**, *6*, 10335-10342.
49. Majewski, P. W.; Yager, K. G. *ACS Nano* **2015**, *9*, 3896-3906.
50. Yu, S.; Sun, Y.; Ni, Y.; Zhang, X.; Zhou, H. *ACS Appl. Mater. Interfaces* **2016**, *8*, 5706-5714.
51. Palchesko, R. N.; Zhang, L.; Sun, Y.; Feinberg, A. W. *PloS One* **2012**, *7*, e51499.
52. Lapedus, M., What Happened to DSA? In *Semiconductor Engineering* [online], 2016, <http://semiengineering.com/what-happened-to-dsa/>.
53. Singh, G.; Batra, S.; Zhang, R.; Yuan, H.; Yager, K. G.; Cakmak, M.; Berry, B.; Karim, A. *ACS Nano* **2013**, *7*, 5291-5299.
54. Majewski, P. W.; Yager, K. G. *Nano Lett.* **2015**, *15*, 5221-5228.
55. Stafford, C. M.; Roskov, K. E.; Epps, T. H., III; Fasolka, M. J. *Rev. Sci. Instrum.* **2006**, *77*, 023908.
56. Davis, R. L.; Michal, B. T.; Chaikin, P. M.; Register, R. A. *Macromolecules* **2015**, *48*, 5339-5347.
57. Wu, M. W.; Register, R. A.; Chaikin, P. M. *Phys. Rev. E* **2006**, *74*, 040801.
58. Bang, J.; Jeong, U.; Ryu, D. Y.; Russell, T. P.; Hawker, C. J. *Adv. Mater.* **2009**, *21*, 4769-4792.
59. Forrey, C.; Yager, K. G.; Broadaway, S. P. *ACS Nano* **2011**, *5*, 2895-2907.
60. Ham, S.; Shin, C.; Kim, E.; Ryu, D. Y.; Jeong, U.; Russell, T. P.; Hawker, C. J. *Macromolecules* **2008**, *41*, 6431-6437.
61. Huang, E.; Pruzinsky, S.; Russell, T. P.; Mays, J.; Hawker, C. J. *Macromolecules* **1999**, *32*, 5299-5303.
62. Huang, E.; Russell, T. P.; Harrison, C.; Chaikin, P. M.; Register, R. A.; Hawker, C. J.; Mays, J. *Macromolecules* **1998**, *31*, 7641-7650.

63. In, I.; La, Y.-H.; Park, S.-M.; Nealey, P. F.; Gopalan, P. *Langmuir* **2006**, *22*, 7855-7860.
64. Mansky, P.; Russell, T. P.; Hawker, C. J.; Pitsikalis, M.; Mays, J. *Macromolecules* **1997**, *30*, 6810-6813.
65. Mansky, P.; Russell, T. P.; Hawker, C. J.; Mays, J.; Cook, D. C.; Satija, S. K. *Phys. Rev. Lett.* **1997**, *79*, 237-240.
66. Albert, J. N. L.; Bogart, T. D.; Lewis, R. L.; Beers, K. L.; Fasolka, M. J.; Hutchison, J. B.; Vogt, B. D.; Epps, T. H., III. *Nano Lett.* **2011**, *11*, 1351-1357.
67. Peng, J.; Kim, D. H.; Knoll, W.; Xuan, Y.; Li, B.; Han, Y. *J. Chem. Phys.* **2006**, *125*, 064702.
68. She, M.-S.; Lo, T.-Y.; Ho, R.-M. *Macromolecules* **2014**, *47*, 175-182.
69. Choi, E.; Park, S.; Ahn, H.; Lee, M.; Bang, J.; Lee, B.; Ryu, D. Y. *Macromolecules* **2014**, *47*, 3969-3977.
70. Kulkarni, M. M.; Yager, K. G.; Sharma, A.; Karim, A. *Macromolecules* **2012**, *45*, 4303-4314.
71. Yager, K. G.; Berry, B. C.; Page, K.; Patton, D.; Karim, A.; Amis, E. J. *Soft Matter* **2009**, *5*, 622-628.
72. Yager, K. G.; Forrey, C.; Singh, G.; Satija, S. K.; Page, K. A.; Patton, D. L.; Douglas, J. F.; Jones, R. L.; Karim, A. *Soft Matter* **2015**, *11*, 5154-5167.
73. Man, X.; Tang, J.; Zhou, P.; Yan, D.; Andelman, D. *Macromolecules* **2015**, *48*, 7689-7697.
74. Man, X.; Zhou, P.; Tang, J.; Yan, D.; Andelman, D. *Macromolecules* **2016**, *49*, 8241-8248.
75. Sivaniah, E.; Hayashi, Y.; Matsubara, S.; Kiyono, S.; Hashimoto, T.; Fukunaga, K.; Kramer, E. J.; Mates, T. *Macromolecules* **2005**, *38*, 1837-1849.
76. Han, Y.; Liu, Y.; Wang, W.; Leng, J.; Jin, P. *Soft Matter* **2016**, *12*, 2708-2714.

77. Huckfeldt, H.; Ahrend, F.; Holzinger, D.; Klein, H.; Engel, D.; Melzer, M.; Makarov, D.; Schmidt, O. G.; Fuhrmann-Lieker, T.; Ehresmann, A. *Adv. Funct. Mater.* **2015**, *25*, 6768-6774.
78. Zong, C.; Zhao, Y.; Ji, H.; Han, X.; Xie, J.; Wang, J.; Cao, Y.; Jiang, S.; Lu, C. *Angew. Chem.* **2016**, 3931-3935.
79. Kobatake, S.; Takami, S.; Muto, H.; Ishikawa, T.; Irie, M. *Nature* **2007**, *446*, 778-781.
80. Shima, P. D.; Philip, J. *J. Phys. Chem. C* **2011**, *115*, 20097-20104.
81. Zhou, J.; Turner, S. A.; Brosnan, S. M.; Li, Q.; Carrillo, J.-M. Y.; Nykypanchuk, D.; Gang, O.; Ashby, V. S.; Dobrynin, A. V.; Sheiko, S. S. *Macromolecules* **2014**, *47*, 1768-1776.
82. Ware, T. H.; McConney, M. E.; Wie, J. J.; Tondiglia, V. P.; White, T. J. *Science* **2015**, *347*, 982-984.
83. White, T. J.; Broer, D. J. *Nat. Mater.* **2015**, *14*, 1087-1098.
84. Jeong, H.-C.; Park, H.-G.; Jung, Y. H.; Lee, J. H.; Oh, B.-Y.; Seo, D.-S. *Langmuir* **2016**, *32*, 7138-7143.
85. Sinturel, C.; Bates, F. S.; Hillmyer, M. A. *ACS Macro Lett.* **2015**, *4*, 1044-1050.
86. Claudia, S.; Worawut, K.; Nikolaos, K.; Mathieu, S.; Marc, Z.; Michael, A. M.; Clivia, M. S. T. *Nanotechnology* **2014**, *25*, 175703.
87. Van Look, L.; Rincon Delgadillo, P.; Lee, Y.-T.; Pollentier, I.; Gronheid, R.; Cao, Y.; Lin, G.; Nealey, P. F. *Microelectron. Eng.* **2014**, *123*, 175-179.
88. Borah, D.; Shaw, M. T.; Holmes, J. D.; Morris, M. A. *ACS Appl. Mater. Interfaces* **2013**, *5*, 2004-2012.
89. Harriott, L. R. *Proc. IEEE* **2001**, *89*, 366-374.
90. Ito, T.; Okazaki, S. *Nature* **2000**, *406*, 1027-1031.
91. Matsen, M. W. *Macromolecules* **2012**, *45*, 2161-2165.
92. Cavicchi, K. A.; Russell, T. P. *Macromolecules* **2007**, *40*, 1181-1186.

93. Pitet, L. M.; Wuister, S. F.; Peeters, E.; Kramer, E. J.; Hawker, C. J.; Meijer, E. W. *Macromolecules* **2013**, *46*, 8289-8295.
94. Jeong, J. W.; Park, W. I.; Kim, M.-J.; Ross, C. A.; Jung, Y. S. *Nano Lett.* **2011**, *11*, 4095-4101.
95. Cushen, J. D.; Otsuka, I.; Bates, C. M.; Halila, S.; Fort, S.; Rochas, C.; Easley, J. A.; Rausch, E. L.; Thio, A.; Borsali, R.; Willson, C. G.; Ellison, C. J. *ACS Nano* **2012**, *6*, 3424-3433.
96. Martter, T. D.; Foster, M. D.; Yoo, T.; Xu, S.; Lizzaraga, G.; Quirk, R. P.; Butler, P. D. *Macromolecules* **2002**, *35*, 9763-9772.
97. Alward, D. B.; Kinning, D. J.; Thomas, E. L.; Fetters, L. J. *Macromolecules* **1986**, *19*, 215-224.
98. Matsen, M. W.; Schick, M. *Macromolecules* **1994**, *27*, 6761-6767.
99. Shi, W.; Tateishi, Y.; Li, W.; Hawker, C. J.; Fredrickson, G. H.; Kramer, E. J. *ACS Macro Lett.* **2015**, *4*, 1287-1292.
100. Ijichi, Y.; Hashimoto, T.; Fetters, L. J. *Macromolecules* **1989**, *22*, 2817-2824.
101. Hashimoto, T.; Ijichi, Y.; Fetters, L. J. *J. Chem. Phys.* **1988**, *89*, 2463-2472.
102. Lo, T.-Y.; Dehghan, A.; Georgopoulos, P.; Avgeropoulos, A.; Shi, A.-C.; Ho, R.-M. *Macromolecules* **2016**, *49*, 624-633.
103. Poelma, J. E.; Ono, K.; Miyajima, D.; Aida, T.; Satoh, K.; Hawker, C. J. *ACS Nano* **2012**, *6*, 10845-10854.
104. Isono, T.; Satoh, Y.; Miyachi, K.; Chen, Y.; Sato, S.-I.; Tajima, K.; Satoh, T.; Kakuchi, T. *Macromolecules* **2014**, *47*, 2853-2863.
105. Drolet, F.; Fredrickson, G. H. *Phys. Rev. Lett.* **1999**, *83*, 4317-4320.
106. Lodge, T. P. *Macromol. Chem. Phys.* **2003**, *204*, 265-273.
107. Vu, T.; Mahadevapuram, N.; Perera, G. M.; Stein, G. E. *Macromolecules* **2011**, *44*, 6121-6127.
108. Kim, S.; Yoo, M.; Baettig, J.; Kang, E.-H.; Koo, J.; Choe, Y.; Choi, T.-L.; Khan, A.; Son, J. G.; Bang, J. *ACS Macro Lett.* **2015**, *4*, 133-137.

109. Shelton, C. K.; Epps, T. H., III *Polymer* **2016**, 105, 545-561.
110. Russell, T. P. *Mater. Sci. Rep.* **1990**, 5, 171-271.
111. Hammouda, B., Probing Nanoscale Structures: The SANS Toolbox. NIST: 2008.
112. Pynn, R. *Los Alamos Science* **1990**, 19, 1-31.
113. Imae, T.; Kanaya, T.; Furusaka, M.; Torikai, N., *Neutrons in Soft Matter*. Wiley: 2011.
114. Hexemer, A.; Muller-Buschbaum, P. *IUCrJ* **2015**, 2, 106-125.
115. Muller-Buschbaum, P. *Polym. J.* **2013**, 45, 34-42.
116. Wang, W.; Metwalli, E.; Perlich, J.; Papadakis, C. M.; Cubitt, R.; Müller-Buschbaum, P. *Macromolecules* **2009**, 42, 9041-9051.
117. Wang, W.; Metwalli, E.; Perlich, J.; Troll, K.; Papadakis, C. M.; Cubitt, R.; Müller-Buschbaum, P. *Macromol. Rapid Commun.* **2009**, 30, 114-119.
118. Zhang, X.; Berry, B. C.; Yager, K. G.; Kim, S.; Jones, R. L.; Satija, S.; Pickel, D. L.; Douglas, J. F.; Karim, A. *ACS Nano* **2008**, 2, 2331-2341.
119. Müller-Buschbaum, P.; Cubitt, R.; Petry, W. *Langmuir* **2003**, 19, 7778-7782.
120. Müller-Buschbaum, P. *Eur. Polym. J.* **2016**, 81, 470-493.
121. *European Spallation Source Activity Report 2015*; European Spallation Source: Lund, Sweden, 2015.
122. Dimeo, R.; Ibberson, R.; O'Kelly, S.; Neumann, D.; Cappelletti, R.; Gehring, P. *Neutron News* **2013**, 24, 29-31.
123. Simmons, J. M.; Cook, J. C.; Ibberson, R. M.; Majkrzak, C. F.; Neumann, D. A. *J. Appl. Crystallogr.* **2013**, 46, 1347-1352.

Appendix A

SUPPORTING INFORMATION FOR CHAPTER 3

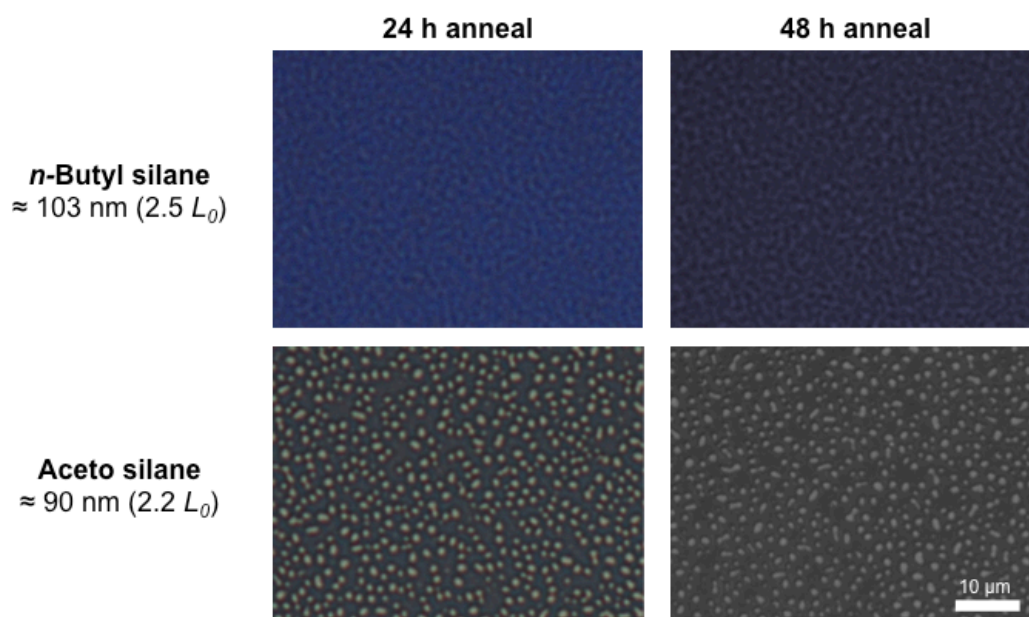


Figure A.1: Optical micrographs of ≈ 103 nm (2.5 domain spacings [L_0]) thick poly(methyl methacrylate-*b*-*n*-butyl methacrylate) (PMMA-*Pn*BA) films on *n*-butyl silane substrates and ≈ 90 nm ($2.2L_0$) thick PMMA-*Pn*BA films on aceto silane substrates after thermal annealing at 175 °C for 24 or 48 h. On *n*-butyl silane substrates, 103 nm was an incommensurate film thickness, but coherent island and hole formations were not expected due to the minimal propagation depth of the *n*-butyl silane surface field. On aceto silane substrates, 90 nm was an incommensurate film thickness, and island and hole formations were expected and present. As there were no distinct changes in the imaged structures at 24 h vs. 48 h, 24 h appeared to be sufficient time for microdomain equilibration. Reprinted with permission from Shelton, C. K. and Epps, T. H., III *Macromolecules* **2016**, 49, 574-580.¹

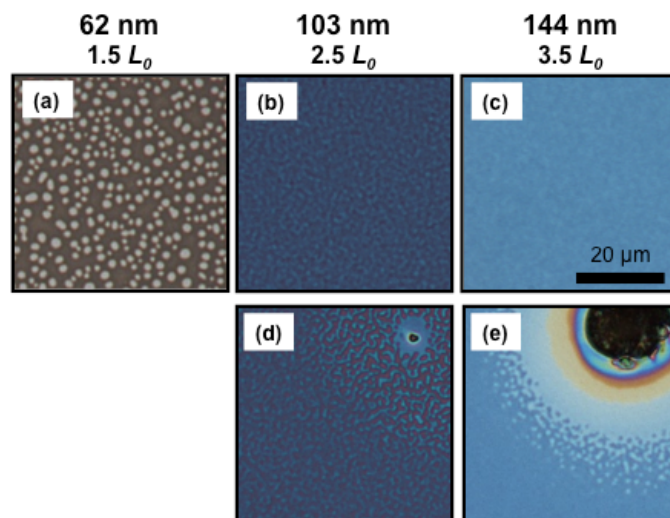


Figure A.2: Optical micrographs of PMMA-*P*nBA films on *n*-butyl silane modified substrates displayed distinct island and hole formations at (a) 62 nm thicknesses, less defined islands and holes at (b) 103 nm, and no distinct islands and holes at (c) 144 nm thicknesses. For the specimens shown in images b and c, it is likely that the enthalpic competition between the substrate and free surfaces hindered island and hole formation.^{2,3} Proximal to defects on thicker films (d, e), islands and holes were more prominent likely due to additional entropic interactions that enhanced the substrate surface field influence.⁴ The scale bar applies to all micrographs. Reprinted with permission from Shelton, C. K. and Epps, T. H., III *Macromolecules* **2016**, 49, 574-580.¹

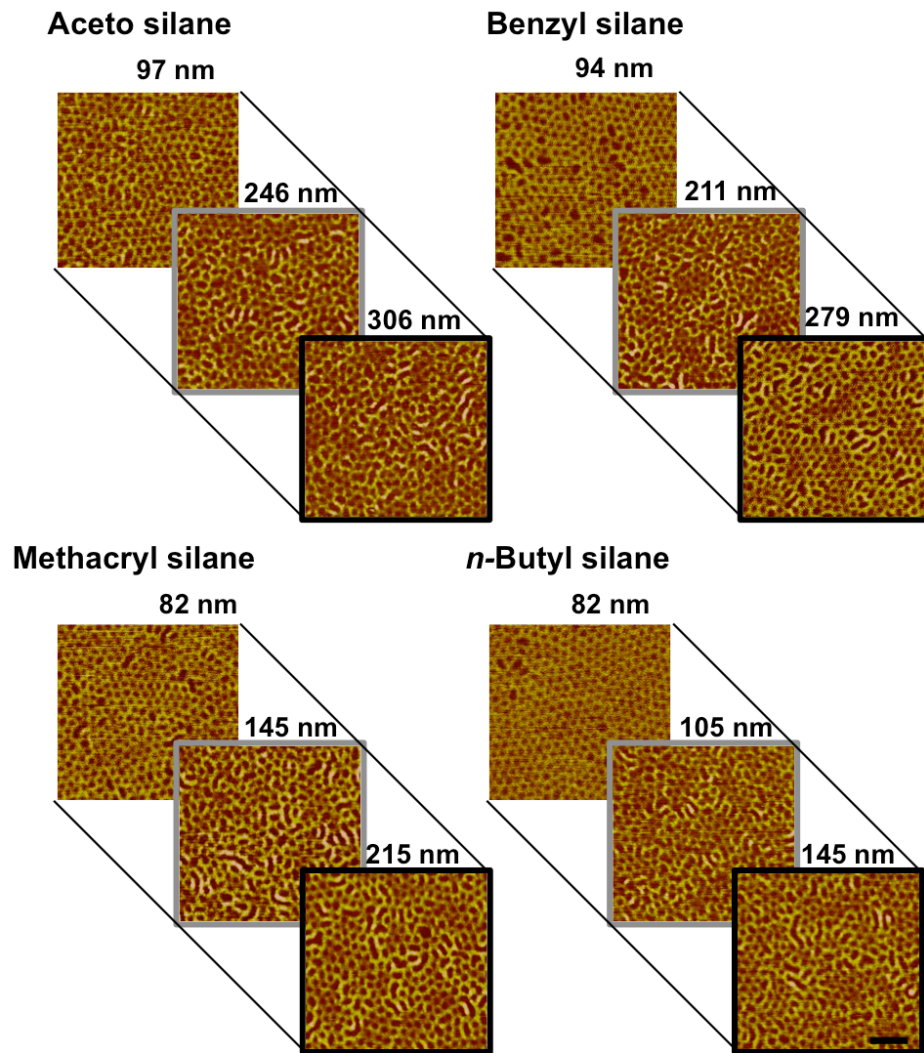


Figure A.3: Atomic force microscopy (AFM) images of PMMA-PnBA films at substrate dominant (no outline), transition (gray outline), and substrate/free surface competition (black outline) thicknesses on chlorosilane-modified substrates. A change in the free surface nanostructure from perpendicular cylinders to parallel, or folded, cylinders was noted once the transition thickness was reached on each substrate. The change in nanostructure orientation was correlated directly to the disappearance of islands and holes measured by optical microscopy as shown in Figure 3.6. The scale bar represents 200 nm and applies to all images. Reprinted with permission from Shelton, C. K. and Epps, T. H., III *Macromolecules* **2016**, 49, 574-580.¹

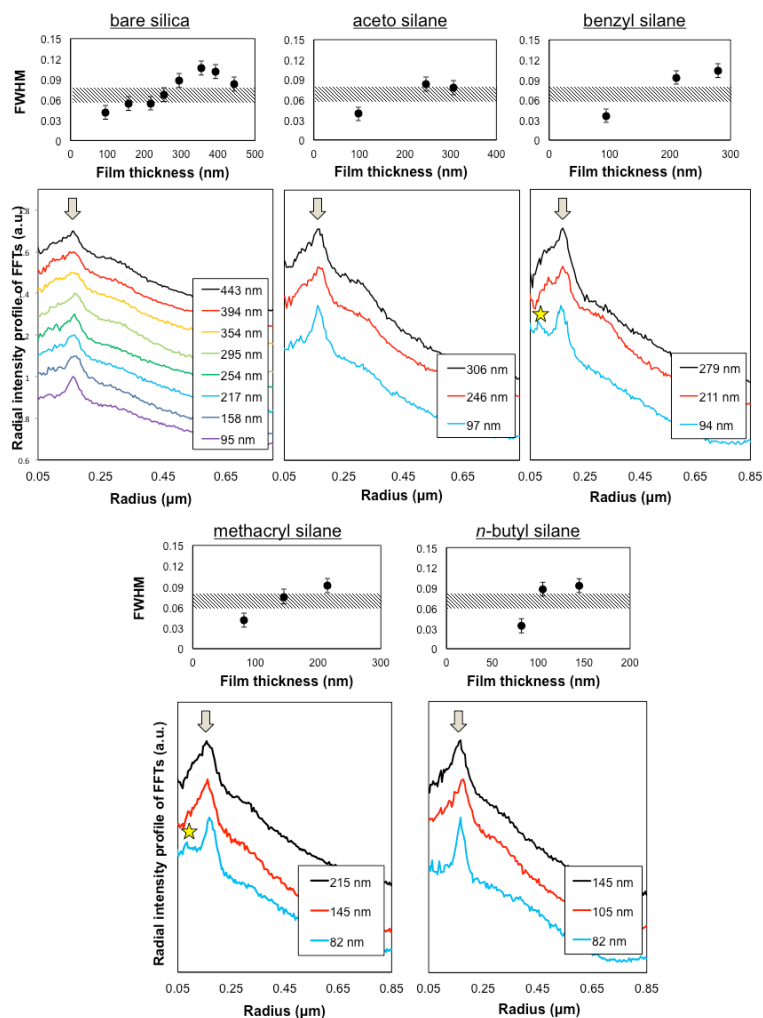


Figure A.4: Plots of full-width half-max (FWHM) values calculated from azimuthally averaged fast Fourier transformation intensity spectrum measured from free surface AFM images of gradient thickness PMMA-*P**n*BA films on bare silica and chlorosilane-modified substrates. The plots revealed an increase in the FWHM of the primary peak (location marked by an arrow) indicating the transition of film thickness from the substrate dominant region to the substrate/free surface competition region. The onset of the transition was consistent for all substrate surfaces (shaded region; FWHM \approx 0.06-0.08) and matched the transition region measured *via* optical microscopy. The extra peaks found on the benzyl and methacryl silane traces (location marked by stars) were artifacts from the AFM/FFT processing and not free surface structures. Reprinted with permission from Shelton, C. K. and Epps, T. H., III *Macromolecules* **2016**, 49, 574-580.¹

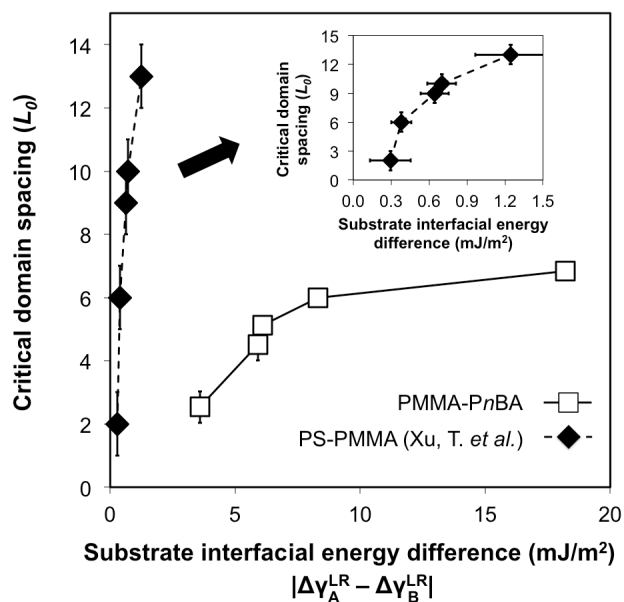


Figure A.5: Comparison of critical propagation depths of the substrate surface field between two AB diblock copolymer (PMMA-PnBA and poly[styrene-*b*-methyl methacrylate] [PS-PMMA]) systems using long-range interfacial energy differences and film thicknesses normalized by system-dependent L_0 's. PS-PMMA data were taken from literature, and the same initial linear increase followed by the possible onset of a plateau as interfacial energy difference increased was noted.² The inset plot is rescaled to focus on the PS-PMMA data for clarity. The lines between data points are to guide the eye. Reprinted with permission from Shelton, C. K. and Epps, T. H., III *Macromolecules* **2016**, 49, 574-580.¹

REFERENCES

1. Shelton, C. K.; Epps, T. H., III. *Macromolecules* **2016**, 49, 574-580.
2. Xu, T.; Hawker, C. J.; Russell, T. P. *Macromolecules* **2005**, 38, 2802-2805.
3. Ji, S.; Liu, C.-C.; Liao, W.; Fenske, A. L.; Craig, G. S. W.; Nealey, P. F. *Macromolecules* **2011**, 44, 4291-4300.
4. Yager, K. G.; Berry, B. C.; Page, K.; Patton, D.; Karim, A.; Amis, E. J. *Soft Matter* **2009**, 5, 622-628.

Appendix B

SUPPORTING INFORMATION FOR CHAPTER 4

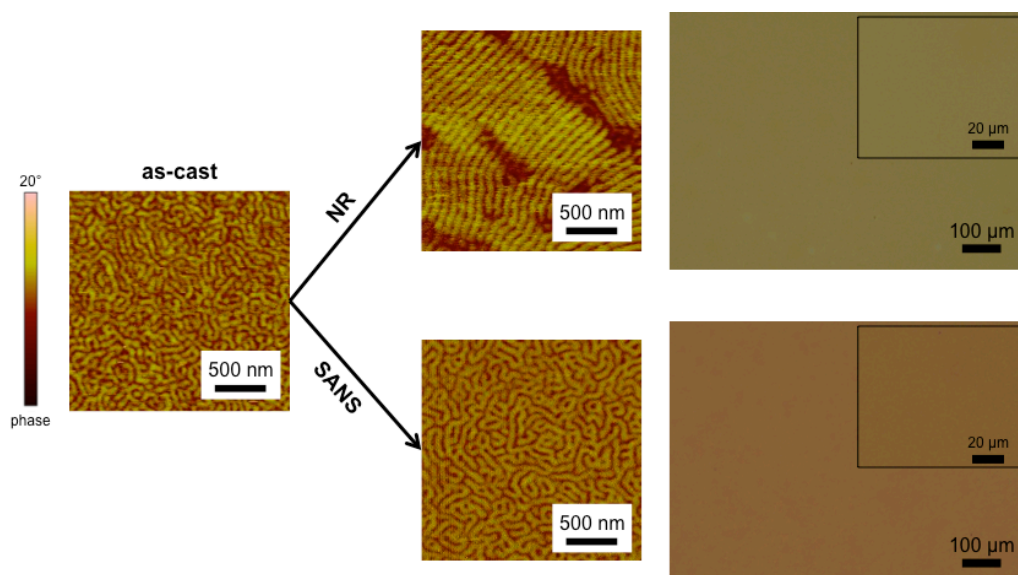


Figure B.1: Atomic force microscopy (AFM) images of as-cast and solvent annealed poly(styrene-*b*-isoprene-*b*-styrene) (SIS) films (cylindrical nanostructures) used in the neutron reflectometry (NR) and small-angle neutron scattering (SANS) experiments. SIS films exposed to *d*-benzene during SANS showed a marginal improvement (2.5 h anneal) in ordering in comparison to as-cast films, but the ordering greatly improved in films exposed to *d*-benzene during NR (8 h anneal). The shorter SANS data collection times were desired to ensure that the *C* variable (intensity) in the broad peak models was changing solely as a function of the solvent concentration and not as a function of improved ordering. *Note: the SVA times used herein were not long enough to cause damage to the films (e.g., dewetting) as demonstrated by optical micrographs of films following SVA (see rightmost panels).* Reprinted with permission from Shelton, C. K. *et al. Macromolecules* **2016**, 49, 7525-7534, Copyright 2016 American Chemical Society.¹

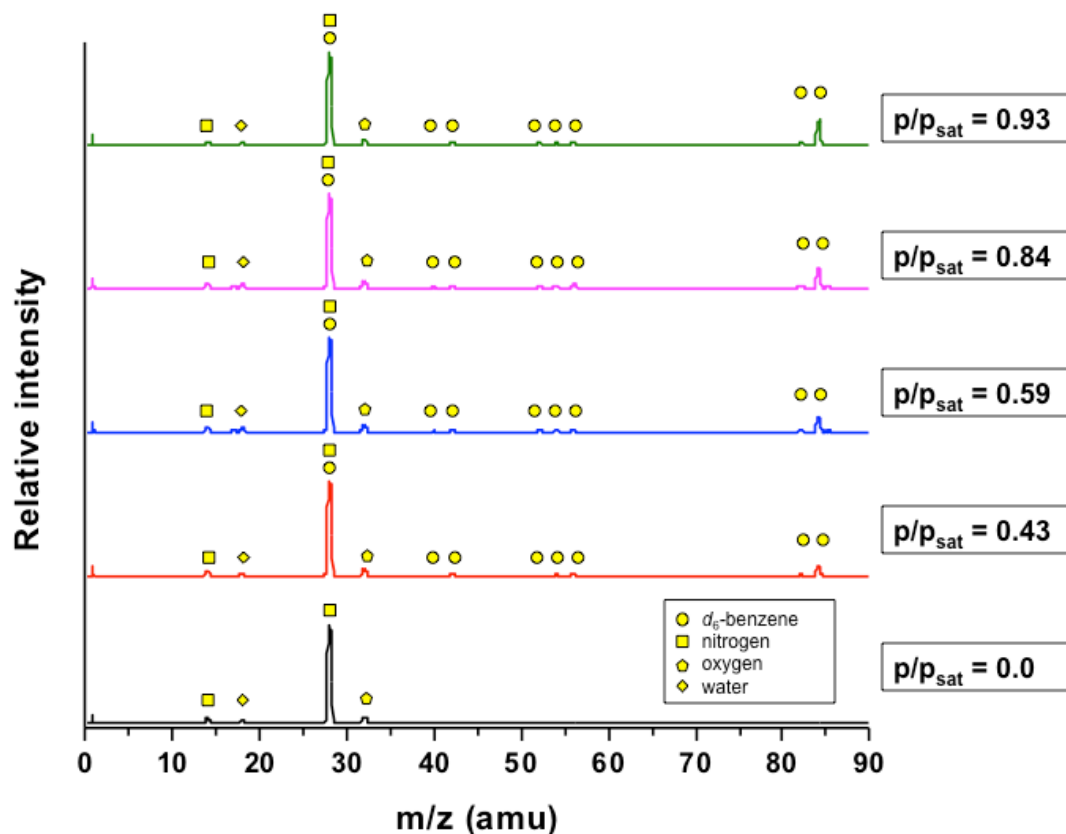


Figure B.2: Mass spectrometry (MS) profiles for nitrogen bubbled through deuterated benzene (d_6 -benzene) obtained at the chamber outlet. Solvent partial pressure was adjusted by changing the ratio of the volumetric flow rates of nitrogen as a pure stream and d_6 -benzene-rich nitrogen. Fragmentation patterns for d_6 -benzene, nitrogen, oxygen, and water were used to identify the components associated with each MS peak as well as the relative amount of each component in the gaseous stream.² The relative amount of d_6 -benzene (p) was divided by the saturated vapor pressure (p_{sat}) of d_6 -benzene at 25 °C to calculate the p/p_{sat} values used in the analyses.³ Reprinted with permission from Shelton, C. K. *et al. Macromolecules* **2016**, 49, 7525-7534, Copyright 2016 American Chemical Society.¹

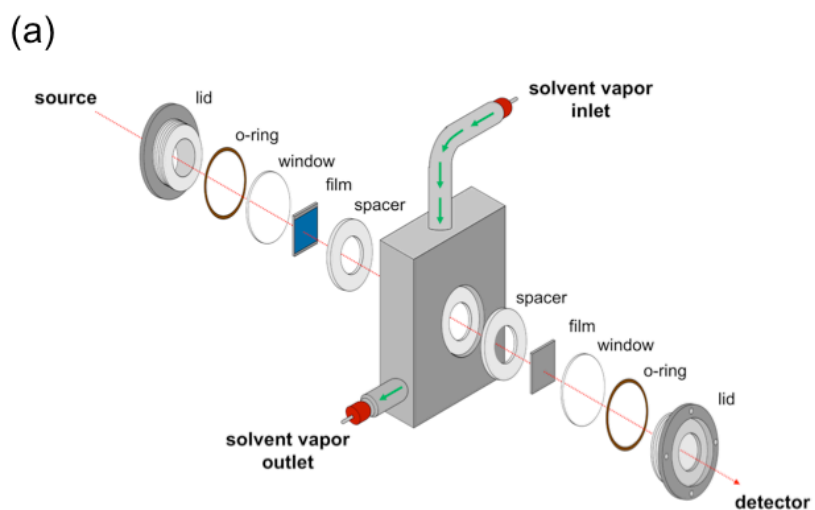


Figure B.3: (a) Illustration and (b) photograph of SANS sample cell for *in situ* SVA experiments. The sample cell housed two SIS films (400 ± 4 nm each) facing inward, towards a sealed air gap. Spacers were utilized to create the air gap through which solvent vapor flowed. Quartz glass windows were used as neutron transparent windows to reduce scattering from the sample cell. Adapted with permission from Shelton, C. K. *et al. Macromolecules* **2016**, 49, 7525-7534, Copyright 2016 American Chemical Society.¹

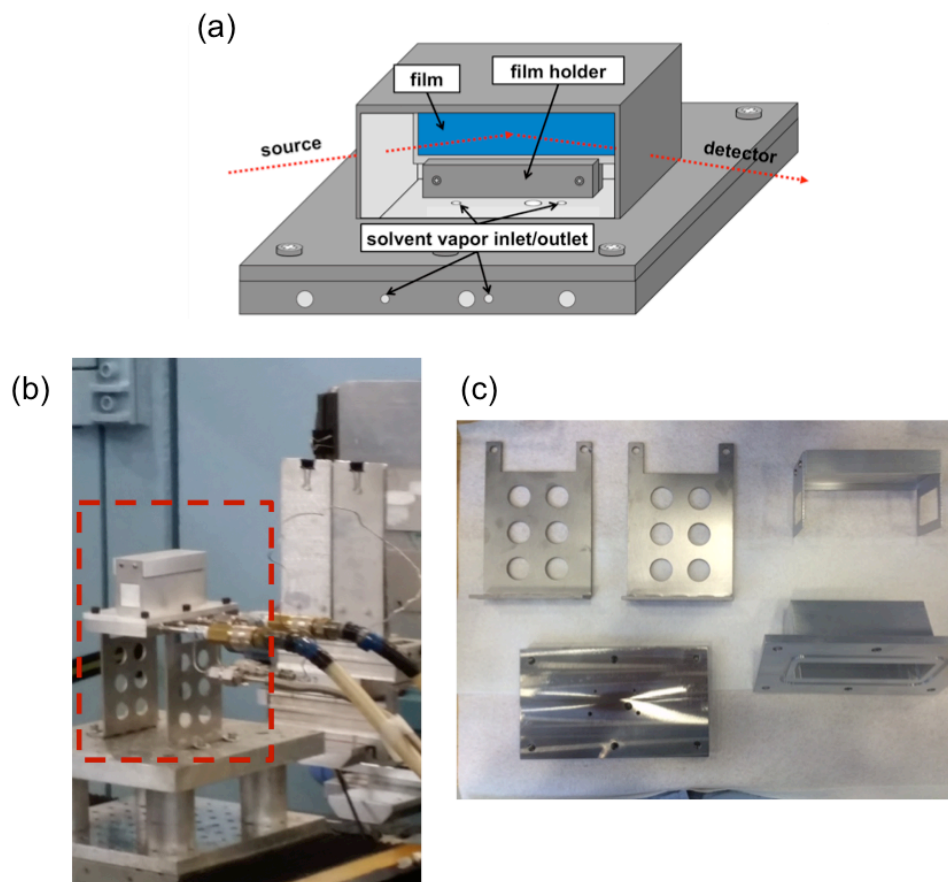


Figure B.4: (a) Illustration and (b) photograph of NR *in situ* SVA sample cell. The aluminum sample cell housed a 200 ± 2 nm thick SIS films with inlets and outlets for solvent vapor exposure and was mounted at a reflectivity geometry with the neutron beam. Borated aluminum shields (not shown in illustration) were placed around the neutron beam inlet and outlet to prevent scattering from the film holder or screws from reaching the detector. The dismantled sample chamber is shown in (c) and the schematics for the different components are presented in Figures B.5 to B.12. Adapted with permission from Shelton, C. K. *et al.* *Macromolecules* **2016**, 49, 7525-7534, Copyright 2016 American Chemical Society.¹

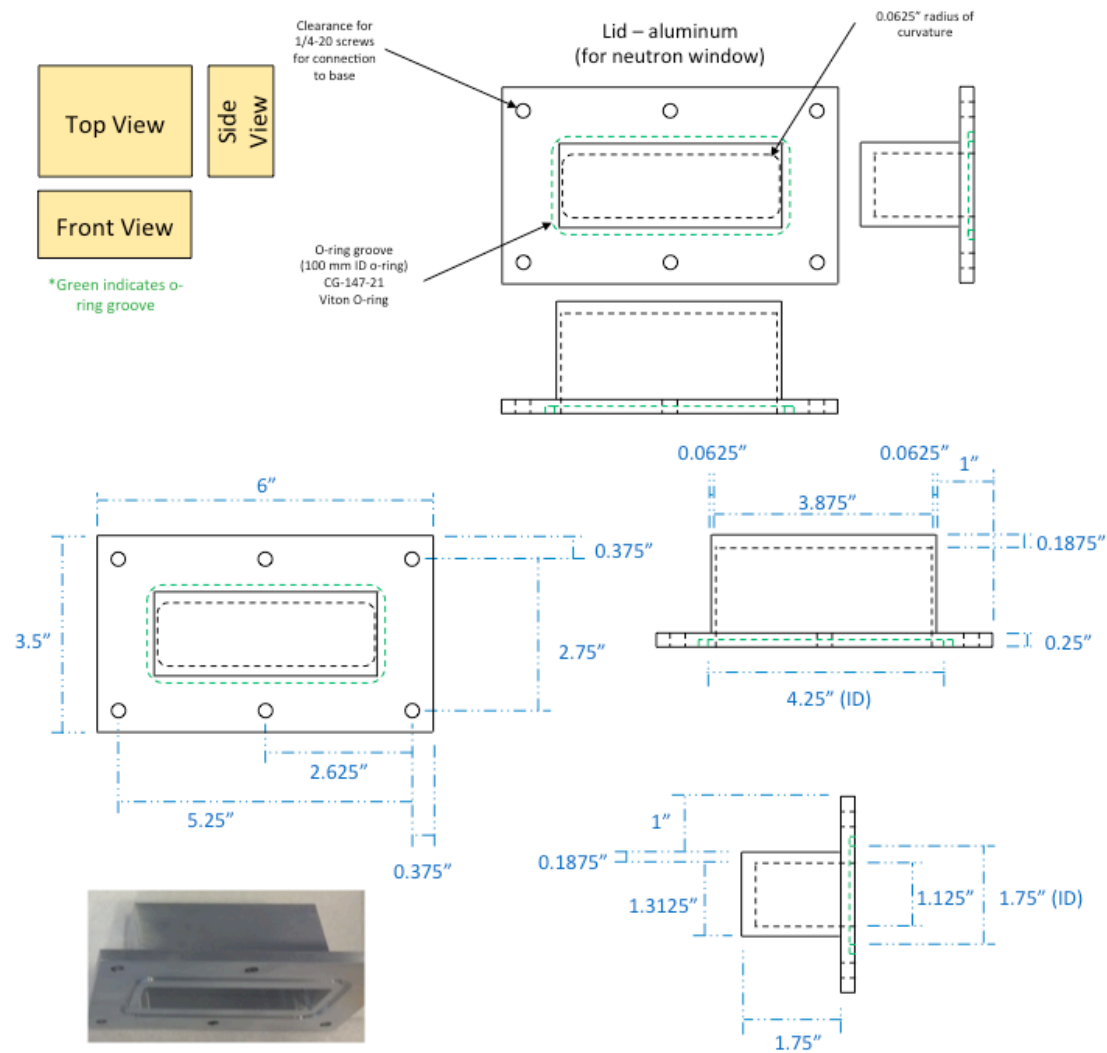


Figure B.5: Schematic for NR *in situ* SVA sample cell lid with photograph for reference. The lid enclosed the film sample to trap solvent vapor inside the chamber during annealing.

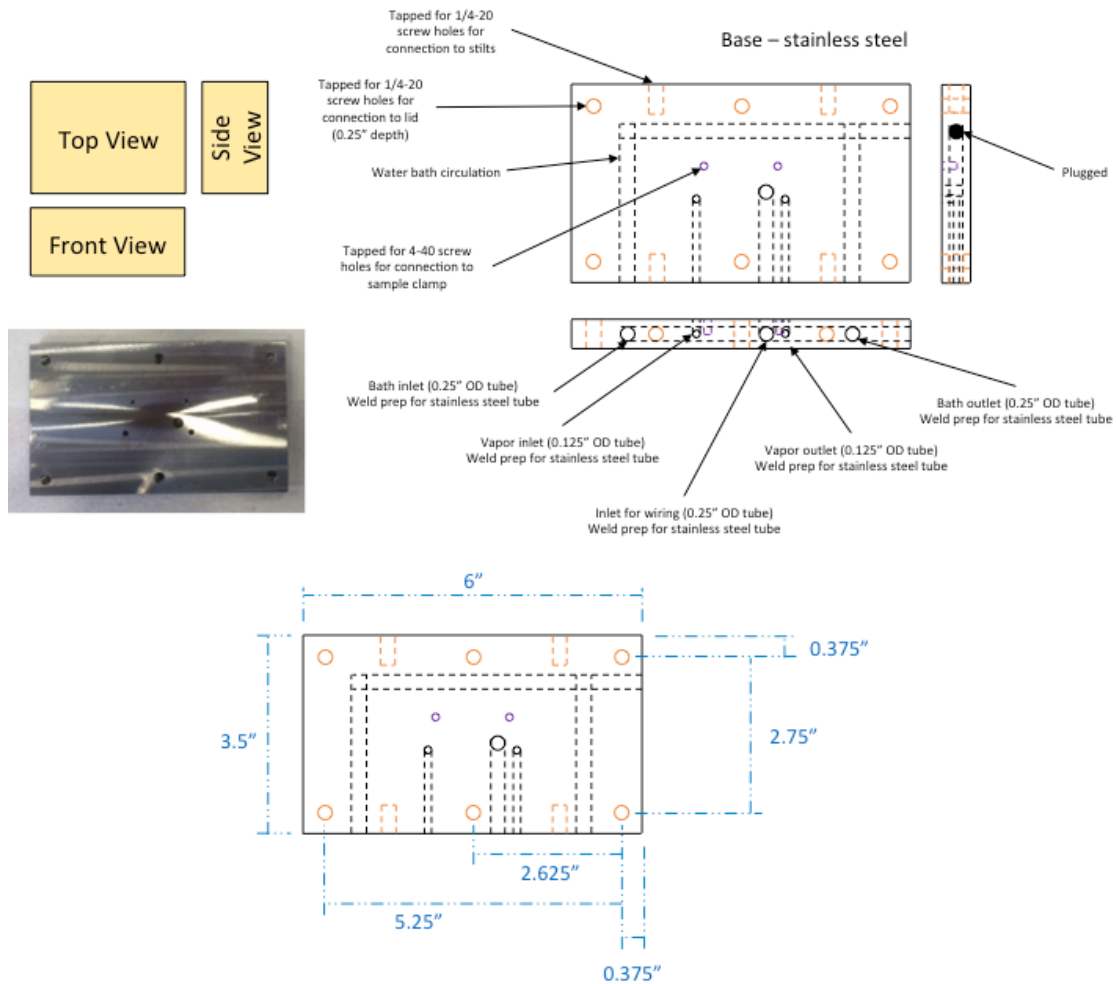


Figure B.6: Schematic for NR *in situ* SVA sample cell base plate with photograph for reference. The base plate housed the solvent inlet and outlet and the piping for a continuous circulating water bath to control the temperature.

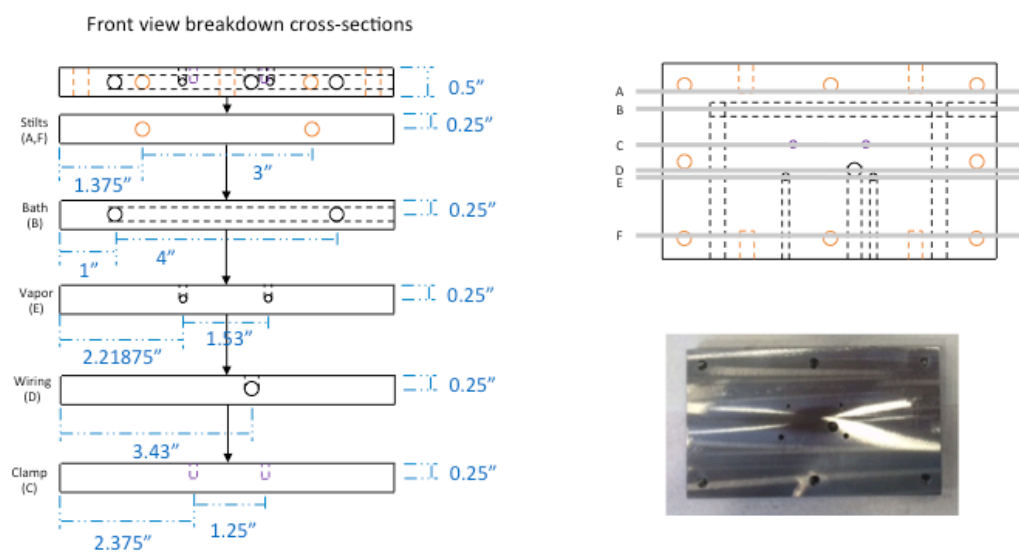
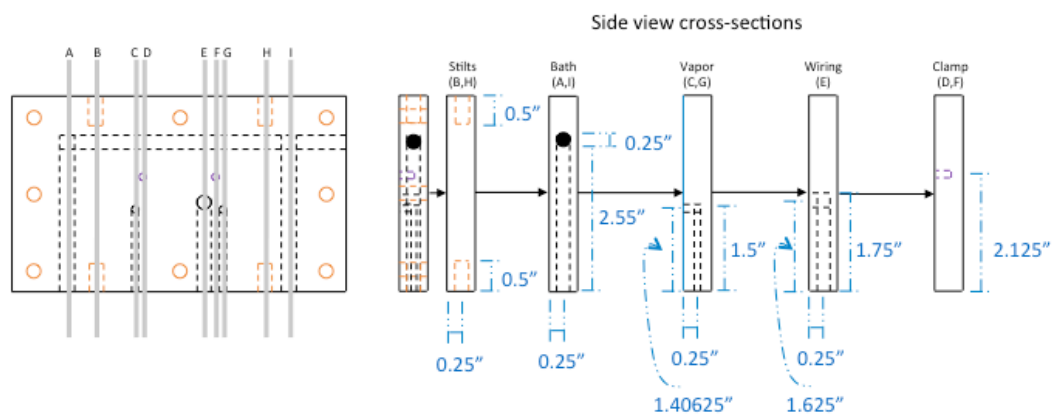


Figure B.7: More detailed schematic of base plate features with photograph for reference. Each breakdown describes where different holes or ports are located for a given application (*e.g.*, solvent inlet, solvent outlet, water bath inlet, water bath outlet).

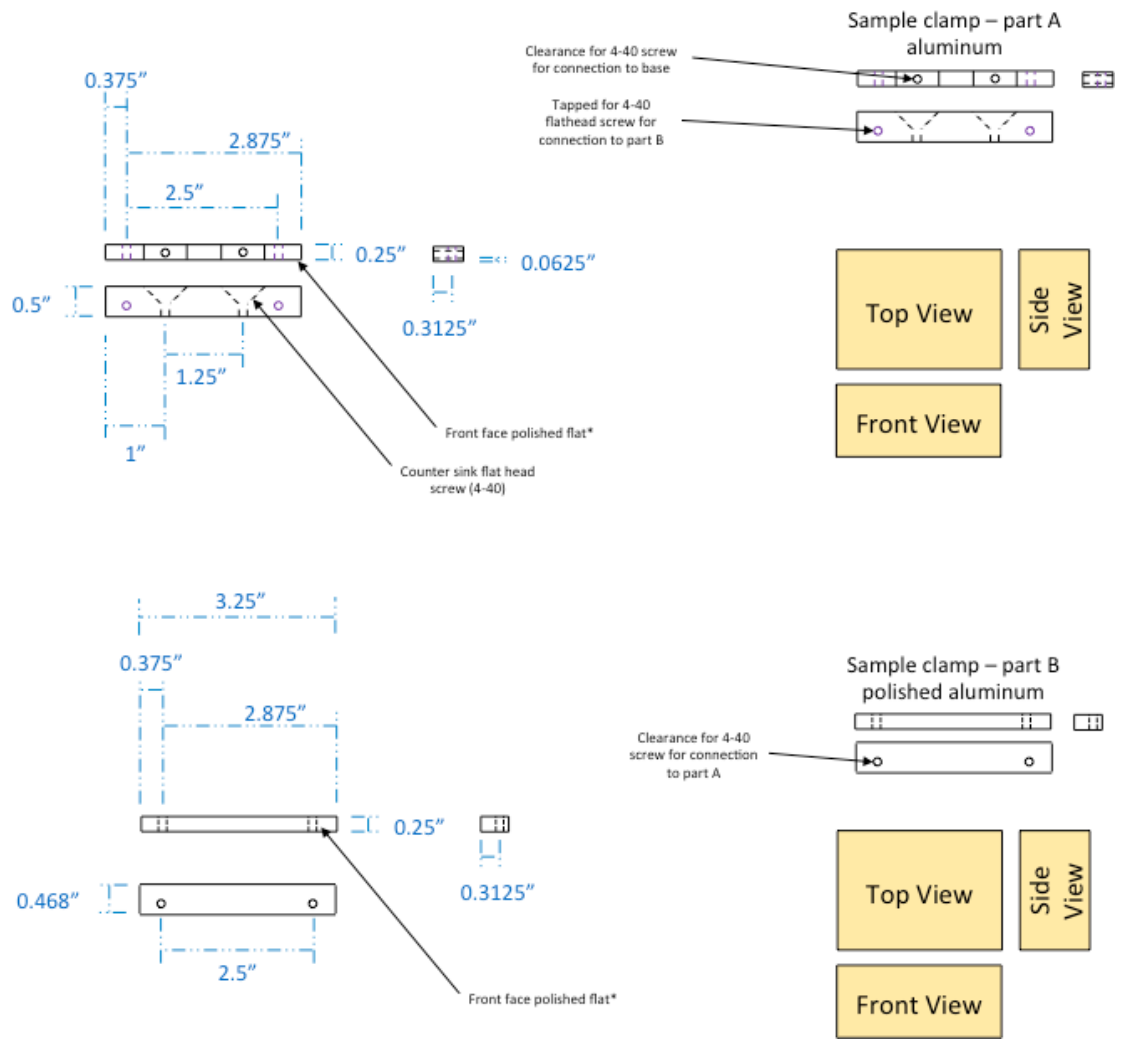


Figure B.8: Schematic for NR *in situ* SVA sample cell clamps, which were used to hold the films upright in the neutron beam.

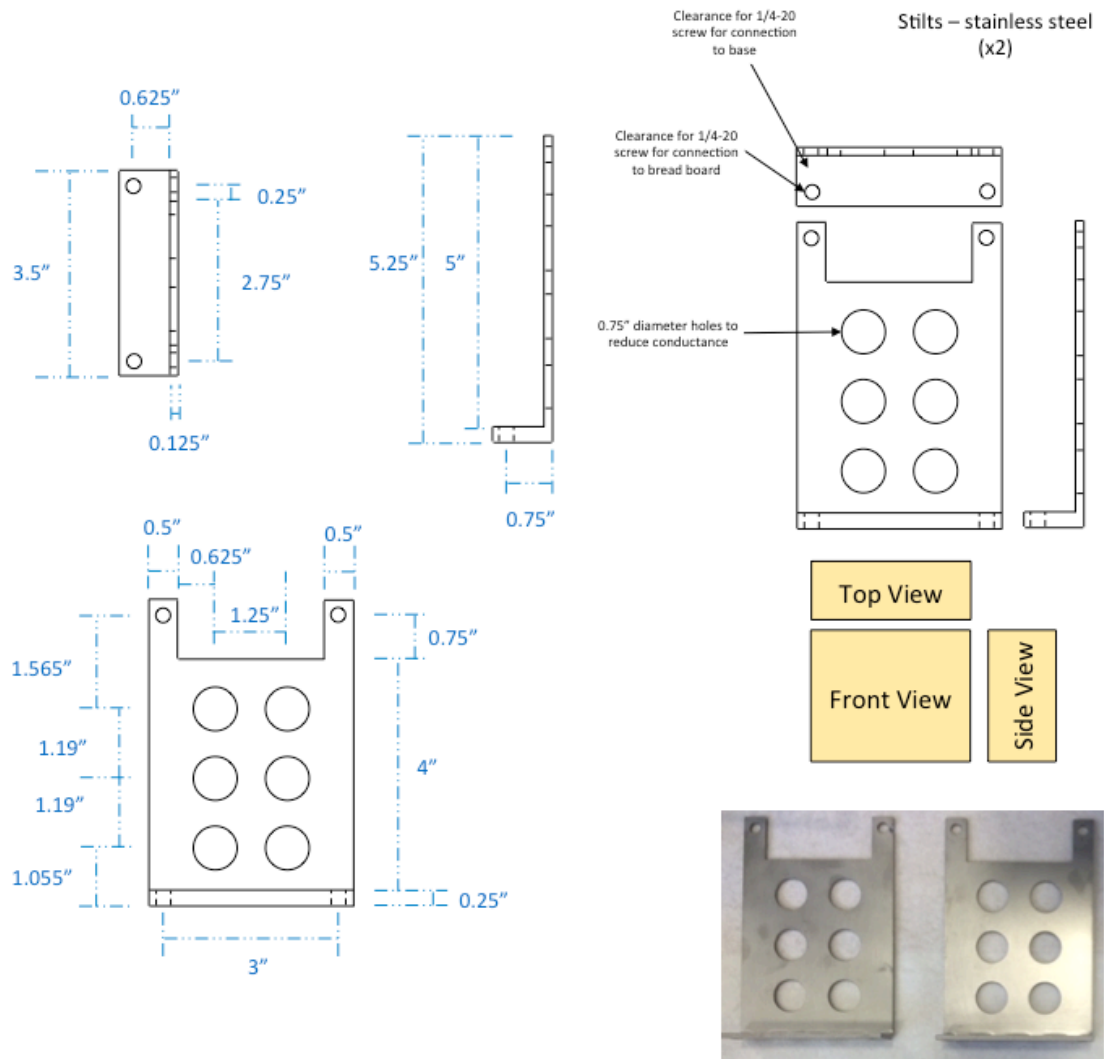


Figure B.9: Schematic for NR *in situ* SVA sample cell stilts with photograph for reference. The stilts were used to raise the sample into the neutron beam. Holes were cut in the stilts to help cool them if higher temperatures are used during annealing.

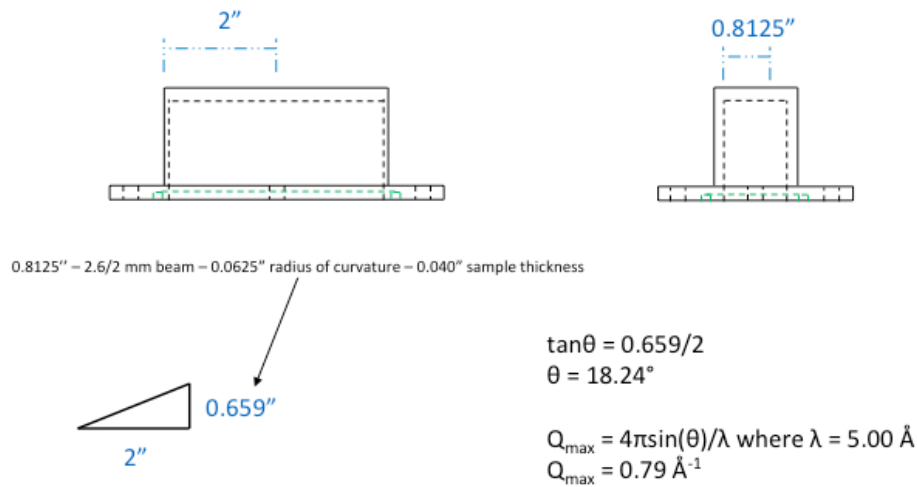
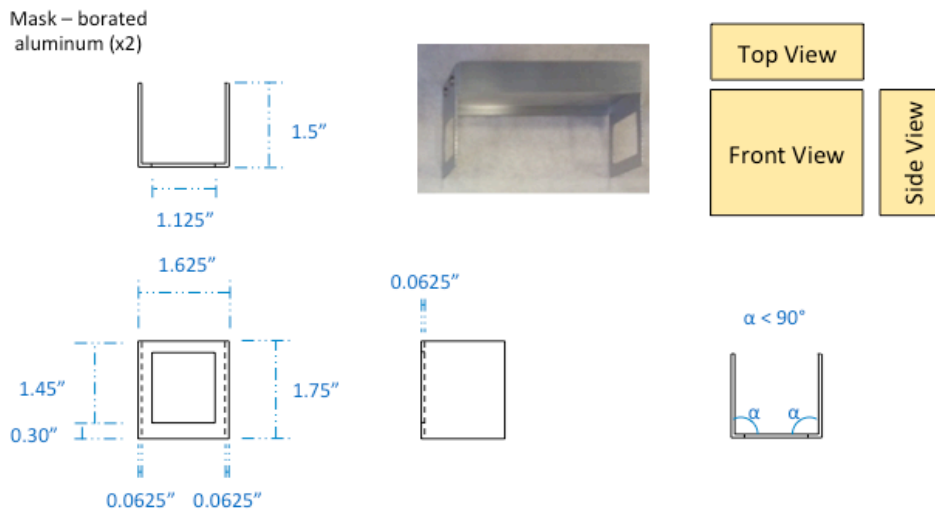


Figure B.10: Schematic for NR *in situ* SVA sample cell mask and photograph for reference. The mask was used to prevent scattering from hardware (e.g., screws) that might otherwise affect NR profiles. A calculation for the max Q was conducted to ensure appropriate Q ranges could be reached with the masks.

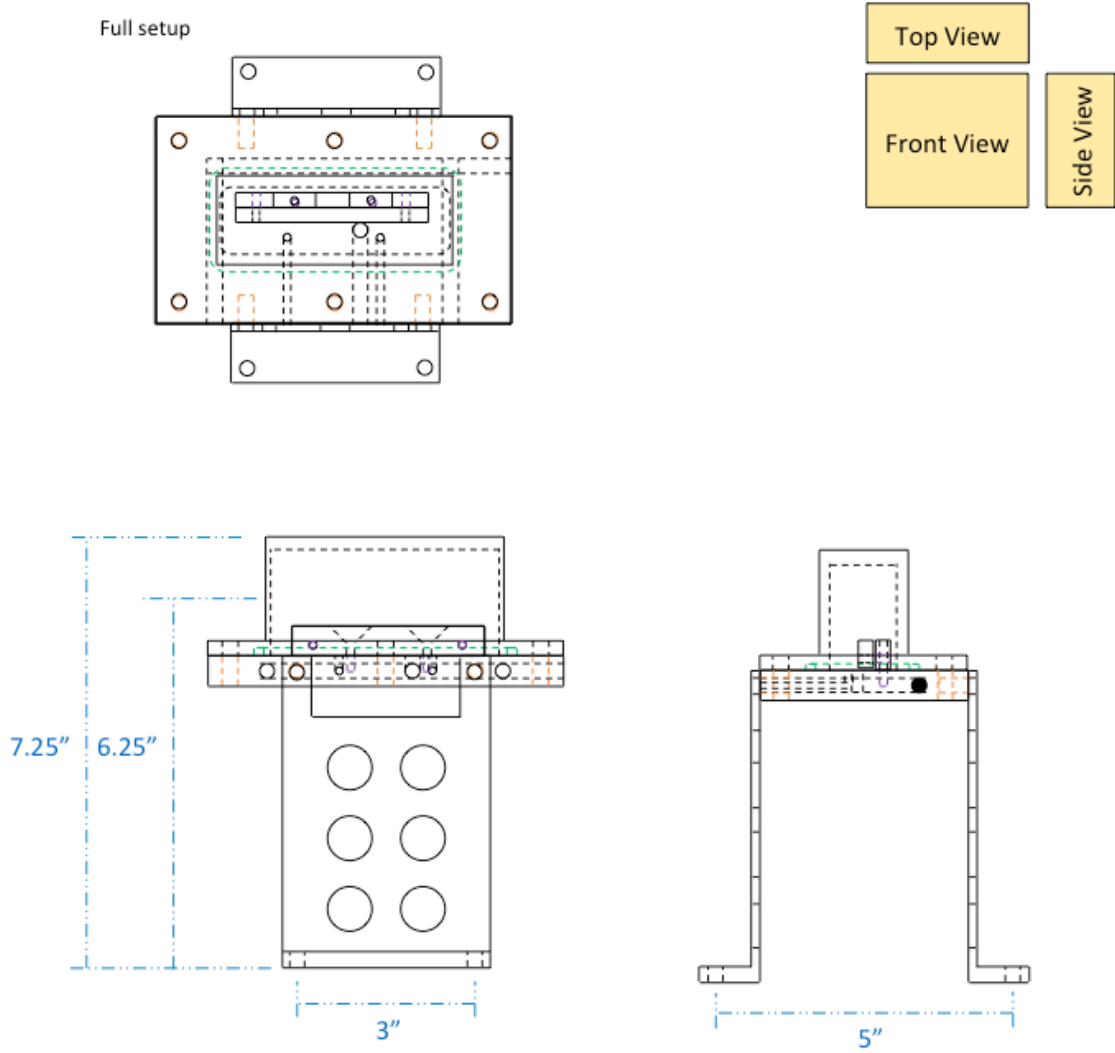


Figure B.11: Schematic for the full, assembled NR *in situ* SVA sample cell.

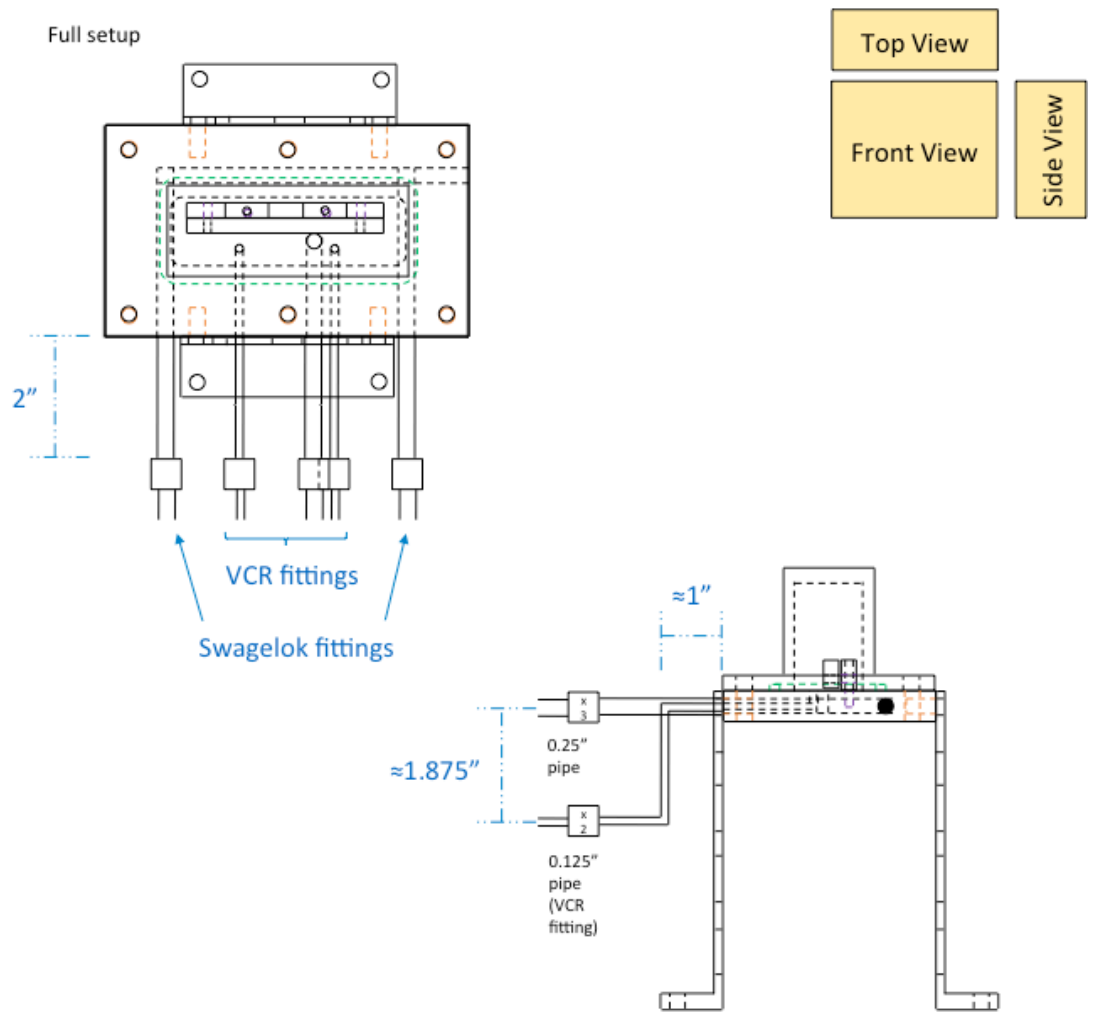


Figure B.12: Schematic for NR *in situ* SVA sample cell with water bath and solvent vapor ports added.

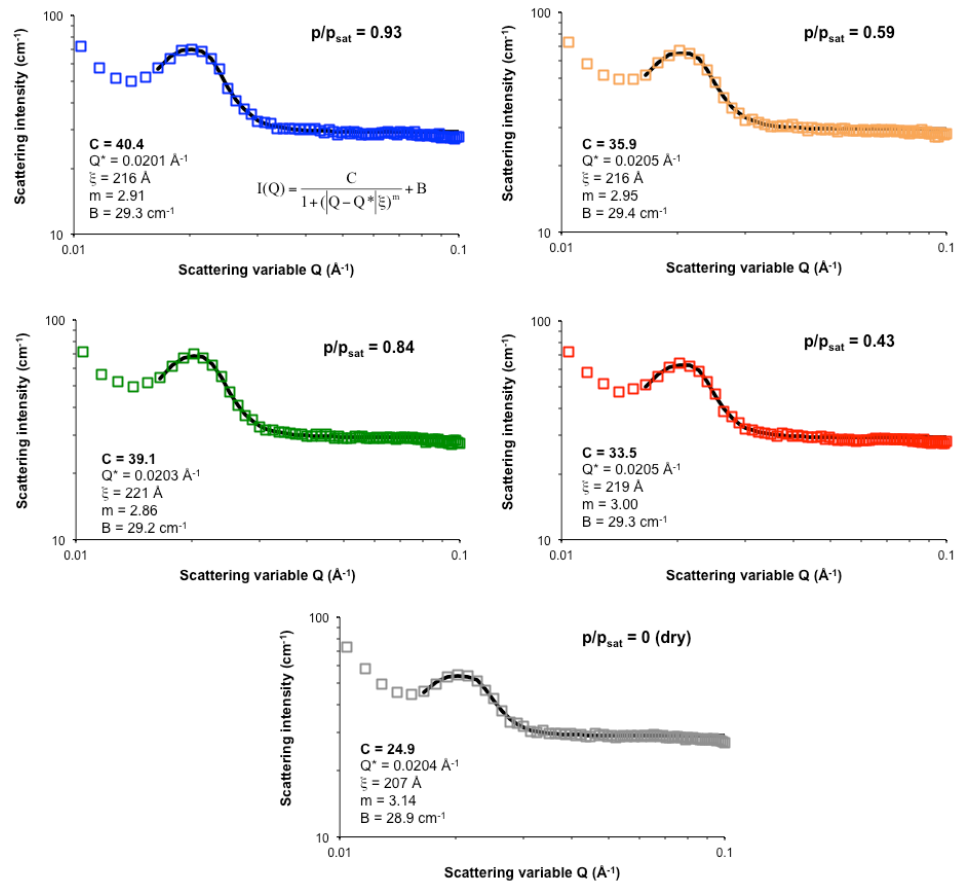


Figure B.13: Broad peak model fits to small-angle neutron scattering 1-D profiles at different values of p/p_{sat} . In the broad peak model, the parameters C , Q^* , ξ , m , and B represent the intensity of the primary peak, the Q location of the primary peak, the correlation length of the features, a scaling factor, and background in the scattering, respectively. The model fit parameters were optimized using SASView software. Most of the parameters remained relatively constant with changing p/p_{sat} , including the Q location of the primary peak (Q^*) at $\approx 0.02 \text{ \AA}^{-1}$, which indicated the domain spacing (L_0) was effectively constant with p/p_{sat} . The C parameter varied with p/p_{sat} and described the change in amplitude of the primary peak. The decrease in C with p/p_{sat} indicated that the contrast between domains had decreased. The value of C was used to calculate the contrast ($[\Delta\rho]^2$) between the polymer domains ($[\Delta\rho]^2 = [\rho_{PS/d\text{-benzene}} - \rho_{PI/d\text{-benzene}}]^2$) at each p/p_{sat} as described in Section B.1. Reprinted with permission from Shelton, C. K. *et al. Macromolecules* **2016**, 49, 7525-7534, Copyright 2016 American Chemical Society.¹

B.1 SANS Broad Peak Model Analysis to Calculate Solvent Concentration

This approach was modified from a similar technique that used a broad peak model to calculate the effect of temperature changes on contrast.⁴ The C values obtained from broad peak model fits were related to the contrast in the system ($[\Delta\rho]^2 = [\rho_{PS/d\text{-benzene}} - \rho_{PI/d\text{-benzene}}]^2$) at each p/p_{sat} value to calculate the amount of solvent in the PS and PI domains. For this calculation, the dry film and an assumed zero contrast system were used to extrapolate $(\Delta\rho)^2$ at a given value of C . For the dry film, $(\Delta\rho)^2$ was equal to the square of the difference in ρ between PS ($1.41 \times 10^{-6} \text{ \AA}^{-2}$) and PI ($0.273 \times 10^{-6} \text{ \AA}^{-2}$) at 25 °C.⁵ For a zero contrast system, the value of C was assumed to equal zero. A linear interpolation between the two neat components was utilized to develop a relationship between $(\Delta\rho)^2$ and C for d -benzene and SIS shown in Equation B.1.

$$C = 1.93 \times 10^{13} (\Delta\rho)^2 \quad (\text{B.1})$$

To determine $(\Delta\rho)^2$ in d -benzene swollen PS and PI domains as a function of solvent mole fraction ($x_{PS/sol}$ and $x_{PI/sol}$), a linear interpolation between the ρ of pure polymer, by volume fraction, ($\phi_{PS/sol}$, $\phi_{PI/sol} = 0$) and pure solvent, by volume fraction, ($\phi_{PS/sol}$, $\phi_{PI/sol} = 1$; $\rho_{d\text{-benzene}} = 5.43 \times 10^{-6} \text{ \AA}^{-2}$ at 25 °C)⁴ was used (Equations B.2 and B.3).

$$\rho_{PS/d\text{-benzene}} = 4.02 \times 10^{-6} (\phi_{PS/sol}) + 1.41 \times 10^{-6} \quad (\text{B.2})$$

$$\rho_{PI/d\text{-benzene}} = 5.16 \times 10^{-6} (\phi_{PI/sol}) + 0.273 \times 10^{-6} \quad (\text{B.3})$$

Next, the volume fraction of solvent in PS and PI domains ($\phi_{PS/sol}$ and $\phi_{PI/sol}$) was quantified using Equations B.4 and B.5, respectively.

$$\phi_{PS/sol} = \frac{v_{PS/sol}}{v_{PS} + v_{PS/sol}} \quad (\text{B.4})$$

$$\phi_{PI/sol} = \frac{v_{PI/sol}}{v_{PI} + v_{PI/sol}} \quad (\text{B.5})$$

In Equations B.4 and B.5, v_{PS} , v_{PI} , $v_{PS/sol}$, and $v_{PI/sol}$ refer to the volume of PS, the volume of PI, the volume of solvent in the PS domain, and the volume of solvent in the PI domain, respectively. An assumed total volume of film and solvent (V_{tot}) was used to calculate v_{PS} and v_{PI} from the known volume fraction ratios of PS and PI in the SIS BP (0.268:0.732) and the known solvent volume fraction (ϕ_{sol}) in the film at each p/p_{sat} measured *via* NR. Additionally, an error of ± 5 vol% total solvent in the film was assumed for all calculations. Then, $v_{PS/sol}$ and $v_{PI/sol}$ were related to each other through Equation B.6 and V_{tot} .

$$V_{tot}\phi_{sol} = v_{PS/sol} + v_{PI/sol} \quad (\text{B.6})$$

Finally, Equations B.1-B.5 were combined as shown in Equation B.7 to calculate the amount of solvent present in each polymer domain for a given C value.

$$\frac{C}{1.93 \times 10^{13}} = (\Delta\rho)^2 = \left[\left(\frac{4.02 \times 10^{-6} v_{PS/sol}}{v_{PS} + v_{PS/sol}} + 1.41 \times 10^{-6} \right) - \left(\frac{5.16 \times 10^{-6} v_{PI/sol}}{v_{PI} + v_{PI/sol}} + 0.273 \times 10^{-6} \right) \right]^2 \quad (\text{B.7})$$

Equations B.6 and B.7 were coupled to calculate the volume of solvent in PS and PI domains and, subsequently, the volume fraction of solvent in PS and PI domains using V_{tot} . These values were converted to mole fractions using the molar volume of PS (100 cm³/mol), the molar volume of PI (76 cm³/mol), and the molar volume of *d*-benzene (89 cm³/mol) at 25 °C.⁴ Reprinted with permission from Shelton, C. K. *et al. Macromolecules* **2016**, 49, 7525-7534, Copyright 2016 American Chemical Society.¹

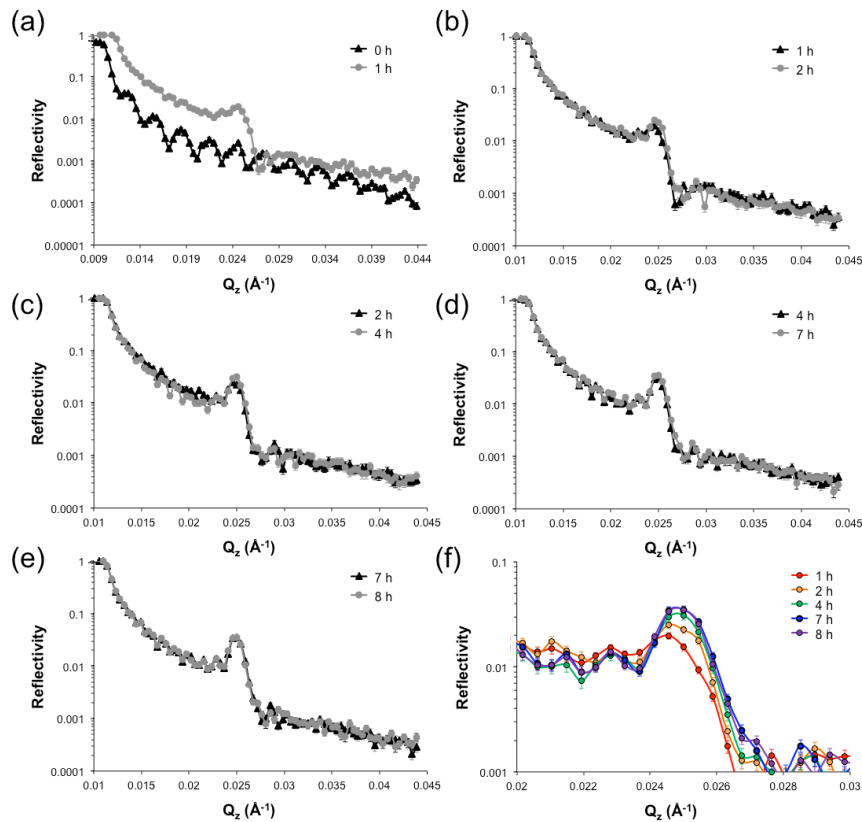


Figure B.14: Temporal NR profiles of SIS films from a dry, as-cast state to a p/p_{sat} value of 0.93. The different plots show the change in the profile from (a) an initial, dry state (time = 0 h) to 1 h after solvent exposure, (b) a 1 h to 2 h solvent exposure time, (c) a 2 h to 4 h after solvent exposure time, (d) a 4 h to 7 h after solvent exposure time, and (e) a 7 h to 8 h after solvent exposure time. During SVA exposure, the gap between Kiessig fringes narrowed, and a Bragg peak developed, which indicated the film swelled (at a rate of at least 2.3 nm/min), and a repeating out-of-plane structure formed (parallel cylinders), respectively. The SIS film was annealed until two or three profiles overlapped (e) to indicate that a steady-state condition had been reached. The bottom right plot (f) focuses on the Bragg peak, as the peak changed more significantly than the rest of the profile and therefore was the most noteworthy indicator of steady-state. Reprinted with permission from Shelton, C. K. *et al. Macromolecules* **2016**, 49, 7525-7534, Copyright 2016 American Chemical Society.¹

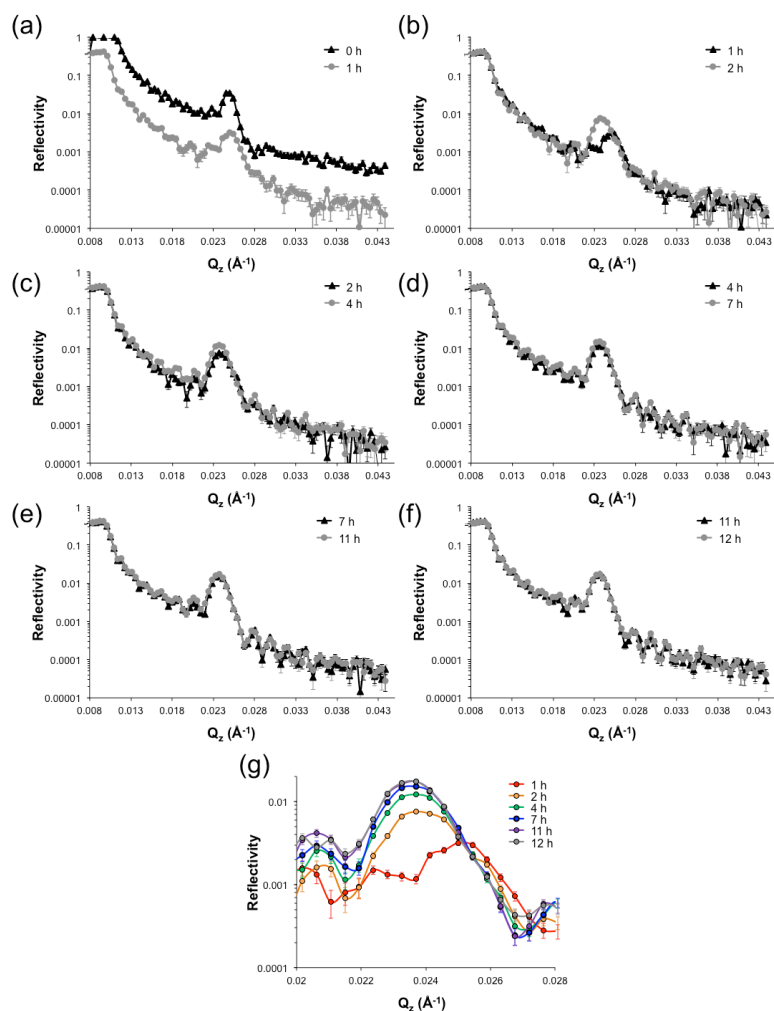


Figure B.15: Temporal NR profiles of SIS films from a p/p_{sat} value of 0.93 to a p/p_{sat} value of 0.84. The different plots show the change in the profile from (a) a fully swollen film ($p/p_{sat} = 0.93$ at time = 0 h) to a 1 h $p/p_{sat} = 0.84$ annealing time, (b) a 1 h to 2 h $p/p_{sat} = 0.84$ annealing time, (c) a 2 h to 4 h $p/p_{sat} = 0.84$ annealing time, (d) a 4 h to 7 h $p/p_{sat} = 0.84$ annealing time, (e) a 7 h to 11 h $p/p_{sat} = 0.84$ annealing time, and (f) an 11 h to 12 h $p/p_{sat} = 0.84$ annealing time. Upon deswelling, the gap between Kiessig fringes widened, and the Bragg peak location shifted to lower Q_z , which indicated the film thickness decreased (at a rate of at least 0.9 nm/min), and the layer spacing (L_z) increased. The bottom plot (g) focuses on the Bragg peak, as the peak changed more significantly than the rest of the profile and therefore was the most noteworthy indicator of equilibration. Reprinted with permission from Shelton, C. K. *et al. Macromolecules* **2016**, 49, 7525-7534, Copyright 2016 American Chemical Society.¹

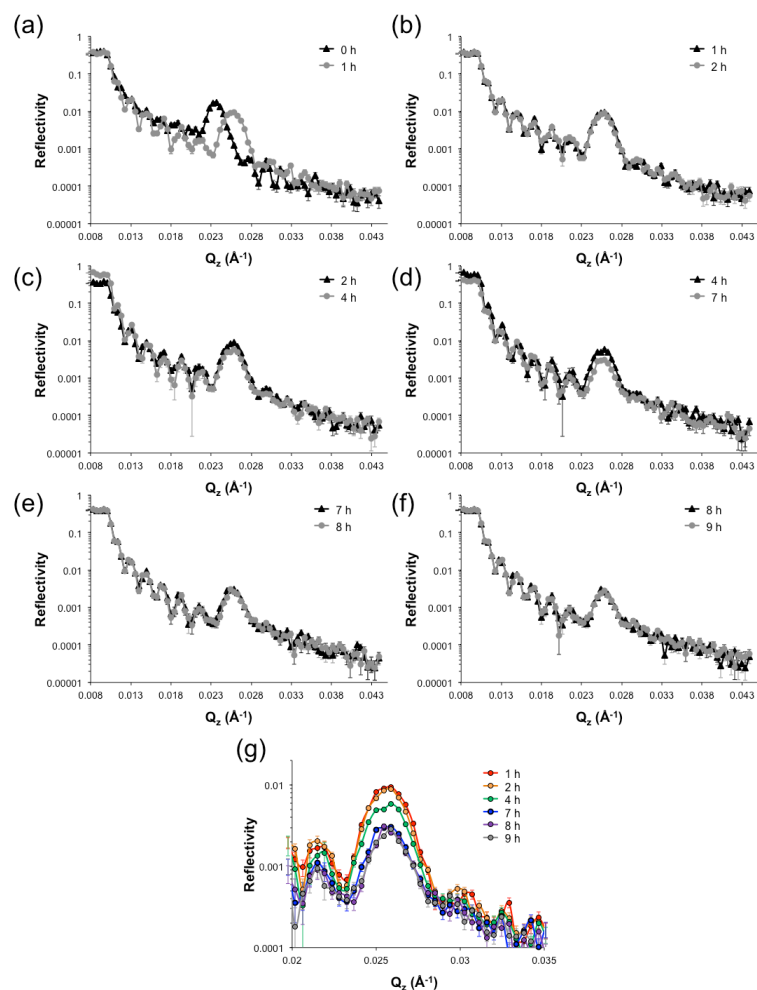


Figure B.16: Temporal NR profiles of SIS films from a p/p_{sat} value of 0.84 to a p/p_{sat} value of 0.59. The different plots show the change in the profile from (a) an equilibrated $p/p_{sat} = 0.84$ state (at time = 0 h) to a 1 h $p/p_{sat} = 0.59$ annealing time, (b) a 1 h to 2 h $p/p_{sat} = 0.59$ annealing time, (c) a 2 h to 4 h $p/p_{sat} = 0.59$ annealing time, (d) a 4 h to 7 h $p/p_{sat} = 0.59$ annealing time, (e) a 7 h to 8 h $p/p_{sat} = 0.59$ annealing time, and (f) an 8 h to 9 h $p/p_{sat} = 0.59$ annealing time. Upon deswelling, the gap between Kiessig fringes widened, and the Bragg peak location shifted to higher Q_z , which indicated the film thickness decreased (at a rate of at least 0.9 nm/min), and the L_z decreased. The bottom plot (g) focuses on the Bragg peak, as the peak changed more significantly than the rest of the profile and therefore was the most noteworthy indicator of equilibration. Reprinted with permission from Shelton, C. K. *et al. Macromolecules* **2016**, 49, 7525-7534, Copyright 2016 American Chemical Society.¹

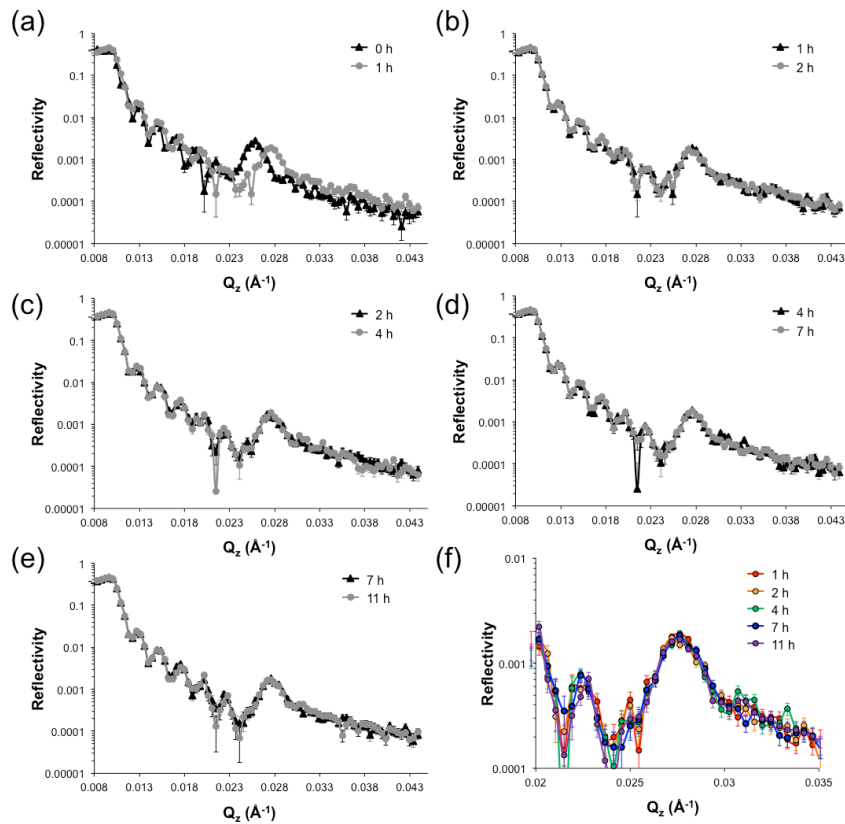


Figure B.17: Temporal NR profiles of SIS films from a p/p_{sat} value of 0.59 to a p/p_{sat} value of 0.43. The different plots show the change in the profile from (a) an equilibrated $p/p_{sat} = 0.59$ state (at time = 0 h) to a 1 h $p/p_{sat} = 0.43$ annealing time, (b) a 1 h to 2 h $p/p_{sat} = 0.43$ annealing time, (c) a 2 h to 4 h $p/p_{sat} = 0.43$ annealing time, (d) a 4 h to 7 h $p/p_{sat} = 0.43$ annealing time, and (e) a 7 h to 11 h $p/p_{sat} = 0.43$ annealing time. Upon deswelling, the gap between Kiessig fringes widened, and the Bragg peak location shifted to higher Q_z , which indicated the film thickness decreased (at a rate of at least 0.9 nm/min), and the L_z decreased. The bottom right plot (f) focuses on the Bragg peak, as the peak changed more significantly than the rest of the profile and therefore was the most noteworthy indicator of equilibration. Reprinted with permission from Shelton, C. K. *et al. Macromolecules* **2016**, 49, 7525-7534, Copyright 2016 American Chemical Society.¹

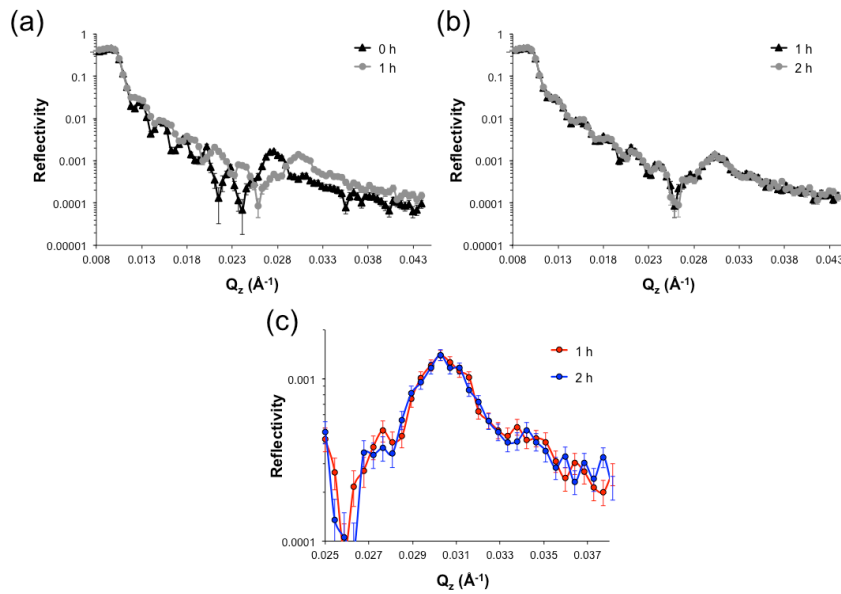


Figure B.18: Temporal NR profiles of SIS films from a p/p_{sat} value of 0.43 to a redried state. The different plots show the change in the profile from (a) an equilibrated $p/p_{sat} = 0.43$ state (at time = 0 h) to a 1 h exposure to a dry nitrogen flow and (b) a 1 h to 2 h exposure time to a dry nitrogen flow. Upon deswelling, the gap between Kiessig fringes widened, and the Bragg peak location shifted to higher Q_z , which indicated the film thickness decreased (at a rate of at least 0.9 nm/min), and the L_z decreased. The bottom plot (c) focuses on the Bragg peak, as the peak changed more significantly than the rest of the profile and therefore was the most noteworthy indicator of equilibration. Reprinted with permission from Shelton, C. K. *et al. Macromolecules* **2016**, 49, 7525-7534, Copyright 2016 American Chemical Society.¹

B.2 Incommensurability Between Film Thickness, Layer Thickness, and Number of Layers

At a value of $p/p_{sat} = 0.93$, the increased solvent content created both rougher surfaces and rougher polymer-polymer interfaces than at other values of p/p_{sat} , as seen by the decreased amplitude of the Kiessig fringes and the diminishing amplitude of the ρ profile oscillations in Figure 4.6. The increased roughness accounted for the additional 0.8 layer incommensurability between the fit number of layers ($n = 12$) and the film thickness ($t = 347$ nm) at an L_z of 27 nm ($t/L_z = 12.8$ layers). Similarly roughened surfaces and interfaces have been reported in literature for highly solvent swollen films.⁶ Reprinted with permission from Shelton, C. K. *et al. Macromolecules* **2016**, 49, 7525-7534, Copyright 2016 American Chemical Society.¹

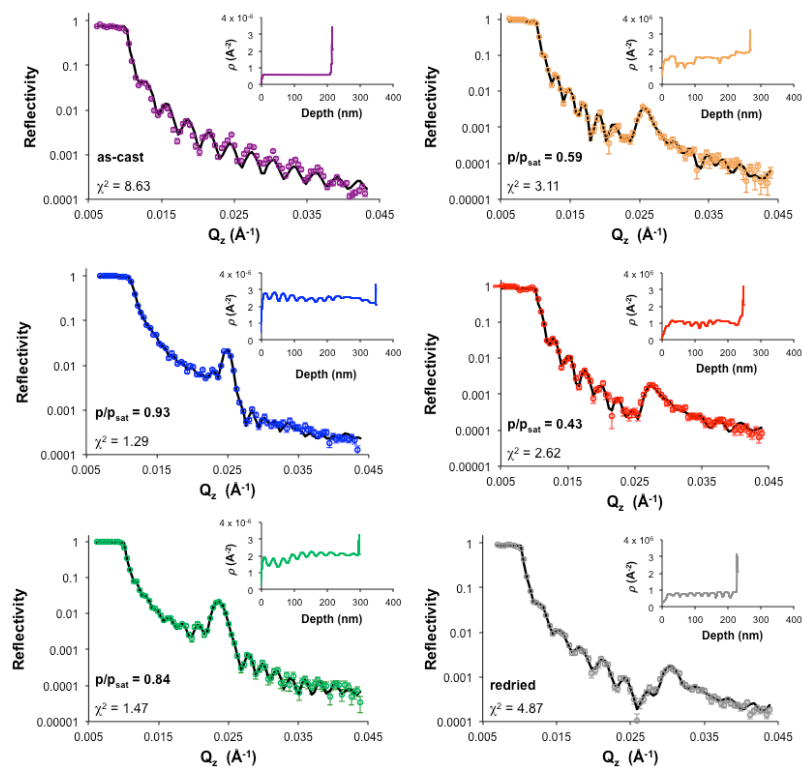


Figure B.19: Multilayer model fits (black lines) to NR data (open colored circles) for the as-cast and redried films as well as at each value of p/p_{sat} . The model parameters accounted for n number of layers with individual thickness and ρ parameters. Using this model and refl1D fitting software,⁷ the calculated profiles demonstrated good agreement with the measured profiles ($\chi^2 < 5$) and produced a free surface (depth = 0) to substrate ρ profile shown in the inset plots. For p/p_{sat} values of 0.93 and 0.84, the ρ profiles showed an oscillatory trend that likely was caused by the difference in solvent uptake of pure PI and mixed PI/PS layers. At values of $p/p_{sat} \leq 0.59$, the oscillatory trend was not as consistent (regions of lower amplitude oscillations) due to the PS domain transitioning to a glassy state that limited solvent diffusion through the film. Additionally, the Bragg peak was broader for values of $p/p_{sat} \leq 0.59$, which suggested greater disorder in the layered structure. Once all the solvent was removed from the film (redried), the oscillatory trend returned due to the ordered layering of domains. The solvent concentration through the film thickness at each p/p_{sat} was extracted from the resulting ρ profiles using known polymer and solvent ρ values, and molar fractions of the PS and PI domains in the dry SIS BP. Reprinted with permission from Shelton, C. K. *et al. Macromolecules* **2016**, 49, 7525-7534, Copyright 2016 American Chemical Society.¹

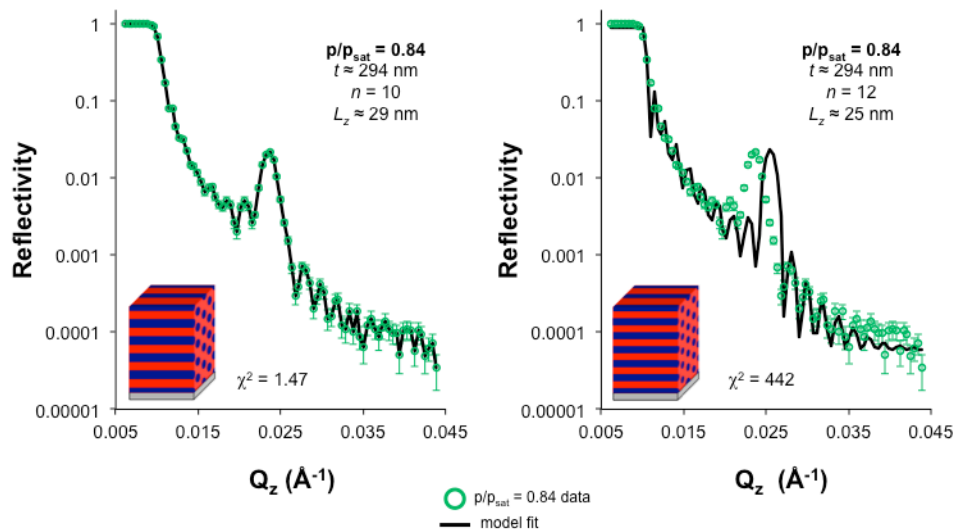


Figure B.20: Multilayer model fits (black lines) to $p/p_{sat} = 0.84$ reflectivity profiles (open green circles) consisting of ten (left) or twelve (right) repeating layers (n). The total film thickness (t) remained constant for each fit, but the layer thickness (L_z) changed to achieve commensurability between the t and n . The $n = 10$ model fit the reflectivity data with a $\chi^2 = 1.47$. The $n = 12$ model had a significantly higher χ^2 ($\chi^2 = 442$) due to mismatched Bragg peak and Kiessig fringe locations when comparing the reflectivity data to the model fit. This large discrepancy between the refined $n = 12$ model fit and the reflectivity data provides a further indication that there was a change in the number of layers (from 12 to 10) in the film upon deswelling. Reprinted with permission from Shelton, C. K. *et al. Macromolecules* **2016**, 49, 7525-7534, Copyright 2016 American Chemical Society.¹

REFERENCES

1. Shelton, C. K.; Jones, R. L.; Dura, J. A.; Epps, T. H., III *Macromolecules* **2016**, 49, 7525-7534.
2. Stein, S. E., Mass Spectra. In *NIST Chemistry WebBook*, National Institute of Standards and Technology: Gaithersburg, MD.
3. Zhao, H.; Unhannant, P.; Hanshaw, W.; Chickos, J. S. *J. Chem. Eng. Data* **2008**, 53, 1545-1556.
4. Hammouda, B., Probing Nanoscale Structures: The SANS Toolbox. NIST: 2008.
5. Sears, V. F. *Neutron News* **1992**, 3, 26-37.
6. Papadakis, C. M.; Di, Z.; Posselt, D.; Smilgies, D.-M. *Langmuir* **2008**, 24, 13815-13818.
7. Kienzle, P. A.; O'Donovan, K. V.; Ankner, J. F.; Berk, N. F.; Majkrzak, C. F. <http://www.ncnr.nist.gov/reflpak> **2000-2006**.

Appendix C

SUPPORTING INFORMATION FOR CHAPTER 5

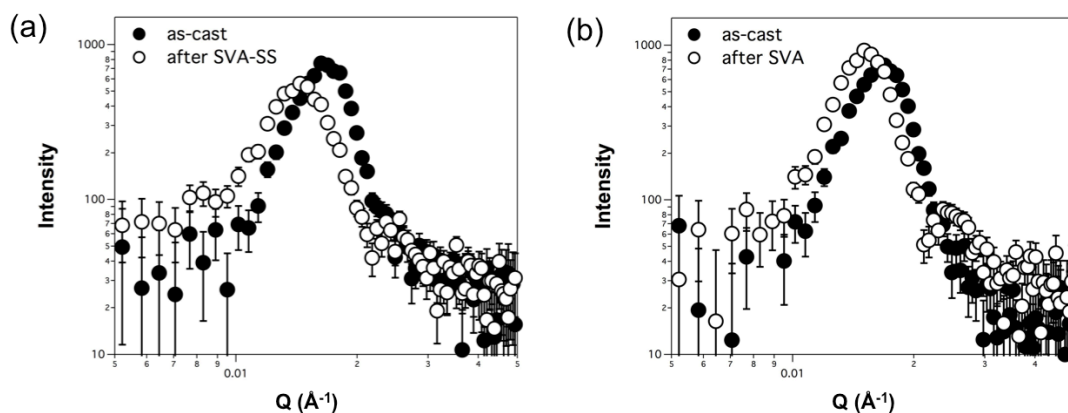


Figure C.1: Small-angle neutron scattering (SANS) azimuthally-averaged intensity profiles for poly(deuterated styrene-*b*-isoprene-*b*-deuterated styrene) (*dSIIdS*) films subjected to toluene solvent vapor annealing (SVA) (a) with or (b) without soft shear. SVA with soft shear (SVA-SS) was implemented through the placement of polydimethylsiloxane (PDMS) pads on the films to induce shear forces as the pad swelled and deswelled while in contact with the film. SVA-SS or SVA was conducted with a 3 h swelling time and 10 mL/min toluene-rich nitrogen flow rates during swelling, and 3 mL/min diluent nitrogen flow rates during film deswelling. For both SVA-SS and SVA, the location of the primary peak shifted from $Q = 0.018 \text{ \AA}^{-1}$ to $Q = 0.015 \text{ \AA}^{-1}$, which was indicative of an increase in domain spacing (L_0) from 35 nm to 42 nm. Also, there was a difference in intensity of the primary peak for SVA-SS vs. SVA; the primary peak intensity decreased for samples treated by SVA-SS and increased slightly for samples treated *via* SVA.¹

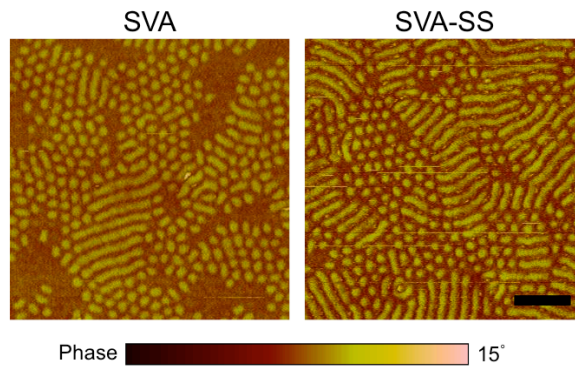


Figure C.2: AFM images of *dSIIdS* films after SVA or SVA-SS with the same swelling (10 mL/min toluene-rich nitrogen flow rate for 3 h) and deswelling (3 mL/min diluent nitrogen flow rate) conditions. The SVA-SS image was obtained from a portion of the film that the PDMS pad did not shear. Both micrographs indicate a mixture of parallel and perpendicular cylinders and featureless areas. The scale bar represents 250 nm and applies to both images.¹

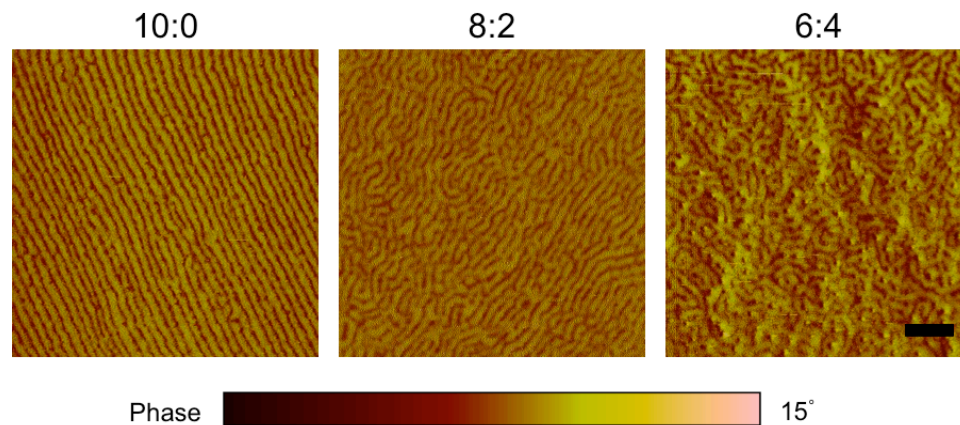


Figure C.3: AFM images of *dSIIdS* films exposed to different toluene-rich to diluent stream flow rate ratios (10:0, 8:2, or 6:4) during SVA-SS swelling. Shear forces from the swelling of the PDMS pad resulted led to well-ordered and aligned nanostructures across the film in the 10:0 sample. At an 8:2 ratio (reduced PDMS swelling relative to 10:0), the shear fields appear to be sufficient to align domains but not large enough to generate either a high degree of ordering or defect removal. At a 6:4 ratio, shear-alignment was not readily apparent. The scale bar represents 250 nm and applies to all images.¹

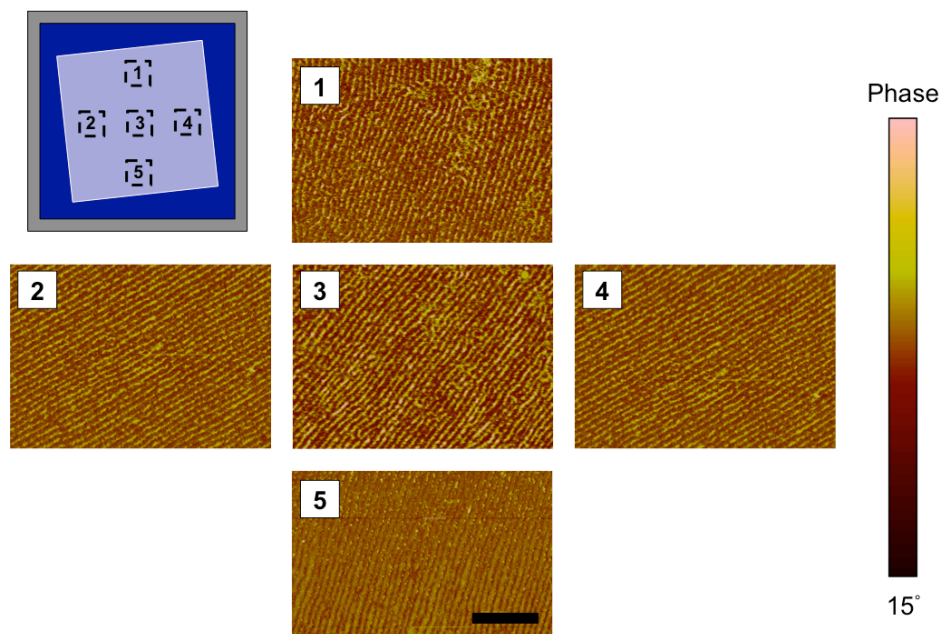


Figure C.4: AFM images from a *dSIaS* film subjected to toluene SVA-SS using a PDMS pad fabricated with a 20:1 elastomer to curing agent ratio and a 2° gradient in thickness. The location of the AFM images in the figure is relative to where the images were taken in the film as indicated by the schematic in the top left corner. The alignment direction of the nanostructures remained consistent throughout the film. Slight differences in the apparent alignment direction likely were the result of orientation changes of the AFM when moving between locations. The scale bar represents 500 nm and applies to all images.¹

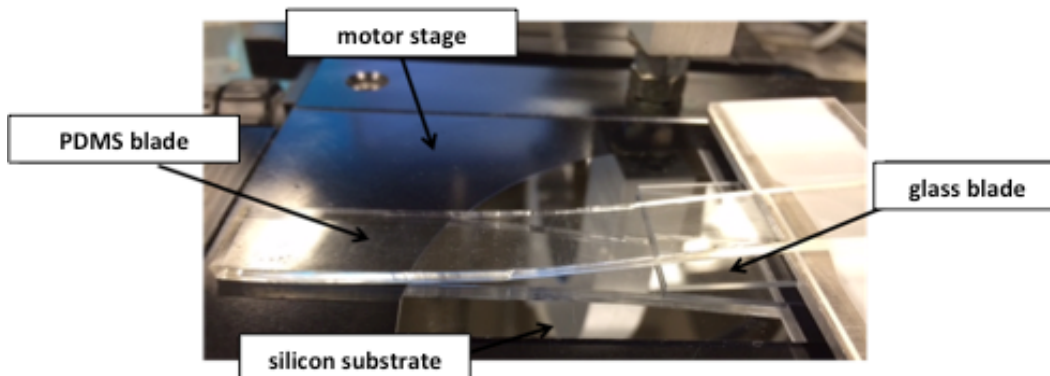


Figure C.5: Photograph of shear casting device in which the flexible PDMS, shearing blade was attached to the same holder as the glass, casting blade (schematic of this setup is shown in Figure 5.8). A silicon substrate was placed on a motor stage, which was programmed to move at a set speed for film casting. A polymer solution was deposited between the glass blade and silicon substrate to produce a film upon movement of the stage. The flexible blade dragged across the top of the film immediately after casting to shear-align the nanostructure. This setup used a single device to hold the two blades but offered less control over the distance between the two blades and the downward force of the flexible blade.²

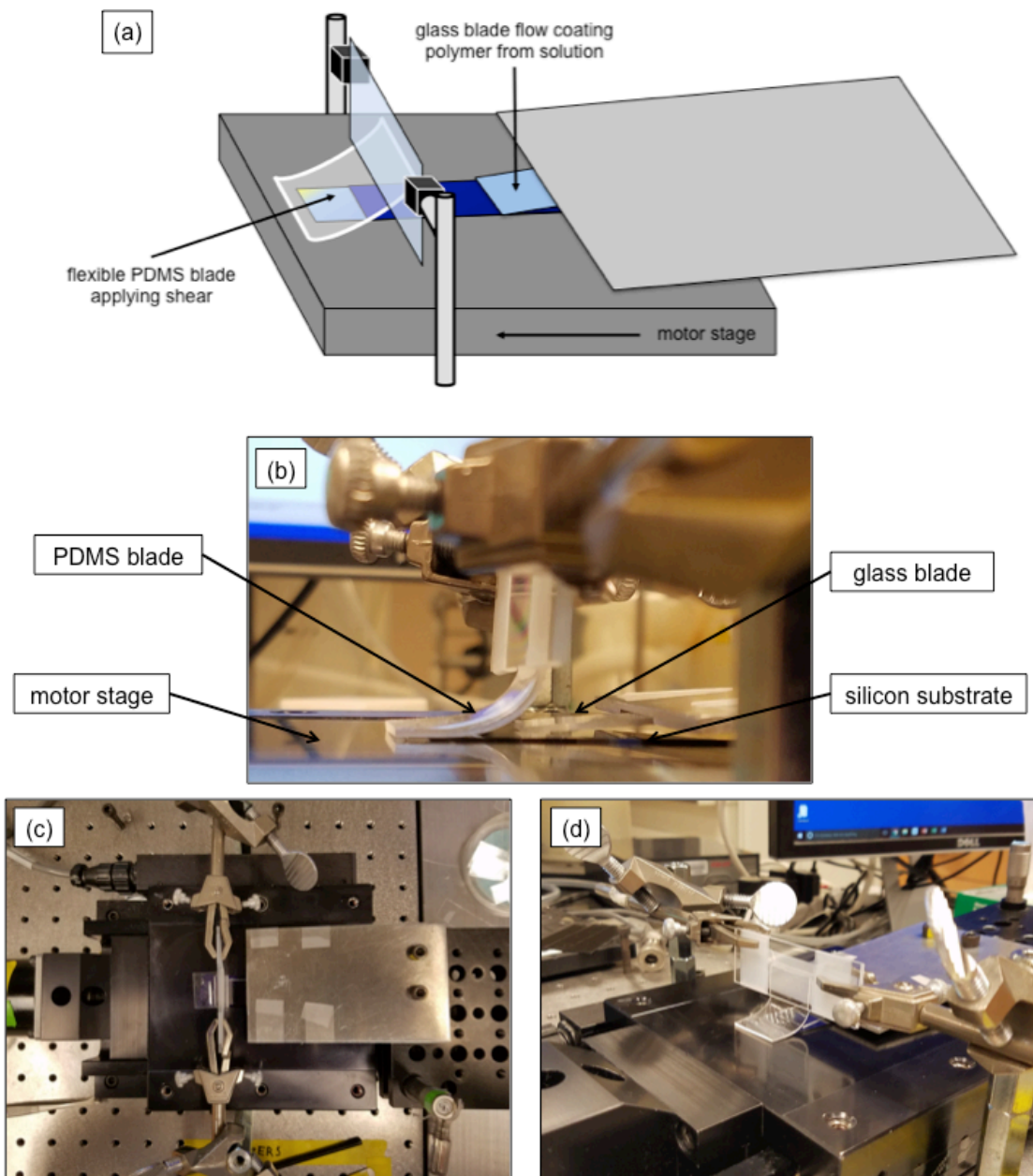


Figure C.6: (a) Schematic of shear casting device in which the flexible PDMS, shearing blade and glass, casting blade were attached to separate, stationary holders along with photographs of the setup: (b) side view, (c) top view, and (d) front view. This setup provided more control over the distance between the two blades and the downward force of the flexible blade. Photos courtesy of John Saltwick.

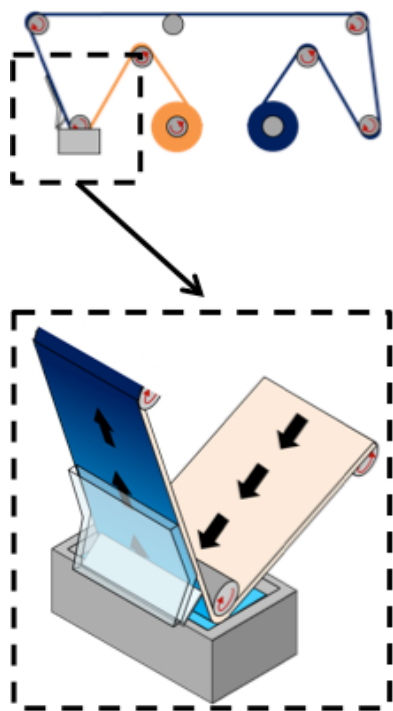


Figure C.7: Illustration of potential shear casting device for industrial scale roll-to-roll processing. A flexible substrate is dipped into a reservoir of polymer solution to generate a film that is thinned by a rigid blade (*i.e.*, thickness control is provided by the rigid blade). A flexible blade shears the drying film immediately after casting to align the nanostructure before the substrate is transferred to the next step in the process.²

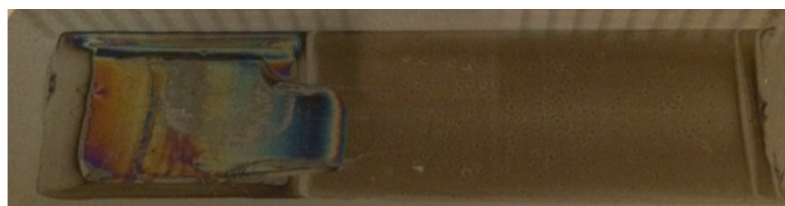


Figure C.8: Photograph of a poly(styrene-*b*-isoprene-*b*-styrene) film after shear casting that depicts significant film damage (left side of image). The damage was caused by the presence of too much solvent in the film when the flexible, PDMS blade was dragged across the free surface. The PDMS blade did not interact with the right side of the film (undamaged area).

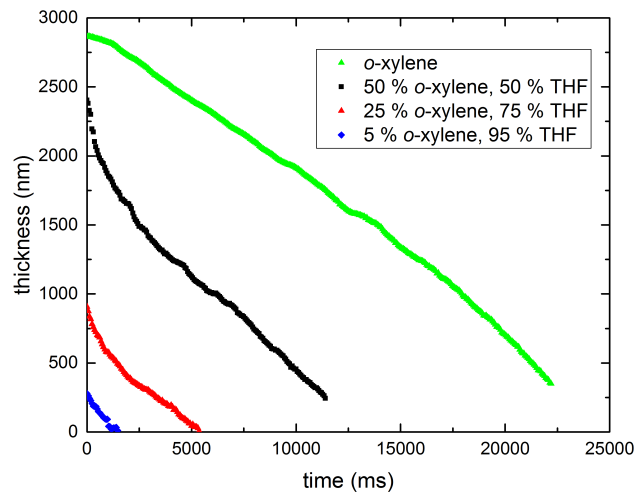


Figure C.9: Plot of drying curves for pure *o*-xylene (green data points) and 50:50 (black data points), 25:75 (red data points), and 5:95 (blue data points) mixtures (mass%:mass%) of *o*-xylene:tetrahydrofuran (THF). The THF evaporated almost immediately after casting, and an increase in the *o*-xylene content increased the drying time. The green and black lines did not reach a thickness of zero because measurements were stopped before the solvent had dried completely. Figure courtesy of John Saltwick.

REFERENCES

1. Shelton, C. K.; Jones, R. L.; Epps, T. H., III. *in preparation*.
2. Shelton, C. K.; Epps, T. H., III *Device and Method for Making Shear-Aligned, Solvent-Cast Films*. U.S. Prov. Pat. Appl. 62/264986, filed Dec. 9, 2015. U.S. Pat. Appl. Filed on Dec. 8, 2016.

Appendix D

SUPPORTING INFORMATION FOR CHAPTER 6

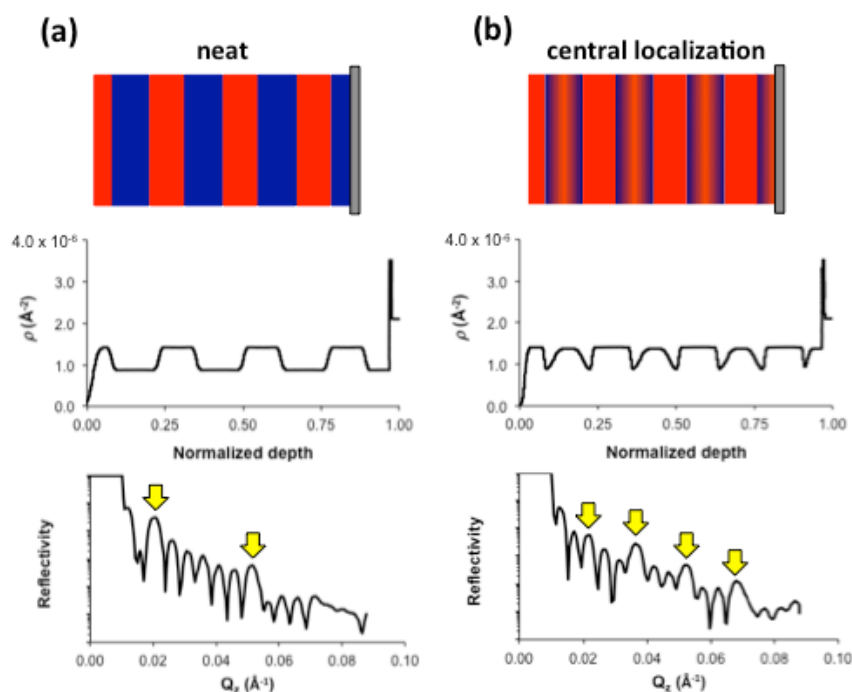


Figure D.1: Poly(styrene-*b*-oligo[oxyethylene] methacrylate) (PS-POEM) films doped with lithium salt as viewed by neutrons (blue = scattering length density [ρ] of POEM; red = ρ of PS) at the PS-POEM contrast match point (top row) along with predictive ρ (middle row) and neutron reflectometry (NR; bottom row) profiles. Films without salt-doping (a) result in NR profiles with Bragg peaks (highlighted with yellow arrows) related to the domain spacing. (b) Central localization of the salt within the POEM layers results in additional Bragg peaks related to the thickness between low ρ portions of the film (*i.e.*, PS-POEM interfaces). Depths were normalized such that 0.00 is the free surface and 1.00 is the substrate surface.¹

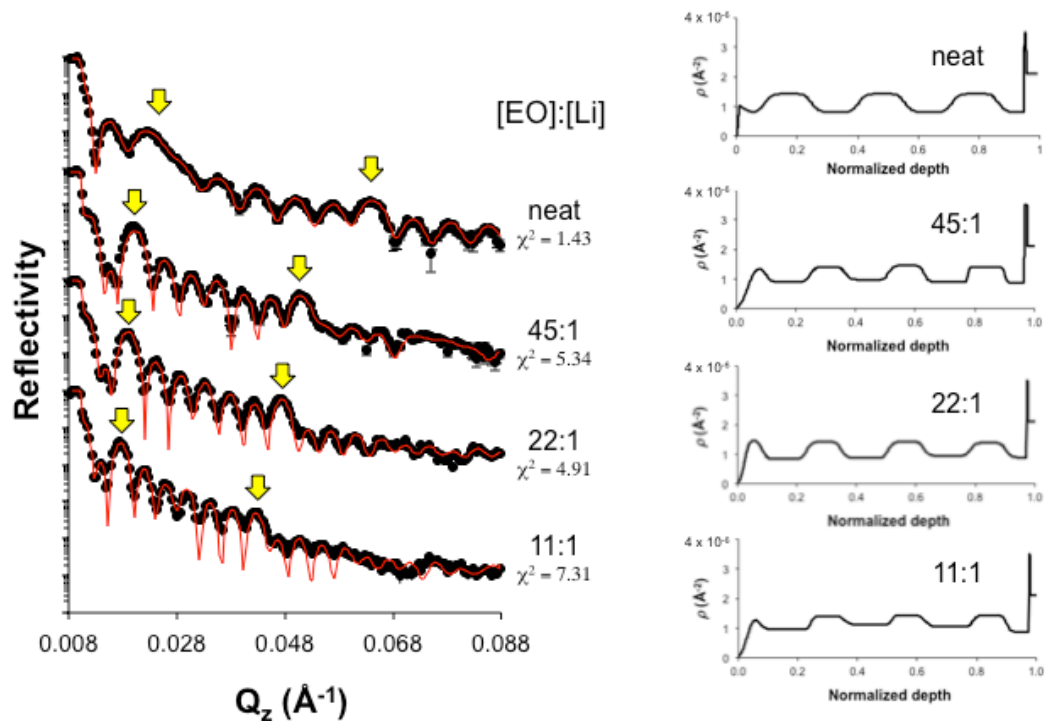


Figure D.2: NR profiles (black data points) and model fits (red lines) for neat PS-POEM films and films doped with lithium trifluoromethanesulfonate (Li triflate) at 45:1, 22:1, and 11:1 [EO]:[Li] ratios (left side), and ρ profiles as a function of film depth (right side; normalized from 0.0 [free surface] to 1.0 [substrate surface]). As the salt concentration increased, the $\rho_{POEM/salt}$ values increased (as indicated by ρ profiles and the decrease in relative intensity of Bragg peaks [highlighted by yellow arrows]), but a contrast match point was not reached at the [EO]:[Li] ratios studied, herein. Error bars in NR profiles represent one standard deviation from the measured intensity and were calculated during data reduction.¹

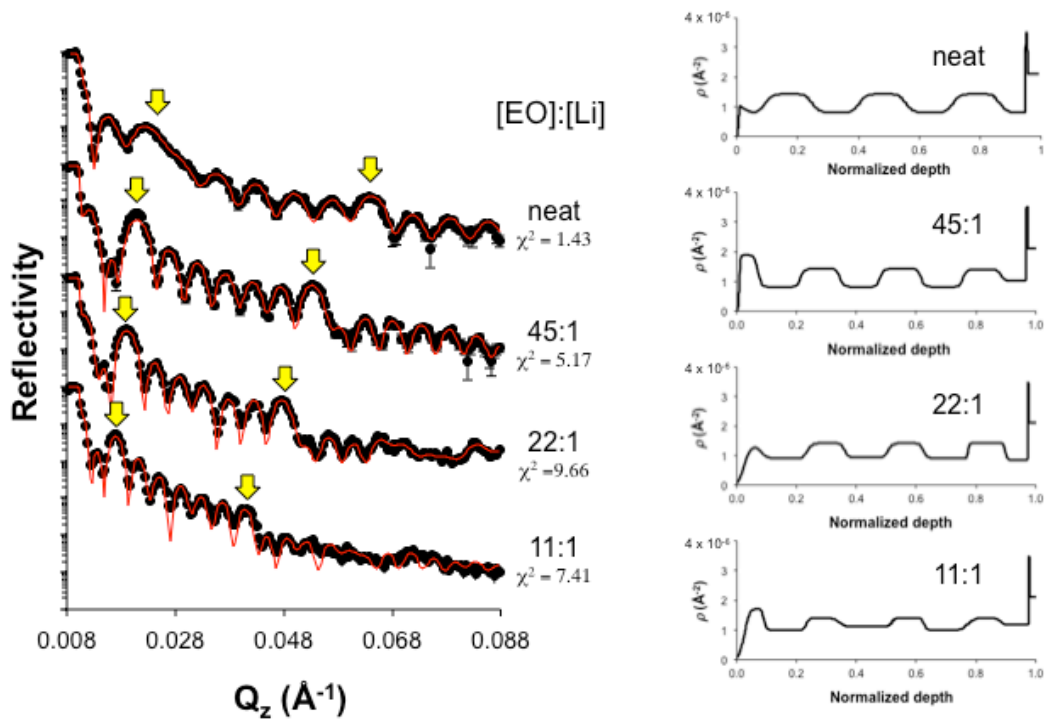


Figure D.3: NR profiles (black data points) and model fits (red lines) for neat PS-POEM films and films doped with lithium perchlorate (Li perchlorate) at 45:1, 22:1, and 11:1 [EO]:[Li] ratios (left side), and ρ profiles as a function of film depth (right side; normalized from 0.0 [free surface] to 1.0 [substrate surface]). As the salt concentration increased, the $\rho_{POEM/salt}$ values increased (as indicated by ρ profiles and the decrease in relative intensity of Bragg peaks [highlighted by yellow arrows]), but a contrast match point was not reached at the [EO]:[Li] ratios studied, herein. Error bars in NR profiles represent one standard deviation from the measured intensity and were calculated during data reduction.¹

D.1 Salt-Doped POEM Contrast Match with PS Calculations

The expected [EO]:[Li] ratios at which PS and POEM domains would be contrast matched during NR were calculated with Equations D.1 – D.3 for each salt (LiTFSI, Li triflate, Li perchlorate). In Equation D.1, the volume fraction of a given salt at the contrast match point ($\phi_{salt,CM}$) was determined from the scattering length densities of neat PS and POEM (ρ_{PS} and ρ_{POEM} , respectively).

$$\phi_{salt,CM} = 1 - \frac{\rho_{PS} - \rho_{salt}}{\rho_{POEM} - \rho_{salt}} \quad (D.1)$$

Then, the $\phi_{salt,CM}$ value from Equation D.1 was input into Equation D.2 to calculate the moles of salt at the contrast match point ($n_{salt,CM}$; assumed one mole total POEM and salt) using the density (d_{salt}) and molar mass (MM_{salt}) of the given salt.

$$n_{salt,CM} = \phi_{salt,CM} \frac{d_{salt}}{MM_{salt}} \quad (D.2)$$

Finally, the [EO]:[Li] value at the contrast match point ($[EO]:[Li]_{CM}$) was computed by dividing the moles of EO, determined by converting $\phi_{salt,CM}$ with the density (d_{PEO}) and molar mass (MM_{PEO}) of the PEO side chains in POEM, by $n_{salt,CM}$ as shown in Equation D.3.

$$[EO]:[Li]_{CM} = \frac{(1 - \phi_{salt,CM}) \frac{d_{PEO}}{MM_{PEO}}}{n_{salt,CM}} \quad (D.3)$$

From these calculations, [EO]:[Li]_{CM} ratios of 13:1, 6:1, and 5:1 were determined for LiTFSI, Li triflate, and Li perchlorate salts, respectively.

REFERENCES

1. Gartner, T. E., III; Morris, M. A.; Shelton, C. K.; Dura, J. A.; Epps, T. H., III. *in preparation*.

Appendix E

TEXT AND FIGURE REPRINT PERMISSIONS



RightsLink®

[Home](#)
[Account Info](#)
[Help](#)


Title: Directed self-assembly of block copolymers: a tutorial review of strategies for enabling nanotechnology with soft matter

Author: Hanqiong Hu, Manesh Gopinadhan, Chinedum O. Osuji

Publication: Soft Matter

Publisher: Royal Society of Chemistry

Date: Mar 21, 2014

Copyright © 2014, Royal Society of Chemistry

Logged in as:
Cameron Shelton
Account #:
3001024212

[LOGOUT](#)

Order Completed

Thank you for your order.

This Agreement between Cameron K Shelton ("You") and Royal Society of Chemistry ("Royal Society of Chemistry") consists of your license details and the terms and conditions provided by Royal Society of Chemistry and Copyright Clearance Center.

Your confirmation email will contain your order number for future reference.

[Printable details.](#)

License Number	4093650339336
License date	Apr 21, 2017
Licensed Content Publisher	Royal Society of Chemistry
Licensed Content Publication	Soft Matter
Licensed Content Title	Directed self-assembly of block copolymers: a tutorial review of strategies for enabling nanotechnology with soft matter
Licensed Content Author	Hanqiong Hu, Manesh Gopinadhan, Chinedum O. Osuji
Licensed Content Date	Mar 21, 2014
Licensed Content Volume	10
Licensed Content Issue	22
Type of Use	Thesis/Dissertation
Requestor type	academic/educational
Portion	figures/tables/images
Number of figures/tables/images	1
Distribution quantity	50
Format	print and electronic
Will you be translating?	no
Order reference number	
Title of the thesis/dissertation	Directed Self-Assembly in Block Polymer Thin Films: An Investigation with Neutron Scattering and In Situ Analysis Tools
Expected completion date	Jun 2017
Estimated size	350
Requestor Location	Cameron K Shelton 150 Academy Street

Billing Type Invoice
Billing address NEWARK, DE 19716
United States
Attn: Cameron K Shelton
Cameron K Shelton
150 Academy Street

Total NEWARK, DE 19716
United States
Attn: Cameron K Shelton
0.00 USD

[ORDER MORE](#)

[CLOSE WINDOW](#)

Copyright © 2017 [Copyright Clearance Center, Inc.](#) All Rights Reserved. [Privacy statement.](#) [Terms and Conditions.](#)
Comments? We would like to hear from you. E-mail us at customercare@copyright.com



RightsLink®

[Home](#)[Create Account](#)[Help](#)

Title: Effect of Architecture on the Phase Behavior of AB-Type Block Copolymer Melts

Author: M. W. Matsen

Publication: Macromolecules

Publisher: American Chemical Society

Date: Feb 1, 2012

Copyright © 2012, American Chemical Society

[LOGIN](#)

If you're a **copyright.com user**, you can login to RightsLink using your copyright.com credentials. Already a **RightsLink user** or want to [learn more?](#)

PERMISSION/LICENSE IS GRANTED FOR YOUR ORDER AT NO CHARGE

This type of permission/license, instead of the standard Terms & Conditions, is sent to you because no fee is being charged for your order. Please note the following:

- Permission is granted for your request in both print and electronic formats, and translations.
- If figures and/or tables were requested, they may be adapted or used in part.
- Please print this page for your records and send a copy of it to your publisher/graduate school.
- Appropriate credit for the requested material should be given as follows: "Reprinted (adapted) with permission from (COMPLETE REFERENCE CITATION). Copyright (YEAR) American Chemical Society." Insert appropriate information in place of the capitalized words.
- One-time permission is granted only for the use specified in your request. No additional uses are granted (such as derivative works or other editions). For any other uses, please submit a new request.

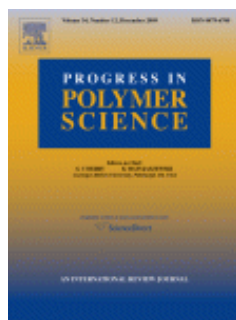
If credit is given to another source for the material you requested, permission must be obtained from that source.

[BACK](#)[CLOSE WINDOW](#)

Copyright © 2017 [Copyright Clearance Center, Inc.](#) All Rights Reserved. [Privacy statement](#). [Terms and Conditions](#). Comments? We would like to hear from you. E-mail us at customercare@copyright.com



RightsLink®

[Home](#)
[Account Info](#)
[Help](#)


Title: Polydispersity and block copolymer self-assembly
Author: Nathaniel A. Lynd, Adam J. Meuler, Marc A. Hillmyer
Publication: Progress in Polymer Science
Publisher: Elsevier
Date: September 2008

Logged in as:
Cameron Shelton
Account #:
3001024212

[LOGOUT](#)

Copyright © 2008 Elsevier Ltd. All rights reserved.

Order Completed

Thank you for your order.

This Agreement between Cameron K Shelton ("You") and Elsevier ("Elsevier") consists of your license details and the terms and conditions provided by Elsevier and Copyright Clearance Center.

Your confirmation email will contain your order number for future reference.

[Printable details.](#)

License Number	4093650712751
License date	Apr 21, 2017
Licensed Content Publisher	Elsevier
Licensed Content Publication	Progress in Polymer Science
Licensed Content Title	Polydispersity and block copolymer self-assembly
Licensed Content Author	Nathaniel A. Lynd, Adam J. Meuler, Marc A. Hillmyer
Licensed Content Date	September 2008
Licensed Content Volume	33
Licensed Content Issue	9
Licensed Content Pages	19
Type of Use	reuse in a thesis/dissertation
Portion	figures/tables/illustrations
Number of figures/tables/illustrations	1
Format	both print and electronic
Are you the author of this Elsevier article?	No
Will you be translating?	No
Order reference number	
Original figure numbers	Figure 1
Title of your thesis/dissertation	Directed Self-Assembly in Block Polymer Thin Films: An Investigation with Neutron Scattering and In Situ Analysis Tools
Expected completion date	Jun 2017
Estimated size (number of pages)	350
Elsevier VAT number	GB 494 6272 12
Requestor Location	Cameron K Shelton 150 Academy Street NEWARK, DE 19716 United States Attn: Cameron K Shelton
Publisher Tax ID	98-0397604

Total

0.00 USD

[ORDER MORE](#)

[CLOSE WINDOW](#)

Copyright © 2017 [Copyright Clearance Center, Inc.](#) All Rights Reserved. [Privacy statement](#). [Terms and Conditions](#).
Comments? We would like to hear from you. E-mail us at customer care@copyright.com



RightsLink®

[Home](#)[Create Account](#)[Help](#)

Title: Interfacial Interaction
Dependence of Microdomain
Orientation in Diblock
Copolymer Thin Films

Author: Ting Xu, Craig J. Hawker,
Thomas P. Russell

Publication: Macromolecules

Publisher: American Chemical Society

Date: Apr 1, 2005

Copyright © 2005, American Chemical Society

[LOGIN](#)

If you're a [copyright.com user](#), you can login to RightsLink using your copyright.com credentials. Already a [RightsLink user](#) or want to [learn more?](#)

PERMISSION/LICENSE IS GRANTED FOR YOUR ORDER AT NO CHARGE

This type of permission/license, instead of the standard Terms & Conditions, is sent to you because no fee is being charged for your order. Please note the following:

- Permission is granted for your request in both print and electronic formats, and translations.
- If figures and/or tables were requested, they may be adapted or used in part.
- Please print this page for your records and send a copy of it to your publisher/graduate school.
- Appropriate credit for the requested material should be given as follows: "Reprinted (adapted) with permission from (COMPLETE REFERENCE CITATION). Copyright (YEAR) American Chemical Society." Insert appropriate information in place of the capitalized words.
- One-time permission is granted only for the use specified in your request. No additional uses are granted (such as derivative works or other editions). For any other uses, please submit a new request.

If credit is given to another source for the material you requested, permission must be obtained from that source.

[BACK](#)[CLOSE WINDOW](#)

Copyright © 2017 [Copyright Clearance Center, Inc.](#) All Rights Reserved. [Privacy statement](#). [Terms and Conditions](#).
Comments? We would like to hear from you. E-mail us at customercare@copyright.com



RightsLink®

[Home](#)
[Account Info](#)
[Help](#)


Title: Reordering transitions during annealing of block copolymer cylinder phases

Author: Pawel W. Majewski, Kevin G. Yager

Publication: Soft Matter

Publisher: Royal Society of Chemistry

Date: Oct 6, 2015

Copyright © 2015, Royal Society of Chemistry

Logged in as:
Cameron Shelton
Account #:
3001024212

[LOGOUT](#)

Order Completed

Thank you for your order.

This Agreement between Cameron K Shelton ("You") and Royal Society of Chemistry ("Royal Society of Chemistry") consists of your license details and the terms and conditions provided by Royal Society of Chemistry and Copyright Clearance Center.

Your confirmation email will contain your order number for future reference.

[Printable details.](#)

License Number	4093650910842
License date	Apr 21, 2017
Licensed Content Publisher	Royal Society of Chemistry
Licensed Content Publication	Soft Matter
Licensed Content Title	Reordering transitions during annealing of block copolymer cylinder phases
Licensed Content Author	Pawel W. Majewski, Kevin G. Yager
Licensed Content Date	Oct 6, 2015
Licensed Content Volume	12
Licensed Content Issue	1
Type of Use	Thesis/Dissertation
Requestor type	academic/educational
Portion	figures/tables/images
Number of figures/tables/images	1
Distribution quantity	50
Format	print and electronic
Will you be translating?	no
Order reference number	
Title of the thesis/dissertation	Directed Self-Assembly in Block Polymer Thin Films: An Investigation with Neutron Scattering and In Situ Analysis Tools
Expected completion date	Jun 2017
Estimated size	350
Requestor Location	Cameron K Shelton 150 Academy Street

NEWARK, DE 19716

4/21/2017

Rightslink® by Copyright Clearance Center

Billing Type United States
Billing address Attn: Cameron K Shelton
Invoice
Cameron K Shelton
150 Academy Street

Total NEWARK, DE 19716
United States
Attn: Cameron K Shelton
0.00 USD

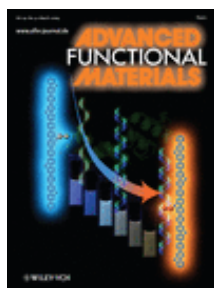
[ORDER MORE](#)

[CLOSE WINDOW](#)

Copyright © 2017 [Copyright Clearance Center, Inc.](#) All Rights Reserved. [Privacy statement](#). [Terms and Conditions](#).
Comments? We would like to hear from you. E-mail us at customercare@copyright.com



RightsLink®

[Home](#)
[Account Info](#)
[Help](#)


Title: Widely Tunable Morphologies in Block Copolymer Thin Films Through Solvent Vapor Annealing Using Mixtures of Selective Solvents

Author: Michelle A. Chavis, Detlef-M. Smilgies, Ulrich B. Wiesner, Christopher K. Ober

Publication: Advanced Functional Materials

Publisher: John Wiley and Sons

Date: Apr 11, 2015

© 2015 WILEY-VCH Verlag GmbH & Co. KGaA, Weinheim

Logged in as:
Cameron Shelton
Account #:
3001024212

[LOGOUT](#)

Order Completed

Thank you for your order.

This Agreement between Cameron K Shelton ("You") and John Wiley and Sons ("John Wiley and Sons") consists of your license details and the terms and conditions provided by John Wiley and Sons and Copyright Clearance Center.

Your confirmation email will contain your order number for future reference.

[Printable details.](#)

License Number	4093651065741
License date	Apr 21, 2017
Licensed Content Publisher	John Wiley and Sons
Licensed Content Publication	Advanced Functional Materials
Licensed Content Title	Widely Tunable Morphologies in Block Copolymer Thin Films Through Solvent Vapor Annealing Using Mixtures of Selective Solvents
Licensed Content Author	Michelle A. Chavis, Detlef-M. Smilgies, Ulrich B. Wiesner, Christopher K. Ober
Licensed Content Date	Apr 11, 2015
Licensed Content Pages	9
Type of use	Dissertation/Thesis
Requestor type	University/Academic
Format	Print and electronic
Portion	Figure/table
Number of figures/tables	1
Original Wiley figure/table number(s)	Figure 2
Will you be translating?	No
Title of your thesis / dissertation	Directed Self-Assembly in Block Polymer Thin Films: An Investigation with Neutron Scattering and In Situ Analysis Tools
Expected completion date	Jun 2017
Expected size (number of pages)	350
Requestor Location	Cameron K Shelton 150 Academy Street

Publisher Tax ID
Billing Type
Billing address

NEWARK, DE 19716
United States
Attn: Cameron K Shelton
EU826007151
Invoice
Cameron K Shelton
150 Academy Street

Total

NEWARK, DE 19716
United States
Attn: Cameron K Shelton
0.00 USD

Would you like to purchase the full text of this article? If so, please continue on to the content ordering system located here: [Purchase PDF](#)

If you click on the buttons below or close this window, you will not be able to return to the content ordering system.

[ORDER MORE](#)

[CLOSE WINDOW](#)

Copyright © 2017 [Copyright Clearance Center, Inc.](#) All Rights Reserved. [Privacy statement.](#) [Terms and Conditions.](#)
Comments? We would like to hear from you. E-mail us at customercare@copyright.com



RightsLink®

[Home](#)
[Account Info](#)
[Help](#)


Title: Epitaxial self-assembly of block copolymers on lithographically defined nanopatterned substrates

Logged in as:
Cameron Shelton
Account #:
3001024212

Author: Sang Ouk Kim, Harun H. Solak, Mark P. Stoykovich, Nicola J. Ferrier, Juan J. de Pablo et al.

[LOGOUT](#)

Publication: Nature

Publisher: Nature Publishing Group

Date: Jul 24, 2003

Copyright © 2003, Rights Managed by Nature Publishing Group

Order Completed

Thank you for your order.

This Agreement between Cameron K Shelton ("You") and Nature Publishing Group ("Nature Publishing Group") consists of your license details and the terms and conditions provided by Nature Publishing Group and Copyright Clearance Center.

Your confirmation email will contain your order number for future reference.

[Printable details.](#)

License Number	4093651250555
License date	Apr 21, 2017
Licensed Content Publisher	Nature Publishing Group
Licensed Content Publication	Nature
Licensed Content Title	Epitaxial self-assembly of block copolymers on lithographically defined nanopatterned substrates
Licensed Content Author	Sang Ouk Kim, Harun H. Solak, Mark P. Stoykovich, Nicola J. Ferrier, Juan J. de Pablo et al.
Licensed Content Date	Jul 24, 2003
Licensed Content Volume	424
Licensed Content Issue	6947
Type of Use	reuse in a dissertation / thesis
Requestor type	academic/educational
Format	print and electronic
Portion	figures/tables/illustrations
Number of figures/tables/illustrations	1
High-res required	no
Figures	Figure 1
Author of this NPG article	no
Your reference number	
Title of your thesis / dissertation	Directed Self-Assembly in Block Polymer Thin Films: An Investigation with Neutron Scattering and In Situ Analysis Tools
Expected completion date	Jun 2017
Estimated size (number of pages)	350
Requestor Location	Cameron K Shelton 150 Academy Street

4/21/2017

Rightslink® by Copyright Clearance Center

NEWARK, DE 19716
United States
Attn: Cameron K Shelton

Billing Type
Billing address

Invoice
Cameron K Shelton
150 Academy Street

NEWARK, DE 19716
United States
Attn: Cameron K Shelton

Total

0.00 USD

[ORDER MORE](#)

[CLOSE WINDOW](#)

Copyright © 2017 [Copyright Clearance Center, Inc.](#) All Rights Reserved. [Privacy statement.](#) [Terms and Conditions.](#)
Comments? We would like to hear from you. E-mail us at customercare@copyright.com



RightsLink®

Home

Account
Info

Help



Title: Directed self-assembly of block copolymer films on atomically-thin graphene chemical patterns

Author: Tzu-Hsuan Chang, Shisheng Xiong, Robert M. Jacobberger, Solomon Mikael, Hyo Seon Suh et al.

Publication: Scientific Reports

Publisher: Nature Publishing Group

Date: Aug 16, 2016

Copyright © 2016, Rights Managed by Nature Publishing Group

Logged in as:
Cameron Shelton
Account #:
3001024212

LOGOUT

Creative Commons

The article for which you have requested permission has been distributed under a Creative Commons CC-BY license (please see the article itself for the license version number). You may reuse this material without obtaining permission from Nature Publishing Group, providing that the author and the original source of publication are fully acknowledged, as per the terms of the license.

For license terms, please see <http://creativecommons.org/>

CLOSE WINDOW

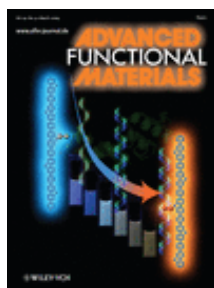
Are you the [author](#) of this NPG article?

To order reprints of this content, please contact the Nature Publishing Group reprint office by e-mail: reprints@nature.com.

Copyright © 2017 [Copyright Clearance Center, Inc.](#) All Rights Reserved. [Privacy statement.](#) [Terms and Conditions.](#)
Comments? We would like to hear from you. E-mail us at customercare@copyright.com



RightsLink®

[Home](#)
[Account Info](#)
[Help](#)


Title: Integration of Density Multiplication in the Formation of Device-Oriented Structures by Directed Assembly of Block Copolymer–Homopolymer Blends

Author: Guoliang Liu, Carla S. Thomas, Gordon S. W. Craig, Paul F. Nealey

Publication: Advanced Functional Materials

Publisher: John Wiley and Sons

Date: Mar 25, 2010

Copyright © 2010 WILEY-VCH Verlag GmbH & Co. KGaA, Weinheim

Logged in as:
Cameron Shelton
Account #:
3001024212

[LOGOUT](#)

Order Completed

Thank you for your order.

This Agreement between Cameron K Shelton ("You") and John Wiley and Sons ("John Wiley and Sons") consists of your license details and the terms and conditions provided by John Wiley and Sons and Copyright Clearance Center.

Your confirmation email will contain your order number for future reference.

[Printable details.](#)

License Number	4093651423034
License date	Apr 21, 2017
Licensed Content Publisher	John Wiley and Sons
Licensed Content Publication	Advanced Functional Materials
Licensed Content Title	Integration of Density Multiplication in the Formation of Device-Oriented Structures by Directed Assembly of Block Copolymer–Homopolymer Blends
Licensed Content Author	Guoliang Liu, Carla S. Thomas, Gordon S. W. Craig, Paul F. Nealey
Licensed Content Date	Mar 25, 2010
Licensed Content Pages	7
Type of use	Dissertation/Thesis
Requestor type	University/Academic
Format	Print and electronic
Portion	Figure/table
Number of figures/tables	1
Original Wiley figure/table number(s)	Figure 4
Will you be translating?	No
Title of your thesis / dissertation	Directed Self-Assembly in Block Polymer Thin Films: An Investigation with Neutron Scattering and In Situ Analysis Tools
Expected completion date	Jun 2017
Expected size (number of pages)	350
Requestor Location	Cameron K Shelton 150 Academy Street

Publisher Tax ID NEWARK, DE 19716
United States
Attn: Cameron K Shelton
Billing Type EU826007151
Invoice
Billing address Cameron K Shelton
150 Academy Street

Total NEWARK, DE 19716
United States
Attn: Cameron K Shelton
0.00 USD

Would you like to purchase the full text of this article? If so, please continue on to the content ordering system located here: [Purchase PDF](#)

If you click on the buttons below or close this window, you will not be able to return to the content ordering system.

[ORDER MORE](#)

[CLOSE WINDOW](#)

Copyright © 2017 [Copyright Clearance Center, Inc.](#) All Rights Reserved. [Privacy statement](#). [Terms and Conditions](#).
Comments? We would like to hear from you. E-mail us at customercare@copyright.com



RightsLink®

[Home](#)[Account Info](#)[Help](#)

Title: Millisecond Ordering of Block Copolymer Films via Photothermal Gradients

Author: Pawel W. Majewski, Kevin G. Yager

Publication: ACS Nano

Publisher: American Chemical Society

Date: Apr 1, 2015

Copyright © 2015, American Chemical Society

Logged in as:
Cameron Shelton
Account #:
3001024212

[LOGOUT](#)

PERMISSION/LICENSE IS GRANTED FOR YOUR ORDER AT NO CHARGE

This type of permission/license, instead of the standard Terms & Conditions, is sent to you because no fee is being charged for your order. Please note the following:

- Permission is granted for your request in both print and electronic formats, and translations.
- If figures and/or tables were requested, they may be adapted or used in part.
- Please print this page for your records and send a copy of it to your publisher/graduate school.
- Appropriate credit for the requested material should be given as follows: "Reprinted (adapted) with permission from (COMPLETE REFERENCE CITATION). Copyright (YEAR) American Chemical Society." Insert appropriate information in place of the capitalized words.
- One-time permission is granted only for the use specified in your request. No additional uses are granted (such as derivative works or other editions). For any other uses, please submit a new request.

If credit is given to another source for the material you requested, permission must be obtained from that source.

[BACK](#)[CLOSE WINDOW](#)

Copyright © 2017 [Copyright Clearance Center, Inc.](#) All Rights Reserved. [Privacy statement.](#) [Terms and Conditions.](#) Comments? We would like to hear from you. E-mail us at customercare@copyright.com



RightsLink®

[Home](#)
[Account Info](#)
[Help](#)


Title: A generalized method for alignment of block copolymer films: solvent vapor annealing with soft shear

Author: Zhe Qiang, Yuanzhong Zhang, Jesse A. Groff, Kevin A. Cavicchi, Bryan D. Vogt

Publication: Soft Matter

Publisher: Royal Society of Chemistry

Date: Jun 20, 2014

Copyright © 2014, Royal Society of Chemistry

Logged in as:
Cameron Shelton
Account #:
3001024212

[LOGOUT](#)

Order Completed

Thank you for your order.

This Agreement between Cameron K Shelton ("You") and Royal Society of Chemistry ("Royal Society of Chemistry") consists of your license details and the terms and conditions provided by Royal Society of Chemistry and Copyright Clearance Center.

Your confirmation email will contain your order number for future reference.

[Printable details.](#)

License Number	4093660056816
License date	Apr 21, 2017
Licensed Content Publisher	Royal Society of Chemistry
Licensed Content Publication	Soft Matter
Licensed Content Title	A generalized method for alignment of block copolymer films: solvent vapor annealing with soft shear
Licensed Content Author	Zhe Qiang, Yuanzhong Zhang, Jesse A. Groff, Kevin A. Cavicchi, Bryan D. Vogt
Licensed Content Date	Jun 20, 2014
Licensed Content Volume	10
Licensed Content Issue	32
Type of Use	Thesis/Dissertation
Requestor type	academic/educational
Portion	figures/tables/images
Number of figures/tables/images	1
Distribution quantity	50
Format	print and electronic
Will you be translating?	no
Order reference number	
Title of the thesis/dissertation	Directed Self-Assembly in Block Polymer Thin Films: An Investigation with Neutron Scattering and In Situ Analysis Tools
Expected completion date	Jun 2017
Estimated size	350
Requestor Location	Cameron K Shelton 150 Academy Street

Billing Type Invoice
Billing address NEWARK, DE 19716
United States
Attn: Cameron K Shelton
Cameron K Shelton
150 Academy Street

Total NEWARK, DE 19716
United States
Attn: Cameron K Shelton
0.00 USD

[ORDER MORE](#)

[CLOSE WINDOW](#)

Copyright © 2017 [Copyright Clearance Center, Inc.](#) All Rights Reserved. [Privacy statement.](#) [Terms and Conditions.](#)
Comments? We would like to hear from you. E-mail us at customercare@copyright.com



RightsLink®

[Home](#)[Account Info](#)[Help](#)

Title: Spatial and Orientation Control of Cylindrical Nanostructures in ABA Triblock Copolymer Thin Films by Raster Solvent Vapor Annealing

Logged in as:
Cameron Shelton
Account #:
3001024212

[LOGOUT](#)

Author: Jonathan E. Seppala, Ronald L. Lewis, Thomas H. Epps

Publication: ACS Nano

Publisher: American Chemical Society

Date: Nov 1, 2012

Copyright © 2012, American Chemical Society

PERMISSION/LICENSE IS GRANTED FOR YOUR ORDER AT NO CHARGE

This type of permission/license, instead of the standard Terms & Conditions, is sent to you because no fee is being charged for your order. Please note the following:

- Permission is granted for your request in both print and electronic formats, and translations.
- If figures and/or tables were requested, they may be adapted or used in part.
- Please print this page for your records and send a copy of it to your publisher/graduate school.
- Appropriate credit for the requested material should be given as follows: "Reprinted (adapted) with permission from (COMPLETE REFERENCE CITATION). Copyright (YEAR) American Chemical Society." Insert appropriate information in place of the capitalized words.
- One-time permission is granted only for the use specified in your request. No additional uses are granted (such as derivative works or other editions). For any other uses, please submit a new request.

If credit is given to another source for the material you requested, permission must be obtained from that source.

[BACK](#)[CLOSE WINDOW](#)

Copyright © 2017 [Copyright Clearance Center, Inc.](#) All Rights Reserved. [Privacy statement](#). [Terms and Conditions](#).
Comments? We would like to hear from you. E-mail us at customercare@copyright.com



RightsLink®

[Home](#)[Account Info](#)[Help](#)

Title: Decoupling Substrate Surface Interactions in Block Polymer Thin Film Self-Assembly

Logged in as:
Cameron Shelton
Account #:
3001024212

Author: Cameron K. Shelton, Thomas H. Epps

[LOGOUT](#)

Publication: Macromolecules

Publisher: American Chemical Society

Date: Jul 1, 2015

Copyright © 2015, American Chemical Society

PERMISSION/LICENSE IS GRANTED FOR YOUR ORDER AT NO CHARGE

This type of permission/license, instead of the standard Terms & Conditions, is sent to you because no fee is being charged for your order. Please note the following:

- Permission is granted for your request in both print and electronic formats, and translations.
- If figures and/or tables were requested, they may be adapted or used in part.
- Please print this page for your records and send a copy of it to your publisher/graduate school.
- Appropriate credit for the requested material should be given as follows: "Reprinted (adapted) with permission from (COMPLETE REFERENCE CITATION). Copyright (YEAR) American Chemical Society." Insert appropriate information in place of the capitalized words.
- One-time permission is granted only for the use specified in your request. No additional uses are granted (such as derivative works or other editions). For any other uses, please submit a new request.

[BACK](#)[CLOSE WINDOW](#)

Copyright © 2017 [Copyright Clearance Center, Inc.](#) All Rights Reserved. [Privacy statement.](#) [Terms and Conditions.](#) Comments? We would like to hear from you. E-mail us at customercare@copyright.com



RightsLink®

[Home](#)[Account Info](#)[Help](#)

Title: Mapping Substrate Surface Field Propagation in Block Polymer Thin Films

Logged in as:
Cameron Shelton
Account #:
3001024212

Author: Cameron K. Shelton, Thomas H. Epps

[LOGOUT](#)

Publication: Macromolecules

Publisher: American Chemical Society

Date: Jan 1, 2016

Copyright © 2016, American Chemical Society

PERMISSION/LICENSE IS GRANTED FOR YOUR ORDER AT NO CHARGE

This type of permission/license, instead of the standard Terms & Conditions, is sent to you because no fee is being charged for your order. Please note the following:

- Permission is granted for your request in both print and electronic formats, and translations.
- If figures and/or tables were requested, they may be adapted or used in part.
- Please print this page for your records and send a copy of it to your publisher/graduate school.
- Appropriate credit for the requested material should be given as follows: "Reprinted (adapted) with permission from (COMPLETE REFERENCE CITATION). Copyright (YEAR) American Chemical Society." Insert appropriate information in place of the capitalized words.
- One-time permission is granted only for the use specified in your request. No additional uses are granted (such as derivative works or other editions). For any other uses, please submit a new request.

[BACK](#)[CLOSE WINDOW](#)

Copyright © 2017 [Copyright Clearance Center, Inc.](#) All Rights Reserved. [Privacy statement.](#) [Terms and Conditions.](#) Comments? We would like to hear from you. E-mail us at customercare@copyright.com



RightsLink®

[Home](#)[Account Info](#)[Help](#)

Title: Tracking Solvent Distribution in Block Polymer Thin Films during Solvent Vapor Annealing with in Situ Neutron Scattering

Logged in as:
Cameron Shelton
Account #:
3001024212

Author: Cameron K. Shelton, Ronald L. Jones, Joseph A. Dura, et al

[LOGOUT](#)

Publication: Macromolecules

Publisher: American Chemical Society

Date: Oct 1, 2016

Copyright © 2016, American Chemical Society

PERMISSION/LICENSE IS GRANTED FOR YOUR ORDER AT NO CHARGE

This type of permission/license, instead of the standard Terms & Conditions, is sent to you because no fee is being charged for your order. Please note the following:

- Permission is granted for your request in both print and electronic formats, and translations.
- If figures and/or tables were requested, they may be adapted or used in part.
- Please print this page for your records and send a copy of it to your publisher/graduate school.
- Appropriate credit for the requested material should be given as follows: "Reprinted (adapted) with permission from (COMPLETE REFERENCE CITATION). Copyright (YEAR) American Chemical Society." Insert appropriate information in place of the capitalized words.
- One-time permission is granted only for the use specified in your request. No additional uses are granted (such as derivative works or other editions). For any other uses, please submit a new request.

[BACK](#)[CLOSE WINDOW](#)

Copyright © 2017 [Copyright Clearance Center, Inc.](#) All Rights Reserved. [Privacy statement.](#) [Terms and Conditions.](#) Comments? We would like to hear from you. E-mail us at customercare@copyright.com



RightsLink®

[Home](#)[Account Info](#)[Help](#)

Title: Symmetric Diblock Copolymer Thin Films on Rough Substrates. Kinetics and Structure Formation in Pure Block Copolymer Thin Films

Logged in as:
Cameron Shelton
Account #:
3001024212

[LOGOUT](#)

Author: E. Sivaniah, Y. Hayashi, S. Matsubara, et al

Publication: Macromolecules

Publisher: American Chemical Society

Date: Mar 1, 2005

Copyright © 2005, American Chemical Society

PERMISSION/LICENSE IS GRANTED FOR YOUR ORDER AT NO CHARGE

This type of permission/license, instead of the standard Terms & Conditions, is sent to you because no fee is being charged for your order. Please note the following:

- Permission is granted for your request in both print and electronic formats, and translations.
- If figures and/or tables were requested, they may be adapted or used in part.
- Please print this page for your records and send a copy of it to your publisher/graduate school.
- Appropriate credit for the requested material should be given as follows: "Reprinted (adapted) with permission from (COMPLETE REFERENCE CITATION). Copyright (YEAR) American Chemical Society." Insert appropriate information in place of the capitalized words.
- One-time permission is granted only for the use specified in your request. No additional uses are granted (such as derivative works or other editions). For any other uses, please submit a new request.

If credit is given to another source for the material you requested, permission must be obtained from that source.

[BACK](#)[CLOSE WINDOW](#)

Copyright © 2017 [Copyright Clearance Center, Inc.](#) All Rights Reserved. [Privacy statement.](#) [Terms and Conditions.](#) Comments? We would like to hear from you. E-mail us at customercare@copyright.com



RightsLink®

[Home](#)[Account Info](#)[Help](#)

Title: Combinatorial Block Copolymer
Ordering on Tunable Rough
Substrates

Logged in as:
Cameron Shelton
Account #:
3001024212

Author: Manish M. Kulkarni, Kevin G.
Yager, Ashutosh Sharma, et al

[LOGOUT](#)

Publication: Macromolecules

Publisher: American Chemical Society

Date: May 1, 2012

Copyright © 2012, American Chemical Society

PERMISSION/LICENSE IS GRANTED FOR YOUR ORDER AT NO CHARGE

This type of permission/license, instead of the standard Terms & Conditions, is sent to you because no fee is being charged for your order. Please note the following:

- Permission is granted for your request in both print and electronic formats, and translations.
- If figures and/or tables were requested, they may be adapted or used in part.
- Please print this page for your records and send a copy of it to your publisher/graduate school.
- Appropriate credit for the requested material should be given as follows: "Reprinted (adapted) with permission from (COMPLETE REFERENCE CITATION). Copyright (YEAR) American Chemical Society." Insert appropriate information in place of the capitalized words.
- One-time permission is granted only for the use specified in your request. No additional uses are granted (such as derivative works or other editions). For any other uses, please submit a new request.

If credit is given to another source for the material you requested, permission must be obtained from that source.

[BACK](#)[CLOSE WINDOW](#)

Copyright © 2017 [Copyright Clearance Center, Inc.](#) All Rights Reserved. [Privacy statement.](#) [Terms and Conditions.](#)
Comments? We would like to hear from you. E-mail us at customercare@copyright.com



RightsLink®

[Home](#)
[Account Info](#)
[Help](#)


Title: Voxelated liquid crystal elastomers

Author: Taylor H. Ware, Michael E. McConney, Jeong Jae Wie, Vincent P. Tondiglia, Timothy J. White

Logged in as:
Cameron Shelton
Account #:
3001024212

[LOGOUT](#)

Publication: Science

Publisher: The American Association for the Advancement of Science

Date: Feb 27, 2015

Copyright © 2015, Copyright © 2015, American Association for the Advancement of Science

Order Completed

Thank you for your order.

This Agreement between Cameron K Shelton ("You") and The American Association for the Advancement of Science ("The American Association for the Advancement of Science") consists of your license details and the terms and conditions provided by The American Association for the Advancement of Science and Copyright Clearance Center.

Your confirmation email will contain your order number for future reference.

[Printable details.](#)

License Number	4093661329434
License date	Apr 21, 2017
Licensed Content Publisher	The American Association for the Advancement of Science
Licensed Content Publication	Science
Licensed Content Title	Voxelated liquid crystal elastomers
Licensed Content Author	Taylor H. Ware, Michael E. McConney, Jeong Jae Wie, Vincent P. Tondiglia, Timothy J. White
Licensed Content Date	Feb 27, 2015
Licensed Content Volume	347
Licensed Content Issue	6225
Volume number	347
Issue number	6225
Type of Use	Thesis / Dissertation
Requestor type	Scientist/individual at a research institution
Format	Print and electronic
Portion	Figure
Number of figures/tables	1
Order reference number	
Title of your thesis / dissertation	Directed Self-Assembly in Block Polymer Thin Films: An Investigation with Neutron Scattering and In Situ Analysis Tools
Expected completion date	Jun 2017
Estimated size(pages)	350
Requestor Location	Cameron K Shelton 150 Academy Street

Billing Type NEWARK, DE 19716
United States
Attn: Cameron K Shelton
Billing address Invoice
Cameron K Shelton
150 Academy Street

Total NEWARK, DE 19716
United States
Attn: Cameron K Shelton
0.00 USD

[ORDER MORE](#)

[CLOSE WINDOW](#)

Copyright © 2017 [Copyright Clearance Center, Inc.](#) All Rights Reserved. [Privacy statement.](#) [Terms and Conditions.](#)
Comments? We would like to hear from you. E-mail us at customercare@copyright.com



RightsLink®

[Home](#)[Account Info](#)[Help](#)

Title: Surface Morphology Diagram for Cylinder-Forming Block Copolymer Thin Films

Logged in as:
Cameron Shelton
Account #:
3001024212

Author: Xiaohua Zhang, Brian C. Berry, Kevin G. Yager, et al

[LOGOUT](#)

Publication: ACS Nano

Publisher: American Chemical Society

Date: Nov 1, 2008

Copyright © 2008, American Chemical Society

PERMISSION/LICENSE IS GRANTED FOR YOUR ORDER AT NO CHARGE

This type of permission/license, instead of the standard Terms & Conditions, is sent to you because no fee is being charged for your order. Please note the following:

- Permission is granted for your request in both print and electronic formats, and translations.
- If figures and/or tables were requested, they may be adapted or used in part.
- Please print this page for your records and send a copy of it to your publisher/graduate school.
- Appropriate credit for the requested material should be given as follows: "Reprinted (adapted) with permission from (COMPLETE REFERENCE CITATION). Copyright (YEAR) American Chemical Society." Insert appropriate information in place of the capitalized words.
- One-time permission is granted only for the use specified in your request. No additional uses are granted (such as derivative works or other editions). For any other uses, please submit a new request.

If credit is given to another source for the material you requested, permission must be obtained from that source.

[BACK](#)[CLOSE WINDOW](#)

Copyright © 2017 [Copyright Clearance Center, Inc.](#) All Rights Reserved. [Privacy statement.](#) [Terms and Conditions.](#) Comments? We would like to hear from you. E-mail us at customercare@copyright.com